Near-vent processes of the 273 ka Poris eruption (Tenerife)

Thesis submitted in accordance with the requirements
of the University of Liverpool for the degree of

Doctor in Philosophy

by
Natasha Joanne Smith
March 2012

Abstract

Near-vent processes during caldera-forming explosive eruptions are poorly known, as are relations between proximal and counterpart distal ignimbrites. Consequently, understanding of the full course of these eruptions and how to analyse their deposits for purposes of hazard assessment has been limited. This study aims to address the limitations by using a lithofacies architecture approach to investigate a proximal succession that has a closely studied distal counterpart. The Poris Formation (273 ka) of Tenerife is well exposed in the Diego Hernandez wall of Las Cañadas and detailed interpretations of its distal-flank ignimbrites have been published. In this study, Poris proximal lithofacies architecture is described, geochemical and stratigraphic analyses are used to correlate the proximal and distal successions, and a coherent model for the Poris eruption is presented.

The proximal Poris succession records an opening Plinian phase, followed by the generation of a pyroclastic density current (PDC) that was partly blocked by near-vent topography. The upper part of the current surmounted the barrier and deposited an ignimbrite veneer. During a widespread hiatus in flow, ash and various ash aggregates were deposited from a hybrid cloud that included parts of both the Plinian and co-ignimbrite plumes. Phreatomagmatic explosivity then generated an erosive PDC rich in fine lithics; initial waxing was followed by pulsatory current waning, recorded in repeated sets of inversely graded tuff. Hybrid deposition ensued, as coarse pumice fallout and ballistic material entered PDCs to become deposited as a stratified pumice-block tuff. A main phase of PDC activity then occurred, recorded by 9 m of massive lapilli tuff with evidence of widespread scour and bypass, and including lithic-rich layers that record incremental edifice disruption. Laterally variable stratification and load structures show that the PDC was highly non-uniform and unsteady at this time. Climactic caldera collapse is recorded proximally as a lithic-block layer in erosive contact with the underlying ignimbrite, which marks widespread bypass to distal slopes. A pumice-block breccia 10 m thick records the eruption waning.

Published accounts of the distal Poris stratigraphy are described and correlation with the proximal record is made based on physical characteristics and geochemical trends. The occurrence of distinctive grey accretionary pellets in an ash layer above the proximal phreatomagmatic unit and in the distal Magua Member (of Brown and Branney, 2004) is regarded as an ‘entrachron’, marking temporal correlatives. The influx of lithics that accompanied climactic collapse is recorded at the main lithic-block layer proximally and in distal lithic-breccia deposits; these constitute another entrachron. Geochemical analysis finds that two petrogenetically distinct magmas were continuously available throughout the Poris eruption: a high-Zr series and a low-Zr series. Both the proximal hybrid unit and a distal Plinian unit (the Caballos Member of Brown and Branney, 2004) have a relatively low Zr signature, linking the two and providing evidence of increased mingling between the magma series at this stage in the eruption. The low-Zr magma was tapped extensively following climactic collapse; the predominance of black and banded pumice blocks in the

resultant deposits is a further correlative marker linking the proximal and distal records.

The Poris eruption involved 8 distinct phases: Plinian deposition, first PDC generation, phreatomagmatism, hybrid fall and flow, main stage PDC activity and ignimbrite deposition with scour and bypass, caldera collapse, waning PDC, and waning fallout. In contrast to the model founded on the distal succession, which invokes four PDCs, it is found that only two were generated during the Poris eruption: the first, relatively small, and the second, large and sustained. Distal flow hiatuses occurred during waning following the phreatomagmatic and hybrid phases, but flow continued in the proximal zone at these times.

This work is relevant to studies of ash aggregates, as it highlights differences between proximal and distal deposits and those at different levels in the stratigraphy, and it is relevant to studies of Plinian deposits. The evidence of widespread hybrid deposition emphasises that the use of isopach maps in the study of very large eruptions that form widespread PDCs can only ever provide minimum estimates of Plinian deposition, with the possibility of misleading dispersal information, because the amount of Plinian fallout material deposited along with ignimbrite is impossible to quantify. The new information presented here concerning the frequency and behaviour of PDCs during the Poris eruption may have implications for the planning of risk mitigation during future explosive eruptions on Tenerife. The effect of topographic interaction is a particularly important consideration, as similar effects due to the Cañadas landscape may be anticipated during future eruptions.

Contents

List of figures

List of tables

Acknowledgements

Throughout the past four years, many people have provided me with help, advice and support. New friends have made Liverpool a home for me, and without them this PhD may not have been finished; Oirish, Vickee, Gemski, Johnald, Jutley, Kirstoid, and Paddy, you are all stars- I don't know what I would have done without the regionality, the fancy dress, the dancing, and the wine, cheese, and haggis appreciation. Gem, you were a fantastic flatmate and truly kept me sane (well, as sane as I ever get!).

Thanks to my office mate Salah for being on hand with advice and olives, and to all the postgrads and lecturers who have made the department (and the AJ!) such a good place to be. Massive thanks to old friends who have always been there for me, to give me a break from science where needed; Luke, Nai, Sooz, Kim, M, Dan, Matt, Joi, Nats, Sam, Emily, Inka, and Karen, cheers for all the reunions and for getting me through my first degrees!

In terms of technical help and advice, I am grateful to Stephen Crowley, Betty Mariani, James Utley and Alan Boyle at Liverpool, and to Rob Wilson, Rob Kelly and Nick Marsh at Leicester. Thanks also to Becky, Chris and Nina at Leicester, who were great company during the weeks of monotonous sample analysis, and to Laura, Iain, Matt, and the UCL crowd for making conferences good fun! Some interesting and inspiring conversations have been had with Rich Brown and Mike Branney over the last few years, and I thank them both for taking the time to come down to Liverpool to discuss distal Poris exposures and the relevance of my findings. I am grateful to Johnald and Rob for assistance in the field, to Joan Martí for useful discussions and obtaining permits for Teide National park, and to Paula Houghton for patiently helping me book flights and organise my budgets! Thanks also go to Pete and Mike for collecting the distal samples.

I feel honoured to have worked with Pete Kokelaar. Thank you Pete, for dealing with my tantrums, tears, speed-talking, and confusion! I appreciate you and Helen visiting me in the field, and am very grateful for the forthright wisdom, humour, and support (both academic and personal) that you have given me during the last four years. Your encouragement made me believe in myself more than I thought possible.

My family have supported me through all of my crazy life choices, and I am eternally grateful for their unconditional love and guidance. Mum, Dad, Steve, Rupa, and Amara, you are my favourite people in the world.

This thesis is dedicated to my friend Devika, who passed away before she could complete her own.

"It's not the road you walk, it is the walking."
K. Vatsyayan

Chapter One
Introduction

This thesis reports a study of the near-vent processes that occur during explosive, ignimbrite-forming volcanic eruptions. The Poris eruption of Tenerife was chosen for investigation because of the accessibility of exposures of Poris ignimbrite in the proximal region of Las Cañadas and the availability of detailed descriptions of distal Poris deposits at the coast (Edgar et al., 2002; Brown and Branney, 2004b). This study employs the lithofacies description method, and the concept of progressive aggradation of ignimbrites, formulated by Branney and Kokelaar (2002) and aims to determine how deposition at the flow boundary zone of pyroclastic density currents (PDCs) varies in response to dynamically variable conditions experienced in the near-vent environment.

1.1 Thesis objectives and outline

Proximal ignimbrite lithofacies architecture is a reflection of the conditions within the flow boundary zone of pyroclastic density currents soon after they are generated from the eruptive source. Various, potentially interacting, processes occur in the near-vent zone of explosive eruptions, including fountaining from the eruptive jet, fallout from the Plinian plume, dispersal of ballistic clasts and small-scale collapse of column margins (Houghton *et al.*, 2004). Topography may be dramatic and liable to change, and atmospheric conditions may be greatly different from those occurring in lower-altitude distal zones. The behaviour of PDCs in this near-vent zone is relatively poorly known.

The primary objectives of this study are to document the proximal deposits of an explosive eruption, to discover what phases of an ignimbrite-forming eruption are recorded close to the source, to assess how near-vent conditions affect deposition, and to correlate the proximal record with its distal counterpart. The investigation of the entire proximal record reveals information about phreatomagmatism, the interaction between fallout and density current flow, and the pre-Poris environment, such as vent location and palaeotopography.

This chapter outlines the methods and terminology implemented in the study, summarises key concepts pertinent to the work and presents an introduction to Tenerife and the Diego Hernandez wall study area. Previous studies of the structural evolution of the Las Cañadas region are reviewed in Chapter 2. Chapter 3 reports the general stratigraphy of the upper Diego Hernandez wall to put the study into context, and the lithofacies of the proximal Poris succession are described in Chapter 4. Proximal lithofacies architecture is discussed in Chapter 5, and the geochemical analysis of proximal and distal Poris samples is reported in Chapter 6. Proximal and distal studies are compared and correlated and a new coherent model for the deposition of proximal and distal Poris lithofacies is presented in Chapter 7. Chapter 8 considers the implications of the work and discusses further research possibilities.

1.2 Methods of study

This research reflects 4 months of fieldwork on the Diego Hernandez wall, carried out between October 2008 and October 2010. A general vertical section of the eruptive units exposed in the upper wall was established, together with a detailed analysis of the proximal Poris record. The latter involved mapping lithofacies across the wall and creating stratigraphic logs and sketches to describe their characteristics. A series of mini-logs was also created to investigate small-scale lithofacies associations. A small-scale study of features exposed near the *base* of the Diego Hernandez wall was carried out to address issues of similarity and palaeoenvironment; aspects of this work are discussed where relevant and the full study can be found in the Appendix.

Stratigraphic sampling of proximal lithofacies was carried out in summer 2009 by NJS and distal lithofacies were stratigraphically sampled in December 2009 by PK and MB. Samples were geochemically analysed using the XRF and EPMA facilities at Leicester University during March 2010. Further sampling was carried out by NJS in October 2010 and thin sections of pumices and bulk tuff material were created for optical analysis (see Chapter 6 for further detail).

1.3 Terminology

In this thesis, the term 'pyroclastic density current', or PDC, is used to describe a gaseous gravity current containing volcanic pyroclasts, and the material deposited by a PDC is referred to as 'ignimbrite'. The term 'lithofacies' (Table 1.1) is used here to refer to a part of an ignimbrite deposit that has distinct physical characteristics (after Branney and Kokelaar, 2002). Each non-genetic lithofacies name is attributed based upon these characteristics and abbreviated using the appropriate code. 'Architecture' is the overall structure of the ignimbrite and how the lithofacies are arranged. The term ignimbrite 'veneer' is used as a non-genetic description for thin ignimbrite deposits on topographic highs. The grain-size system used on all stratigraphic logs is that developed by Cas *et al.* (2008) for volcanic nomenclature. The terms 'proximal' and 'distal' denote the present caldera area and the Bandas del Sur coastal zone respectively.

1.4 Key concepts

1.4.1 Deposition from pyroclastic density currents

Pyroclastic density currents have fascinated scientists since the characteristics of *nuée ardentes* of the 1902 Mt. Pelée eruption on Martinique were observed and reported to the world (e.g. Anderson and Flett, 1903). Although many studies have been undertaken to improve understanding of these 'glowing clouds' and their associated sediments (e.g. Fisher, 1966; Walker, 1971; Sparks *et al.*, 1973; Sparks, 1976; Wright and Walker, 1981; Branney and Kokelaar, 1992; Druitt, 1998), the processes by which they deposit material has long remained a controversial theme in volcanology. A brief review of the most influential research is given below.

Ignimbrite, the deposit generated by sedimentation from pyroclastic density currents, is, for the most part, typically poorly sorted and matrix-supported. Pumice lapilli, lithic clasts and crystal fragments are supported in an ashy matrix of vitric shards, in a variably compacted deposit. Ignimbrites may exhibit different degrees of welding, which can be classified in terms of 'grade' (after Walker, 1983; Branney and Kokelaar, 1992); fountain-fed lava-like ignimbrites are high grade examples, and non-welded ignimbrites are low-grade (see Figure 1 in Branney and Kokelaar, 1992).

Lithofacies characteristic	**Lithocode**
Structure	
massive	m
stratified	s
diffuse-stratified	ds
cross-stratified	xs
parallel-bedded	//b
parallel-stratified	//s
breccia	Br
Nature of clasts	
lapilli tuff	LT
tuff/ash	T
pumice-rich	p
lithic-rich	l
crystal-rich	cr
pumice block-rich	pB
bearing accretionary pellets	acc
bearing elutriation pipes	pip

Table 1.1 Lithofacies are given a non-genetic name based upon physical characteristics, and are abbreviated using the appropriate code (after Branney and Kokelaar, 2002).

In 1966, Fisher proposed that the boundary layer concept of fluid mechanics could be applied to pyroclastic flows to explain the poorly sorted nature of ignimbrites. Drag resistance between the current and the ground creates a transitional zone of lower velocity, and fragments from the flow, travelling along irregular paths in the main part of the turbulent current, enter this zone at random and are deposited. This scenario was proposed to account for the vertical changes in mineral content present in the John Day ignimbrites of northeast Oregon; Fisher envisaged that compositional variations in the magma chamber were recorded as ignimbrite deposition progressed with time (Fisher, 1966).

Fisher's view of progressive ignimbrite deposition was not widely accepted, and in the 1970s a different mechanism was proposed. Sparks, Self and Walker invoked the 'standard ignimbrite flow unit', emplaced when a pyroclastic flow comes to a halt en masse (Sparks *et al.*, 1973; Sparks, 1976). Features observed in the deposit were believed to reflect features present within the current immediately before it became 'frozen'. The standard ignimbrite flow unit was described as having a moderately sorted and stratified basal layer (layer 1) overlain by a less well sorted inverse-graded layer (layer 2a), in turn overlain by a massive division with normally graded lithics and inverse graded pumices (layer 2b), capped by a fine deposit (layer 3) (see Figure 1 in Sparks *et al.*, 1973). Sparks (1976) interpreted layer 3 as a result of elutriation of fines from within a partially fluidised system, and the inverse grading of pumices in layer 2b as evidence that the flow was poorly expanded. In the model, the poor sorting exhibited by many ignimbrites was considered to be evidence that they are deposited by high concentration dispersions, and flow was suggested to be predominantly laminar, with only large pyroclastic flows involving turbulence in their early stages (Sparks, 1976). Vertical changes in ignimbrite deposits, such as those reported by Fisher (1966), were attributed to the rapid accumulation of many flow units, although this aspect was never fully elaborated.

The influential standard flow unit model was developed over the following years as it was found that some ignimbrite features were inconsistent with the original version. A prominent example is in the review by Walker (1983), which distinguishes between high and low aspect ratio ignimbrites. Evidence of high mobility with ability to overcome large topographic obstacles, in the Taupo low-

aspect ratio ignimbrite, was interpreted to reflect an unusually high emplacement velocity of 200 m s^{-1}. Walker proposed that thin, veneer-type ignimbrites are *not* the result of en-masse deposition and that an ignimbrite a few centimetres thick could be deposited by a pyroclastic flow many metres deep; it was stated that whilst most high-aspect ratio ignimbrites were formed by en-masse deposition, "the thickness of a deposit at any point is no guide to the thickness of the ash flow that passed that point" (Walker, 1983).

Research in the 1990s was significant in suggesting that pyroclastic flows could be more turbulent and expanded than was previously believed. Dense-flow and expanded-flow models were reviewed by Fisher *et al.* (1993) with respect to the Campanian ignimbrite, where it was found using deposit distribution and AMS data that only an expanded, turbulent flow could have surmounted the 1000 m obstacles present in the area to create the extant deposit distribution. In 1996 a new model for the contentious Taupo ignimbrite was created by Dade and Huppert, who suggested that previous notions of settling velocities of lithic and pumice clasts and their implications for the presence or absence of turbulent flow were incorrect. They reported that the pumice boulders present at large distances from the Taupo vent area are consistent with deposition from a *dilute and turbulent* density current (Dade and Huppert, 1996).

In 1992, Branney and Kokelaar redeveloped Fisher's concept of progressive aggradation, particularly applying the mechanism to explain changes from low-grade to high-grade ignimbrite within a massive flow unit. Their work addressed a number of problematic issues associated with the en-masse deposition model, including chemical zonation within single flow units, displacement of particle fluid as the flow 'freezes', and the physical problem of how a flow could stop at exactly the same time across its whole extent, irrespective of topography and without deposit pile-up or attenuation. In their progressive aggradation model, a pyroclastic density current can lie anywhere on a spectrum of characteristics, from an unsteady, short-lived flow to a relatively steady flow that may persist for hours. En-masse deposition is regarded as an end-member of current unsteadiness, and any stratification or vertical changes reflect variations in the nature of the flow and/or changes in the supply of material from source (Branney and Kokelaar, 1992). A low grade ignimbrite is thus

a result of the progressive deposition of pumice, ash and lithic material at a depositional boundary zone between the particulate flow and the aggrading deposit. Very high grade ignimbrites reflect progressive deposition of hot, viscous droplets that weld together immediately (agglutinate) within the depositional flow boundary zone between particulate and non-particulate flow. A further boundary exists between the non-particulate flow and the stationary tuff below (Branney and Kokelaar, 1992).

Although some research in the early 1990s continued to advocate ignimbrite emplacement by en-masse deposition (e.g. modelling by Battaglia, 1993), the model of progressive aggradation was developed and further supported. Branney and Kokelaar (1997) reported that the compositionally zoned Acatlán ignimbrite in Mexico, previously interpreted by Wright and Walker to have been deposited by en-masse deposition from a poorly expanded flow (Wright and Walker, 1977; 1981), was in fact formed by progressive deposition over time from a sustained pyroclastic density current. This new interpretation explained how later parts of the current were able to deposit more extensively and across topographic highs as valleys became infilled with material, and it could also account for the lack of flow unit boundaries within the transition zone from rhyolitic to andesitic material (Branney and Kokelaar, 1997). Bryan, Cas and Martí (1998a) proposed that vertical sequences of bedforms overlain by stratified and then massive tuff in several Tenerife ignimbrites were a result of progressive deposition from a sustained current, and Hughes and Druitt (1998) considered progressive aggradation a possible mechanism for the formation of ignimbrites of the Upper Laacher See tephra.

In 2002, Branney and Kokelaar published a seminal work bringing together the evidence for progressive aggradation and setting out a conceptual framework to account for the sedimentation of the wide variety of structures and fabrics observed in ignimbrites in the field (Fig. 1.1). The key concept of the work is that pyroclastic density currents are inhomogeneous in time and space, and that depositional mechanisms and ignimbrite lithofacies are dependent on conditions at the depositional flow boundary zone, which can be different from conditions higher in the current (Branney and Kokelaar, 2002).

Recent work in distal zones has supported the paradigm of progressive aggradation in the deposition of ignimbrite (e.g. Brown and Branney, 2004a; Pittari *et al.*, 2006; Girolami *et al.*, 2010; Sulpizio *et al.*, 2010; Williams, 2010; Andrews and Branney, 2011). Some studies of density current deposits have included evidence from proximal zones (e.g. Edgar *et al.*, 2002; Bear *et al.*, 2009a; Maeno and Taniguchi, 2009; Sulpizio *et al.*, 2010), and detailed studies of proximal Plinian fallout processes have been carried out recently at Novarupta in Alaska and at Askja in Iceland (e.g. Houghton *et al.*, 2004; Carey *et al.*, 2008a), but until this work there has been no really detailed study of proximal ignimbrite lithofacies architecture made to understand the entire record of proximal processes of a caldera-forming, large magnitude explosive eruption.

Density stratification and topographic blocking

Density stratification within PDCs may lead to the formation of a concentrated lower part with a dilute overriding cloud during or soon after flow initiation, a phenomenon first recognised in the *nuées ardentes* formed during the 1902 Mt. Pelée eruption (Smith, 1960 and references therein). The two parts have different flow properties and the upper part may 'decouple' from the lower (Fisher, 1990, 1995). The term 'flow-stripping' has been applied to this process in turbidity currents (Piper and Normark, 1983) and is used here to avoid the implication that the current originally consisted of distinct parts (after Branney and Kokelaar, 2002). Density stratification can evolve rapidly and the level and/or amount of current stripped will depend on several variables, not least the current velocity profile and the form of the blocking topography.

Flow-stripping and density stratification were observed at Soufrière Hills Volcano, Montserrat, during 1997. Following evolution of dilute currents above dome-collapse flows, topographically stripped upper parts became re-stratified to create relatively dense granular-fluid ground-hugging currents with greater run-out distances than their parent current (Druitt *et al.*, 2002). The devastating 1991 Unzen

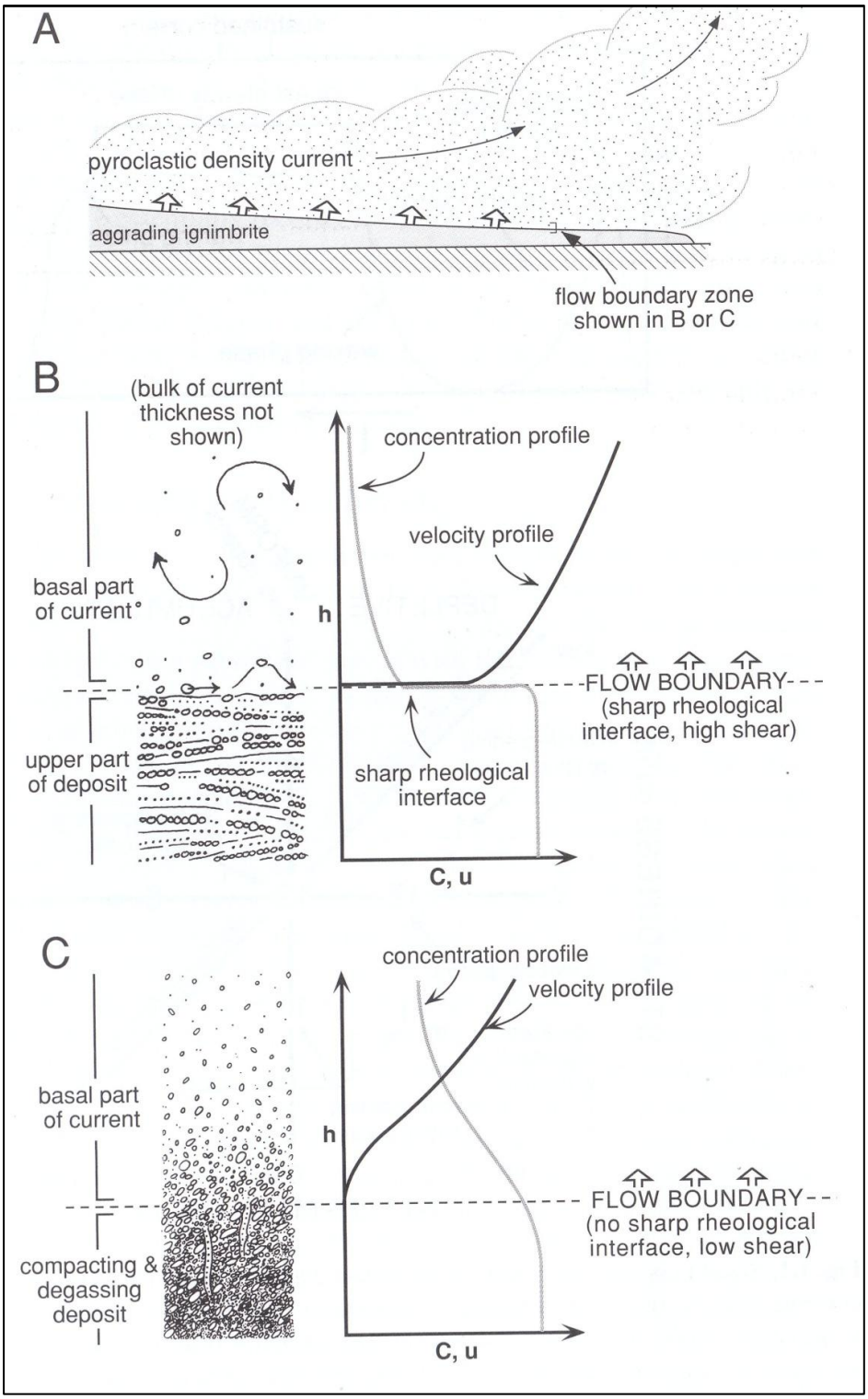

Figure 1.1 Progressive aggradation (from Branney and Kokelaar, 2002). (A) shows position of the flow boundary zone, which includes the lowermost part of the current and the uppermost part of the deposit. (B) and (C) represent two end-member types of flow boundary zone. (B) is a fully dilute (low-concentration) current, where there is a sharp decrease in velocity and a sharp increase in concentration down towards the deposit. Turbulence impinges at the deposit surface and traction occurs. (C) shows a high concentration at the flow boundary zone (granular fluid-based current), where there is a gradational decrease in velocity and a gradational increase in concentration down towards the flow boundary zone. Traction here is suppressed and a massive deposit aggrades.

eruption provides a further example in which stratified currents formed following dome collapse and were topographically stripped. Here, the 43 fatalities, including the volcanologists Harry Glicken and Maurice and Katia Kraft, occurred when a dilute 'ash-cloud' detached from the basal, relatively dense, block-and-ash type current at a valley bend and surmounted topography to travel directly an additional 0.8 km (Yamamoto *et al.*, 1993).

Where ridges or mountain ranges obstruct large pyroclastic density currents, flow-stripping may be intensified (Fisher, 1995). In a dilute stratified density current, the movement of a parcel of fluid up and over a topographic obstacle is to an extent resisted due to it having to rise, against gravity, into a region of lower density. To proceed over the obstacle the velocity of the material must be great enough to counteract this negative buoyancy effect (Valentine, 1987). The level in a current above which fluid has the energy needed to surmount the obstacle is known as the 'dividing streamline'; below this level material is blocked or moves around the obstacle (see Figure 1 inValentine, 1987). Blocking of this nature has been observed at both Mount St. Helens and Unzen (Fisher, 1990; Yamamoto *et al.*, 1993). Thin deposits of the Alaskan Fisher Tuff upon the 500-m-high Tugamak mountain range have been interpreted as evidence of the passage of a stratified and partially blocked PDC. The dense lower part was blocked and deposited thick valley-filling ignimbrite in front of the range whereas the upper dilute cloud was able to surmount the topography, later becoming re-stratified (Gardner *et al.*, 2007).

1.4.2 Caldera formation

Cataclysmic eruption of tens or thousands of cubic kilometres of volcanic material from a magma 'chamber' can lead to chamber collapse and subsidence, creating a topographic depression called a caldera. These depressions can be vast, such as the 35 x 75 km La Garita Caldera in Colorado, and they are commonly partially infilled with silicic ignimbrites deposited during the climatic stages of the eruption (Lipman, 2000b). Williams (1942) and Smith and Bailey (1968) proposed that caldera collapse is initiated when large volumes of magma have been evacuated from a magma chamber. Understanding caldera development is crucial to understanding the behaviour of large eruptions.

Caldera subsidence and its associated volcanic activity have been studied for over 100 years; significant early works include those on Kilauea (Dutton, 1884), Krakatau (Verbeek, 1886), and Santorini (Fouque, 1879). In recent years attempts have been made to identify the processes of caldera formation. The structural processes involved and their geometries have been major topics of debate and it has become clear that there is a great variety of caldera structures. Some confusion has arisen owing to imprecise nomenclature, confusion of syn-collapse and post-collapse structures, e.g. fault planes versus mass-wasting structures, and from differing views according to levels of preservation and exposure (Lipman, 2000a)

Caldera formation geometry

Five end-member caldera types have been defined and are commonly referred to in the literature (e.g. Walker, 1984; Lipman, 1997). *Piston susbsidence* constrained within a ring fault (e.g. Clough *et al.*, 1909), *downsag* involving tilting or rotation of strata with or without faulting (e.g. Branney, 1995; Milner *et al.*, 2002a), *piecemeal*, incremental subsidence of multiple blocks (e.g. Branney and Kokelaar, 1994; Rosi *et al.*, 1996; Moore and Kokelaar, 1997, 1998), *trapdoor* asymmetric collapse (e.g. Kennedy *et al.*, 2004; Smith *et al.*, 2006), and *funnel*, cone-shaped depressions (e.g. Martí *et al.*, 1994a). Recent reviews have attempted to clarify caldera terminology and formation mechanisms (Lipman, 2000a; Cole *et al.*, 2005).

The circular form of calderas and the concentric arrangement of surface features and intrusions within them have commonly been interpreted to be evidence of subsidence along a relatively simple circular fault (e.g. Smith and Bailey, 1968). This view of caldera formation was first developed in a seminal study undertaken by Clough and others (1909), in which the caldera volcano of Glencoe in Scotland is postulated to have formed as a result of subsidence of a coherent piston-like crustal block along a peripheral "ring fault". Glencoe, a deeply eroded and dissected caldera (sometimes termed a 'cauldron'), has been used to exemplify this form of collapse in subsequent studies (e.g. Lipman, 1984; Walker, 1984), although the circular faults have commonly been drawn inwards (e.g. Smith and Bailey, 1968). Such inward dips, taken simplistically, would be mechanically impossible in the absence of overall extension or shortening of the subsided block, owing to the space problem. It is common for caldera cross-sections to show a subsided block of 'keystone' shape

with no explanation of how such subsidence could occur (e.g. Fig. 7 of Marti and Gudmundsson, 2000). Although it has become common to infer a ring fault to be the structural limit of a caldera, there is little field evidence of such fractures (Walker, 1984).

Experiments have been undertaken to investigate caldera formation. Martí and others (1994a) used balloons of different shapes submerged within a container of fused alumina powder and proposed that the effects of the inflation and deflation of balloons of different shapes upon the alumina are analogous to the effects of tumescence and deflation of a magma chamber in the Earth's crust. Results are interpreted as showing that the larger the magma chamber, the larger the caldera produced upon deflation and that the deflation of magma bodies at shallow depths within the crust produces larger calderas than deflation of magma bodies of the same size residing deeper within the crust (Martí *et al.*, 1994a). Steeply dipping ring faults were formed in all experiments during subsidence; the authors propose that such faults may become pathways for magma ascent (Martí *et al.*, 1994a).

Many calderas, however, exhibit evidence of subsidence by downsag not confined within a ring fault and so do not fit this traditional model (Branney, 1995). Others show 'piecemeal', incremental collapse along variously dipping faults, with or without downsag (e.g. Scafell, Lake District; Branney and Kokelaar, 1994). Glencoe, the classic 'ring fault' caldera, has recently been found to be an example of multiple piecemeal subsidence with strong tectonic control (Moore and Kokelaar, 1997, 1998; Kokelaar and Moore, 2006). Experiments by Roche *et al.* (2000) suggest that caldera subsidence begins with the formation of outward dipping faults, which then trigger the development of normal inward-dipping faults. Structures observed in ice-melt pits, suggested to be analogous to caldera collapse geometries (Branney, 1995), include outward-dipping ring fractures, trapdoor structures, downsag pits, pits with associated graben and crevasses, and highly fragmented piecemeal structures (Branney and Gilbert, 1995). The geometry of caldera collapse is typically significantly more complicated than originally conceived.

Caldera formation mechanisms

Caldera collapse occurs as a result of withdrawal of magmatic support from the chamber roof, via the formation of fractures within the volcanic edifice and its substrate, in response to stress changes (Williams *et al.*, 1970). It has been postulated that caldera collapse involves creation of 'superfaults' that have displacements of > 100 m occurring at > 10 m s^{-1} (Spray, 1997). Kokelaar (2007) presents a model based upon friction-melt rocks (pseudotachylites) along fault intrusions at Glencoe caldera in Scotland, whereby rapid caldera subsidence leads to the generation of friction melts and almost immediately then to rapid fault-plane dilation and explosion of the surrounding hydrothermal system. Hot-water-rich rocks are explosively excavated from the fault walls and decompressed friction melts plaster the walls of resultant cavities created, as froth or spray; rapidly ascending magma then erupts with lithic breccias (Kokelaar, 2007).

1.4.3 Volcanic ash aggregates

Aggregation of ash is an important process in volcanic eruptions. Aggregates have greater fall velocities than their constituent single particles, so aggregation can significantly enhance ash removal from the atmosphere and may also affect deposit grain-size distribution on the ground (Carey and Sigurdsson, 1982; Sorem, 1982; Lane *et al.*, 1993; Durant *et al.*, in press). Volcanic ash can pose a significant hazard to both human health and aviation (e.g. Horwell and Baxter, 2006; Prata and Tupper, 2009), and following the 2010 eruptions of Eyjafjallajökull and Puyehue-Cordon Caulle there has been a drive to improve understanding of the behaviour of volcanic ash in the atmosphere (e.g. Rose and Durant, 2011; Taddeucci *et al.*, 2011; Brown *et al.*, in press). Deposits of aggregated ash and their modes of formation have been studied widely (e.g. Moore and Peck, 1962; Sorem, 1982; Reimer, 1983; Schumacher and Schmincke, 1991; Gilbert and Lane, 1994; Schumacher and Schmincke, 1995; Textor *et al.*, 2006; Brown *et al.*, 2010; Costa *et al.*, 2010), and very recently reviewed (Brown *et al.*, in press), but the processes of ash aggregation are still not completely understood.

Ash aggregates have been observed falling from the atmosphere during volcanic eruptions, as loose ash clusters that disintegrate readily on impact with the ground

(e.g. Sorem, 1982), as fluid droplets of ash-laden 'mud rain' (e.g. Lacroix, 1904; Pratt, 1911), and as relatively dry or 'moist', compact, spherical or sub-spherical agglomerations (e.g. Stearns, 1925; Tomita *et al.*, 1985; Gilbert and Lane, 1994). This latter type is the most readily preserved and examples have been described from pyroclastic deposits of a various ages (e.g. Moore and Peck, 1962; Fisher and Waters, 1970; Heiken, 1971; Lorenz, 1974; Self and Sparks, 1978; Howells *et al.*, 1979; Heinrichs, 1984; Branney, 1991; Schumacher and Schmincke, 1991; Brown *et al.*, 2010), and from suevite deposits formed during catastrophic meteorite impact (e.g. Graup, 1981; Warme *et al.*, 2002; Branney and Brown, 2011). These spherical aggregates constitute useful stratigraphic markers, can act as strain indicators (e.g. Oertel, 1970), and may indicate the depositional regime of their host rock (e.g. Branney, 1991).

Characteristics of ash aggregates

Ash aggregates vary from loose clusters of ash particles, to unstructured spherical 'pellets', to central unstructured aggregates surrounded by concentric rims of fine ash. In some instances the central part can be a small pumice or lithic clast. The number of concentric ash 'rims' accreted to the central particle varies; in some cases none are present. The grain-size of ash accreted to form the aggregate typically decreases from the central part to the outermost rim, and individual rims may be internally graded (Moore and Peck, 1962; Schumacher and Schmincke, 1991). The primary shape of the aggregates is commonly spherical, although they can become coalesced or flattened as a result of wet-state impact (deposition) and/or wet burial and compaction (Rosi, 1992). They can also become broken prior to deposition or due to ground impact, and complete spheres can be deposited alongside rim fragments. Aggregate size can vary; eye witnesses of the 1906 Vesuvius eruption described falling mud balls 'as large as an egg' (Perret, 1924), but most occurrences in volcanic deposits tend to be <4 cm in diameter.

Nomenclature

The term 'accretionary lapilli' (Wentworth and Williams, 1932; Wentworth, 1937) has been used widely to describe spherical volcanic ash aggregates (e.g. Moore and Peck, 1962; Self and Sparks, 1978; Fisher and Schmincke, 1984; Cas and Wright,

1987), sometimes without description of aggregate structure. Various schemes of nomenclature have been proposed to characterise ash aggregates more thoroughly (e.g. Reimer, 1983; Schumacher and Schmincke, 1991; Thordarson, 2004; Brown *et al.*, 2010), but there is considerable confusion in the terminology used. A new scheme by Brown *et al.* (in press) proposes terminology that avoids grain-size connotations, and this is adopted here. 'Accretionary pellets' are subdivided into three categories; poorly structured subspherical pellets (AP1), pellets with concentric structure (AP2) and liquid pellets, droplets of water containing ash that break upon impact (AP3). Fragile particle clusters are divided into ash clusters (PC1) and crystal or lithic fragments partly coated in ash (PC2) (Table 1.2).

Occurrence

Accretionary pellets have been documented in various deposit types. Early descriptions of eruptions often associate them with ash fallout (e.g. Hovey, 1902; Pratt, 1911; Stearns, 1925), and they have more recently been documented in various ancient tuffs of fallout origin; examples include silicic airfall tuffs in the Western US and subaerial phreatomagmatic air-fall tuffs of the Whorneyside formation of the English Lake District and of the Ontong Java Plateau (Moore and Peck, 1962; Branney, 1991; Thordarson, 2004). Accretionary pellets have also been reported in beds deposited by dilute PDCs formed during phreatomagmatic eruptions (e.g. Fisher and Waters, 1970; Lorenz, 1974; Self and Sparks, 1978), and in the deposits of granular fluid-based PDCs, i.e. ignimbrites, at Laacher See and in the Bandas del Sur of Tenerife (Schumacher and Schmincke, 1991, 1995; Brown and Branney, 2004b; Brown *et al.*, 2010). Accretionary aggregates occur with suevite deposits related to meteorite impact (Graup, 1981; Yancey and Guillemette, 2008; Branney and Brown, 2011), and it has been suggested that they may also occur in deposits of basaltic Plinian eruptions on Mars (Wilson and Head, 2007).

Table 1.2 (overleaf) Features of ash aggregates (taken from Brown *et al.*, in press). Alternative name for PC1 and PC2: 'dry aggregate' (Gilbert and Lane, 1994; Sparks *et al.*, 1997). Alternative names for AP1 accretionary pellets: 'core-type accretionary lapilli' (Schumacher and Schmincke, 1991), 'type II accretionary lapilli' (Reimer, 1983), 'ash pellets' (Thordarson, 2004; Brown *et al.*, 2010). Alternative names for AP2 accretionary pellets: 'rim-type accretionary lapilli' (Schumacher and Schmincke, 1991), 'type I accretionary lapilli' (Reimer, 1983), 'armoured lapilli' and 'cored lapilli' (with lithic or pumice cores) 'accretionary lapilli' and 'coated pellets' (Brown *et al.*, 2010). Alternative name for AP3: 'mud rain' (Gilbert and Lane, 1994; Sparks *et al.*, 1997).

Aggregate type	Typical aggregate size range (diameter)	Particle size range (diameter)	Description	Occurrence in deposit	Examples
Particle clusters (PC)					
PC1 (ash clusters)	Few 10 s μm up to ~10 cm	<1–40 μm: rare particles >200 μm	Fragile, irregular-shaped aggregate with densities of (~60–200 kg m^{-3}, which commonly disaggregate on deposition; can be cemented	Poorly preserved as discrete morphologies in ash fall deposits, (but they may be inferred from the particle size distribution of the deposit)	Hobbs et al. (1981), Sorem (1982), Gilbert and Lane (1994), Schumacher (1994), Sparks et al. (1997), Bonnadonna et al. (2002b), James et al. (2002, 2003)
PC2 (coated particles)	0.05–2 mm	<1–40 μm	Fragile aggregates comprised of a crystal, crystal fragment or pumice or lithic clast partially covered in fine ash particles. Particles fall off on impact with the ground	Poorly preserved as discrete morphologies in ash fall deposits	Sparks et al. (1997), Bonadonna et al. (2002)
Accretionary pellets (AP)					
AP1 (poorly-structured pellets)	100 μm up to a few mm	<1–400 μm; median values of 30–90 μm; rare particles >1 mm	Fragile; massive or poorly structured; subspherical or slightly prolate or oblate; 30–50% porosity; densities of 1200–1600 kg m^{-3}; can show evidence of compaction or partial disaggregation on deposition, or brittle fragmentation; similar to cores of AP2; may contain subspherical vesicles (20–200 μm) in concentric layers or isolated; may have larger particles inside acting as nucleus. May contain ice on deposition	Clast-supported fall deposits	Schumacher and Schmincke (1991), Gilbert and Lane (1994), Sisson (1995), Sparks et al (1997), Bonnadonna et al. (2002b), Brown et al. (2010)
AP2 (pellets with concentric structure)	2–15 mm; Rarely >30 mm	Cores: typical median values of <25–50 μm Rims: median values of 10–15 μm	Subspherical, typically massive or poorly structured ash core (similar to AP1) surrounded by rim (cross-section width 0.6–1.5 mm) of one or more multiple very fine-grained ash laminae (cross-section thickness <200–500 μm); individual lamina are continuous or pinch out; gradational to sharp grainsize variations in successive rims; cores may contain subspherical vesicles (20–200 μm); may include a lithic or pumice lapilli, crystal or organic particle (e.g., twig or leaf) within the core; may be wholly or partially coated in a 0.2–6 mm thick very fine-grained ash layer	Matrix or clast-supported aggregates dispersed within massive beds or concentrated in layers and lenses of PDC flow deposits; scarce occurrences in clast-supported fall layers	Moore and Peck (1962), Lorenz (1974), Sheridan and Wohletz (1983), Bednarz and Schminche (1990), Schumacher and Schmincke (1991), Cole et al. (2001), Bonadonna et al. (2002a), Scolamacchia et al. (2005), Brown et al. (2010)
AP3 (liquid pellets)	0.1–6 mm	Wide range of particle sizes (0.001–1 mm)	Liquid water drops containing ash particles; break up on impact; poorly sorted	poor preservation in geological record	Brazier et al. (1982), Gilbert and Lane (1994), Lane et al. (1993), Sparks et al. (1997), Watanabe et al. (1999), Bonnadonna et al. (2002b)

Interactions of ash clouds formed above PDCs with those around eruptive jets and buoyant columns potentially render interpretation of ash aggregate deposits difficult, especially in vent-proximal regions. Stratified ash beds can be deposited by both direct ash fallout and by dilute PDCs with fallout-dominated or traction-dominated flow boundary zones (Branney and Kokelaar, 2002), so the origin of ash aggregates in such beds can be ambiguous. It is not clear how to distinguish between ash fallout from the margins of an eruption plume and that from so-called 'co-ignimbrite' clouds (phoenix clouds), particularly in the proximal zone where both may reasonably be anticipated. Evidence of context, both spatial on the volcano and stratigraphic, is needed to interpret ash aggregate-bearing deposits, but in proximal regions there may always remain ambiguity.

Models of ash aggregate formation

Ash aggregation occurs via processes of contact and binding, controlled by particle characteristics, liquid and gas composition and concentration, and humidity, temperature and turbulence (Gilbert and Lane, 1994). Possible mechanisms of aggregation include collisions and interlocking due to variable fall velocities, electrostatic attraction, hydrometeor (rain, hail, snow) formation, surface tension capillary forces, secondary mineral crystallisation and Van der Waals forces (e.g. Sorem, 1982; Reimer, 1983; Schumacher and Schmincke, 1991; Gilbert and Lane, 1994; Schumacher and Schmincke, 1995; Textor *et al.*, 2006; Durant *et al.*, 2009; Lane *et al.*, 2011). Regimes of aggregation are not fully known and various models have been proposed, including rain flushing of an ash laden atmosphere or the formation of 'mud rain' (Hovey, 1902; Pratt, 1911; Woods, 1993), particle creation by raindrops falling on freshly deposited ash and growth by saltating and rolling across a soft ash substrate (Scrope, 1829; Lacroix, 1904), the falling of a core particle through various envelopes of a turbulent eruption column to accrete layers (Moore and Peck, 1962), particle collision and binding within eruption plumes (e.g. Schumacher and Schmincke, 1991; Gilbert and Lane, 1994), and the descent of an ash pellet formed in a co-ignimbrite cloud through a thermally stratified PDC (Brown *et al.*, 2010).

Ash aggregation in eruption plumes

In their review of the occurrences of accretionary lapilli in the western US, Moore and Peck (1962) proposed a mechanism of formation whereby water vapour in ash clouds condenses as the cloud rises and cools, causing agglutination of ash to form an 'accretionary lapillus core'. As this core falls through the eruption cloud, ash sticks to the moist surface, creating an outer shell. The observed grain-size decrease from core to rim is interpreted as due to increasing temperatures in lower parts of the cloud, which reduce available moisture and therefore hinder the accretion of larger particles. According to the model, parts of the outer shell may then become 'sandblasted' by the dust-charged air, leading to erosion and breakage of some accretionary lapilli. The notion that multi-rimmed aggregates form by saltation and rolling across the ground is rejected by these authors, because this would create an irregular or spiral accretion rather than the observed concentric ash layers (Moore and Peck, 1962).

Wind tunnel experiments established that collision of ash particles with thin liquid coatings could create spherical ash aggregates with concentric layers. Larger particles were found to scavenge smaller particles that fell more slowly; build up of concentric grain-size zones was proposed to result from differences in the supply of grain-size to the evolving aggregate (Gilbert and Lane, 1994). Conversely, it was found that ash particles scavenged by a falling liquid drop will preferentially accrete into *horizontal* layers within the drop according to their densities (Gilbert and Lane, 1994).

The occurrence of spherical, flattened, and broken ash aggregates within tuff recovered from a drill site in the Ontong Java plateau has been interpreted as evidence of subaerial or emergent phreatomagmatic activity (Thordarson, 2004). The lack of imbrication of inequant fragments and the decimetre-scale plane-parallel stratification of beds were taken to indicate fallout from an ash-cloud, where ash deposition was initiated by the flocculation of particles to form aggregates. The preservation of loosely packed ash clusters was interpreted as evidence of subaerial deposition and ovoid accretionary lapilli were attributed to impact with the ground. A similarly stratified tuff containing single-rimmed ash aggregates – the 450 my-old Whorneyside bedded tuff in the English Lake District – is interpreted by Branney

(1991), as resulting from a 'rapid succession' of localised ash showers during a phreatoplinian eruption. Showering from a long-lived umbrella cloud is inferred to have been promoted by combinations of rain flushing, ash accretion and convective instabilities (Branney, 1991).

An example of a Plinian pumice-fall unit including layers rich in ash aggregates, in the Fasnia formation of Tenerife, is described by Brown *et al*. (2010). A framework-supported mixture of ash pellets (AP1) and rimmed pellets (AP2), some with a lithic or pumice core, occurs layered between beds of Plinian pumices in a topography-draping sequence. The aggregates lack brittle outer rims and rim fragments are not present. The ash aggregate-bearing layers exhibit soft-state deformation, resemble other phreatoplinian units (e.g. Self, 1983) and are interpreted to record direct fallout from a large, moist, turbulent eruption column (Brown *et al.*, 2010).

Ash aggregation associated with pyroclastic density currents

Self and Sparks (1978) argued that ash aggregates must form at low levels in eruption clouds for them to be present with phreatomagmatic 'surge' deposits (i.e. deposits from dilute PDCs), because such 'surge' currents do not attain great heights.

Experimental work, together with the description of accretionary lapilli in ignimbrites at Laacher See volcano, led Schumacher and Schmincke (1995) to propose that ash aggregation occurs in lateral flows and overriding 'elutriation clouds' where turbulent conditions cause particle collisions and electrostatic effects and condensed moisture cause aggregation. They considered that rim-type pellets form proximally, where they thought fine grained rims are accreted electrostatically, whereas distally ongoing condensation and increased moisture promote moist accretion of core-type lapilli. This model proved consistent with a thermodynamic-mathematical model that found that ash aggregates may form in *both* collapsing fountains and in PDCs formed during phreatomagmatic eruptions (Koyaguchi and Woods, 1996).

Recently, another variant model for the formation of accretionary lapilli within PDCs has been based on detailed observations of ignimbrite successions in the Bandas del Sur, on Tenerife (Brown *et al.*, 2010). The upper parts of PDC deposits in 11

ignimbrite successions were found to be rich in multi-rimmed and broken accretionary pellets (AP2). These mLTacc deposits are overlain by layers of clast-supported unstructured ash pellets (AP1) that extend beyond the associated PDC deposit and are interpreted as co-PDC ashfall layers. Brown *et al.* (2010) suggest that the similarity between the unstructured pellets and the cores of the multi-rimmed aggregates indicates a genetic link, whereby the ash pellets formed in a moist, co-PDC ash cloud and then accreted rims of ash as they fell through lower parts of the density current.

Brown *et al.* (2010) also considered tuff ring deposits on Tenerife, and found that they contain similar sequences of multi-rimmed aggregates overlain by layers of unstructured ash pellets. However, in the tuff ring deposits the multi-rimmed accretionary pellets were present at the base and ash pellets were commonly coated with at least one ash layer. These differences are attributed to the pulsatory nature and short-lived currents of tuff-ring phreatomagmatic explosivity, during which the atmosphere may have remained ash-rich for long durations allowing pellets to acquire ash coatings (Brown *et al.*, 2010).

Both unstructured pellets (AP1) and concentric accretionary pellets (AP2) occur in an ash bed near the base of the proximal ignimbrite succession considered in this study. The significance of this occurrence, and how the unit may correlate with similar deposits found distally, is discussed in Chapters 4 and 7.

1.5 Study Area

1.5.1 Geological setting

The Canary Islands lie on Jurassic oceanic crust of the African tectonic plate, forming a 500 km-wide archipelago 100 km off the southern coast of Morocco (Fig. 1.2). The islands are mostly constructed of alkali-basalts and volcanoes on the two largest islands, Tenerife and Gran Canaria, have erupted phonolitic magmas derived by the fractional crystallisation of alkali-basalt (Martí *et al.*, 1994b). The near-stationary tectonic location of the islands, close to the pole of rotation of the African plate, has allowed the construction of large volcanic edifices despite lower melt productivity than occurs at other ocean island volcanoes (Marti and Wolff, 2000). The origin of the islands is contentious. Some authors consider the magmatism of the archipelago to originate from a hot spot, like the Hawaiian islands (Wilson, 1963; Carracedo *et al.*, 1998), while others believe that the low melt productivity, temporal and spatial chemical diversity and multiple cycles of volcanism reflects decompression melting of discrete and dispersed 'blobs' of mantle (Hoernle and Schmincke, 1993). The 'propagating fracture hypothesis' (Anguita and Hernan, 1975) proposed the existence of a 'leaky megashear' that geologically connects the cyclical structure of growth of the Canary Islands to the compressive phases dated at the African Atlas Mountains. Anguita and Hernan have published a unifying model based on previous theories, whereby magmas are tapped via a propagating fracture from a thermal anomaly related to a 'fossil' plume under the African plate (Anguita and Hernán, 2000).

Tenerife is the largest of the Canary Islands, at 2058 km^2, and has a distinctive three-pronged shape. El Teide, the highest of Spain's mountains at 3718 m, is located at the centre of the island within a large structural depression known as 'Las Cañadas'. Las Cañadas depression is approximately 16 x 9 km in size and is partly encircled by a topographic wall that stretches for 27 km from the southwest around to the east of El Teide (Fig. 1.3). The highest point in the wall, Guajara Peak, is 600 m above the floor of the depression, and drill-holes within the depression have found >500 m of Teide-Pico Viejo lava infill without reaching the older rocks beneath; thus the central area of the depression was originally >1100 m beneath the existing rim (Martí *et al.*, 1997).

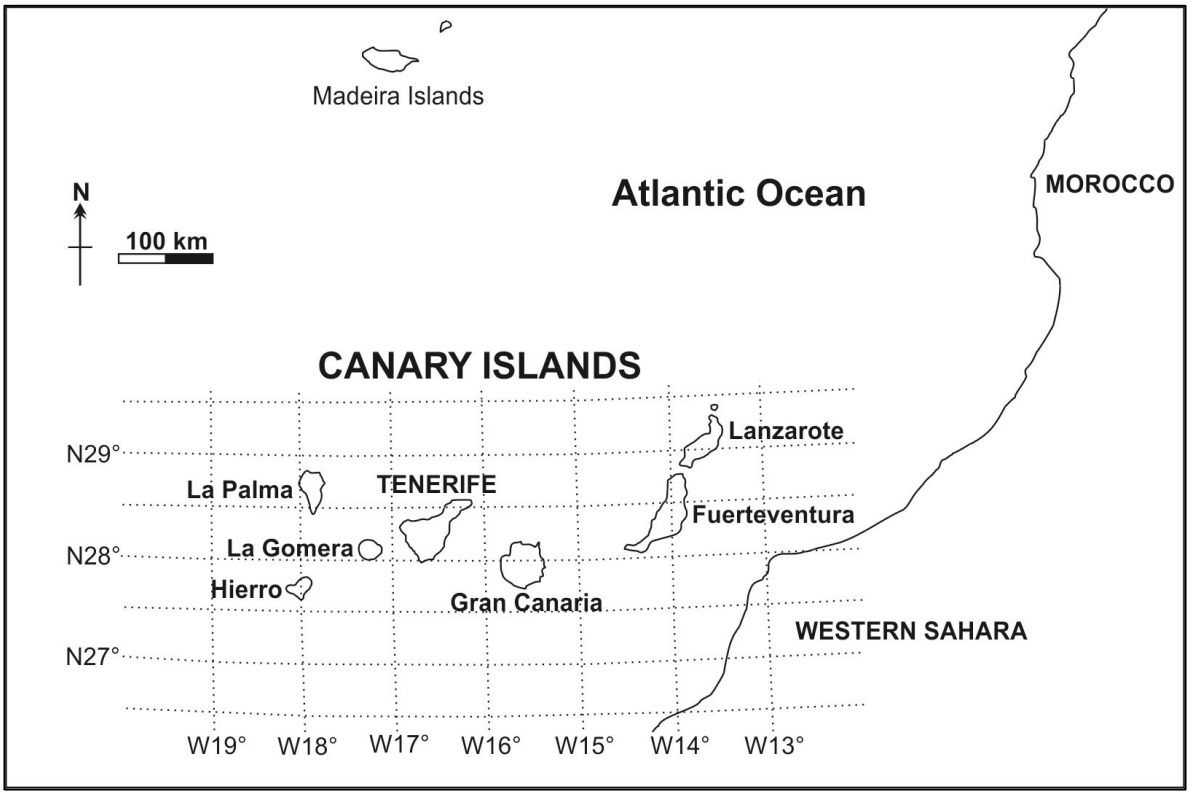

Figure 1.2 Location of Tenerife and the Canary Islands.

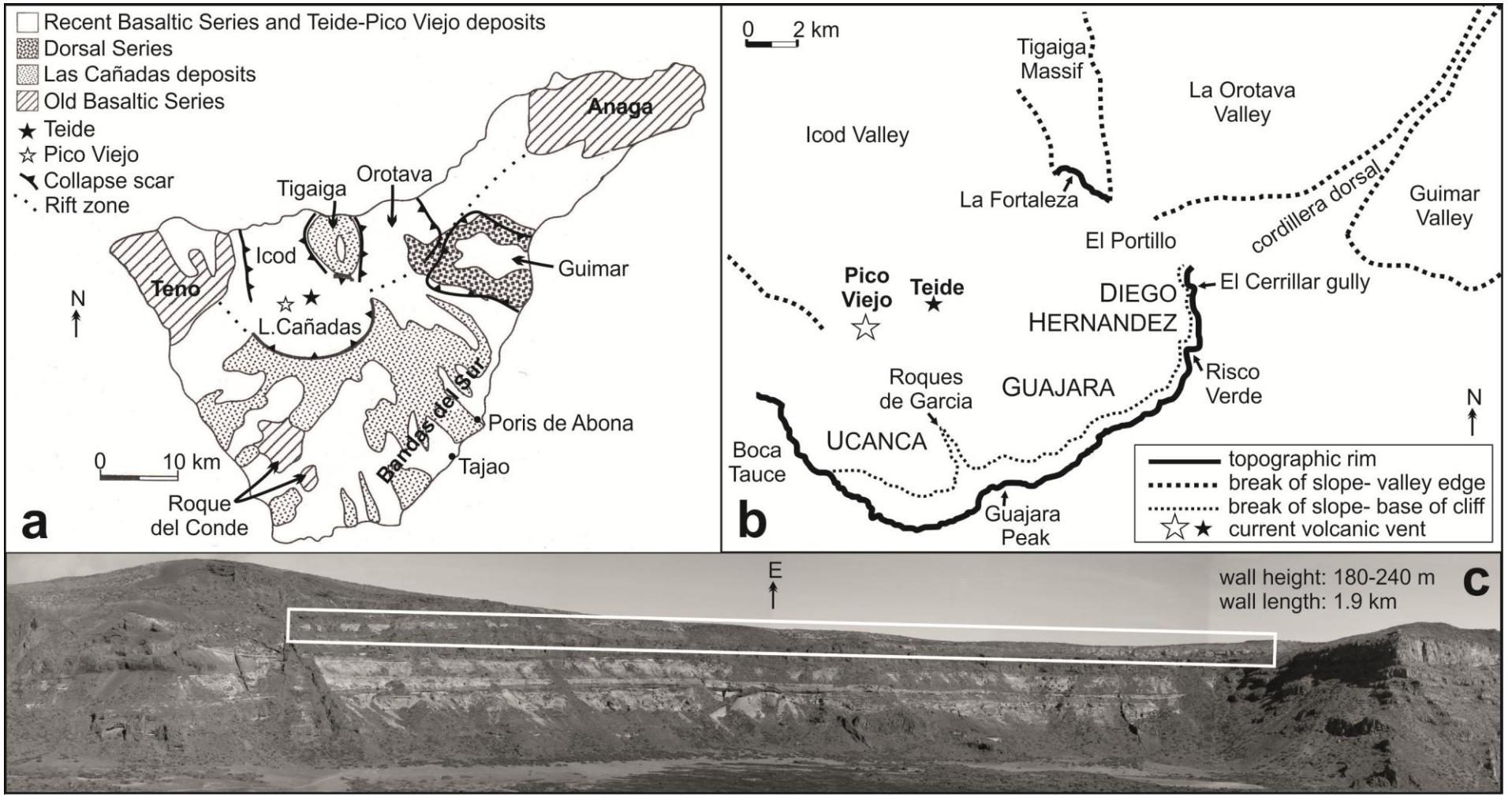

Figure 1.3 (a) Simplified geological map of Tenerife, adapted from Ancochea *et al*. (1990) and Martí *et al*. (1994), showing the location of Las Cañadas depression at the centre. (b) Las Cañadas depression, showing the position of the Diego Hernandez wall and El Cerrillar gully in relation to the current Teide-Pico Viejo stratovolcano edifice. (c) The Diego Hernandez wall. White box highlights the proximal Poris ignimbrite; the exposures are in 27 pale coloured, rounded cliffs surrounded by vegetation and scree.

Tenerife has a complex geological history spanning more than 11 million years. The oldest rocks exposed are those of the 'Old Basaltic Series', products of subaerial shield volcanism for which dates range from 11.6 Ma to 3.5 Ma (Ancochea *et al.*, 1990). They are basaltic lavas and pyroclastic deposits and form three massifs: Teno in the northwest, Anaga in the northeast, and Roque del Conde, deeply eroded and largely buried, in the south of the island (Fig. 1.3). It seems unlikely that three volcanic centres were located so closely with no volcanism occurring centrally between them during this time period, particularly in the view of the subsequent volcanic activity that otherwise would have had no precursor; it is possible that shield volcanism was present throughout the whole area from 11 Ma to 3.5 Ma, but that more recent post-shield volcanism has covered evidence of an early edifice in the central area. The gravity study of Gottsmann *et al.* (2008) finds no evidence to support the existence of three isolated volcanic islands, and suggests that the central area of the shield system may have been removed by lateral collapse early in the history of the island.

Early K-Ar dating (Ancochea *et al.*, 1990) found the oldest post-shield deposits to be 2-0.17 Ma, which suggests a period of quiescence and erosion following the production of the Old Basaltic Series. However, more recent radiometric work places some post-shield deposits at >3.5 Ma (e.g. Martí *et al.*, 1994b; Ancochea *et al.*, 1999 and references therein), suggesting no hiatus in volcanism. The oldest post-shield volcanic deposits (3.8-3.5 Ma) are part of Boca Tauce, a large mafic edifice now buried beneath the southwest of Las Cañadas, identified by gravity and magnetic surveys (Ablay and Hürlimann, 2000; Ablay and Kearey, 2000).

Post-shield basalts, trachytes, and phonolites occur in the central area of Tenerife, between the eroded remnants of the Old Basaltic Series. The pyroclastic deposits and lavas are exposed in the wall of Las Cañadas depression, providing evidence of both explosive and effusive volcanism. Different workers have classified the deposits according to age information and stratigraphic position; Martí *et al.* (1994b) refer to 'Lower' and 'Upper' groups, and Ancochea *et al.* (1999) identify deposits in terms of 'Cañadas I, II and III'. A detailed discussion of the differences in these deposit classifications is outside the scope of this appraisal. Ignimbrite classification schemes are discussed in Chapter 2. Following Martí *et al.* (1994b), the 'Lower

Group' rocks are at the base of the Cañadas wall and have been dated at ~3.5-1.8 Ma. The 'Upper Group' comprises the Ucanca [1.57-1.07 Ma], Guajara [0.85-0.57 Ma] and Diego Hernandez [0.37-0.17 Ma] formations (Martí *et al.*, 1994b). The DH phase of volcanism culminated at ~0.17 Ma with the deposition of the Abrigo ignimbrite, which is exposed widely on the southeast volcano flanks beyond the Cañadas wall and down to the coast in the Bandas del Sur region (Edgar *et al.*, 2007).

The deposits in Las Cañadas wall, recording over 2 million years of activity, are often referred to as part of a single Las Cañadas "volcano" or "edifice" (e.g. Araña and Brandle, 1969; Araña, 1971; Martí *et al.*, 1994b; Martí *et al.*, 1997; Martí 1998; Ancochea *et al.*, 1999). This title is somewhat misleading, and will be discussed further in Section 2.4. In this thesis, these deposits will be referred to as having been erupted in the Cañadas 'episode', so as not to obscure the important issue of how many individual stratovolcano edifices were constructed and destroyed during this time. In the later stages of the Cañadas episode, between 0.9 Ma and 0.43 Ma, the basaltic 'Cordillera Dorsal' series was erupted along the NE 'arm' of the island (Ancochea *et al.*, 1990) (Fig. 1.3b).

The current Teide-Pico Viejo stratovolcano has been constructed of basalts, trachytes and phonolites. Activity began soon after the eruption of the Abrigo ignimbrite at 0.17 Ma, with no significant hiatus (Martí 1998). The most recent activity of the Teide-Pico Viejo edifice was the Chacharro eruption (VEI 3) on the southwest flank in 1798 (Global Volcanism Program, 2008), whereas the most recent volcanism on Tenerife was in the 'Recent Basaltic Series' (Fuster *et al.*, 1968) of scoria cones with coeval lavas; Chinyero in the NW rift zone was the most recent scoria cone and lava eruption, in 1909 (Global Volcanism Program, 2008).

1.5.2 Geomorphology and topographic profile

Las Cañadas

Las Cañadas depression has a scalloped wall in which the three predominantly felsic formations occur (see above). The wall has undergone degradation and weathering, and numerous intrusions are visible. The scalloped edge roughly designates three

areas within the depression; Ucanca in the southwest, Guajara in the south and Diego Hernandez in the east. An outcrop of breccias and intrusions known as the Roques de Garcia is exposed close to the putative boundary of the Ucanca and Guajara sectors. La Fortaleza, a steep escarpment in the northeast, is separated from the main topographic wall by the opening at El Portillo (Fig. 1.3). To the north any possible continuation of the topographic depression has been buried by the Teide-Pico Viejo stratovolcano (Martí *et al.*, 1994b), and it is thus unclear whether the depression had any bounding feature in this direction. The Fortaleza outcrop in the NE constitutes a hint that perhaps full closure of the depression did once exist. The Ucanca section of the wall contains the oldest volcanic deposits, and the stratigraphic sequence is progressively younger towards the east (Martí *et al.*, 1994b).

Wide Valleys

The Cordillera Dorsal series of volcanic deposits forms a ridge aligned roughly NE-SW, to the east of Las Cañadas. North and south of this ridge are two large, wide valleys with steep headwalls, known as La Orotava and Guimar respectively. Initial dating of the oldest material emplaced within these valleys suggests that both formed between 0.83 and 0.78 Ma (Ancochea *et al.*, 1990); more recent study dates Guimar to 0.83-0.57 Ma and La Orotava to 0.57-0.54 Ma (Gottsmann *et al.*, 2008). A third wide valley, Icod, is located north of the Cañadas depression (Fig. 1.3). This apparently formed more recently, at 0.2-0.13 Ma (Gottsmann *et al.*, 2008).

Barrancos

The flanks of the current Cañadas region are deeply incised by valleys known as barrancos, which can be over 200 m wide and more than 100 m deep. The presence of thick ignimbrite deposits within these valleys distally indicates that they have acted as a topographic control upon density currents during previous eruptions. Although they are mostly dry, the occurrence of the barrancos implies fluvial erosion, possibly during episodes of high precipitation over high altitude zones of the island.

Topographic profile

In order to better understand the topographic changes pyroclastic density currents may have experienced during passage from the vent across proximal and distal slopes historically, two topographic profiles are shown in Fig. 1.4, illustrating the modern Tenerife landscape. Both start at the modern vent of Mt. Teide and cross the Diego Hernandez wall (the study area for this thesis) in the east. Section (a) traverses the edge of the Guimar valley close to the sea, while section (b) is a traverse of the coastline south of Guimar. Deposit analysis by previous workers has demonstrated that pyroclastic density currents generated during eruptions of the Diego Hernandez episode of volcanism travelled in east-southeast directions (Brown *et al.*, 2003).

1.5.3 Palaeoclimate and vegetation

The Canary Islands presently experience a maritime-semiarid climate (von Suchodoletz *et al.*, 2009). Lanzarote and Fuerteventura in the east are desert-like, whereas the mountains of western islands act as a topographic barrier to trade winds and create a Mediterranean-style climate of hot, dry summers and warm, wet winters on Tenerife, Gran Canaria, La Gomera, Hierro and La Palma (Sperling *et al.*, 2004). At high altitude, Tenerife experiences orographic precipitation, often as snowfall during winter. On the volcanic flanks laurel forest dominates, as a response to orographic cloud formation during the dry season (Sperling *et al.*, 2004). Trees can reach over 20 m in height. In the lowland coastal reaches, vegetation is relatively sparse, with low shrubs and cacti such as prickly pear common.

The laurel forests on Tenerife and the nearby islands represent the remnants of a formerly widely distributed Neogene oak-laurel community, which developed in the circum-Mediterranean region at ~20 Ma, during conditions of far higher summer rainfall than presently occurs (Sperling *et al.*, 2004). The forests have decreased in size due to increased aridity since the Neogene, and have become restricted to more humid mountainous areas (Sperling *et al.*, 2004). In recent years, forest and vegetation cover has been affected by human habitation of the islands. It thus seems likely that vegetation cover on Tenerife during the Cañadas episode of volcanism may have been similar, or slightly denser, than that observed today, with similar, if not slightly more humid, climatic conditions.

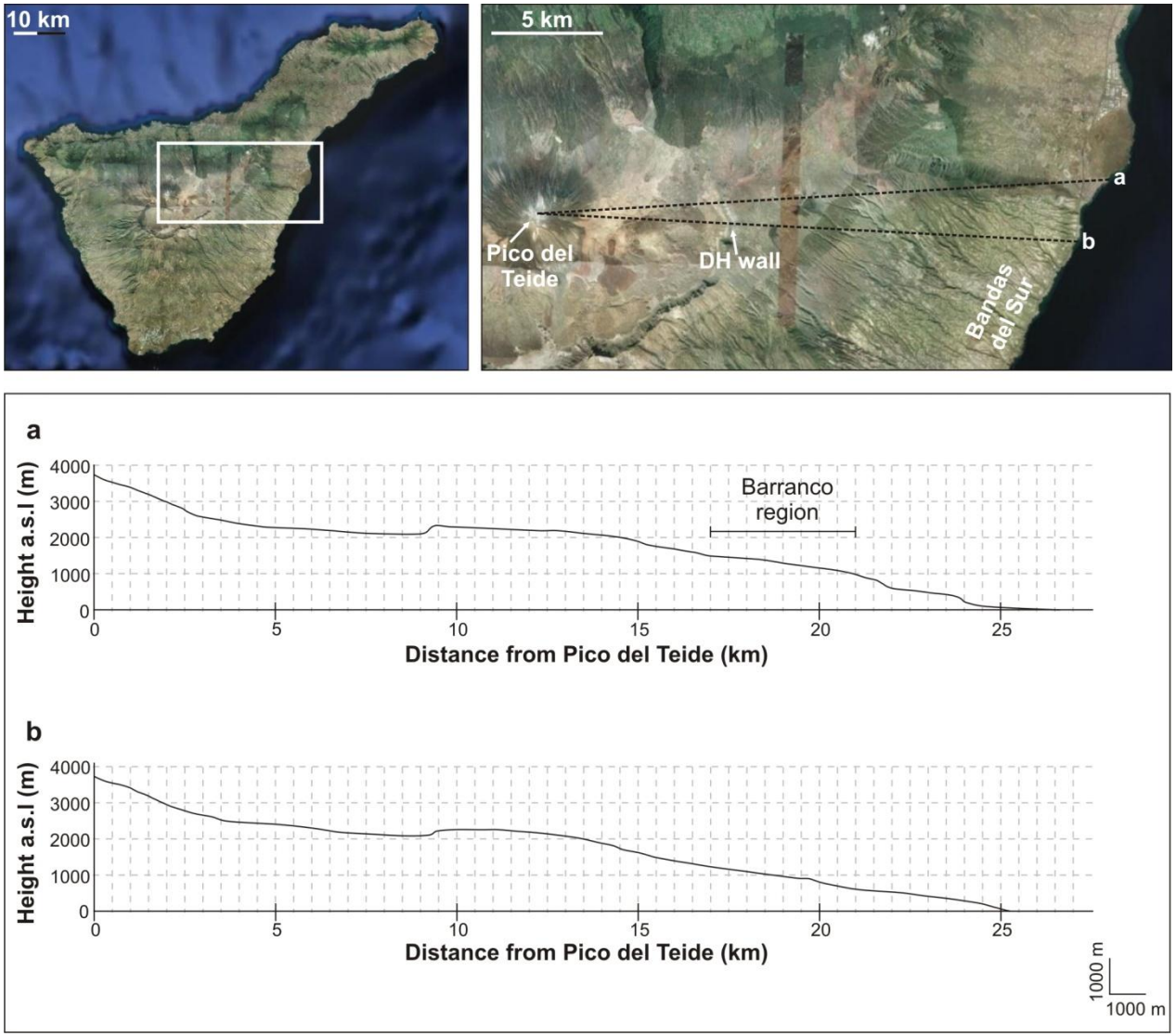

Figure 1.4 Topographic profiles of two transects from Pico del Teide at 3718 m to Puertito del Guimar (a) and Playa de la Caleta (b) at sea level. The zoomed in locality map shows the transect lines and the position of the Diego Hernandez (DH) wall. At ~1000-1500 m above sea level, valleys known as 'barrancos' are common, incising deeply into slopes. On profile (a), the steep sides of the Guimar valley are clearly visible in the lower reaches of the profile.

The presence of in-situ fossils of sparse shrubs at the base of distal Poris ignimbrite deposits, contrasted with allochthonous, imbricated tree moulds in the upper deposits (Brown and Branney, 2004b) is strong evidence that vegetation distribution on Tenerife has not changed significantly in the last 300 000 years.

1.5.4 The Diego Hernandez caldera wall

Diego Hernandez (DH), the eastern topographic wall of Las Cañadas depression, is the field area for this work (Fig. 1.3c). Pyroclastic deposits of at least 5 major explosive eruptions are recorded in the DH cliff face, intercalated with lava flows and buried scoria cones, deposited during the Diego Hernandez episode of volcanism (~3-0.17 Ma). Previous stratigraphic systems for the DH episode are briefly reviewed in Chapter 2. The wall is orientated N-SSW and is approximately 1.9 km in length. It rises 240 m above the Cañadas floor in the north at Montaña Vista, and is 180 m high in the south at Risco Verde.

Middle parts of the steep wall are inaccessible due to sheer cliff faces, but accessible exposure occurs along the upper and lower parts of the main cliff face. Exposure is also found in a gully near Montaña El Cerrillar, just north of Montaña Vista (Fig. 1.3b). The ignimbrite succession that overlies thick lava flows in the upper DH wall is the main focus of this thesis. Exposure of this succession occurs in two forms; as distinctive cliff outcrops that have been weathered into rounded shapes with orange coloured tops, and as scree exposures that follow the gradient of the slopes behind the main cliff outcrops and often require brushing and trench-digging for examination. The lower wall exposures discussed in Chapter 6 occur in a steeper part of the cliff face where exposure is more continuous than in the upper wall but not always as easy to access.

Behind the steep cliff face of the wall, the flanks of Las Cañadas form relatively shallow slopes (see topographic profiles). The slopes are thickly vegetated and often covered by scoria fallout from the nearby vents of the Cordillera Dorsal, and as a result contain very little exposure of DH units.

Chapter Two

The origin and eruptive history of Las Cañadas

2.1 Introduction

Tenerife is one of the largest and most morphologically complex ocean island volcanoes on Earth and it is important to understand its structural evolution. Interpretation of the morphological features of Tenerife has been the focus of much interest, with particular controversy concerning the evolution of the 'Las Cañadas' depression and the large, wide valleys on the island flanks (Fig. 2.1). Two contrasting theories have long coexisted, one of vertical collapse and one of lateral collapse, traditionally with rather little common ground between them.

Navarro and Coello's (1989) study of geomorphologic depressions on Tenerife reported chaotic breccias within the Guimar, La Orotava and Icod valleys, and concluded that they were created by large sector collapses, each possibly involving >100 km^3 of material. Based on this research and more recent seafloor studies, it has been proposed that mass wasting events created the present morphology of Las Cañadas depression (Navarro and Coello, 1989; Ancochea *et al.*, 1990; Cantagrel *et al.*, 1999; Watts and Masson, 2001). In contrast, however, the three-part scalloped shape of the Cañadas depression, and the progressively eastwards-younging stratigraphic sequence in its wall (Fig 2.2), led other workers to suggest that the structure results from three discrete caldera-forming vertical collapses (e.g. Martí *et al.*, 1994b). Recent studies of the ignimbrite successions exposed in the Bandas del Sur region propose that multiple caldera subsidence events have occurred on Tenerife (e.g. Brown *et al.*, 2003; Edgar *et al.*, 2007).

The structural evolution of the Cañadas region is relevant to the interpretation of the eruptions and processes that generated Tenerife's ignimbrite deposits, and should also be considered in hazard assessment and risk mitigation planning for the future. Although large-scale lateral collapses and caldera-forming eruptions have not occurred on the island during historical times, studying evidence of these events in the geological record may aid understanding of how the Teide-Pico Viejo stratovolcano could behave in the future. Either vertical or lateral collapse, along

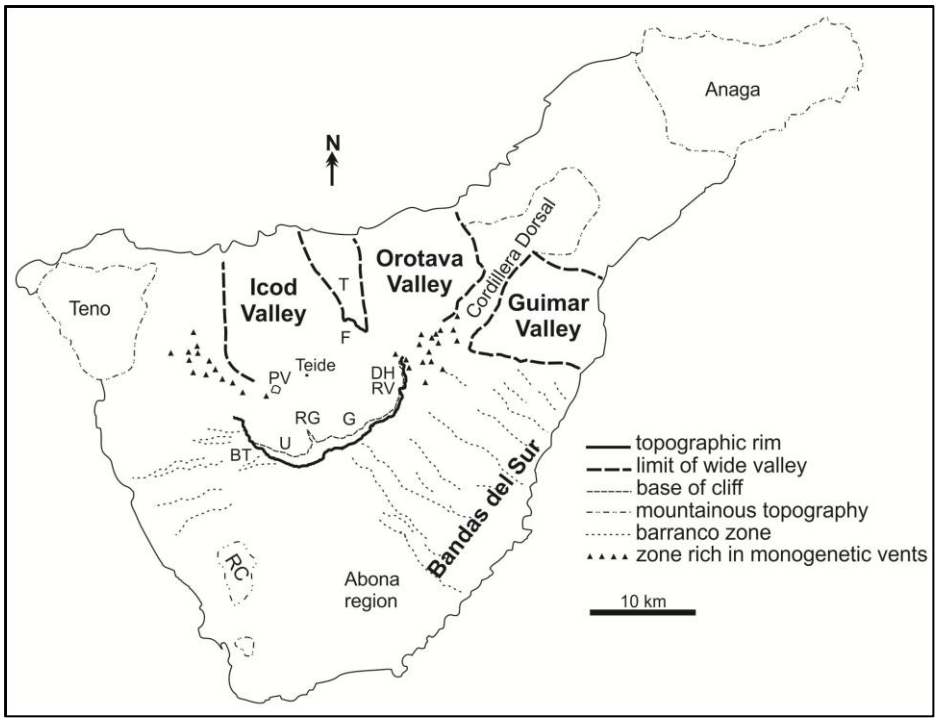

Figure 2.1 Simplified geomorphology of Tenerife. Las Cañadas depression is partly encircled by a topographic rim. North of Teide and Pico Viejo (PV) is the Icod valley, separated from La Orotava valley by the Tigaiga massif (T). To the east is the Guimar valley. Las Cañadas has three zones: Ucanca (U), Guajara (G) and Diego Hernandez (DH). The Roques de García (RG) form a ridge between Ucanca and Guajara and the Risco Verde (RV) 'headland' separates Guajara and Diego Hernandez (DH). Boca Tauce (BT) is west of Ucanca (BT). La Fortaleza (F) is an escarpment northeast of the depression. Roques del Conde (RC), Teno, Anaga and the Cordillera Dorsal are mountainous areas that, along with zones rich in monogenetic vents, loosely form a three-pronged pattern. The volcanic flanks and Bandas del Sur region are deeply incised with barrancos (canyons).

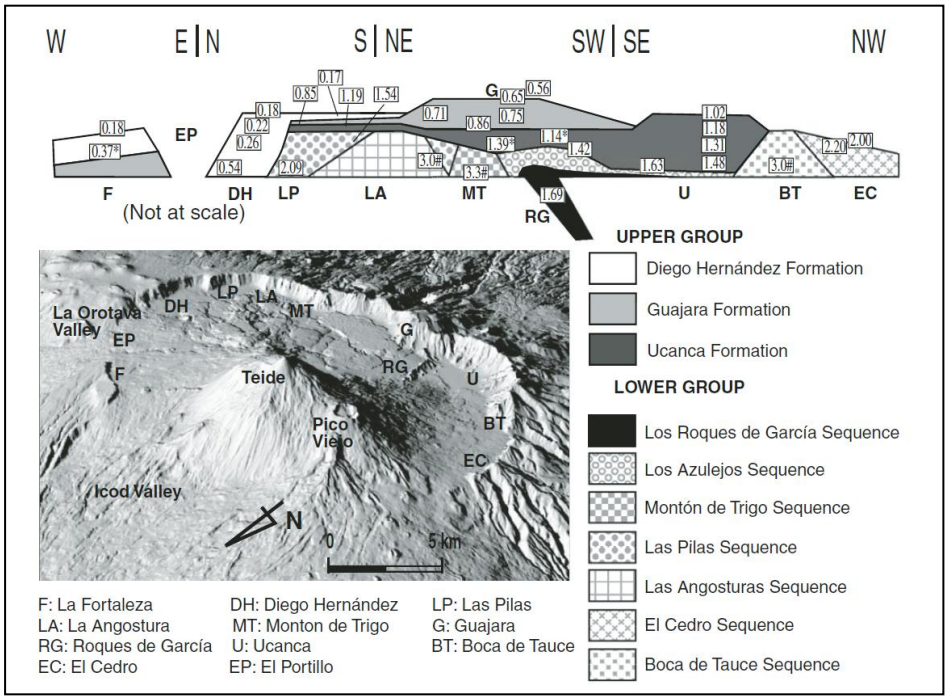

Figure 2.2 Schematic of Las Cañadas stratigraphy, with relative ages of different parts of the topographic rim. The opening to the north of Las Cañadas, infilled with the current Teide-Pico Viejo stratovolcano, is seen in the oblique view (from Martí et al., 2010).

with their associated hazards of pyroclastic density currents and/or large tsunamis, would be potentially catastrophic not just for Tenerife, but also for the other Canary Islands, coastal Africa, and possibly farther afield. This chapter reviews the literature concerning the origin of Las Cañadas, and considers its implications for the pre-Poris landscape.

Las Cañadas is commonly referred to as 'Las Cañadas *Caldera'*, to describe its shape irrespective of origin, by both workers in favour of caldera collapse and those who support lateral collapse (e.g. Ancochea *et al.*, 1990; Martí *et al.*, 1994b; Cantagrel *et al.*, 1999; Marti and Gudmundsson, 2000). Here the structure is referred to as a 'depression' to avoid confusing the issue of its origin.

2.2 Sector Collapse

Volcano sector collapse is a catastrophic process that forms open, U-shaped scars and debris avalanche deposits that extend from them. The latter can form extensive fields of huge (toreva) 'megablocks', hummocks and small mounds, and various massive to layered sediment-gravity flow deposits (Siebert, 1984). Debris avalanches, unlike lahars, are often relatively dry, but if water or explosive activity become involved the deposits of a debris avalanche can be gradational with the deposits of lahars or pyroclastic density currents (Siebert, 1984). The megablocks and hummocks, believed to originate from horst and graben formation during spreading of the deposit, can comprise large homogenous blocks surrounded by fragmented homogenous matrix, very close to other blocks and matrix of different composition, a reflection of incomplete mixing of debris (Coates, 1977). It has been found that deposited massive blocks may retain some primary bedding of the original stratovolcano cone structure (Siebert, 1984).

The sector collapse associated with the Mount St. Helens eruption of 1980 is a well documented example where the initial sliding of massive blocks became more flow-like as fragmentation increased during movement downslope (Glicken, 1996). The collapse coincided with a directed blast from the volcano, which led to the understanding that collapse can create a sudden pressure-release of the volcanic magmatic and hydrothermal systems, triggering explosive activity possibly in the

form of a laterally directed blast and PDC (Siebert, 1984). Similar explosive decompression resulting from flank collapse occurred at Montserrat on 26th December 1997 (e.g. Woods *et al.*, 2002). Sector collapse deposits can be incredibly extensive on land and beneath the sea; the Pungarehu deposit at Mt Egmont in New Zealand consists of over 3000 mounds >5 m high and extends to the coastline, beyond which conical hills occur on the seafloor (Neal, 1979).

Slope instability and lateral collapse are common on the flanks of ocean island volcanoes (Holcomb and Searle, 1991). There have been comprehensive studies of the Hawaiian chain (e.g. Moore *et al.*, 1989; Moore *et al.*, 1994; Morgan *et al.*, 2003) and Reunion (e.g. Labazuy, 1996; Oehler *et al.*, 2004), as well as work on island arc volcanoes such as Stromboli (e.g. Kokelaar and Romagnoli, 1995; Tibaldi, 2001; Romagnoli *et al.*, 2009) and Montserrat (Deplus *et al.*, 2001; Le Friant *et al.*, 2004). Various lines of evidence have been put forward for the occurrence of lateral collapses throughout the history of Tenerife and this research is reviewed here.

2.2.1 Evidence for sector collapse

The ages and locations of landslides proposed to have occurred on Tenerife, and the types of evidence cited in support of them, vary between research groups. Table 2.1 is a summary of the sector collapses proposed in the literature, the various ages that have been assigned to each, and the evidence used to support the research.

Onshore

Bravo (1952, 1962; discussed in Carracedo *et al.*, 1999) was the first to propose a connection between the structural evolution of Tenerife and gravitational block sliding. 'Chaotic breccias' within La Orotava valley were interpreted to be the cause of gradual landsliding of the overlying volcanic mass, as the brecciated material underwent plastic behaviour following alteration and water saturation. However, other workers did not believe the broad valleys to be related to lateral collapse; Hausen (1956) proposed Guimar and La Orotava to be graben and Ridley (1971) suggested that they are eruption-related calderas involving a trap door mechanism. In a review of the debate surrounding the origin of La Orotava valley, Palacios

Study	Evidence cited	Ages reported for Tenerife sector collapses (ka)							
		Anaga[b]	Teno[b]	Tigaiga[c]	Roq. de García[c]	Guimar[a]	Orotava[a]	East Dorsal[d]	Icod[a]
Ancochea *et al. (*1990)	K/Ar, GR & CB					<830	780-560		<170-130
Watts & Masson (1998)	SF	>>500	>>500 ?				~ 500		170
Cantagrel *et al*. (1999)	GR & SF	pre-Cañadas	~ 6000	>2300	700-600 ?		~ 600		<150
Ablay & Hürlimann (2000)	SF & GR							<560	
Masson *et al*. (2002)	SF	>1000			? >600	840-780	690-540		170-150
Brown *et al.* (2003)	$^{40}Ar/^{39}Ar$ & GR					830-289			
Walter *et al*. (2005)	$^{40}Ar/^{39}Ar$ & GR	~ 4500							

Table 2.1 Summary of ages provided in the literature for the sector collapses proposed to have occurred in Tenerife's geological history. The original studies proposing the landlsides are shown in superscript. (a) is Navarro & Coello, 1989, (b) is Watts and Masson, 1998, (c) is Ancochea *et al*., 1999 & Cantagrel *et al.*, 1999, and (d) is Ablay & Hürlimann, 2000. Note that studies often quote and employ data from previous workers when re-evaluating geological relationships and proposing new dates. In the 'evidence cited' column, the dating techniques and/or methods of estimating age used in each paper are listed. GR= interpretation of geological relationships, CB= citation of chaotic breccias, and SF= seafloor (bathymetry data, sedimentation rates).

(1994) stated that there is "a total absence of deposits related to slope failure", and suggested that the valley originates from "lateral widening"; it was envisaged that drainage gorges on the flanks of the volcano become covered by lava flows, thus shifting drainage laterally so that the valley becomes broader in a process that can be repeated many times. The chaotic breccias reported by Bravo were subsequently interpreted as collapse-scar fill deposits originating from instantaneous mass movement of up to 100 km^3 of material (Navarro and Coello, 1989) and the breccias in La Orotava, Guimar and Icod were interpreted to be the *result* of mass movement and not the cause (Carracedo *et al.,* 1999).

Older land-slides on Tenerife have been reported from onshore findings. Anchochea *et al.* (1999) proposed that breccia in the northeast section of the depression beneath the Tigaiga massif may represent debris deposits formed by the destruction of a 'Cañadas I edifice' (roughly equivalent to the 'Lower Group' deposits of Martí *et al.,* 1994b) before 2.3 Ma. It was suggested that the 'Tigaiga breccia' may have formed a "detachment level" that favoured the subsequent landslides that formed the Orotava and Icod valleys (Ancochea *et al.,* 1999).

The Roques de García outcrop within Las Cañadas depression has also been proposed to be the remnant of a debris avalanche deposit, with a headwall at the Cañadas wall, dated at "probably >0.6 Ma and possibly >1 Ma" (Ancochea *et al.,* 1999; Cantagrel *et al.,* 1999). The outcrop comprises pyroclastic and sedimentary deposits, predominantly breccias, and is intruded by a dense network of phonolitic sheets and dykes (Martí *et al.,* 2010). As part of this study, geological reconnaissance of the Roques de García outcrop found it unlikely to be any remnant of catastrophic collapse. The brecciated material at the Roques de García is less than 1 km from the present wall of the depression and is prominently heterolithic, so it is unlikely to be the relic of a debris avalanche from this or any nearby wall. In extreme proximal reaches, the clastic material of debris avalanche deposits is typically little-disaggregated, comprising large blocks and mounds of edifice strata and certainly not of thoroughly mixed lithologies (e.g. Glicken, 1996). Marti *et al.* (2010) propose that the 'Roques de García Formation' is an internally consistent stratigraphic succession reflecting primary pyroclastic and secondary epiclastic processes, with evidence of only minor avalanches and intra-formational breccias.

Additionally, stratigraphic relationships show that the Roques de García Formation is older than the Ucanca Formation (Fig 2.2). Phonolitic lavas throughout the formation, proposed by Cantagrel *et al*. (1999) to be megablocks within a landslide deposit, are in fact very similar to intrusions exposed in the Cañadas wall. Marti *et al* (2010) interpret the larger intrusions in the Roques de Garcia formation to be the remains of a large volcanic conduit that fed some of the phonolitic eruptions of Upper Group volcanism (1.57 to 0.17 Ma).

Seafloor

Mapping of deposits forming the sea bed around oceanic islands has been used to infer that large landslides may be a principal agent of their destruction (e.g. Moore *et al.*, 1994; Watts and Masson, 1995; Masson, 1996; Watts and Masson, 2001). Work around the Hawaiian archipelago by Moore *et al.* (1989) found that deposits of landslides from ocean island volcanoes can cover huge areas, with some individual deposits >5000 km^3 in volume. At the time of Palacios' study (1994), the available bathymetric work at Tenerife could not support the concept of large-scale slope failures; evidence of landslide deposits in the adjacent sea had not been found. However, more recent swath bathymetry and GLORIA surveys of the submarine flanks north of Tenerife have been used to map the morphology and backscatter characteristics of the seabed. In 1995, Watts and Masson reported the discovery of landslide material 700 m thick covering 5500 km^2 of seafloor, possibly >1000 km^3 in volume. This feature was interpreted to result from one or more landslides that created the Icod and Orotava valleys.

Martí (1998) recognised that the study by Watts and Masson (1995) proved the occurrence of large-scale collapses, but argued that a single landslide scenario could not fit with the geological record of Tenerife; the valleys of Icod and Orotava have different ages while the Tigaiga outcrop on land between the two valleys is an unmodified intervening massif. Watts and Masson (1998) subsequently described four discrete landslides to the north of the island, each with a distinct backscatter strength: Anaga (>>0.5 Ma), Teno (>>0.5 Ma), La Orotava (~0.5 Ma) and Icod (~0.17 Ma). Walter *et al*. (2005) proposed an age for the Anaga collapse of ~4.5 Ma.

In 1997, Teide Group researchers produced bathymetric evidence and an estimate that the offshore northern Tenerife debris apron contains 1200 km^3 of debris, with three distinct lobes of material. These lobes were interpreted to derive from slumping of the *submarine* flank, unrelated to any onshore structures (Teide Group, 1997). The group's work is not supported by the onshore geological studies described above and was also refuted by Ablay and Hürlimann (2000), who correlated onshore and offshore evidence for sector collapse in northern Tenerife using topographic and bathymetric digital elevation models. In their study, mass wasting deposits are classified into 'Old Post-Shield' (one large event or several events channelled between the Anaga and Teno shield massifs), and 'Young Post-Shield', which includes La Orotava (suggested to comprise two contemporaneous collapses), Icod, and 'East Dorsal', the deposits of which cover the La Orotava slide and are therefore <0.56 Ma (Ablay and Hürlimann, 2000). The authors suggest that a lack of correlation between deposit and valley volumes for the East Dorsal collapse, 100 km^3 versus 25 km^3 respectively, may register the involvement of concurrent failure of submarine slopes. This would suggest that the 'Tigaiga Breccia' of Cantagrel *et al.* (1999) corresponds with the 'Old Post-Shield' landslide. The Roques de García deposits are interpreted as a remnant of *caldera* collapse (Ablay and Hürlimann, 2000).

Elsewhere in the Canary Islands, work on the El Hierro landslide 'El Golfo' using sidescan sonar imaging in the Madeira Abyssal Plain has found evidence to suggest that 7 major turbidite-forming landslides have occurred in the Canary Islands over the course of the past 750 ka (Masson, 1996). In a summary of previous bathymetric and onshore work, Masson *et al.* (2002) describe the landslides that have affected La Palma, El Hierro and Tenerife, and present a shaded relief image of the seabed surrounding Tenerife (Fig 2.3). A landslide deposit beneath the Icod deposit is traced onshore to the west of the Icod valley in order to correlate it with the contentious Roques de García avalanche of Cantagrel *et al.* (1999).

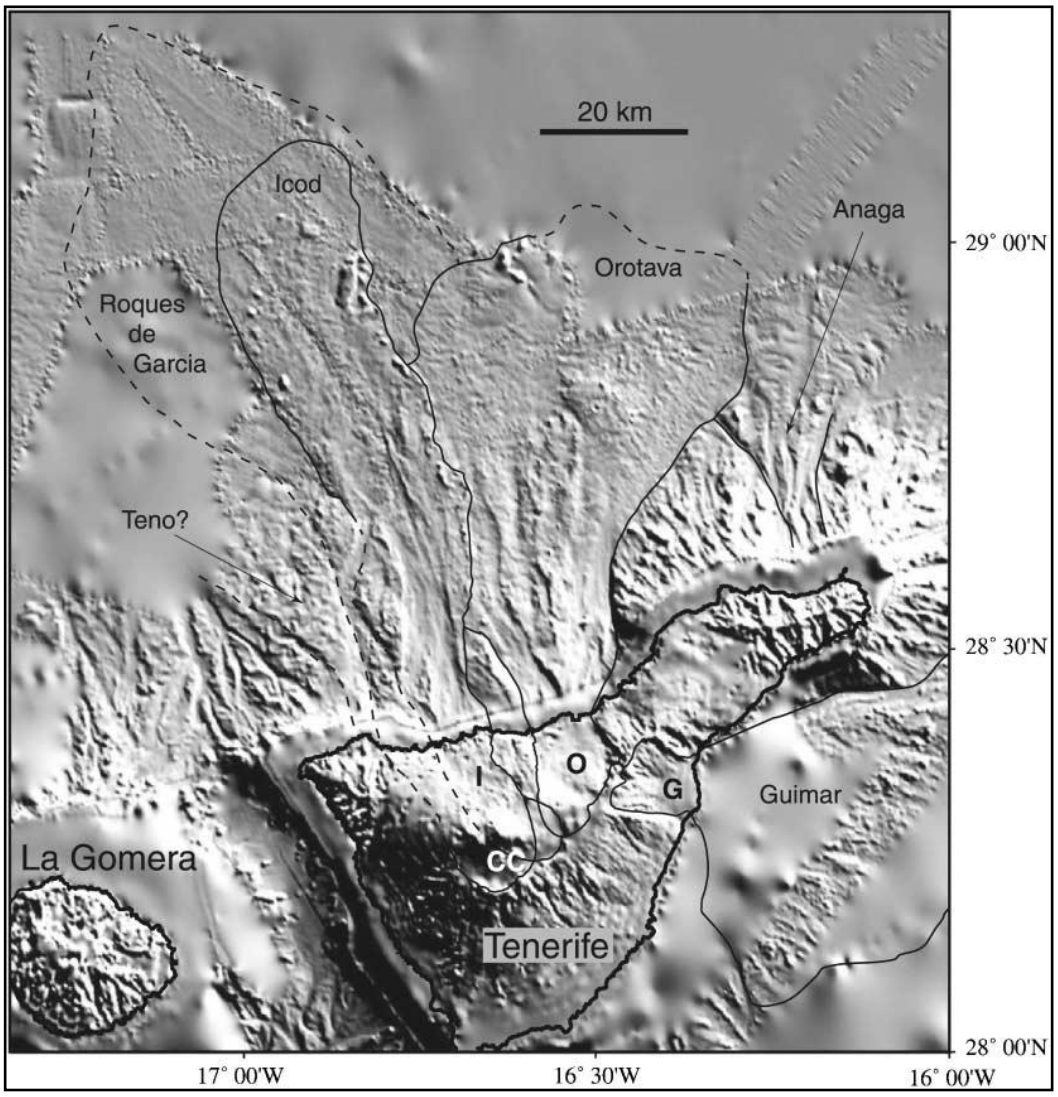

Figure 2.3 Shaded relief image of Tenerife, with areas believed to contain debris avalanche deposits outlined (Masson *et al*., 2002)

2.2.2 Stresses and triggers of sector collapse

Rift zone geometry

The occurrence of giant landslides on Tenerife is suggested by Carracedo (1994, 1996) to be related to the presence of a triaxial rift zone system on the island. The Quaternary vents of Tenerife roughly form NE-SW, NW-SE and N-S alignments that create a 'Mercedes-Benz star' arrangement (Fig. 2.4), which he considered to reflect 'least effort' fracturing caused by magma-induced upwelling and inflation. It was proposed that extensional stresses build orthogonal to the three rift zones, and, on exceeding the rupture threshold, lead to sector collapse. Carracedo states that the tensional stresses can result from overall gravitational instability, from volcanic 'cumulative' stresses (such as build-up of volcanic products), or from volcanic 'ephemeral' stresses (such as seismicity generated by intrusions), and he suggested that the stresses act upon two of the branches with the third acting as a 'buttress': the southern branch on Tenerife is the least active, and gravitational collapses are directed to the north (Carracedo, 1994).

In a comment on Carracedo's work, Martí *et al.* (1996) suggest that there are only two controlling tectonic trends on Tenerife, a hypothesis supported by gravimetric data showing a gravity high where two structural lineaments intersect (Gottsmann *et al.*, 2008). The NW-SE Teno-Santiago rift and the NE-SW Dorsal rift were not found to join beneath Teide-Pico Viejo, but farther south in the Ucanca area, concordant with the findings of Ablay and Kearey (2000). Gottsmann *et al*. (2008) propose that these lineaments have controlled the morphological evolution of the island over the past few million years, by providing preferential pathways for water and magma migration. Ablay and Kearey (2000) report a gravity anomaly at Boca Tauce (Fig 2.1), and interpret it to represent an old buried mafic volcano (~ 3.5 Ma), cored by a large mafic plutonic complex. They suggest that these higher density materials may have caused the buttressing effect noted by Carracedo (1994) and prevented lateral collapse to the south.

Walter and Troll (2003) suggest that the development of the triaxial rift system may be more complicated than the 'least effort' model of Carracedo (1994, 1996). Their

study proposes that a number of triaxial rift zones developed concurrently on Tenerife, and suggests that this process cannot be accounted for by crustal doming.

Triggers of sector collapse

Large landslides occur at volcanic edifices due to the progressive development of gravitational instability; however, the triggers of the catastrophic events are not well understood. Various triggers have been proposed, including seismic activity (e.g. Voight *et al.*, 1983), caldera collapse (e.g. Martí *et al.*, 1997), rift zone reorganisation (Walter *et al.*, 2005), weak substrate (e.g. Borgia *et al.*, 2000), volcanic loading (e.g. Carracedo, 1994), hydrothermal alteration or saturation by hydrothermal waters (e.g. Siebert, 1984), and dyke intrusions and pore fluid pressure increases (e.g. Elsworth and Voight, 1996; Elsworth and Day, 1999). Other, non-volcanic, factors include slope angle, changing sea level and climatic effects (McGuire, 1996). Key studies relevant to Tenerife are reviewed here.

Study of the Orotava valley on Tenerife has found that the deep canyons, steep coastal cliffs and weak palaeosols present throughout the region would have facilitated sliding and sector collapse, but that these features did not cause the collapse itself (Hürlimann *et al.*, 2004). However, the authors propose that the structural axis of the slide was determined by the orientation of dykes intruded into the Dorsal Rift, and the position of volcanic vents.

A key issue is whether dyke intrusion and rifting instigate collapse, or occur as a passive result of failure, 'infilling' fractures and weaknesses created. Dyke direction and instability are functions of the gravitational load-stress field of a volcano, and are therefore intrinsically linked (Walter and Troll, 2003). However, the nature of the linkage is contentious. It has been proposed that dyke swarms lie parallel to the regional maximum horizontal compression, so that the direction of sector collapse is orthogonal to the dyke swarm (Siebert, 1984, Fig. 2.5). Research in Japan (Moriya, 1980) shows that debris avalanches flow and form deposits on average at approximately right angles to lines of the fissure vents, and hence their underlying dykes. Additionally, in Japan, more volcanoes with zones of parallel dykes undergo sector collapse than those without a dominant dyke direction (Siebert, 1984). This correlation is also seen on Tenerife, where the Guimar and Orotava scars both record

collapse perpendicular to the Cordillera Dorsal ridge of aligned dykes; the degraded headwalls of both extend into the zone of scoria cones and dykes.

The experiments of Walter and Troll (2003) found that when a magma analogue is injected into an edifice with homogeneous basal friction, radial fractures will form. However, when the magma is intruded close to an interface between stable and unstable sectors of an edifice, a curved or tangential rift zone may develop, which then may promote a third, 'buttressing' rift. Thus the formation of triaxial rift zones may occur as a response to near-surface volcano deformation. This is supported by further study of the Anaga zone of Tenerife where field and chronology data imply a complicated relationship between rifting and sector collapse (Walter *et al.*, 2005).
It is proposed that a single rift at Anaga became unstable and underwent partial collapse into the sea between 4.7 and 4.1 Ma, and that dykes were intruded tangentially around the unstable sector as the creeping flank underwent extension. This change from a linear rift to a curved rift is suggested to speed up the movement of the unstable zone and promote rift-zone development orthogonal to the failure, creating a third axis (Fig 2.6). This study, however, does not account for the initial simple rifting, and thus the chicken-or-egg situation remains.

The emplacement of dykes has been proposed to trigger sector collapse as a result of pore fluid pressure increases generated by both mechanical and thermal straining (Elsworth and Voight, 1996; Elsworth and Day, 1999). The width and intrusion velocity of dykes are suggested to be primary factors influencing the amount of pore pressure increase, which in turn is proposed to result in an increased uplift force acting on a free block (Elsworth and Voight, 1996). This process is invoked as the main trigger of flank collapse on La Palma and Fogo (Cape Verde) (Elsworth and Day, 1999), but the assumptions of uniform dyke width and velocity, and of a uniform detachment slope, are unbounded and not fully justified.

A hypothesis of cyclical flank collapse has been put forward by authors who follow the 'Cañadas I, II and III' classification for the period 3.5 - 0.17 Ma (e.g. Ancochea *et al.*, 1999; Cantagrel *et al.*, 1999). Each of the three episodes is thought to have lasted over 1 million years, during which stratovolcano cones would have become loaded with enough volcanic material to become gravitationally unstable; each

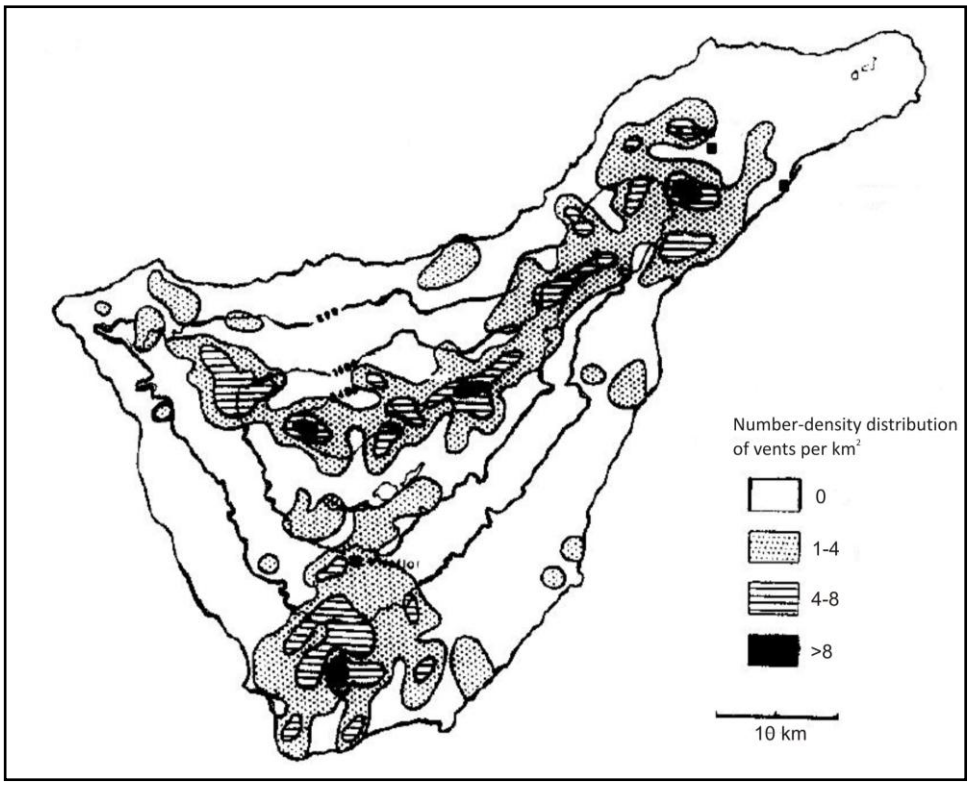

Figure 2.4 Concentration of Quaternary volcanic emissions. A 'Mercedes'-type stellate rift zone arrangement occurs on Tenerife (Carracedo, 1994).

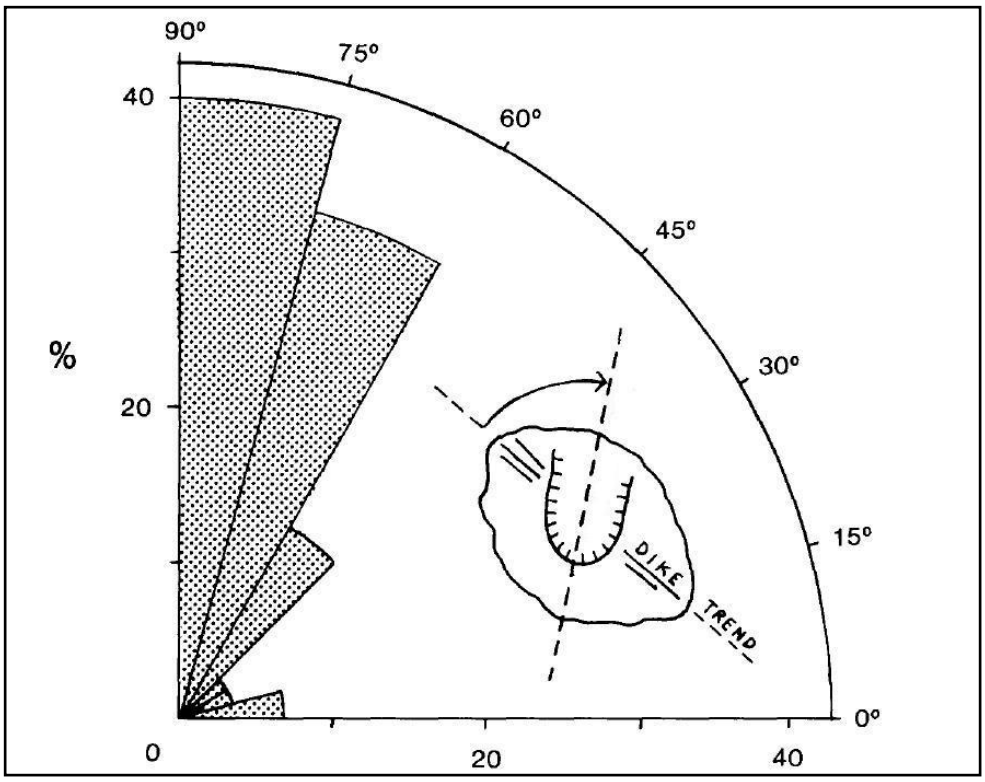

Figure 2.5 Orientation of axis of depressions formed by debris avalanches in relation to trend of linear dykes and parasitic vents for 30 volcanoes. Many debris avalanches occur roughly perpendicular to the trend of dykes, and therefore also perpendicular to the region of maximum horizontal compression (adapted from Siebert, 1984).

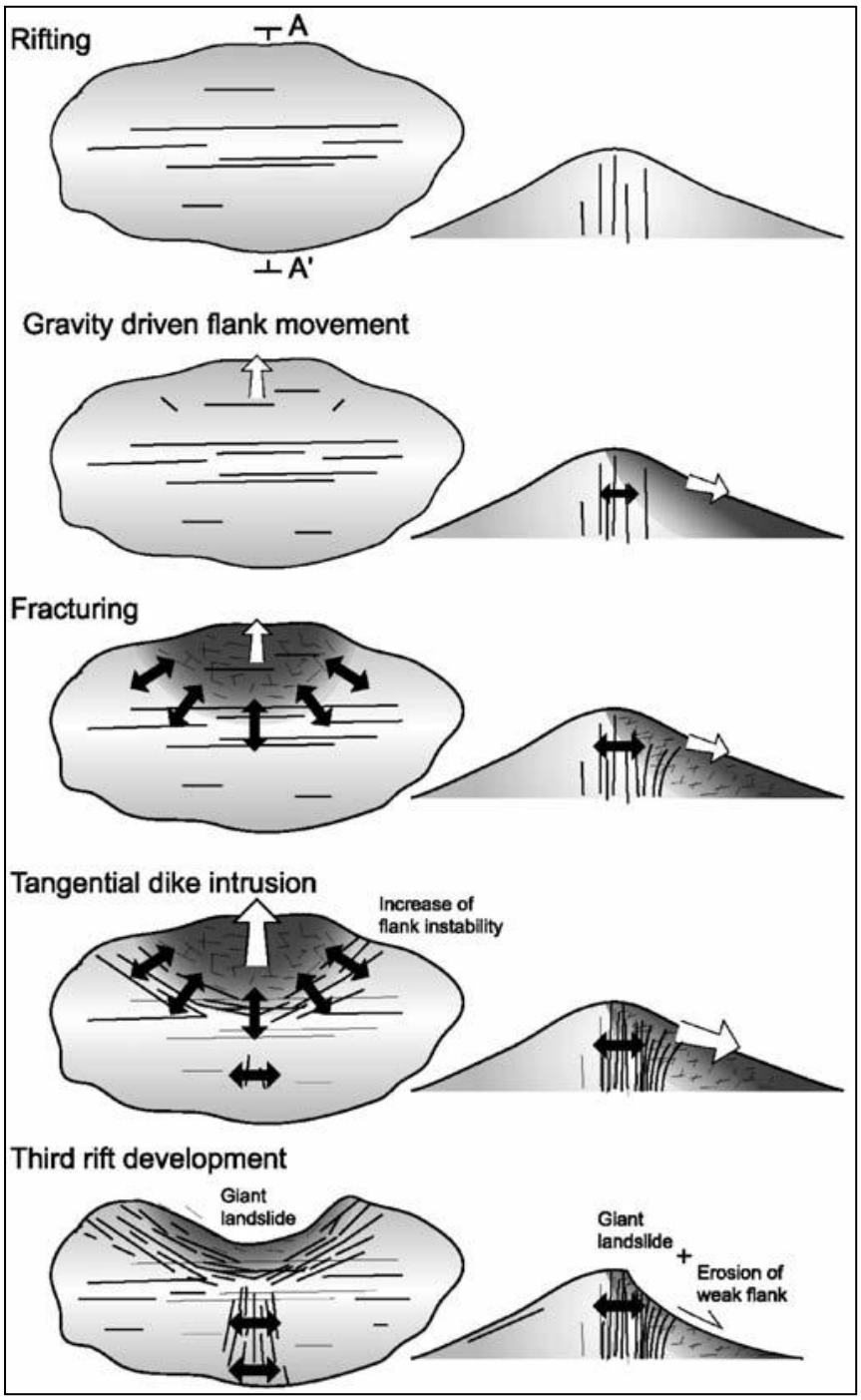

Figure 2.6 Model of rift zone reorganisation at Anaga, Tenerife (Walter *et al.*, 2005)

episode of growth would thus culminate with a flank collapse. Some advocates of the lateral collapse model(s) concede that caldera-forming pyroclastic eruptions did occur in the Cañadas episode, but they suggest that vertical subsidence is not connected to sector collapse in any way and that caldera structures are no longer visible on the island (e.g. Cantagrel *et al.*, 1999).

2.2.3 Sector collapse and the shape of Las Cañadas depression

It has been argued that if the Cañadas wall was created by caldera collapse, the remnants of a wall would exist beneath the Teide-Pico Viejo lavas to the north: but the water-supply galleries ('gallerias') beneath these lavas contain no Cañadas wall deposits (Coello, 1973; Ancochea *et al.*, 1990). Based upon 100-m-thick chaotic breccias found beneath Teide-Pico Viejo lavas in the Icod valley and landslide deposits off the northern coast, the southern Cañadas wall has been interpreted as the ancient headwall of a large sector collapse (Navarro and Coello, 1989; Ancochea *et al.*, 1990; Carracedo, 1994; Watts and Masson, 1998; Watts and Masson, 2001). The scalloped trace of the Cañadas depression is considered to resemble the shape of head scars of large landslides (Cantagrel *et al.*, 1999).

Although seafloor debris avalanche deposits and onshore breccias are evidence that the Icod valley is a remnant of a flank collapse, the location of the Roques de García deposits indicates that this collapse cannot have extended to the southern Cañadas wall. The occurrence of the La Fortaleza escarpment in the northeast of the depression also indicates that the Icod headwall cannot have been in the southern part of Las Cañadas. The southern Cañadas wall is three times wider than the top of the Icod Valley, further evidence that it cannot be the headwall of the collapse. Shallow, high-density bodies to the north of the Teide-Pico Viejo complex have been interpreted as intrusions into the scar left behind by the Icod landslide; therefore the headwall may have been in the vicinity of a northern caldera wall but is now buried beneath deposits of T-PV (Gottsmann *et al.*, 2008). Conceivably, the location of the Icod valley headwall acted as a focus for extensional stresses, and so controlled the location of the present Teide-Pico Viejo edifice in the north of the depression (Ablay and Kearey, 2000). This relationship would be consistent with slope stability experimental modelling (Martí *et al.*, 1997), which shows that where slip is directed

northwards from an analogue Las Cañadas area, collapse begins north of the perimeter of the depression and not within it. Furthermore, although chaotic breccias occur in the Icod valley itself, these have not been found in drill-holes *within* the depression at the same depth (Martí *et al.*, 1997), which should be expected if the Icod landslide extended to the southern Cañadas wall.

Lateral collapse may have influenced the present shape and structure of the *eastern* sector of Las Cañadas depression as well as modifying it to the north. Deposits in the Diego Hernandez (DH) section of the wall unconformably infill a 'palaeovalley', bounded steeply to the south at Risco Verde by an escarpment of phonolites of the Guajara sector of the wall and to the north by a threshold built of Strombolian cones and lavas of the Cordillera Dorsal (Ancochea *et al.*, 1990; Martí *et al.*, 1990; Martí *et al.*, 1994b). Some workers suggest that this palaeovalley has an 'age and position' that indicate a possible relationship with the Orotava sector collapse, and that the lava escarpment at Risco Verde (Fig. 2.1) is part of the Orotava collapse headwall (Ancochea *et al.*, 1990; Martí *et al.*, 1994b; Cantagrel *et al.*, 1999; Hürlimann *et al.*, 2004) (Fig. 2.7). However, this is a speculative extrapolation of the Orotava headwall west across the Dorsal Ridge. It seems equally likely that caldera collapse associated with a pre-Diego Hernandez eruption, such as the Granadilla, created the depression within which the Diego Hernandez units were deposited. The Risco Verde escarpment is positioned at a steep angle to the rest of the Cañadas wall, but work with ice melt structures has shown that shapes analogous to this can readily be created during subsidence (Fig. 2.8) (Branney and Gilbert, 1995). Furthermore, similar structures are known at other calderas such as at Santorini (at Megalo Vouno) or at Valles Caldera (the Toledo Embayment) (e.g. Druitt *et al.*, 1999; Goff *et al.*, 2011).

It is clear that sector collapse has affected the landscape of Tenerife dramatically, forming the contemporary straight-sided and wide valleys of Guimar, La Orotava and Icod in the last million years as well as affecting the landscape farther back in time. Proof of this is found on land and in extensive seafloor deposits. There is, however, convincing evidence to suggest that landslide processes are not solely responsible for the formation of Las Cañadas depression.

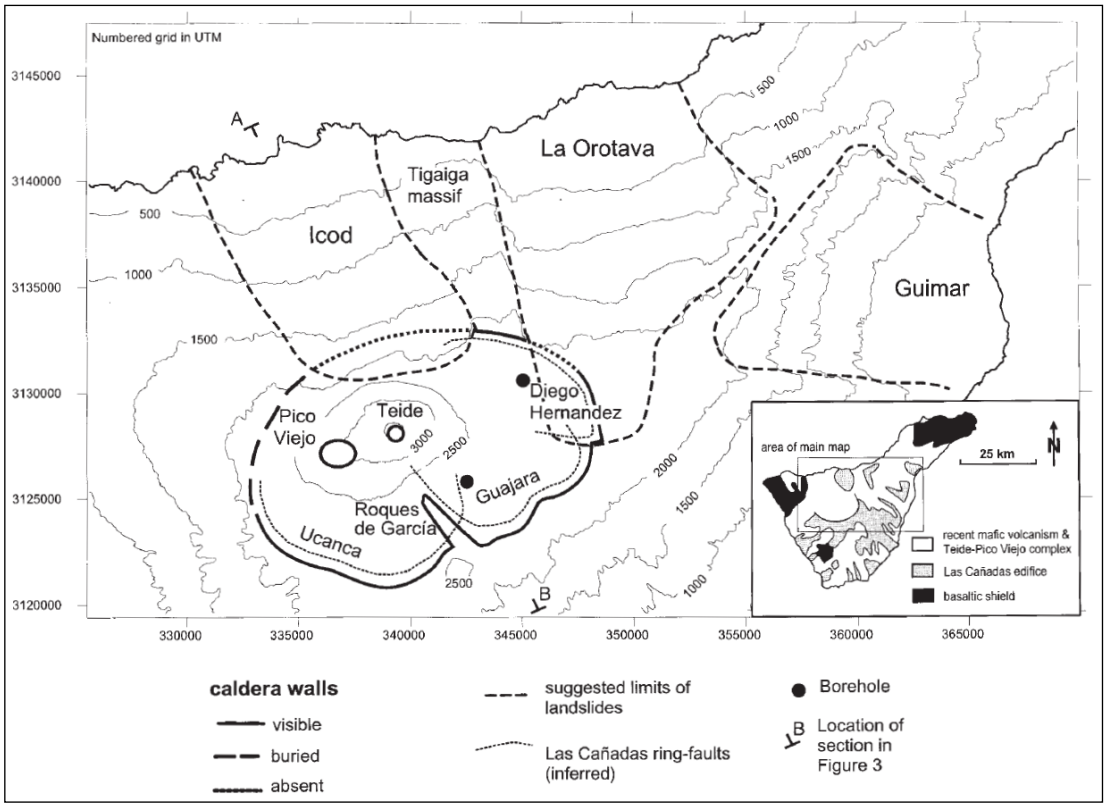

Figure 2.7 Map of the Cañadas area from Marti *et al.* (1997), illustrating how the Orotava collapse is believed to have created the Diego Hernandez palaeovalley in the east of the depression.

Figure 2.8 Ice melt pits at Volcán Hudson, Chile. Initial fractures are outward dipping, producing fractures prone to collapse. (photo credit Mike Branney)

2.3 Vertical collapse

Cataclysmic eruption of tens to thousands of cubic kilometres magma can lead to magma-chamber collapse and roof subsidence, creating a topographic depression called a caldera (Williams, 1942; Smith and Bailey, 1968; Druitt and Sparks, 1984). These depressions can be vast, such as the 35x75 km La Garita Caldera in Colorado, and they are commonly partially infilled with ignimbrites deposited during the climactic stages of the eruption, (Lipman *et al.*, 1984; Lipman, 2000c).

Various field and experimental studies have aimed to constrain the mechanisms and structures related to caldera subsidence (e.g. Clough *et al.*, 1909; Druitt and Sparks, 1984; Branney and Kokelaar, 1994; Martí *et al.*, 1994a; Moore and Kokelaar, 1998; Holohan *et al.*, 2005; Kokelaar, 2007); a brief outline of key research is provided in Chapter 1. It is important to bear in mind that structures beneath calderas need not be of simple 'cauldron'-type subsided blocks bounded by vertical or inward dipping normal faults, but have increasingly been found on detailed examination of dissected systems to be highly faulted and to have involved piecemeal subsidence, commonly with downsag and with outward dipping faults that do not involve any subsidence-space problem (e.g. Branney and Kokelaar, 1994; Branney, 1995; Moore and Kokelaar, 1997; Milner *et al.*, 2002b)

Evidence that caldera collapse has been significant in the topographic evolution of Tenerife is abundant (Bryan *et al.*, 1998a; Marti and Gudmundsson, 2000; Brown *et al.*, 2003; Bryan, 2006; Edgar *et al.*, 2007; Coppo *et al.*, 2008), and it has been suggested that cyclical vertical collapse is responsible for the present shape of Las Cañadas depression (e.g. Martí *et al.*, 1994b). This section reviews these studies.

2.3.1 Evidence for caldera collapse

Ridley (1971) was an early advocate of caldera collapse operating on Tenerife. In his model, the Guimar and Orotava valleys, and possibly also the Cañadas depression, were formed as magma migrated away from fissure zones towards the flanks causing 'trap door' collapse. Booth (1973) interpreted pyroclastic deposits in the southern coastal strip (the 'Granadilla Pumice deposit') as evidence of a large explosive event that took place over 32 000 years and would have been accompanied

by caldera collapse, suggesting that the volume of pyroclastics erupted accounts for the volume of the caldera. Subsequently, the pyroclastic stratigraphy along the south coast was found to represent numerous caldera-forming explosive eruptions, all interpreted as having centred in Las Cañadas depression (e.g. Bryan *et al.*, 1998a; Brown *et al.*, 2003; Edgar *et al.*, 2007).

In a seminal paper, Martí *et al.* (1994b) invoked vertical (caldera) subsidence in the structural evolution of the Cañadas depression, opposing the lateral-collapse concept previously presented by Ancochea *et al.* (1990). Geological findings cited as evidence of caldera collapse include lithic breccias within ignimbrites (discussed further in Section 2.4.1), coarse pumice-fall beds, and strong welding fabrics observed within the wall deposits, typical of proximal caldera-wall facies. Welded deposits of the Guajara formation (0.8-0.57 Ma) are interpreted as mantling the southern part of the Cañadas wall, dipping inwards (Martí *et al.*, 1994b; Martí *et al.*, 1997). This could be a result of eruption of this material during caldera collapse or immediately subsequent to collapse, and provides further evidence that the Icod flank collapse formed further north; the 0.8-0.57 Ma mantling deposits would not be present if the southern wall had been the headwall of the relatively young Icod collapse (>0.17 Ma).

Structural features within the Cañadas area cited as evidence for vertical subsidence include cone sheets, radial and concentric dykes, and steeply inward dipping dykes; dyke orientation is linked to the presence of ring fractures, inferred to be connected to caldera collapse (Martí *et al.*, 1994a; 1994b; 1996). It has been proposed that concentric fractures in the wall that acted as steep conduits for phonolitic magma are not typical of lateral collapse, which often creates curved, normal listric faults, but are consistent with vertical subsidence (Martí *et al.*, 1996). Geophysical studies have been used as evidence for caldera subsidence in the Las Cañadas area. Microgravimetry has been presented to infer a caldera 'double vault' structure (Vieira *et al.*, 1986; Camacho *et al.*, 1991) and a study of electrical resistivity proposed that distortions reflects a "double volcano-tectonic depression" (Ortiz *et al.*, 1986). More recently, electrical resistivity signatures were interpreted to indicate three "funnel-like" forms beneath the depression infill material (Coppo *et al.*, 2008). Gravimetric study (Gottsmann *et al.*, 2008) found shallow high-density bodies in the

Diego Hernandez sector, which were interpreted to be intrusions along a ring fault created during vertical collapse.

Evidence for caldera collapse is not limited to the Cañadas proximal area, but is abundant also in the pyroclastic successions on the lowland southern flanks of Tenerife, known as the 'Bandas del Sur' (Fig. 2.1). Canyons ('barrancos'), extending down to the coast in places, contain excellent exposures of ignimbrites and Plinian fallout tephras recording explosive eruptions of magnitudes that would unavoidably involve caldera collapse. These deposits have been studied for both petrogenesis (e.g. Wolff, 1985) and volcanic processes (e.g. Booth, 1973; Bryan *et al.*, 1998b; Brown *et al.*, 2003; Edgar *et al.*, 2007). The significance of this work is considered below in Section 2.4.

2.3.2 Caldera collapse and the shape of Las Cañadas depression

Frequent repetition of caldera collapse throughout Tenerife's history has only recently been recognised (e.g. Bryan *et al.*, 1998a; Brown *et al.*, 2003; Edgar *et al.*, 2007); previously caldera collapse was believed to have been relatively infrequent on the island, occurring in cycles. Martí *et al*. (1994b) suggested that the three formations comprising the Upper Group of the Cañadas succession should be interpreted as the deposits of felsic centres that migrated northeastwards with time. Caldera collapse was inferred to have been cumulative for each formation, occurring during the final eruption of the Ucanca centre at 1.1 Ma, the final (Granadilla) eruption of the Guajara centre at 0.65 Ma, and the Abrigo eruption of the Diego Hernandez centre at 0.17 Ma (Martí *et al.*, 1994b). Substantial mafic magmatism was supposed to follow each cycle (Martí *et al.*, 1997). The concept that each zone of Las Cañadas correlates to a cycle of volcanism, separated by clear erosional unconformities, was supported by Bryan *et al.* (1998b) (Fig. 2.9), who correlated Cañadas wall deposits and the Bandas del Sur using radiometric dating, phenocryst mineralogy and stratigraphic position.

The tripartite shape of the depression was thus proposed to be due to the migration of the three felsic centres, evidence of which is implied by the eastwards-younging stratigraphy of the 'Upper Group' (Martí *et al.*, 1994b) (Fig 2.10). The steepness

and scalloped shape of the wall, interpreted by some workers as features of the headwalls of lateral collapse (e.g. Cantagrel *et al.*, 1999), can be reconciled with caldera collapse alone (e.g. Martí *et al.*, 1996). The position of Las Cañadas depression was interpreted by Carracedo (1994) to result from intersection of Tenerife's three 'rift zones', but Martí *et al.* (1996) argued that the radiating vent alignments constituting the 'rifts' more probably reflect a stress field and associated fractures related to tumescence above shallow central felsic magma reservoirs. In the caldera subsidence model, flank collapse is not crucial in the formation of the Cañadas depression, but it probably modified the northern sector of the wall formed by caldera collapse.

Citing the scalloped shape of Las Cañadas as indicative of its origin is imprudent, due to the effect of degradation through time. The rim of all calderas is a line of scarp retreat due to mass wasting, while the associated rockfall tends to accumulate in the subsided area; mass wasting therefore enlarges the original depression and controlling faults may be substantially buried and a considerable distance from the evolved rim. The significant role of mass wasting is often omitted from the discussion of Las Cañadas morphology, even though mass-wasting processes are active on the walls of the depression today forming alluvial fans and scree. There is a contrast in the degree of mass wasting modification that has occurred in the three wall segments, with the Ucanca wall most deeply eroded and revealing numerous intrusions of the ancient flanks, the lavas and welded ignimbrites of Guajara wall less so, and the Diego Hernandez wall strongly cut back but comprising cliffs of relatively weak (unwelded) volcaniclastic deposits. None of the modern Cañadas wall remains unmodified by mass wasting and it is not possible to distinguish embayments formed primarily by collapse as opposed to erosion.

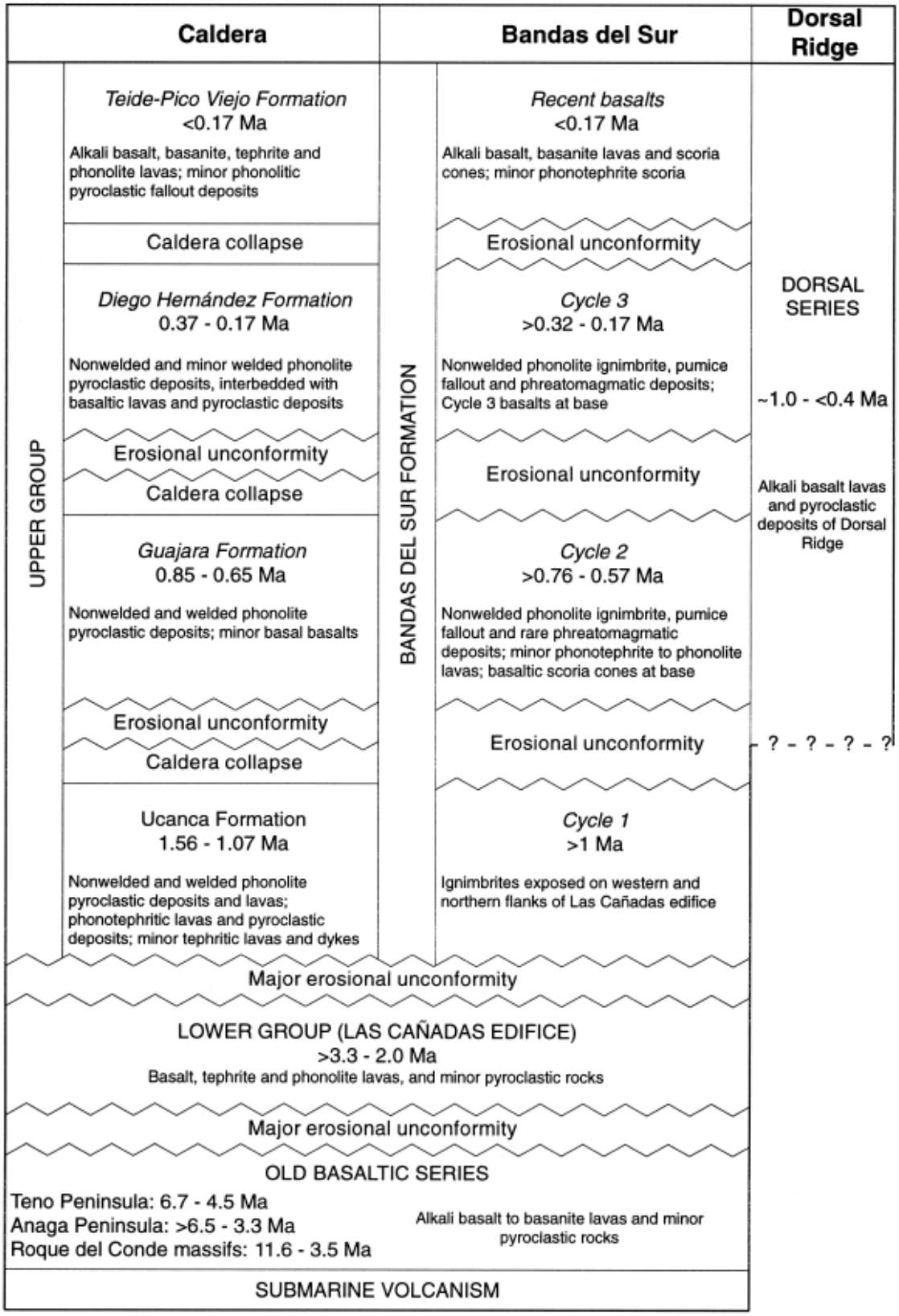

Figure 2.9 The stratigraphic succession of the Bandas del Sur, correlated with the 'Upper Group' of Marti *et al*. (1994). Three discrete cycles are proposed (taken from Bryan *et al.* 1998).

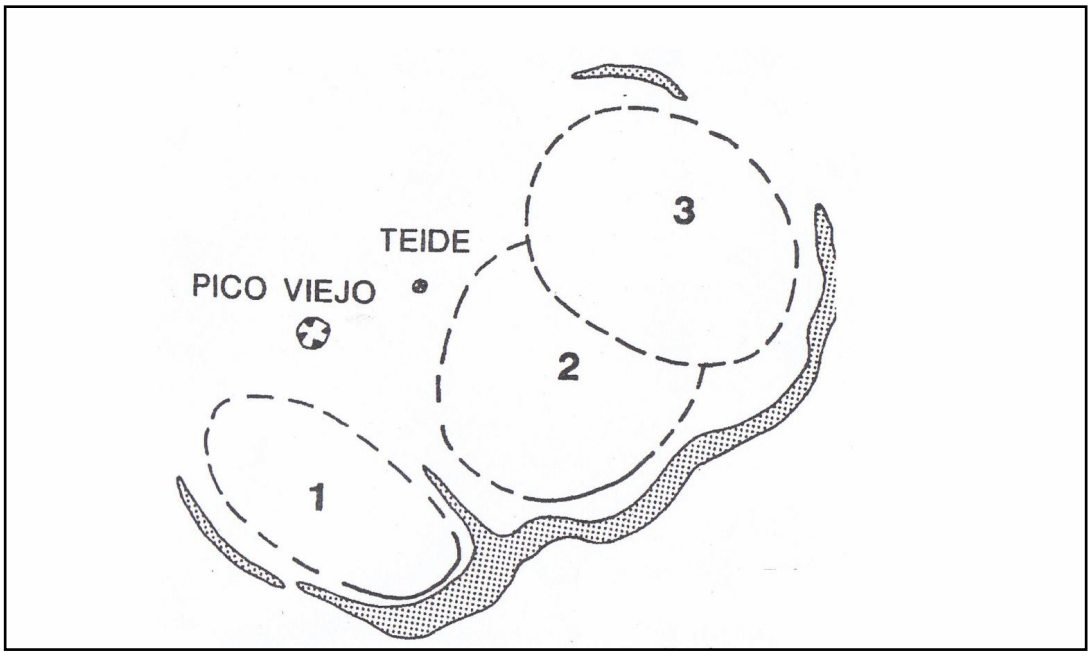

Figure 2.10 Diagram from Mart *et al*. (1994) showing the three distinct caldera boundaries of the vertical subsidence theory.

2.4 Evidence for multiple caldera collapse

2.4.1 Lithic breccias

The existence of lithic breccias towards the top of ignimbrites, originally termed 'lag breccias', has long been associated with caldera collapse (e.g. Williams, 1942; Walker, 1985; Druitt and Bacon, 1986). As large volumes of magma are removed from a chamber, the roof can begin to fracture and founder (Williams, 1942), causing caldera collapse possibly along outward dipping faults (Branney, 1995). Magma chambers are surrounded by hydrothermal systems and rapid dilation of a fault that intersects a hydrothermal system causes liquid water to flash explosively to steam and this vapour to expand (Kokelaar, 2007). Catastrophic depressurisation of the hydrothermal system, as the roof of a magma chamber collapses during the climactic phases of explosive eruptions, would therefore excavate a large amount of brecciated country rock, which may then be ejected along the dilating fault and into the pyroclastic density currents transporting material away from the caldera. It is thus suggested that the presence of lithic breccias in ignimbrite deposits, especially those with hydrothermally altered clasts, may mark the timing of the dilation of caldera 'superfaults' (Kokelaar, 2007) and hence mark main-phase caldera collapse.

The types of lithics in a lithic breccia, and the position of breccia lithofacies within an ignimbrite, can indicate whether the clasts have been sourced from within the volcano or vent or have been picked up by the pyroclastic density current as it moved across the substrate (Bryan *et al.*, 1998a). For example, the presence of syenite clasts, (the plutonic equivalent of phonolite) in a lithic breccia would indicate a sub-vent source and basaltic scoria may indicate that the current moved across a scoria cone. Lithics can be derived from bed erosion, but breccias consisting solely of this type are often of limited extent. A high proportion of vent-sourced clasts near the top of an ignimbrite can be used as an indication of the climactic caldera collapse phase of an explosive eruption (Bryan *et al.*, 1998a). Surface features of clasts may also be significant. Spheroidal spallation of a lithic within a breccia indicates that the entire clast was very hot during transport, and is therefore likely to have originated from beneath the vent; lithic clasts are poor conductors of heat and take a long time to heat or cool completely, so as the hot exterior is chilled and

contracts around a still-hot core, shell-shaped pieces of rock may 'spall' off (Branney and Kokelaar, 2002).

The recognition of lithic breccia lithofacies in Tenerife ignimbrites has been significant in assessing the frequency of caldera collapse in the Cañadas source area. However, some workers implied that the presence of breccias was not always a record of collapse. Bryan *et al.* (1998b) recognised 8 ignimbrites with exposures over 10 m thick in the Bandas del Sur and linked the concentration of lithic clasts towards the top of many of the ignimbrites to a "flux of vent-derived lithic material late in the eruption". However, only two ignimbrites were interpreted to correlate with caldera collapse at Las Cañadas, on the basis that the two largest volume ignimbrites, Granadilla and Abrigo, coincide with the climax of the Guajara and Diego Hernandez cycles respectively (Bryan *et al.*, 1998a; 1998b). This work inferred that caldera collapse could not occur 'mid-cycle' or in an incremental fashion on Tenerife, and this notion was refuted by later stratigraphic studies, detailed below.

Absolute $^{40}Ar/^{39}Ar$ ages for the deposits exposed in the Bandas del Sur (Brown *et al.*, 2003) constituted a significant advance in understanding the stratigraphy of Tenerife. The analysis reduced the number of eruptions and found that some were larger than previously realised. The authors designated the largest eruptions as formations within the Bandas del Sur *Group*, as opposed to the Bandas Del Sur *Formation,* and proposed that there is insufficient evidence to justify the cyclicity invoked by previous workers (e.g. Martí *et al.*, 1994b; Bryan *et al.*, 1998b). A relatively consistent style of large-scale eruption was described, with protracted intervening episodes of non-deposition and erosion that may obscure true eruption volumes. The instances of major lithic breccias in the ignimbrites were interpreted to indicate at least 7 major caldera-forming eruptions (Brown *et al.*, 2003) (Table 2.2).

Edgar *et al*. (2007) reconsidered the 'Diego Hernandez Formation' (Fig. 2.11) using exposures from various locations across the island, with new $^{40}Ar/^{39}Ar$ dates, some new nomenclature and revised volume estimates, and then suggested that vent-derived lithic-breccias in the Abrigo, Fasnia, Poris, and Caleta ignimbrites record individual piecemeal collapse events.

Formation	Eras	Arico	Abades	Granadilla	Fasnia	Poris	La Caleta	Abrigo
Feature								
Basal plinian fall deposits	X	X	?	X	X	X	X	?
Extensive geographic dispersal	?	X	X	X	X	X	X	X
Predominantly phonolite composition	X	X	X	X	X	X	X	X
Banded pumice/magma mingling	X	X	X		X	X	X	X
Condensed sequences		X	X	?	X	X	X	?
Valley-fill and veneer ignimbrite	X	X	X	X	X	X	X	
Extensive lithic breccias		X		X	X	X	X	X
Lithofacies:								
massive	X	X	X	X	X	X	X	X
diffuse-bedded	X	X	X	X	X	X	X	X
diffuse-stratified	X	X	X	X	X	X	X	X
pumice lenses	X	X		X	X	X	X	X
Splay-and-fade stratification (*sensu* Branney & Kokelaar, 2002)		X		X	X	X	X	X
Internal erosion surfaces		X		X	X	X	X	
Compositional zoning	X	X	X	X	X	X	X	X
Lower parts of formation locally stripped by climactic-phase density currents		X		X	X	X		X

Table 2.2 Features shared by ignimbrite deposits in the Bandas del Sur (from Brown et al., 2003). The presence of lithic breccia lithofacies, significant in the caldera collapse debate, is highlighted.

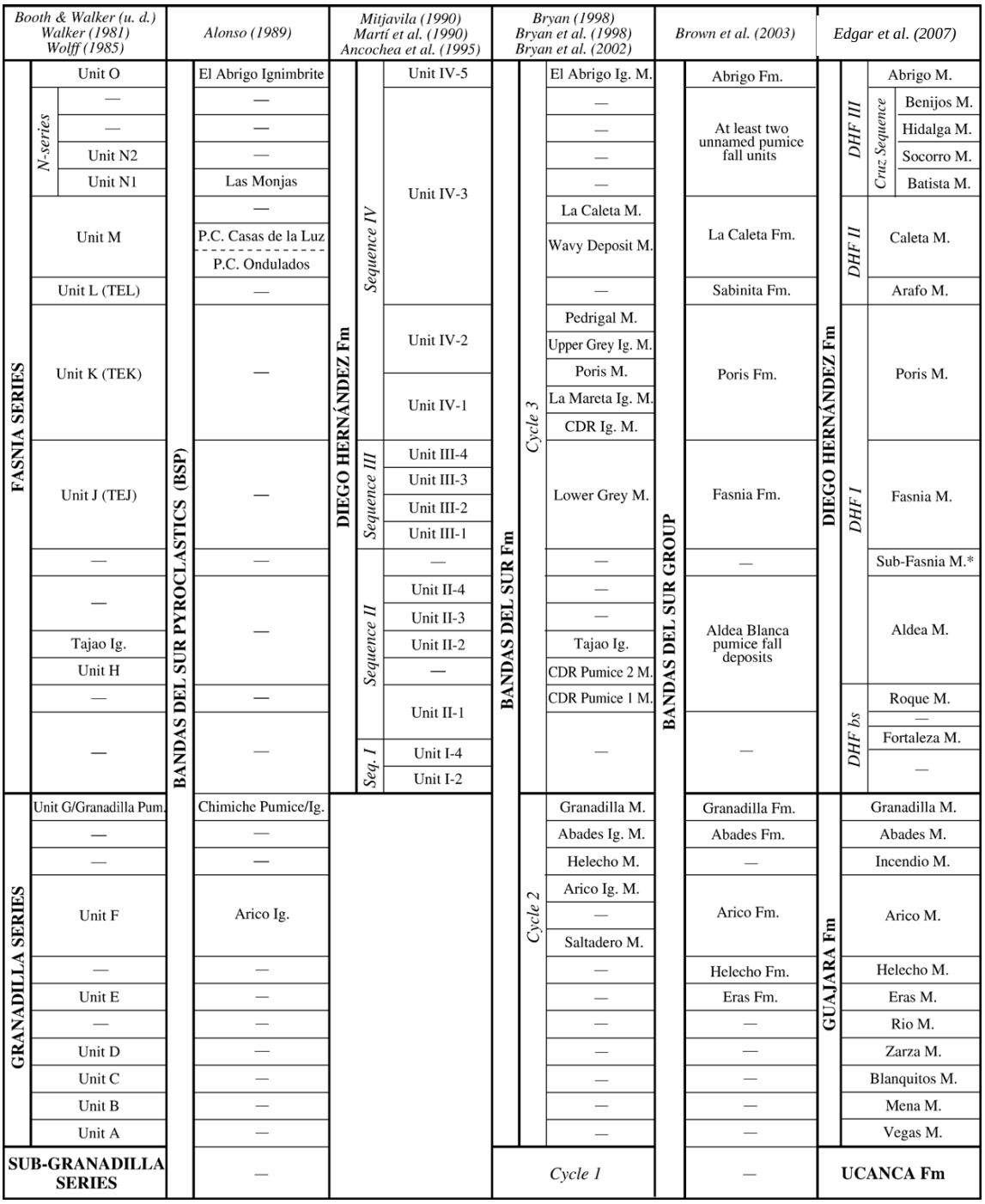

Figure 2.11 Summary of the various stratigraphic schemes proposed for the phonolitic pyroclastic deposits of Tenerife from Edgar *et al*. (2007). *Sub-Fasnia M. includes the Cabezon, Tarasca, Guirres, Espigon, Tosca, Tarta and Taco Members, although their stratigraphic relationship to the Aldea and Roque Members and to each other is unknown. CDR- Caldera del Rey, Fm.- Formation, Ig.- Ignimbrite, M.- Member, P.C.- Piroclastos de Caida (Sp. pyroclastic fall deposit), Pum. - Pumice, u. d. - unpublished data. [Guajara Formation stratigraphy from J. Middleton (unpubl. data)].

2.4.2 Bypass, erosion and volume estimates

The pyroclastic deposits found onshore at Tenerife are believed to represent only a small proportion of the material erupted during each explosive eruption; data from the Ocean Drilling Program (Rodehorst *et al.*, 1998; Schmincke and Sumita, 1998) show that a considerable amount of tephra fall and pyroclastic material from Canary Island eruptions entered the sea, with submarine tephra recording explosive activity from Las Cañadas persistent between 3.8 Ma and 0.3 Ma (Rodehorst *et al.*, 1998). The submarine material from Tenerife reportedly indicates that volcanism in the last 3 Ma has been more frequent than is indicated by the onshore geological record (Schmincke and Sumita, 1998), suggesting that the onshore record is incomplete due to non-deposition or erosion. Work on the Gran Canaria apron implies that previous on-land ignimbrite volume estimates for a particular interval of explosive volcanism on the island should be *doubled* due to the high volumes of volcaniclastic sediment discovered on the seafloor (Schmincke and Sumita, 1998).

Brown *et al.* (2003) propose that the widespread presence of thin, veneer deposits of ignimbrites in the Bandas del Sur region is evidence of the bypass of pyroclastic density currents across the flanks and into the ocean. Further evidence of this bypass is found in a large bed form, >520 m long, in the Poris ignimbrite in the Bandas del Sur (Brown and Branney, 2004a). It comprises sourceward-dipping lenses, ~50 m long, of massive and diffuse-bedded lapilli tuff. Scour surfaces are evidence of localised erosion; thicker, more steeply-dipping lenses cover scour surfaces and drape pre-scour lenses (Fig. 2.12a) (Brown and Branney, 2004a). The bed form indicates that during the passage of the Poris density current, the back-stepping depositional zone was no more than ~50-m-long, between upcurrent and downcurrent zones of PDC bypass. As a lens grew, the topography was altered and the location of deposition migrated sourcewards (Fig. 2.12b). There is little evidence of any substantial erosion or deposition, and it is thus proposed that most of the pyroclastic material bypassed this area of the coastline (Brown and Branney, 2004a).

Caldera subsidence commonly accompanies explosive eruptions that involve more than a few cubic kilometres of material (Lipman, 1997). Brown et *al.* (2003) consider volume estimation of Tenerife ignimbrites to be near impossible, due to the

unknown levels of onshore erosion, unknown volumes of bypass to the ocean, and unknown volumes buried at Las Cañadas by Montaña Blanca-Teide-Pico Viejo lava flows. Edgar *et al.* (2007) estimated maximum ignimbrite volumes for the Diego Hernandez eruptions by extrapolation from onshore deposits, considering dispersal patterns, onshore thickness variations, and offshore data. The largest eruptions, the Abrigo and the Fasnia, were given *maximum* volume estimates of ~20 km^3 (DRE) and ~13.3 km^3 (DRE) respectively, and it was proposed that the major Diego Hernandez eruptions probably each ejected 5-30 km^3 of tephra (1-10 km^3 DRE). This is a moderate volume, similar to other caldera-forming eruptions such as Katmai, 1912 (~3.5 km^3), and Pinatubo, 1991 (4 km^3) (Edgar *et al.*, 2007). Marti *et al.* (1994b) proposed that the whole Bandas del Sur area represents a total of >130 km^3 (DRE) of erupted material; the more recent work estimates that 70 km^3 of magma (DRE) was erupted from the Cañadas area in the Diego Hernandez period alone (0.54-0.13 Ma) (Edgar *et al.*, 2007). Although it is very difficult to estimate the true volumes of ignimbrites erupted, it is clear that even minimum estimates for the explosive eruptions throughout Tenerife's history could be sufficient to induce chamber collapse and vertical subsidence.

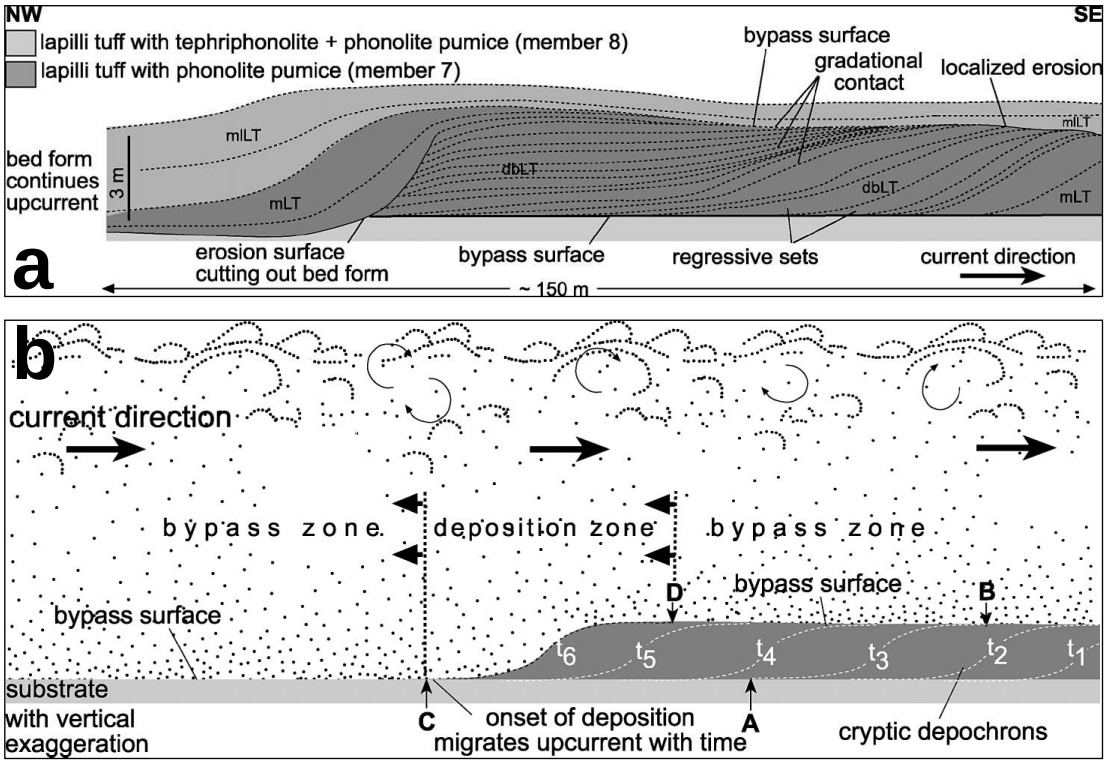

Figure 2.12 Example of giant regressive bed form, from Brown and Branney 2004.
(a) Summary sketch of the bed form. (4x vertical exaggeration. Sourceward dipping diffuse lenses= dashed lines; Localised scour = solid lines; mLT = massive lapilli tuff; DbLT = diffuse bedded lapilli tuff; mlLT = lithic rich massive lapilli tuff. (b) Cartoon illustrating how bed form was constructed during time t_6. Deposition confined to narrow zone. Proximal edge of ignimbrite sheet migrated upcurrent with time (Brown & Branney 2004).

2.5 Discussion

2.5.1 The origin of Las Cañadas

Volume estimates of >130 km^3 (DRE) for the Upper Group deposits spread across the island, and of >140 km^3 for the Cañadas depression before infilling (Martí *et al.*, 1994b) imply a strong relationship between explosive volcanic activity and the morphology of Las Cañadas depression. However, the model of three discrete vertical collapse events forming the present-day morphology of the Cañadas depression is incorrect; there are numerous high-volume caldera-forming eruptions recorded in the stratigraphy. At least 7-8 large-magnitude phonolitic eruptions may have caused caldera collapse in the last ~670 000 years (Brown *et al.*, 2003; Edgar *et al.*, 2007); older, less well exposed eruptive units suggest that the record of caldera collapse goes much further back in time than this (Mike Branney, pers. comm. 2011).

The occurrence of lateral collapse of sectors of the volcano flanks is irrefutable, particularly from the sea-floor record and in scars that are mainly outside of the Cañadas wall trace (e.g. Orotava, Guimar, and Anaga) (Bravo, 1962; Watts and Masson, 2001), but the Roques de García and La Fortaleza outcrops imply that the Cañadas wall has never been the headwall of sector collapse. Evidence of aqueous reworking of sediments and the occurrence of a tuff ring deposit in the lower DH wall (see Appendix 1), and lacustrine sediments at the Roques de García, attest to the presence of significant near-surface water within Las Cañadas at various times. This implies that the depression must have been closed, at least in some places, as openings would have allowed any lake water to drain to the flanks.

The present shape of the Cañadas depression most likely results from a combination of a series of nested caldera collapses with intervening stratovolcano construction, followed by destruction of the northern wall by the Icod collapse.

2.5.2 Mechanical link?

The relationship between caldera and lateral collapse on Tenerife remains obscure. Martí *et al.* (1997) suggest that the climactic eruptions that accompanied the Granadilla and Abrigo eruptions may be linked with the sector collapses of the Orotava and Icod valleys by a mechanical relationship where caldera collapse

prompts flank instability. The Orotava collapse is thought to have occurred between 780 and 540 ka, and the Icod event between 170 and 130 ka (various workers, see Table 2.1). $^{40}Ar/^{39}Ar$ dates for the Granadilla and Abrigo eruptions are 600±18 ka and 169±1 ka respectively (Brown *et al.*, 2003). These ages indicate a connection is possible, but the large interval of uncertainty between events, particularly for the Orotava collapse and Granadilla eruption, make the link tenuous.

2.5.3 Implications for the pre-Poris environment

The lack of evidence concerning age-spatial relationships between previous edifices and overlaps, or nesting of calderas, makes the task of reconstructing the evolution of Las Cañadas morphology particularly difficult. The Cañadas episode of volcanism continued for more than 3.5 Ma (e.g. Ancochea *et al.*, 1990; Martí *et al.*, 1994b), during which multiple stratovolcano edifices would have been constructed and destroyed (the Fasnia volcano, the Granadilla volcano, etc.). However, the positions of such edifices within Las Cañadas depression are cryptic; the Abrigo, the most recent and largest caldera-forming event (Edgar *et al.*, 2007), probably engulfed many predecessor structures, and it therefore cannot be known how the dimensions of these structures affected the present day morphology of the area.

It can be assumed that prior to the Poris eruption, complex caldera topography not unlike the present-day scenario existed in Las Cañadas. The climax of the previous Fasnia eruption involved vertical subsidence (Brown *et al.*, 2003; Edgar *et al.*, 2007), the trace of which would have been imprinted upon that of previous caldera collapse events. The effects of small- or large-scale lateral collapses in the vicinity may have modified this topography.

The location of the Poris vent is unknown, but the lack of welding in Diego Hernandez exposures implies that it may have been farther east than edifices of the Guajara episode. Guajaran deposits are intensely welded, indicating that they were more proximal to the vent; the densely intruded Roques de Garcia outcrop may be the remnant of a plumbing system for a Guajaran-aged stratovolcano system. Welding at La Fortaleza in deposits of Diego Hernandez age indicates that vents may have existed in the northeast of the Cañadas zone at this time (Joan Martí, pers.

comm., 2010). Pre-eruptive landscape and topography is significant when understanding the architecture of proximal ignimbrite successions, and as such is considered throughout this thesis.

2.6 Conclusions

The geological history of Tenerife is protracted and complicated, not least by being incompletely preserved and partly obscured. This is especially true for the Las Cañadas depression. Although workers initially tended to advocate either vertical or lateral collapse to explain the depression (e.g. Martí *et al.*, 1994b; Cantagrel *et al.*, 1999), seafloor studies, stratigraphic and geophysical research, and ignimbrite lithofacies interpretation (e.g. Schmincke and Sumita, 1998; Brown *et al.*, 2003; Brown and Branney, 2004a; Brown and Branney, 2004b; Edgar *et al.*, 2007; Gottsmann *et al.*, 2008) have together shown the origin to be hybrid with many collapse increments and with substantial erosional modification of the successive structures formed.

Chapter Three

Stratigraphy of the upper Diego Hernandez wall

3.1 Introduction

A volcanic stratigraphy for the units exposed in the upper Diego Hernandez wall has been established and correlated with the published stratigraphy (Fig. 3.1). Only the Poris Formation is consistently well exposed in the upper Diego Hernandez wall; units above it are widely covered by scree, hindering study, although trenches excavated in thin scree provided exposures at three northerly locations (see Fig. 3.2). In central parts, deposits are exposed sufficiently to prove the lateral continuity of the upper sequence, while in southern parts the cliffs are lower and less is exposed. Poor exposures near the cliff path (path 8 in the National Park guide) prove southerly continuity. The deposits are described below.

3.2 Poris Formation

A well-exposed pyroclastic succession overlies a 30-m-thick sequence of basanite lavas (Wolff *et al.*, 2000), ~100 m above the base of the Diego Hernandez wall (see Fig. 3.2). A thin (≤5 cm) brown soil occurs between the lavas and a pumice fall deposit overlain by ignimbrite (Fig. 3.3). The ignimbrite succession, up to 29 m thick, is the Poris and is the focus of this thesis. Positive identification of this unit was made using XRF geochemical analysis and is described in Chapter 6. It is subdivided into 11 lithofacies, the nature and architecture of which are described in Chapters 4 and 5. Evidently a period of quiescence locally occurred following eruption of the lavas, which were probably sourced from Strombolian vents amongst those that define the Cordillera Dorsal (NE Rift). The Poris explosive eruption that followed was of sufficient magnitude to deposit extensive fallout tephras and ignimbrite, which have been dated at 273±5 ka (Brown *et al.*, 2003; Edgar *et al.*, 2007). A new depositional model for the Poris eruption that includes information from proximal lithofacies is presented in Chapter 7.

Figure 3.1 (at end of digital document)

Figure 3.2(i) (at end of digital document)

Figure 3.2(ii) (at end of digital document)

3.3 Sabinita pumice deposit

A dark brown weathered layer taken to be a palaeosol, consistently 38 cm thick, is poorly exposed at the top of the uppermost lithofacies of the Poris formation at all three trench locations and in the central area of the wall (boxes a, b and c, Fig 3.2). The layer contains poorly sorted heterogeneous lithics, cream coloured pumices and black scoria clasts, ≤1.5 cm in diameter, loosely consolidated in a brown matrix of sand-sized particles. The top 5 cm of the layer is finer grained, darker and more consolidated.

A distinctive framework-supported white pumice-lapilli deposit is in sharp contact with the brown weathered layer, which in places is coated by a white precipitate (Fig. 3.4a). The pumice deposit is 3.6 m thick at its best exposure, a cliff outcrop in the northern DH wall (Fig. 3.2), and it can be traced beneath scree across the DH wall. Pumice lapilli are white (banding is uncommon), angular to sub-angular and generally range from 0.5 to 4 cm in diameter, although clasts ≤10 cm also occur (Fig. 3.4b), inferring a bimodal characteristic. The glass appears to be less inflated than Poris pumices, although tubular pumices do occur. Lithic clasts, of fine-grained grey lavas and sparse syenite (Fig. 3.4c) are subtly concentrated at the base of the deposit, which overall is lithic-poor. Two ash layers, ≤5 cm thick, occur ~30 cm from the top (Fig 3.2ii), which is marked by a greyish-brown, weathered, clastic layer 20 cm thick.

Interpretation

This deposit is fallout, possibly from a subplinian eruption similar to that which deposited the Montaña Blanca pumice at ~2 ka (Ablay *et al.*, 1995). No ignimbrite is associated, suggesting that it was not generated by a large Plinian eruption. The thin ash layers record temporary hiatuses in pumice deposition, perhaps subtle changes in dispersal direction during which ash was deposited, either as fallout from an ash-laden atmosphere or from the fallout-dominated flow boundary zone of a dilute pyroclastic density current. The stratigraphic position and characteristics of this unit correlate with the Sabinita of Brown et al. (2003) and Arafo of Edgar et al. (2007). On precedence priority 'Sabinita' is used while acknowledging equivalence with the

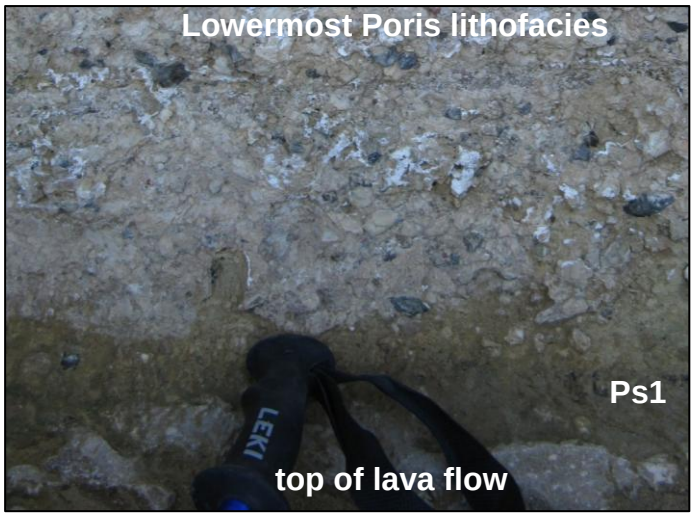

Figure 3.3 Poris pumices overlying a thin soil layer and oxidised fine grained lava. Walking stick handle 10 cm.

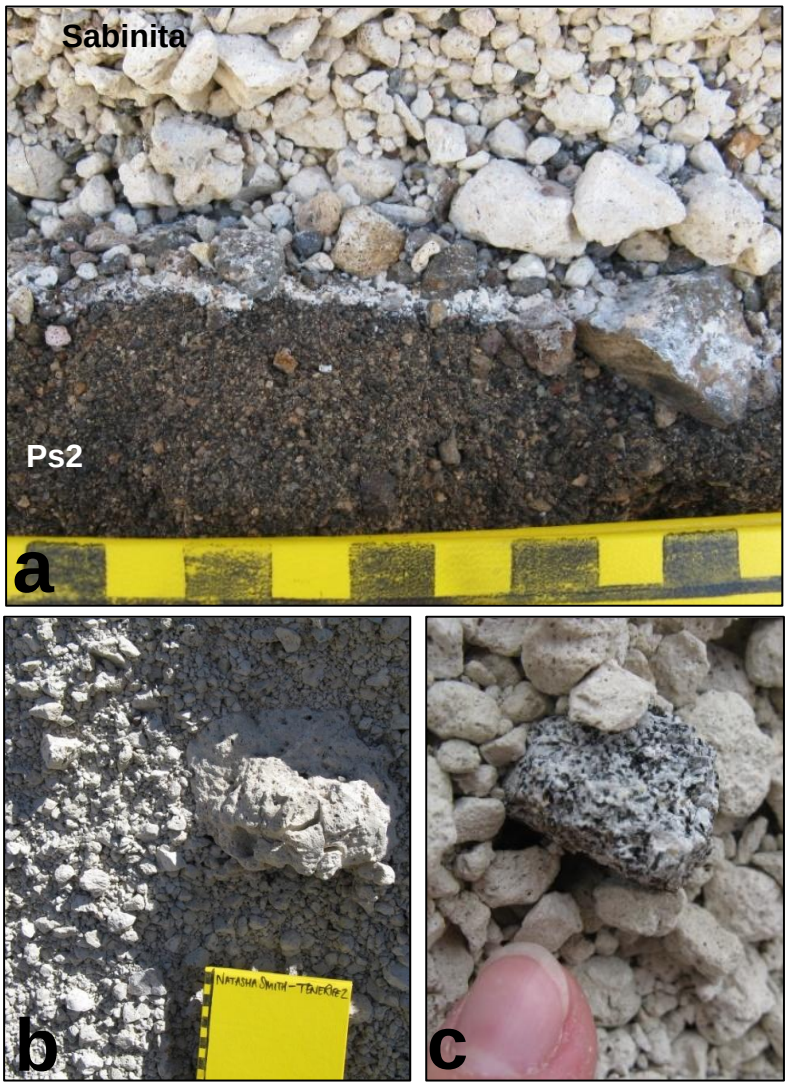

Figure 3.4 The Sabinita pumice deposit (a) White Sabinita pumices in contact with the clastic soil below, which is coated by precipitate (c) The bimodal nature of the Sabinita deposit. Notebook shows cm-scale. (d) Plutonic clast in the Sabinita unit.

'Arafo'. The bimodal clast-size distribution in the proximal deposit is also reported in distal exposures (Brown et al., 2003).

3.4 Unnamed fallout sequence I

Scoria 1

A black, stratified and well sorted unit overlies the Sabinita, and consists of sub-angular scoria clasts, 3-8 mm in diameter. It is 96 cm thick at trench locality 1 and at the Sabinita best exposure, and it occurs as a poorly exposed correlative at trench 3, suggesting considerable lateral continuity. A 2-m-thick black scoria unit occurs at a similar stratigraphic position above the most northerly Poris exposures (visible in box a on Fig 3.2), but poor exposure and inaccessibility hinder certain lateral correlation. Continuity of the scoria elsewhere along the cliff, however, suggests that this northerly exposure is of the same unit.

Bedded yellow pumice

A weathered orange-brown, fine-grained deposit, 10 cm thick, separates Scoria 1 from a pumice lapilli unit above. The lower 25 cm of the pumice lapilli unit is massive, well sorted and framework-supported, comprising yellow pumices 2-3 cm in diameter. The yellow clast colour makes this unit a convenient marker. It grades up into a beige layer, 25 cm thick at the Sabinita best exposure, comprising clasts ≤1.5 cm in diameter. A third bed, paler than those beneath it, is 11 cm thick and consists of pumice clasts ≤3 cm in diameter (Fig. 3.5a). This is exposed at trench 1 and at the southern end of the Sabinita best exposure.

Scoria 2

Overlying the bedded yellow unit and a brown soil ≤10 cm thick is a black scoria layer, 2 cm thick at the Sabinita best exposure and 6 cm farther north at trench 1. The scoria clasts are 1-2 mm in diameter and clast-supported, and the layer is sharply overlain by a white stratified pumiceous deposit.

Stratified pumice

Angular to sub-angular pumices constitute a stratified white layer, ≤50 cm thick, overlying Scoria 2. Some strata are more matrix-rich than others and the size of the

pumice lapilli broadly increases upwards; the uppermost bed is framework-supported and contains the coarsest pumices, ≤5 cm in diameter (Fig 3.5b). This is the uppermost lithofacies preserved at the Sabinita best exposure, and is exposed amidst scree at central exposures.

Scoria 3

At trench 1, the stratified pumice is overlain by a 60-cm-thick clastic soil, the lower part of which is rich in rounded, millimetre-scale pumice clasts. Five centimetres up from the base is a third black scoria deposit, 6 cm thick, containing scoria clasts 2-3 mm in diameter. Above this, the poorly sorted weathered material contains black scoria and sub-rounded white pumices (clasts ≤5 mm and ≤1 cm in diameter respectively) supported in a brown, fines-rich matrix.

Interpretation

After an episode of quiescence and weathering following the Sabinita eruption, a period of Strombolian activity from a scoria cone commenced. Although the exact location of the vent is unclear, the deposit is thicker in the north implying a location in the Cordillera Dorsal rift zone.

The sequence above this relatively thick scoria deposit records at least two unnamed Plinian/subplinian eruptions, two further Strombolian eruptions, and significant intervening periods of quiescence and weathering. The bedded yellow unit records at least one Plinian or subplinian eruption; it is unclear whether beds 2 and 3 result from reworking or further activity. The white stratified deposit records ash deposition and the stratification of pumice lapilli during the interaction of a low-concentration pyroclastic density current with concurrent Plinian or subplinian fallout. These deposits correlate with the 'Minor DHF II units' of Edgar *et al.* (2007) and are not reported in distal areas (Brown, 2001), indicating that the eruptions were of relatively low-magnitude.

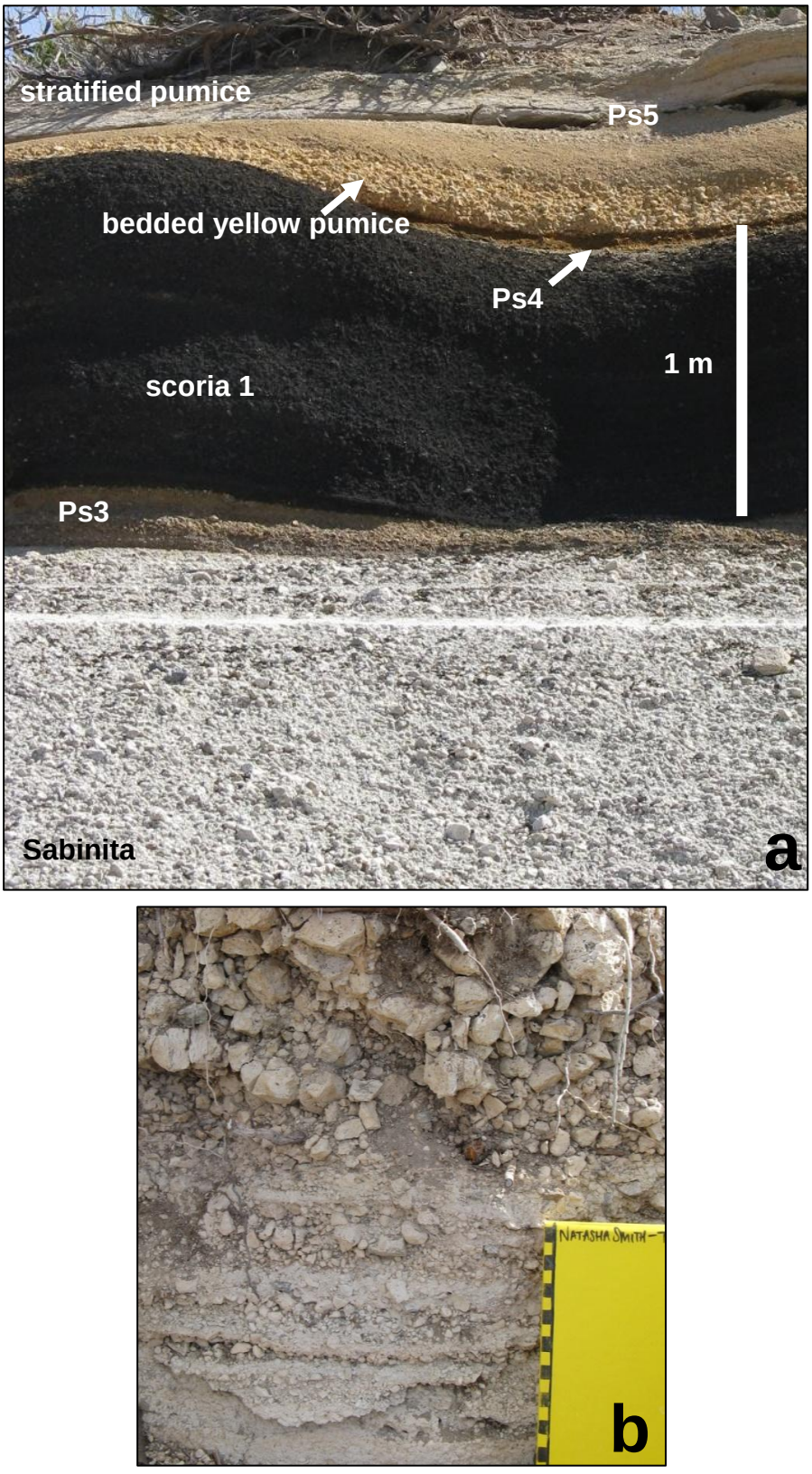

Figure 3.5 Unnamed fallout sequence 1 (a) Scoria 1 on the Sabinita unit, overlain by the bedded yellow pumice deposit. Note the planar, white ash beds near the top of the Sabinita deposit. (b) Close up of the stratified pumice unit. Pumices are roughly stratified in terms of size; some beds are more matrix rich. The uppermost bed contains the coarsest, more framework-supported clasts. Ps = palaeosol. Numbers relate to those on the GVS (Fig 3.1).

3.5 La Caleta Formation

A substantial pyroclastic succession overlies the unnamed scoria-pumice layered sequence (Fig 3.6). It is poorly exposed at all trench locations, but relatively well exposed at the La Caleta best exposure in the DH wall (see Fig 3.2). The basal lithofacies is a 15-cm-thick white ash bed in sharp contact with underlying soil. It contains sparse pumice lapilli and has indistinct stratification, with a thin layer of pumices ≤5 mm in diameter ~5 cm from the top. Framework-supported pumice lapilli sharply overlie the ash and form a unit 20 cm thick. Here pumice clasts are 2-3 cm in diameter, pale cream, and soft due to alteration.

Matrix-supported, fines-rich lapilli tuff, 1.25 m thick, overlies the pumice lapilli layer. This contains pumice clasts ≤3 cm in diameter and lithics that display inverse coarse-tail grading; these also become subtly more concentrated upwards culminating in a lithic breccia layer containing blocks ≤30 cm in diameter (Fig. 3.7a). The breccia, which is rich in grey lava blocks, is laterally continuous in poor scree exposures along the DH cliff face and commonly ≤35 cm thick. Exposures of in-situ lithic blocks occur at 1.6-1.7 m up from the base of the ignimbrite unit at all three trench locations (see Fig. 3.2).

Tuff above the lithic breccia is only 1.5 m thick and only *well* exposed at the La Caleta best exposure. This contains a 40-cm-thick zone rich in accretionary pellets ≤2.5 cm in diameter (Fig. 3.7b). This zone occurs 50 cm above the lithic-rich layer, but it is not laterally continuous. At trench 3, the top of the La Caleta succession is marked by a prominent orange-brown sandy soil, 30 cm thick and with a thin layer of white pumices, ≤3 cm in diameter, at its base.

Interpretation

The proximal pyroclastic succession stratigraphically correlates with the 'La Caleta' ignimbrite identified previously (e.g. Bryan *et al.*, 1998b; Brown *et al.*, 2003; Edgar *et al.*, 2007) and dated at 221±5 ka (Brown *et al.*, 2003). The first activity recorded proximally is ash fall, followed by pumice fallout from a Plinian plume, then deposition from pyroclastic density currents.

Ash hummocks resulting from blanketing of vegetation by fallout tephra, known in the Bandas del Sur as the 'Wavy Deposit' (e.g. Bryan *et al.*, 1998b; Brown *et al.*, 2003), are not found in the proximal La Caleta exposures. This is perhaps not surprising, considering the poor quality of the exposure and the likelihood of sparse vegetation cover. Trace plant fossils occur in ignimbrite near the base of the DH wall, but were not identified in the upper parts of the wall during this study.

The lithic breccia within the ignimbrite is taken as recording enhanced current competence and/or enhanced input of lithic material into the current. No scours are identified associated with the lithic-rich zone, but exposure is extremely limited.
The logs of Edgar *et al.* (2007) document a lithic block layer halfway up a 10-m-thick section of La Caleta and Brown *et al.* (2003) mention a 'block and boulder bearing breccia horizon' occurring towards the top of the ignimbrite. It is difficult to know whether the distal lithic layers correlate with the lithic block layer in the DH wall. In the wall, the La Caleta deposit is just 2.5 m thick; the breccia may thus represent the material deposited by lithic-rich currents that mostly bypassed the proximal region to deposit at the coast during the eruption climax.

The accretionary pellet-rich zone near the top of the Caleta best exposure (see Fig. 3.2) implies deposition from a stratified density current with ash pellet generation in upper, moist parts (Brown *et al.*, 2010). Fine ash and accretionary pellet layers that drape topographically confined ignimbrites in distal La Caleta exposures are reported by Brown *et al.* (2003). The lack of lateral continuity of the accretionary pellet-rich material in the proximal region indicates that accretionary pellets were either not widely present and/or were not able to enter the flow boundary zone in all part of the current across the area. The formation and significance of accretionary pellets is discussed in Chapter 1.

The La Caleta eruption was followed by a period of quiescence and weathering, recorded in the orange-brown soil. The present day scree slopes of the DH wall contain a mixture of lithologies, dispersed by gravity-driven processes, and are an analogue for the heterolithic, clastic soil layers intermittent in the eruption record.

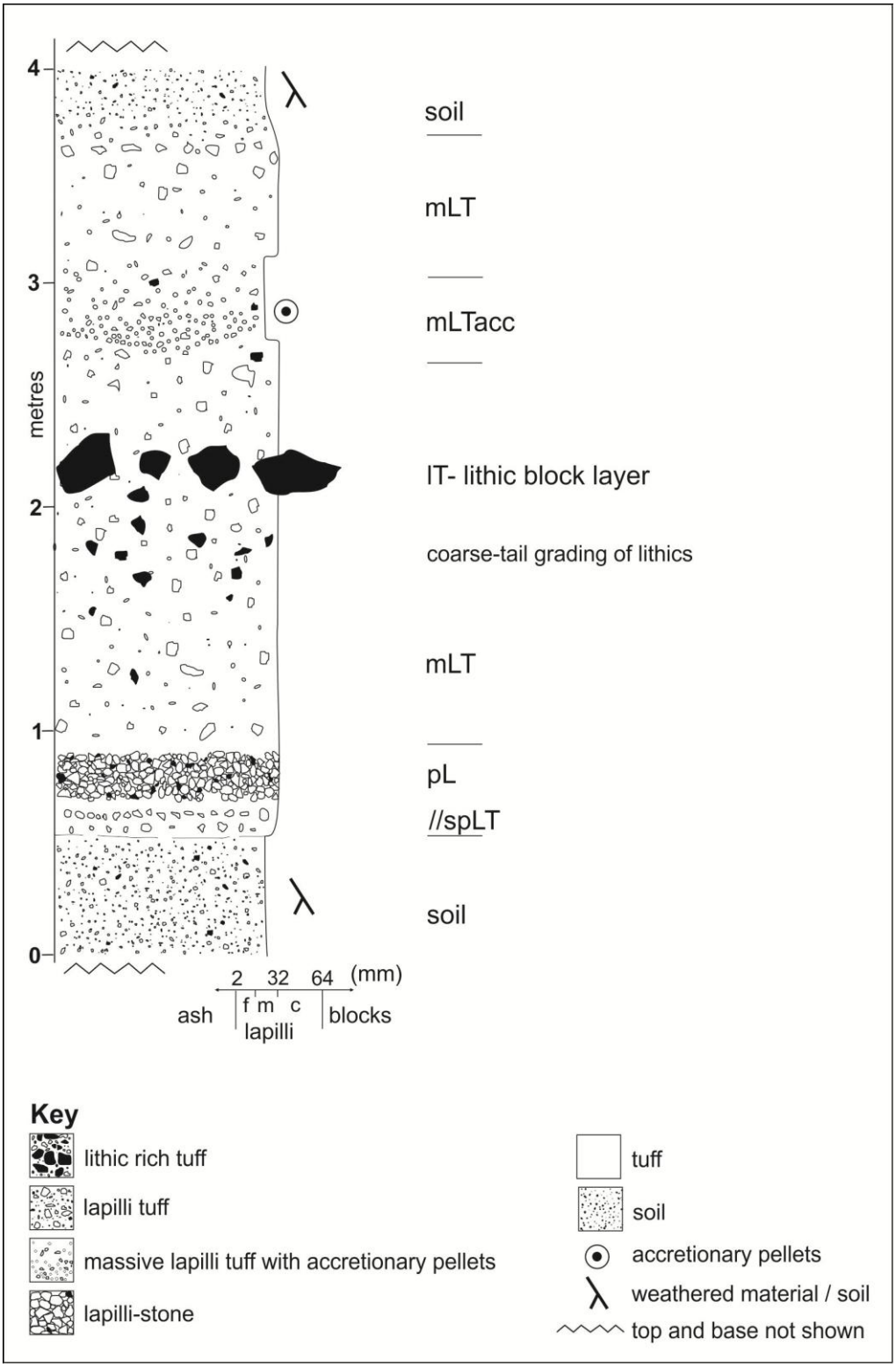

Figure 3.6 Stratigraphic log of the La Caleta Formation in the Diego Hernandez wall, compiled from exposures at Trench 1 and the La Caleta best exposure.

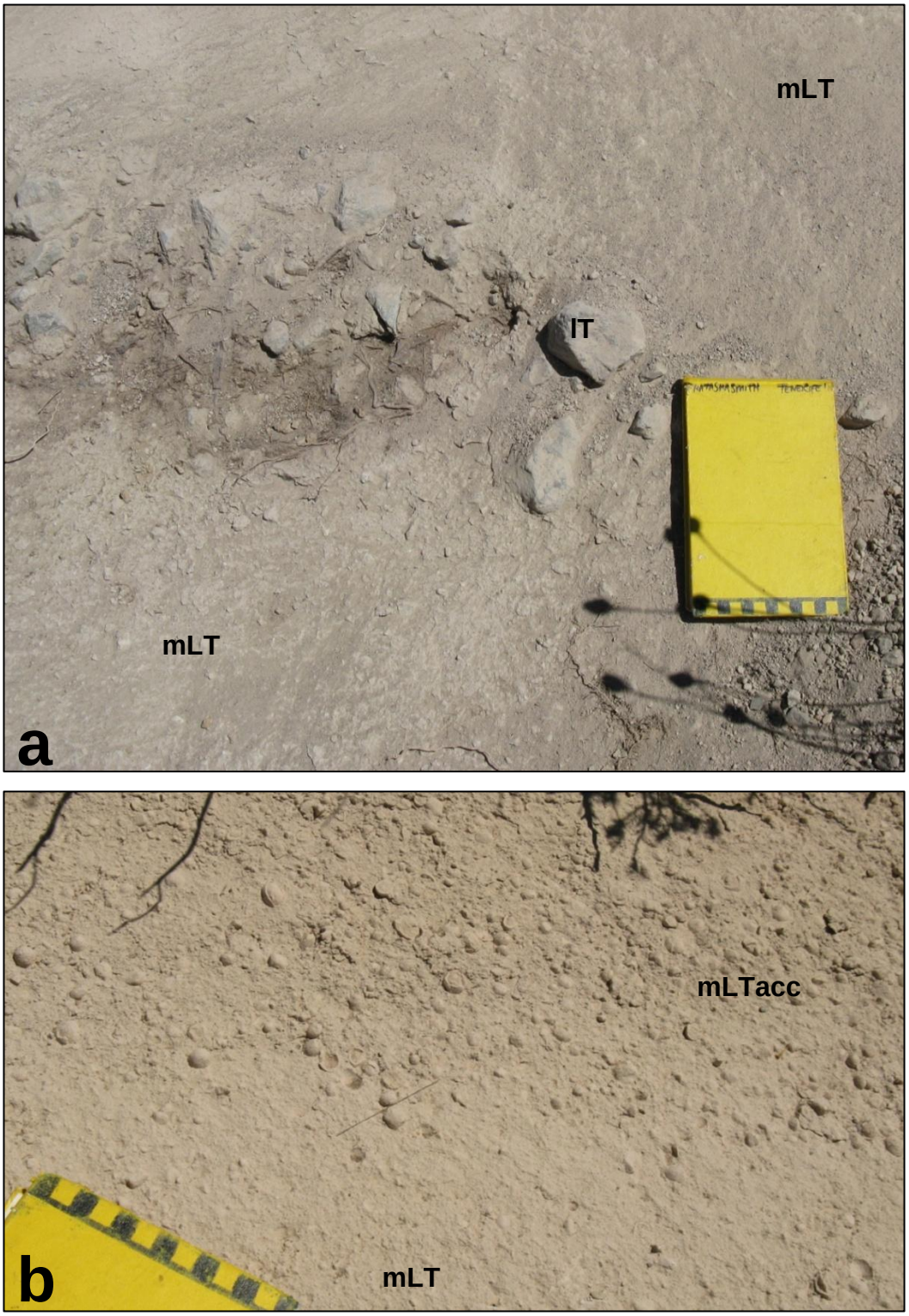

Figure 3.7 La Caleta best exposure (see Fig 3.2 for location). (a) lithic breccia layer in ignimbrite: at this exposure, the clasts clearly are in situ. At other points across the cliff, at the same stratigraphic position, there are poor exposures of in-situ lithic blocks (≤30 cm in diameter) amidst scree slopes. (b) massive lapilli tuff rich in accretionary pellets.

3.6 Unnamed fallout sequence II

Above the La Caleta Formation are two relatively minor pyroclastic deposits. The lower of the two is a 40-cm-thick, clast-supported pumice lapilli facies. The pumices are pale yellow and ≤2 cm in diameter, less coarse than pumice lapilli beds lower in the succession. The lower deposit is separated from the upper by a pale brown, poorly consolidated, fine-grained soil 20 cm thick.

The upper unit comprises 4 beds. The lowermost is a well-sorted pumice lapilli unit, ~60 cm thick, containing pumices ≤3 cm in diameter. This is sharply overlain by a white, fines-rich, matrix-supported tuff, 50 cm thick and containing stratified pumice clasts ≤5 mm in diameter (Fig. 3.8a). This is succeeded by another clast-supported unit, 30 cm thick, of sub-angular pumice lapilli. The uppermost bed, 1 m thick, contains better rounded and smaller (≤1.5 cm) pumice clasts than occur beneath. It is clast-supported, but richer in fines than the two lapilli beds below. These units are only exposed clearly at trench 3 (see Fig. 3.2) and lateral continuity is unknown.

Interpretation

These deposits are interpreted as the product of two Plinian eruptions, primarily pumice fall, with the upper having a component from the fallout-dominated flow boundary zone of a dilute PDC. The rounding of the pumices in the top metre of the second pumice fall, and the slightly looser nature of the material, may indicate the onset of weathering processes, although the poor quality of exposure hinders interpretation.

The units stratigraphically correlate with two 'unnamed pumice fall units' described by Brown *et al.* (2003), which occur above the La Caleta Formation and are unconformably overlain by the Abrigo Formation. They also correlate with the 'Cruz Sequence' of Edgar *et al.* (2007), which is described as 'products of Plinian fall eruptions with a subordinate role for phreatomagmatic and PDC-producing activity'. However, the physical characteristics of the distal deposits described by these authors do not match those in the proximal exposures.

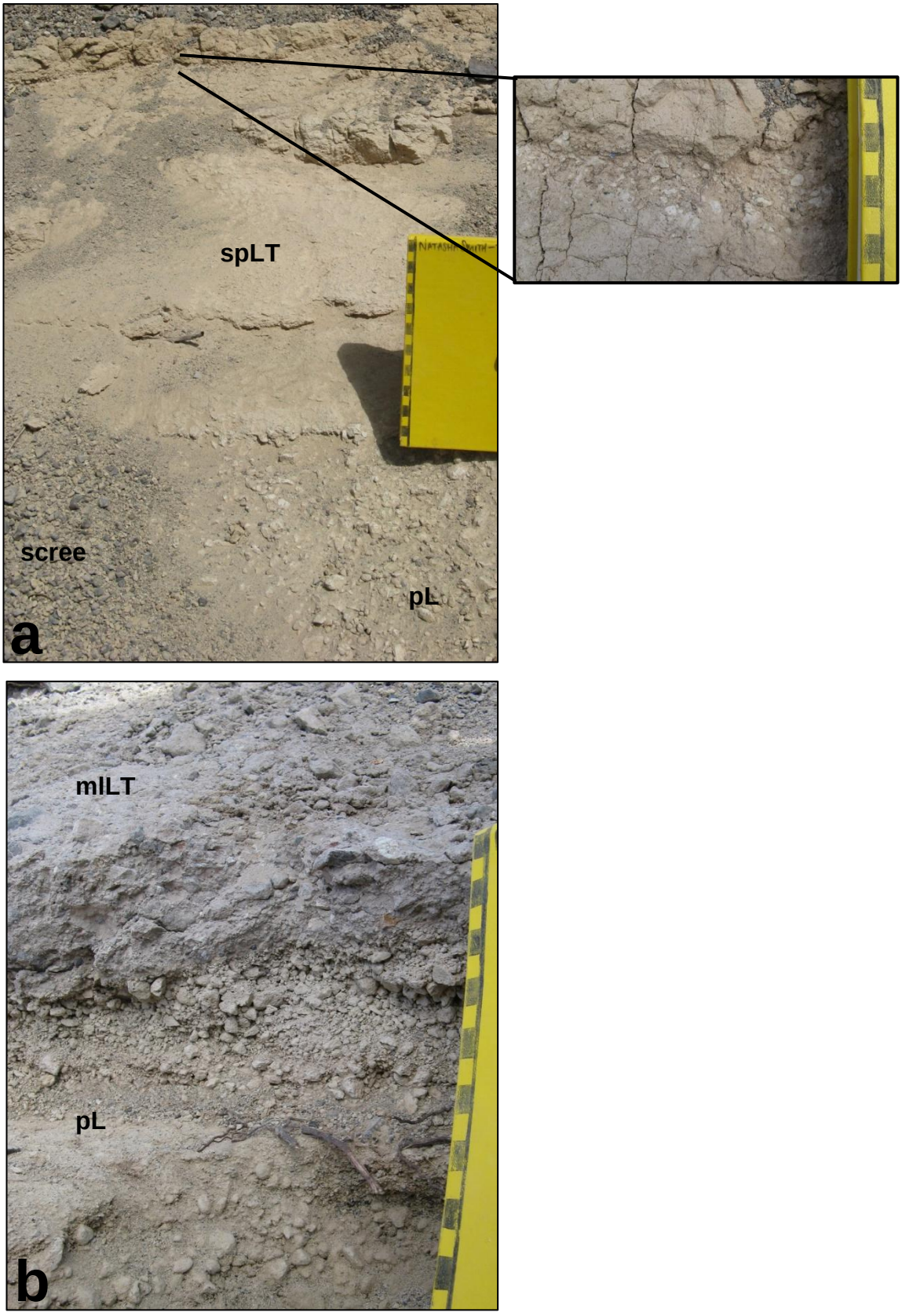

Figure 3.8 Youngest units preserved in the upper DH wall. (a) Upper unit of unnamed fallout sequence 2; clast-supported pumice bed overlain by ash-rich tuff containing stratified pumices (shown in close-up). (b) Pale grey/lilac, lithic-rich, poorly sorted ignimbrite (Abrigo) in contact with poorly preserved sub-rounded pumices below. The sub-rounded pumice bed is poorly sorted and contains beige fine material.

3.7 Abrigo Formation

In sharp contact with the sub-rounded pumices of the material beneath, the uppermost deposit preserved in the Diego Hernandez wall is a pale lilac/grey, matrix-supported ignimbrite. Although exposure quality is extremely poor due to weathering, a high concentration of lithic clasts and poor sorting is evident (Fig. 3.8b). Only ~1 m thickness is exposed at trench 3, due to thick scree cover, but the scree is rich in heterogeneous lithic clasts derived from the underlying deposit, some of which are >1m in diameter.

Interpretation

This deposit derives from the Abrigo eruption, the most recent caldera-forming event of the Cañadas area (Martí *et al.*, 1994b). Lithics present widely atop the Diego Hernandez cliff are believed to be remnants of the eroded lithic-rich Abrigo ignimbrite (Joan Martí, pers. comm., 2009). A K/Ar age of 179±11 ka for this eruption was originally obtained from breccia at the top of the DH wall (Martí *et al.*, 1994b), but this date has more recently been refined to 169±1 ka by $^{40}Ar/^{39}Ar$ dating of sanidines from distal Abrigo deposits (Brown *et al.*, 2003).

The pale grey colour, lithic-rich nature, and lack of Plinian fallout deposit are features of the Abrigo also reported in distal areas (e.g. Brown *et al.*, 2003; Pittari *et al.*, 2006). It has been suggested that only three localities in the Bandas del Sur area (all within 3 km of each other) show any sign of an Abrigo pumice fallout bed, and even at these exposures correlation is uncertain (Pittari *et al.*, 2006). This lack of regionally distributed fallout may mean that, unusually, a Plinian column did not form during this explosive eruption. However, it seems more likely that scour by subsequent lithic-rich waxing currents removed any Plinian deposit; it has been reported that the base of the Abrigo ignimbrite is widely erosive (Brown *et al.*, 2003).

3.8 Conclusions

The proximal stratigraphy reported here corresponds with previous studies of Diego Hernandez ignimbrite stratigraphy. Even though the physical architecture of lithofacies may vary between proximal and distal zones, the relative thicknesses of deposits and presence of distinct marker beds and weathered horizons aids correlation.

This stratigraphic section, which comprises only 43 m of the total height of the Diego Hernandez wall, spans just over 100 000 years of geological time. During this time, at least 8 pyroclastic eruptions occurred; three of these, the Poris, Caleta and Abrigo, were large enough to generate ignimbrite-forming pyroclastic density currents. The occurrence of at least three scoria deposits indicates continuing activity from Strombolian vents, probably of the Cordillera Dorsal. The soil layers represent periods of quiescence that may have each lasted thousands of years.

The excellent exposure and preservation of the Poris ignimbrite make it an ideal deposit for detailed lithofacies study.

Chapter Four

Lithofacies of a proximal ignimbrite

4.1 Introduction

Ignimbrite lithofacies architecture can be interpreted in terms of the depositional characteristics of pyroclastic density currents both temporally and spatially (e.g. Branney and Kokelaar, 2002). Such architectural analysis has been applied to distal ignimbrite deposits with success (e.g. Brown and Branney, 2004a), but has not yet been applied in near-vent settings. Previous research in proximal regions includes the study of the physical characteristics of Plinian fall deposits close to vent (e.g. Houghton *et al.*, 2004; Sable *et al.*, 2006) and the presence of lithic 'lag' breccias (e.g. Druitt and Sparks, 1982; Bear *et al.*, 2009b).

Lithofacies analysis is heavily descriptive, and in this thesis is separated from the discussion and interpretation of architecture for clarity. This chapter reports the characteristics of each lithofacies of the proximal Poris sequence and interprets their mode of deposition. Chapter 5 then describes the architectural relationships of all of the lithofacies and discusses the proximal processes that are recorded. The architectural analysis is dependent upon the individual lithofacies interpretations presented here.

4.1.1 Nature of the exposure

The Poris pyroclastic succession is well exposed above thick lavas along the Diego Hernandez wall. It is exposed at 29 cliff outcrops that project outwards from the wall by up to 7 m and range up to 14 m high and 30 m wide, and also in scree slopes. The slightly rounded outcrops are typically cream coloured at the base and have orange weathered tops that are more strongly lithified and contain holes where pumices have become recess-weathered. In this study the outcrops are split into three groups, southern, central and northern (Fig. 3.2 and 4.1), that are separated by zones of no exposure due to thick scree and fallen lava blocks.

The upper contact of the Poris succession is exposed infrequently in scree above the cliff outcrops and is overlain by a soil 37-40 cm thick, and then the Sabinita deposit. Above southern cliff outcrops this contact is mostly hidden, but two small gully exposures above localities 8 and 9a (Fig. 4.1) confirm lateral continuity.

4.2 Lithofacies

Figure 4.1 shows a generalised vertical section of the Poris Formation in the Diego Hernandez wall, summarising the lithofacies and their distribution. Figures 4.2, 4.3 and 4.4 are fence diagrams of the stratigraphic logs for the southern, central and northern parts of the wall respectively. The lithofacies nomenclature provided below is purely descriptive (after Branney and Kokelaar, 2002); 'flow units' have not been named in the 'X Member' or 'Y Ignimbrite' style. This is because the two previous detailed Poris studies report contradictory nomenclature (Edgar *et al.*, 2002; Brown and Branney, 2004b) and it would add to confusion if names were given to proximal units here. Also it is not straightforward to delineate proximal flow units, as discussed below in Chapter 5.

4.2.1 Parallel bedded pumice lapilli (//bpL and pL)

A pumice lapilli unit (//bpL/pL) is the lowest exposed lithofacies of the succession. It is best exposed, and thickest, at locality 16 (Fig. 4.4), where it is 1 m thick and consists of five beds (Fig. 4.5a). The base is rarely exposed and the maximum unit thickness is unknown.

Beds 1, 3 and 5 comprise framework-supported, cream-white, sub-angular to angular pumice lapilli typically 1-3.5 cm in diameter. Rare banded pumices (Fig. 4.5c) and larger clasts ≤10 cm in diameter occur. Subordinate lithic clasts, the most common of which are dark green obsidian with conchoidal fracture, become subtly more abundant at the top of bed 5, increasing from ~8% to ~20% of the deposit componentry. Pale green clasts of welded ignimbrite and red oxidised clasts of vesicular lava or scoria also occur.

Figure 4.1 (overleaf fold-out) General vertical section of the proximal Poris succession, showing lithofacies descriptions, distribution and interpretation. Log numbers relate to stratigraphic logs shown in Figs 4.2 to 4.4. Stratigraphic thickness is compiled from maximum lithofacies thicknesses across multiple outcrops.

Figure 4.1 (at end of digital document)

Figures 4.2-4.4: Fold-out fence diagrams comprising stratigraphic logs of the proximal Poris ignimbrite succession of the upper Diego Hernandez wall. 4.2 shows southern exposures, 4.3 shows central exposures and 4.4 shows northern exposures. (a) Key and lithocodes. (b) Map of Las Cañadas, with position of the three sets of exposures. Boxes (c) on each figure show outcrop spacing and the position of logs. Logs are positioned relative to actual outcrop location.

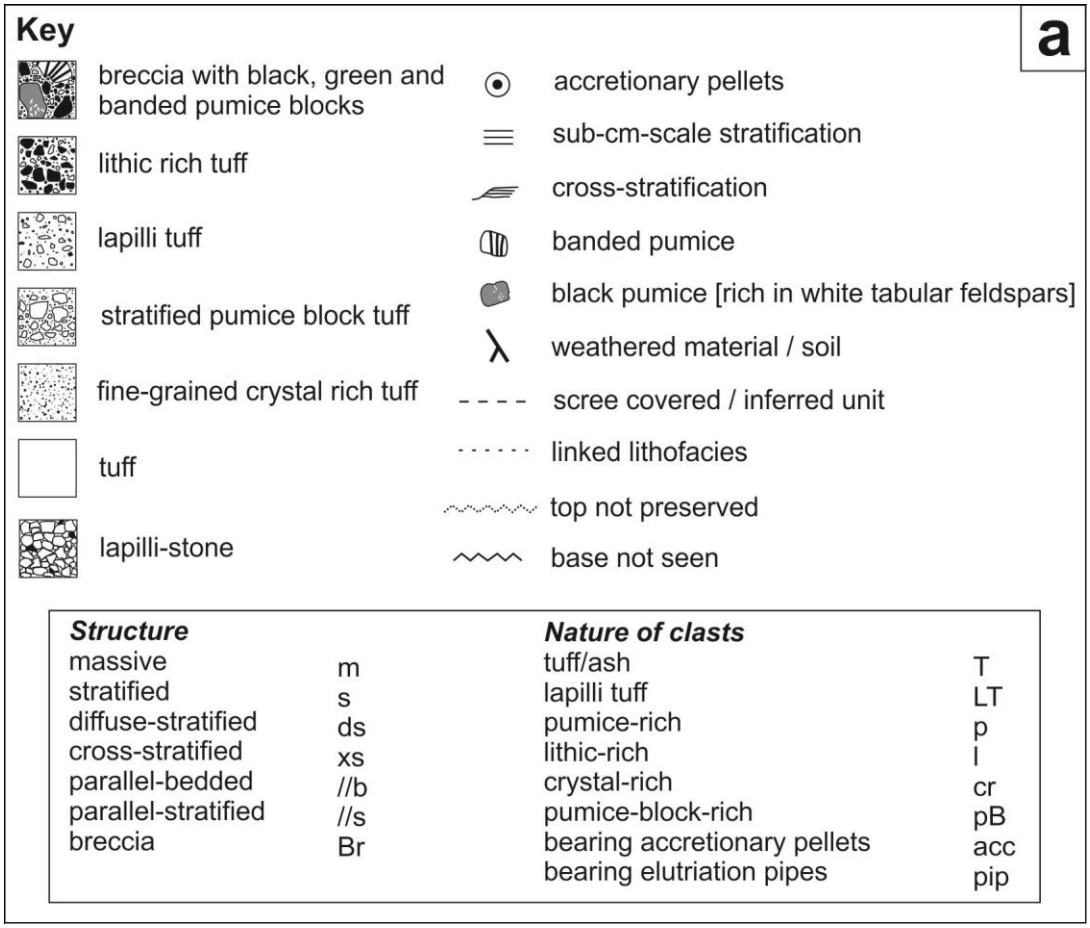

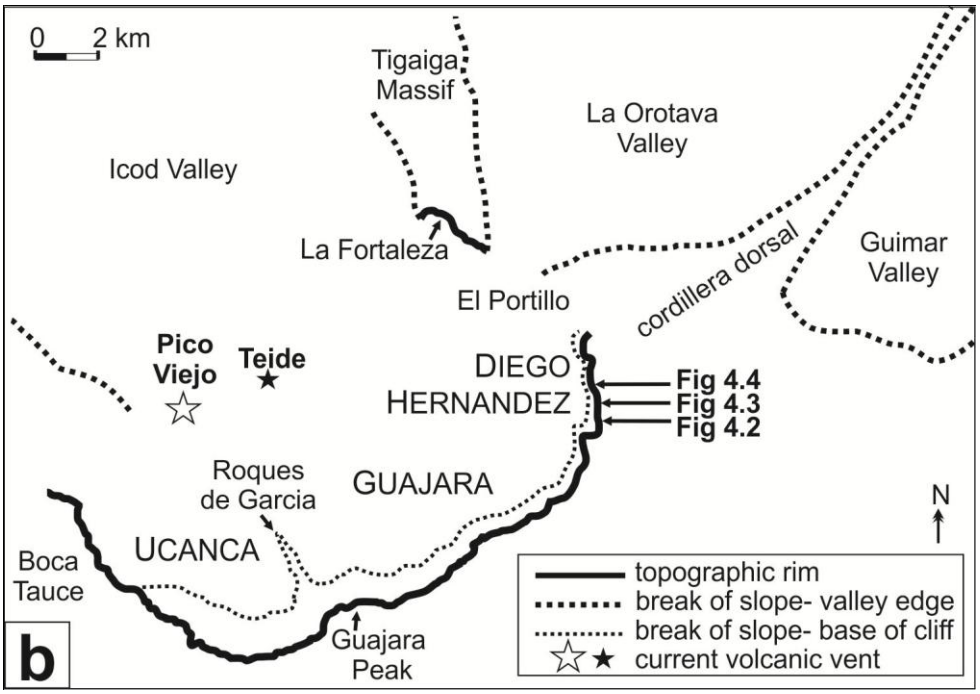

Figure 4.2 (at end of digital document)

Figure 4.3 (at end of digital document)

Figure 4.4 (at end of digital document)

Bed 2 is a ≤5-cm-thick grey ash layer with a clay consistency, containing scattered sub-angular pumices and lithics like those in beds 1, 3 and 5.

Bed 4 is ≤8 cm thick, consists of framework-supported, sub-rounded pumice lapilli ≤2 cm in diameter and has fewer lithics and a higher proportion of fines than beds 1, 3, or 5 (see componentry diagrams on Fig. 4.6).

At locality 16, the upper parts of //bpL are well preserved and pumices can be picked out and sampled, but bed 1 contains softer, more weathered pumices. This variation in pumice quality, which also occurs at other exposures, may be due to water runoff affecting lower parts of the outcrops.

The //bpL lithofacies is best exposed in northern outcrops, where lapilli shape and size are consistent but deposit thickness varies. At locality 14 (Fig. 4.4) it is ≤40 cm thick, massive (pL) and sharply overlies a 5-cm-thick soil above fine-grained, vesicular basanite lava (analysed by Wolff *et al.*, 2000) (Fig. 3.3). At locality 13, the lithofacies is ~50 cm thick and consists of a 40-cm-thick massive bed containing angular to sub-angular lapilli overlying a 10 cm bed of better rounded, smaller lapilli, similar to beds 5 and 4 of locality 16 respectively (Fig. 4.5). Further south, pL is exposed in the lower 10 cm of log 11 and is poorly preserved beneath scree below the outcrop (log 11, Fig. 4.4).

In southern exposures the pumice lapilli unit is not exposed, although abundant angular pumice clasts in the scree below localities 3 and 4 (Fig. 4.5) are evidence of its continuation.

Interpretation

The Poris eruption began with a Plinian phase, recorded in beds 1, 3 and 5. There is no evidence of precursory activity. The angularity of the pumices indicates a fallout origin with little or no abrasion in transit. The lithics present were derived from an obsidian-rich vent zone, broken up during initial activity and entrained in the eruptive jet; the Poris vent may have been close-to, or within, a phonolitic obsidian flow like that of Montaña Blanca. The increase in lithics at the top of bed 5 suggests

an enhanced input of lithics into the jet and hence increased vent erosion. This may have decreased the strength of the jet, promoting fountaining and PDC formation, and seemingly it led to the onset of the next phase of the eruption.

Dilute density currents formed during the Plinian fallout phase, but were recorded only during temporary hiatuses and/or changes in direction of fallout from the plume. Bed 2 is interpreted as recording ash deposition from a fully dilute PDC. The scattered sub-angular Plinian pumices within it are evidence that deposition from the plume had not halted completely at this time. Rainfall may have 'flushed' the material from an ash-laden atmosphere, but there is no evidence that the ash was wet on deposition (such as impact structures beneath the Plinian pumice clasts).

In bed 4 the rounding and relatively small size of pumice lapilli, and the higher proportion of fines, are indicative of abrasion and transport within a PDC and may be a sign that currents were able to transport and rework smaller pumices from the upper parts of the aggrading Plinian deposit during a fallout hiatus.

The top of the lava flow below the Poris is widely covered by scree, which may account for the lack of //bpL exposure in the southern part of the wall. However, this does not explain the irregular thickness of //bpL in northern areas, where the unit differs by up to 50 cm over 100 m. In the proximal zone, Plinian sedimentation can be irregular and intermittent (Houghton *et al.*, 2004) and fallout deposits close to the vent may not be as even as distal examples, but the Poris proximal Plinian unit may have been eroded by subsequent currents. Beds 2 and 4 at locality 16 record dilute currents and it may be that in other parts of the wall these PDCs removed part of the original deposit.

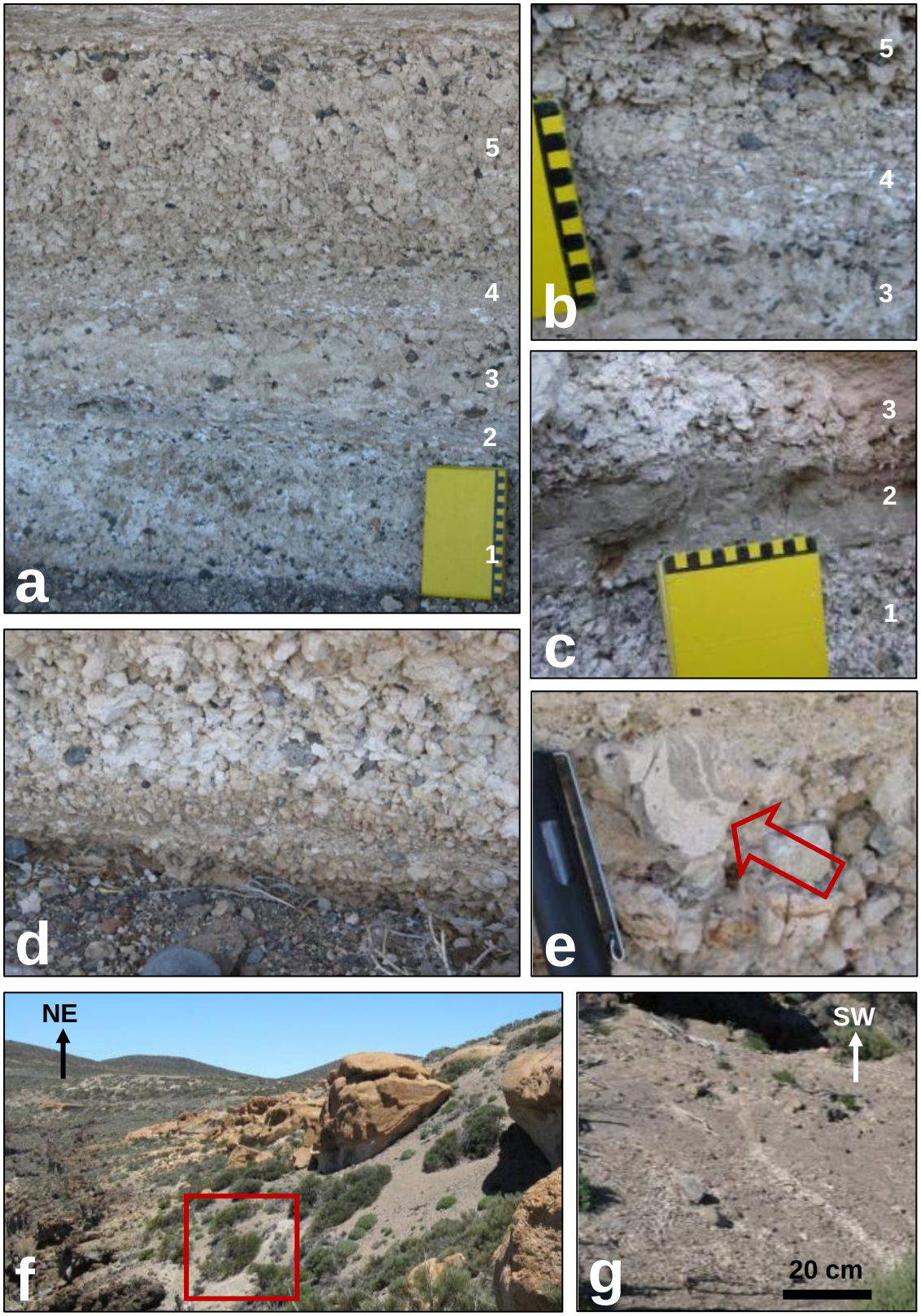

Figure 4.5 Pumice lapilli lithofacies. (a) //bpL at locality 16. (b) Bed 4 at locality 16. (c) Bed 2 at locality 16. (d) Base of //bpL exposure at locality 13; note layer of finer pumices. (e) Banded pumice in //bpL. (f) In northern exposure, //bpL exposure is very poor. Evidence for the lithofacies above the lavas occurs below localities 2 and 3 (red box). (g) Close up of white pumices in scree in area highlighted in red box of (f).

Figure 4.6 (at end of digital document)

4.2.2 Parallel stratified pumice lapilli within tuff (//spLT)

A mainly fine-grained tuff, ≤20 cm thick, overlies the bedded pumice lapilli lithofacies and is exposed in both northern and southern parts of the DH wall. The lower 10 cm contains discrete diffusely stratified to stratified beds, ~2-7 cm thick, of pumice clasts. These beds vary in number and grainsize laterally across the wall, but are consistently well sorted. Detail of these layers is shown in mini-logs (Fig. 4.7). These are separated by matrix-rich layers ~1-6 cm thick comprising ash, crystals and lithics <1 cm in diameter. The pumices are sub-angular to sub-rounded and 0.5-2 cm in diameter. They are preserved relatively fresh in northern exposures, whereas in the south the pumices are recess-weathered and the deposits more cemented. At mini-locality E, a rare fresh exposure shows that the lower beds of //spLT contain angular to sub-angular pumices, 2-3 cm in diameter, larger than the sub-rounded ones and like those in the Plinian population of //bpL below. Here, the contact between the two lithofacies is more gradational than elsewhere (Fig. 4.8).

The matrix material is relatively rich in lithic and crystal material (12-18% of total componentry) compared with //bpL below (~8%) and mTacc above (~5%). At locality 16, where //spLT is thicker than elsewhere, it contains a 10-cm-thick upper massive bed that is grey due to relatively abundant mm-scale crystal fragments and various lithic clasts (mini-log A, Fig. 4.7).

Petrography

Thin sections from four //spLT locations all show pumice clasts, lithic clasts and crystals within a glassy ash matrix. Crystals include anhedral, resorbed and embayed plagioclase feldspars, relatively euhedral clinopyroxene, biotite, amphibole, alkali feldspars with microcline twinning, and rare olivine. Plagioclases commonly display irregular sectoral zoning; some clinopyroxenes are also compositionally zoned. Various lithic clasts are present, generally ~1 mm in diameter (see Fig. 4.8). Clasts rich in white, fine-grained (<100 μm) euhedral plagioclase laths with trachytic texture occur alongside clasts containing plagioclase and amphibole laths with no flow texture. Less common are clasts containing coarser, equant, pale yellow laths with poorly defined edges, clasts stained dark red and brown, presumably oxidised, and clasts of obsidian.

Interpretation

The //spLT lithofacies marks the onset of pyroclastic density current activity in this vicinity, and the cessation of simple deposition from Plinian fallout. This thin 'veneer' unit is interpreted to record deposition from a fully dilute PDC. Pumices were rolled and saltated at the base of the current to induce the stratification and rounding, while continuing fallout from the plume added fresh Plinian pumices and lithics to the flow boundary zone. The massive nature of the grey layer at mini log A may indicate that the flow boundary zone was temporarily thicker and more prone to deposit with less traction at this location. There is no reason to believe that any bypass to distal slopes occurred at this stage; the gradational nature of the contact between //bpL and //spLT indicates continuous deposition.

The fine grainsize of lithics and crystals in the matrix, particularly pronounced in the grey layer of mini-log A, indicate fine fragmentation at source. The lithic material is more heterogeneous in lithology than that in //bpL below, possibly reflecting widening of the vent and consequent erosion there of a larger range of lithologies. Increased explosivity reflecting a change to phreatomagmatic processes is considered in Section 4.2.4.

The lateral continuity of the deposit across the DH wall implies that the current was fairly uniform here, but it is difficult to assess the extent of the current. There appear to be two feasible alternatives. Either a relatively small, fully dilute current deposited the tuff observed, or a larger density-stratified current was partly restricted in access to the present site of the DH wall, so that only the upper fully dilute parts were recorded. The succeeding lithofacies bears on this issue; evidence suggests that the latter scenario is more likely and this is discussed below.

Figure 4.7 Stratigraphic logs of stratified pumices in tuff (//spLT) and overlying massive tuff with accretionary pellets (mTacc) lithofacies. Logs are smaller scale than those shown in previous figures: vertical axis scale is in centimetres. At localities where the contact between //spLT and the bedded pumice lapilli (//bpL) facies below is exposed, only the upper part of //bpL is shown. The lower parts of the cross stratified crystal-rich tuff (xscrT) and/or stratified lithic- and crystal-rich tuff (slcrT) facies are also shown. Each mini-log corresponds to a main locality (Figs 4.1-4.4); this number is shown in parenthesis. Logs are hung according to the non-erosive contact between //spLT and mTacc (where present); this does not necessarily reflect their position along the cliff.

Figure 4.7 (at end of digital document)

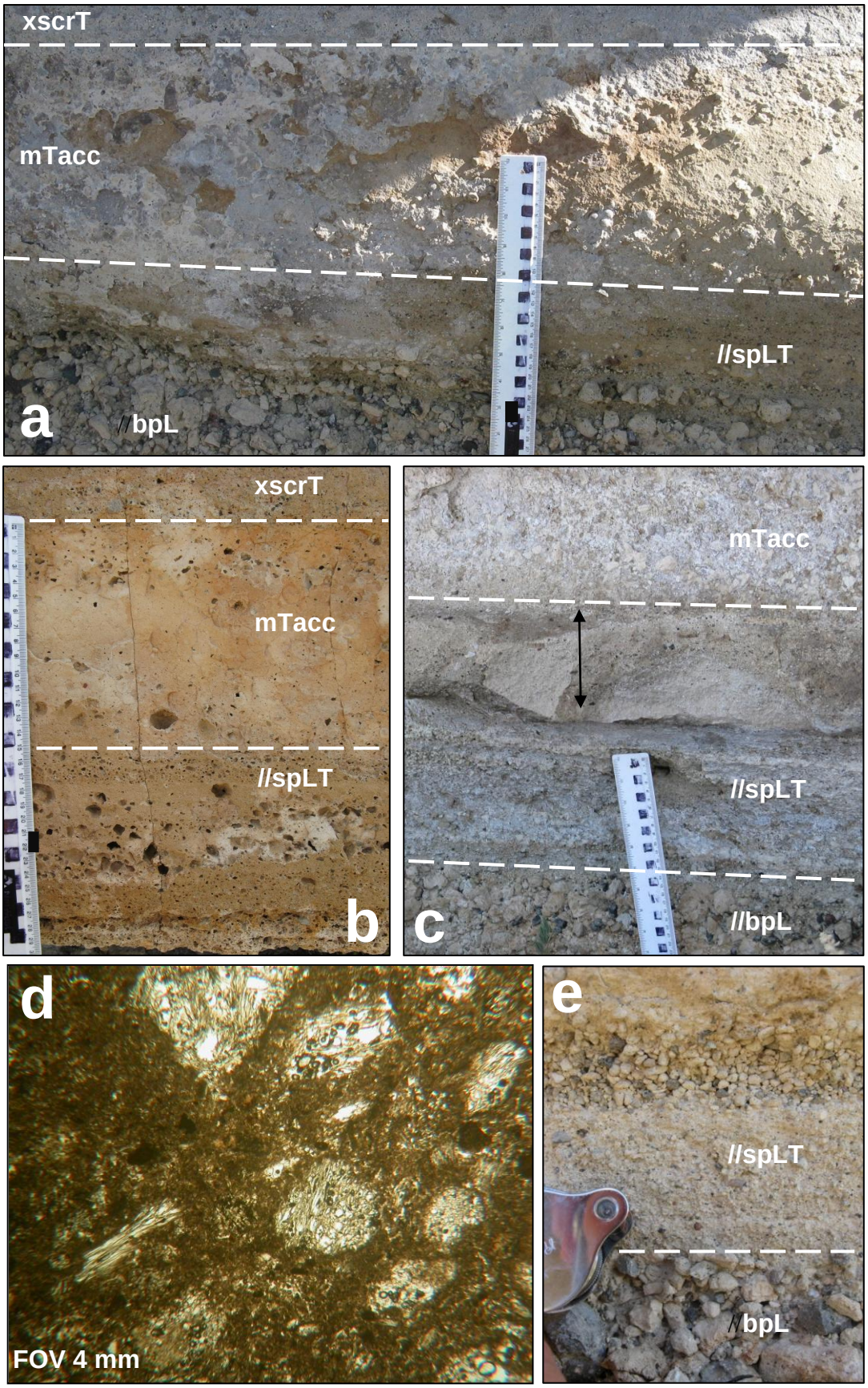

Figure 4.8 Stratified pumice lapilli in tuff. (a) Erosional contact between //bpL and //spLT (b) Recess weathering of pumices highlights stratification of //spLT in a weathered surface. (c) Massive, grey upper bed of //spLT (arrow) exposed at mini-locality a[16]. (d) Thin section view (ppl) of pumice rich layer in //spLT. (e) Close-up of sub-rounded stratified pumices at mini-locality d[11].

4.2.3 Massive tuff with accretionary pellets (mTacc1)

A 20-cm-thick tuff consisting of fine white ash and ash agglomerations overlies //spLT. The contact between the units is well defined due to the change in colour and grainsize, but it is not erosive. The massive ash unit is white and lithic-poor compared to //spLT below (Fig. 4.6), and it contains scattered angular to sub-angular pumices. The pumice lapilli are ≤4 cm in diameter and similar in nature to those of the Plinian population. Accretionary pellets ≤2 cm in diameter occur and commonly display multiple concentric rims of ash. The spherical aggregates have a hardened exterior and it was possible to take some samples without disintegration (see below). At fresh exposures, the matrix appears to contain small ash agglomerations; these are possibly unstructured pellets, or AP1 in the scheme of Brown *et al*. 2011, but their presence is hard to confirm microscopically due to the friability of the material when sampled. 'Cored' accretionary pellets, pumice clasts encircled by layers of ash (Brown *et al.*, 2010), and flattened accretionary pellets also occur. At weathered outcrop, pumice clasts are recess-weathered and accretionary pellets are exposed in cross-section (Fig. 4.9).

The mTacc facies, like the underlying //spLT, occurs at all exposures of the lower lithofacies across the cliff, except at locality 13 where it has been removed and deposits higher in the sequence are in erosional contact with //spLT. The thickness of the deposit varies slightly, seemingly a result of scour from above, but the nature of the ash is consistent at all exposures.

Ash aggregate characteristics

Ash aggregates from mTacc1 were sampled and made into thin sections for detailed analysis (Fig 4.10); various structures are documented. Unstructured pellets comprising ash and fine crystal material, some of which are distinctly vesicular, occur alongside multi-rimmed accretionary pellets. Rims commonly show decreasing grain-size towards the edge of the pellet, and in some cases display subtle grading. The inner part of the multi-rimmed pellets can be unstructured ash, a lithic clast, or a pumice fragment. One pellet sampled contains a core of lithic material and amphibole crystals in unstructured ash, and is coated in just a single rim of fine ash (Fig 4.10h).

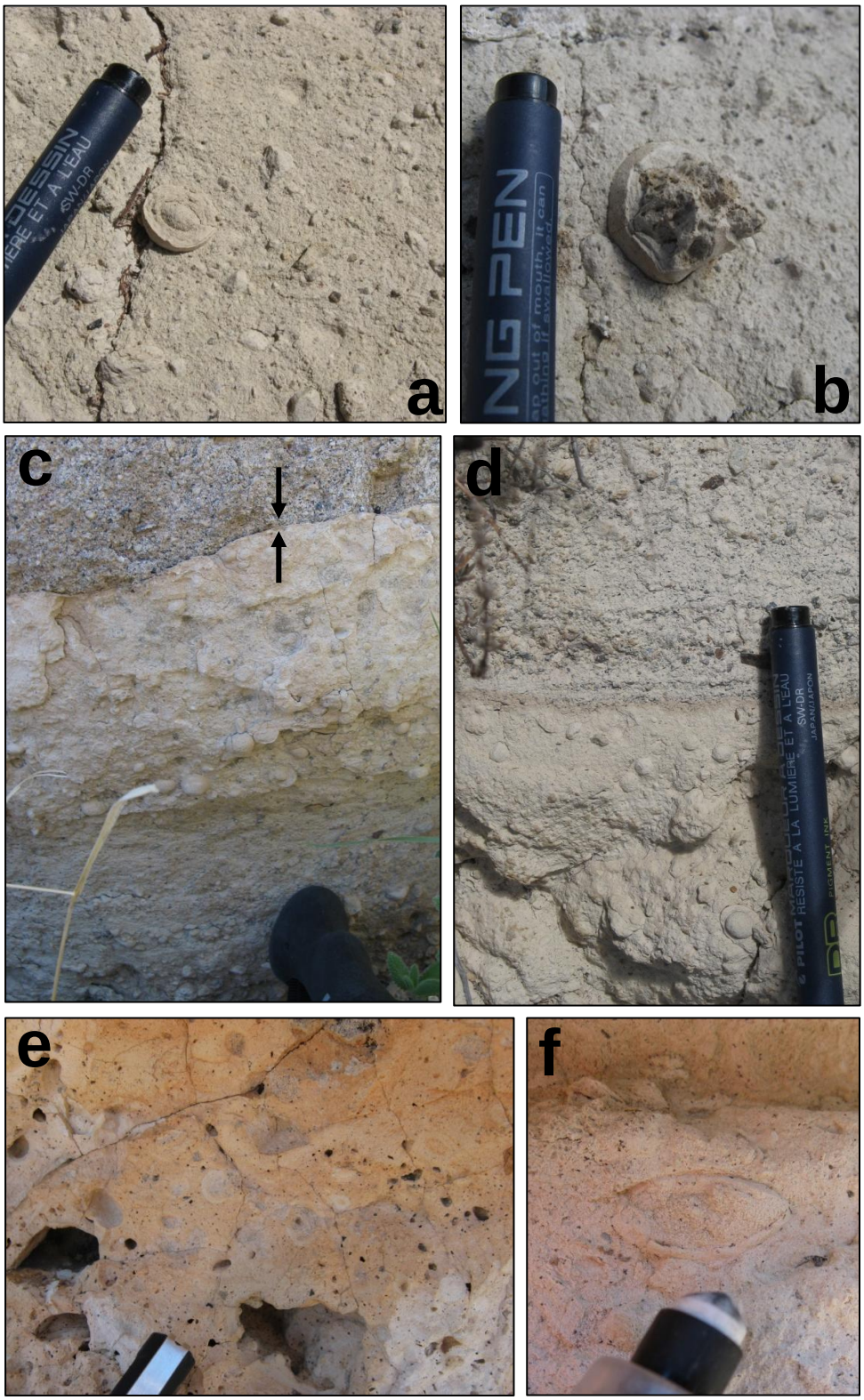

Figure 4.9 Massive tuff with accretionary pellets (mTacc1). (a) Accretionary pellets in lithic-poor matrix, which contains some small angular pumices and has a subtle pellet nature at this location. (b) Pumice clast encased in concentric layers of ash: a 'cored lapillus'. (c) and (d) Views of mTacc in contact with the lithic-rich facies above. Note the erosional contact in photo (c) (arrows). (e) Weathered surface of mTacc where pumices of the Plinian population have become recess weathered, leaving holes. (f) This accretionary lapillus has been flattened, indicating deformation.

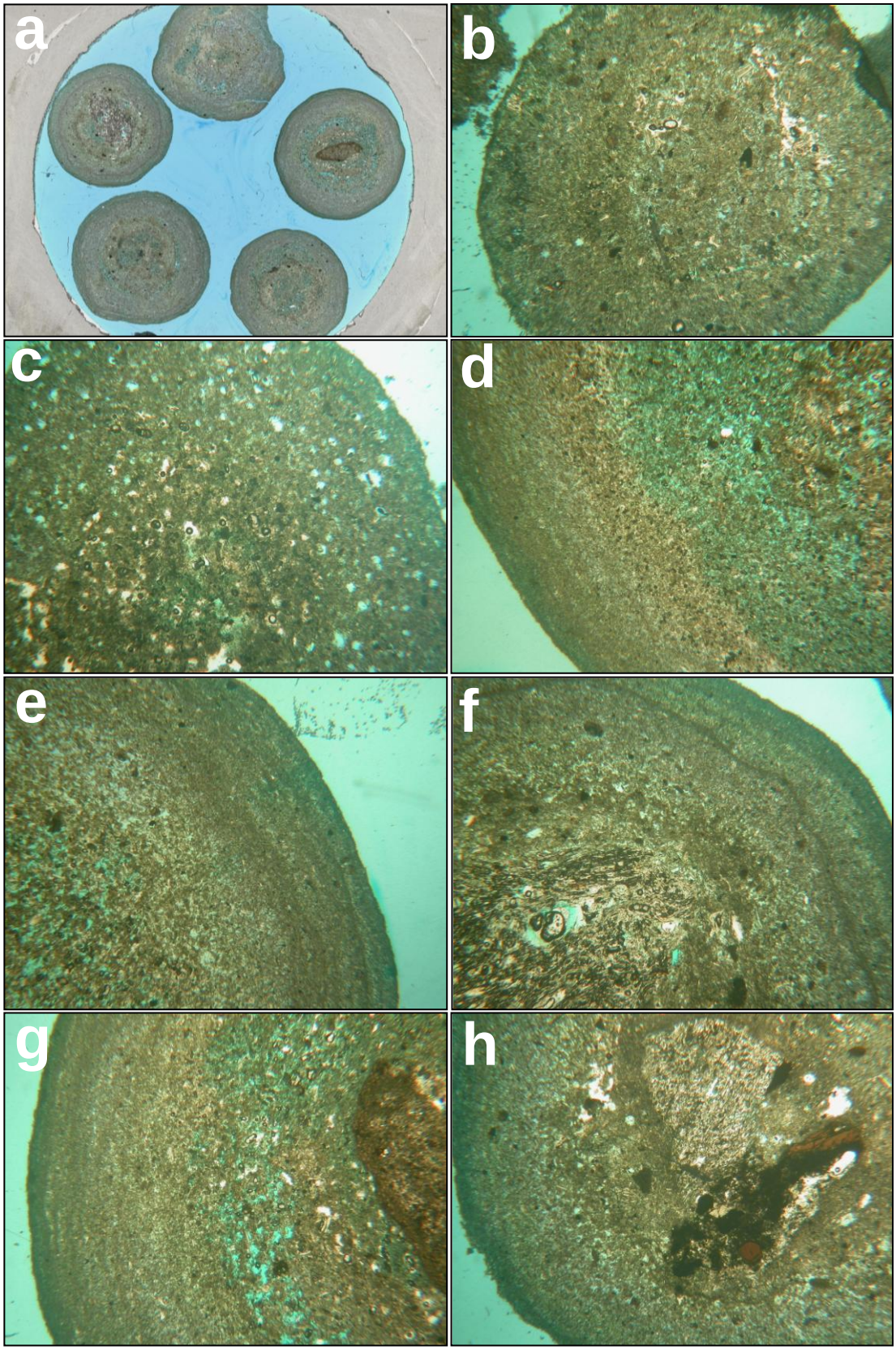

Figure 4.10 Ash aggregates in the mTacc1 lithofacies. (a) One of three slides made containing ash aggregates. Blue circle of resin is 2.5 cm across. (b) Unstructured ash pellet. (c) Vesiculated unstructured pellet. (d) Multiple rims with decreasing grain-size. (e) Multiple rims with graded grain-size. (f) Pumice core with irregular rims. (g) Lithic core with multiple rims. (h) Lithic and amphibole in unstructured ash core coated by a single rim. (b)-(h) field of view = 4 mm.

Interpretation

The formation of ash aggregates is not completely understood; models exist for formation in both the volcanic plume and within density currents (see Section 1.4). In distal Tenerife ignimbrite successions, multi-rimmed pellets (AP2) occur in massive lapilli tuff overlain by clast-supported layers of unstructured pellets (AP1). This lithofacies association is interpreted to reflect formation of unstructured pellets in the co-ignimbrite ash cloud, which may then accrete multiple rims in lower parts of the same current; after the main current has passed by, the AP1 pellets fall out of the co-ignimbrite plume to form a layer that caps the tuff (Brown *et al.*, 2010).

The occurrence of matrix-supported unstructured pellets and multi-rimmed accretionary pellets of a similar size together in the mTacc1 proximal lithofacies has not been previously reported on Tenerife and may be significant. In the vent-proximal region, the plume lofted above a density current and the fringes of the main volcanic plume are likely to converge and become mixed together. Air drawn inwards and upwards towards the main plume will inevitably drag a proximal co-ignimbrite cloud in towards the main column (Fig 4.11). Ash aggregates may be forming in both the main plume and within the PDC in the near-vent zone, and the interaction of these two systems could account for the hybrid aggregates deposited in the proximal mTacc1.

The mTacc1 lithofacies is interpreted here to record deposition of ash and ash aggregates from a near-vent, dilute, ash-rich hybrid plume, during ongoing Plinian deposition of pumice lapilli. The deposition of lapilli tuff had temporarily ceased in the DH area at this stage.

//spLT and mTacc1 lithofacies association

In the distal zone, a lithofacies association similar to that of the thin //spLT unit and overlying mTacc1 facies occurs on topographic ridges between barrancos and is interpreted to reflect the interaction of density-stratified PDCs with local topography (Brown and Branney, 2004b). The proximal lithofacies association of //spLT and mTacc1 is here interpreted in a similar fashion, as an ignimbrite veneer deposited when a large density-stratified pyroclastic current encountered proximal topography

and was partly blocked. The least dense parts surmounted the obstacle and re-stratified; the lower part of this re-stratified current reworked Plinian material and deposited tuff, and the upper part subsequently deposited ash and ash aggregates (Fig 4.11). A small-scale dilute current is ruled out as a possibility for the deposition of these facies based upon the presence of brittle, multi-rimmed ash aggregates that indicate formation within a hot, turbulent PDC system.

4.2.4 Cross stratified crystal-rich tuff (xscrT) and stratified lithic- and crystal-rich tuff (slcrT)

A pale grey, cross-stratified deposit rich in crystal fragments and lithics ≤3 mm in diameter occurs above the white ash facies (Fig. 4.2-4.4). Millimetre-scale fine ash layers and crystal-rich layers are cross-bedded in low angle dune forms with truncations (Fig. 4.12). At the base, the dune forms contain small accretionary pellets, possibly a result of scour into mTacc1 below. At locality 16, the cross-stratified tuff (xscrT) is ≤10 cm thick and in sharp contact with the lithic-rich stratified unit above, whereas at localities 11 and 14 there is a gradational contact between the two. The cross stratification is absent where overlying facies have scouring basal contacts, such as at localities 13 and 16.

The overlying stratified lithic- and crystal-rich (slcrT) facies is ≤1.5 m thick and has a distinctive dark grey base resulting from a high modal content of fine-grained lithics and crystals (up to 40%). This clast-rich ignimbrite grades upwards into paler material as the lithics and crystals decrease in concentration. Sub-angular to sub-rounded pumice lapilli, commonly ≤2 cm in diameter, occur as inversely graded 'sets' at many outcrops (most prominently at localities 4, 5 and 17) (Fig. 4.13). Heterolithic clasts ≤6 cm in diameter also display subtle bedding, but the stratification of pumices is more prominent due to recess-weathering. Stratification is generally planar and on a decimetre-scale but varies laterally; at locality 16 some beds dip subtly <10º across the outcrop face (10/142 NW). At localities 5, 7 and 16 larger lithic clasts are concentrated at the base of slcrT, and the facies is in erosive contact with units below.

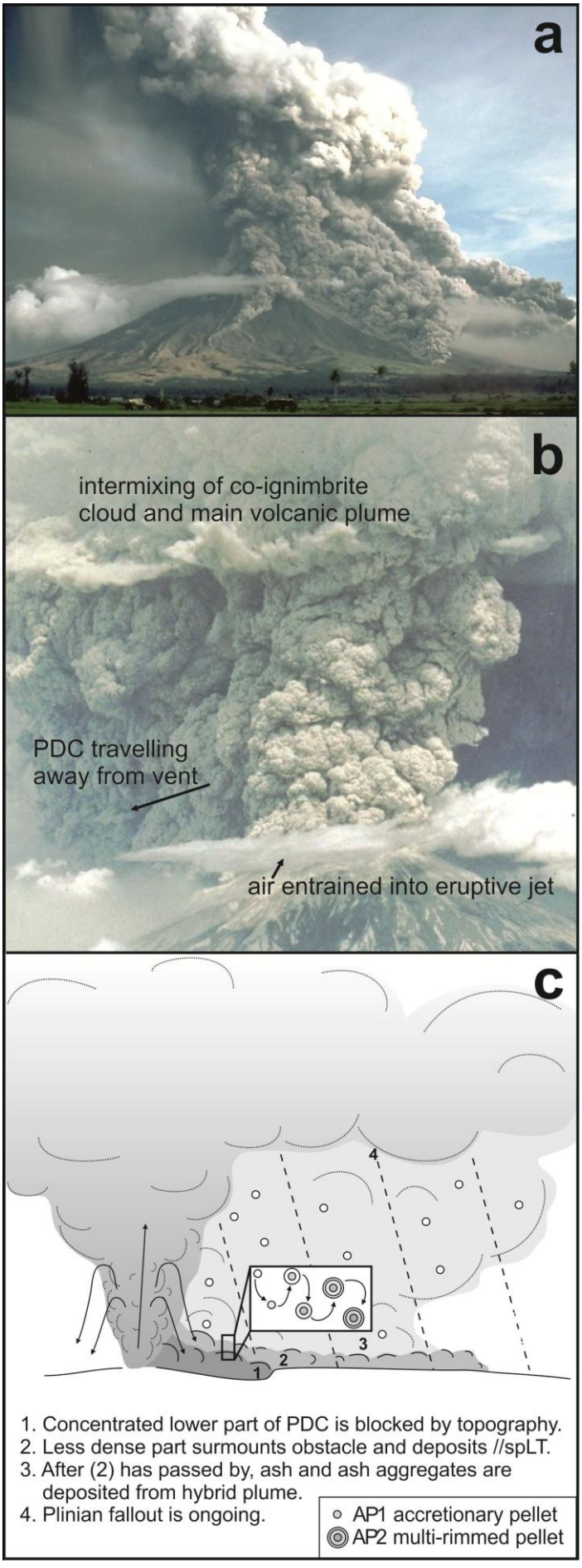

Figure 4.11
(a) Pyroclastic density current generated during the 1984 eruption of Mayon, in the Philippines. The proximal co-ignimbrite cloud is dragged back in towards the main volcanic column (C. Newhall; USGS, 2010). (b) Mount St. Helens, May, 1980. Intermixing of co-ignimbrite cloud and volcanic plume (USGS, courtesy PK). (c) Interpretation of the deposition of the //spLT/ mTacc1 lithofacies association.

Petrography

The mineralogy of slcrT is very similar to //spLT. Embayed and anhedral plagioclase feldspars, alkali feldspars with microcline twinning, and clinopyroxenes, some with oscillatory zoning, occur alongside amphibole and biotite. Rare olivine is present and an opaque oxide occurs, possibly magnetite. Millimetre-scale lithics present include fine-grained plagioclase-rich clasts with flow texture, and more mafic clasts rich in amphibole. In hand specimen, purple, fine-grained clasts and coarser grained red and white lithics occur commonly (e.g. Fig. 4.13), but these degrade easily and do not survive the thin-section making process. They are most probably syenite, according to their coarseness and the common occurrence of syenite lithics in other Tenerife ignimbrites.

Interpretation

The presence of highly fragmented and heterolithic crystal and lithic material in the xscrT and slcrT lithofacies is taken to indicate that this phase of the eruption was phreatomagmatic. There is no evidence of any current hiatus between the deposition of xscrT and slcrT; slcrT contains the same lithic and crystal compositions as in xscrT below, but contains parallel, decimetre-scale stratification as opposed to millimetre-scale cross bedding.

The xscrT lithofacies records the passage of a fully dilute current with tractional processes occurring at the depositional flow boundary zone. The low-angle dune forms contain accretionary pellets at their base, probably picked up from the underlying ash upcurrent of here; the contact between mTacc1 and xscrT is relatively conformable with no evidence of deep scour. This facies could be interpreted to indicate that the phreatomagmatic PDC was relatively dilute at first. Alternatively, the occurrence of xscrT could be evidence that topographic blocking was still occurring for a short time after the deposition of mTacc1, and that only the upper, dilute parts of the lithic-rich waxing currents made it to this location initially, until the obstacle was sufficiently buried to be surmounted by the entire current.

The lithic-rich, planar-stratified lithofacies above records the passage of a PDC with granular-fluid conditions at the lower flow-boundary zone. The scour at the

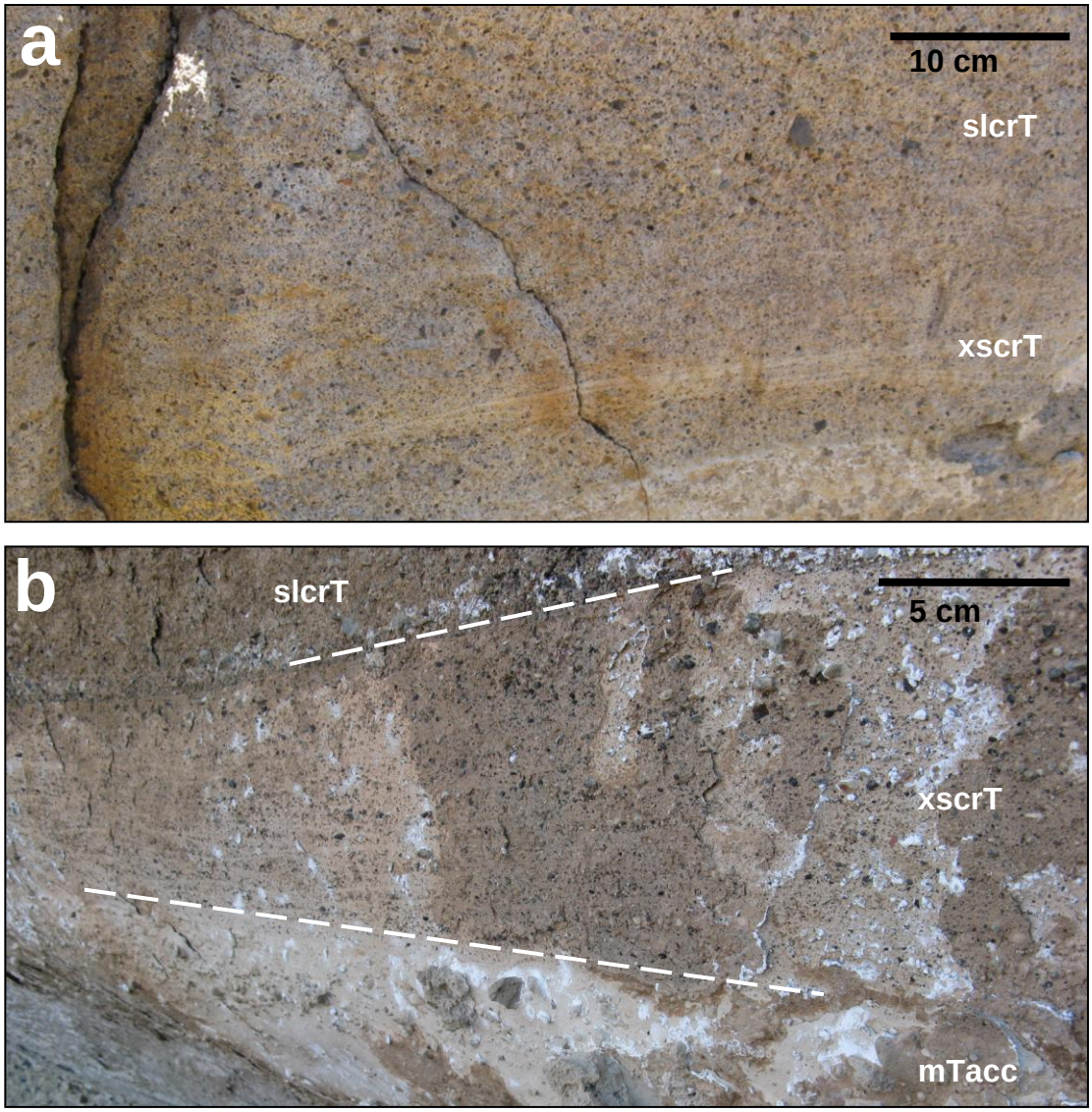

Figure 4.12 The contact between slcrT and xscrT is laterally variable, and can be gradational, such as at locality 14 (a), or sharply defined, as at locality 16 (b).

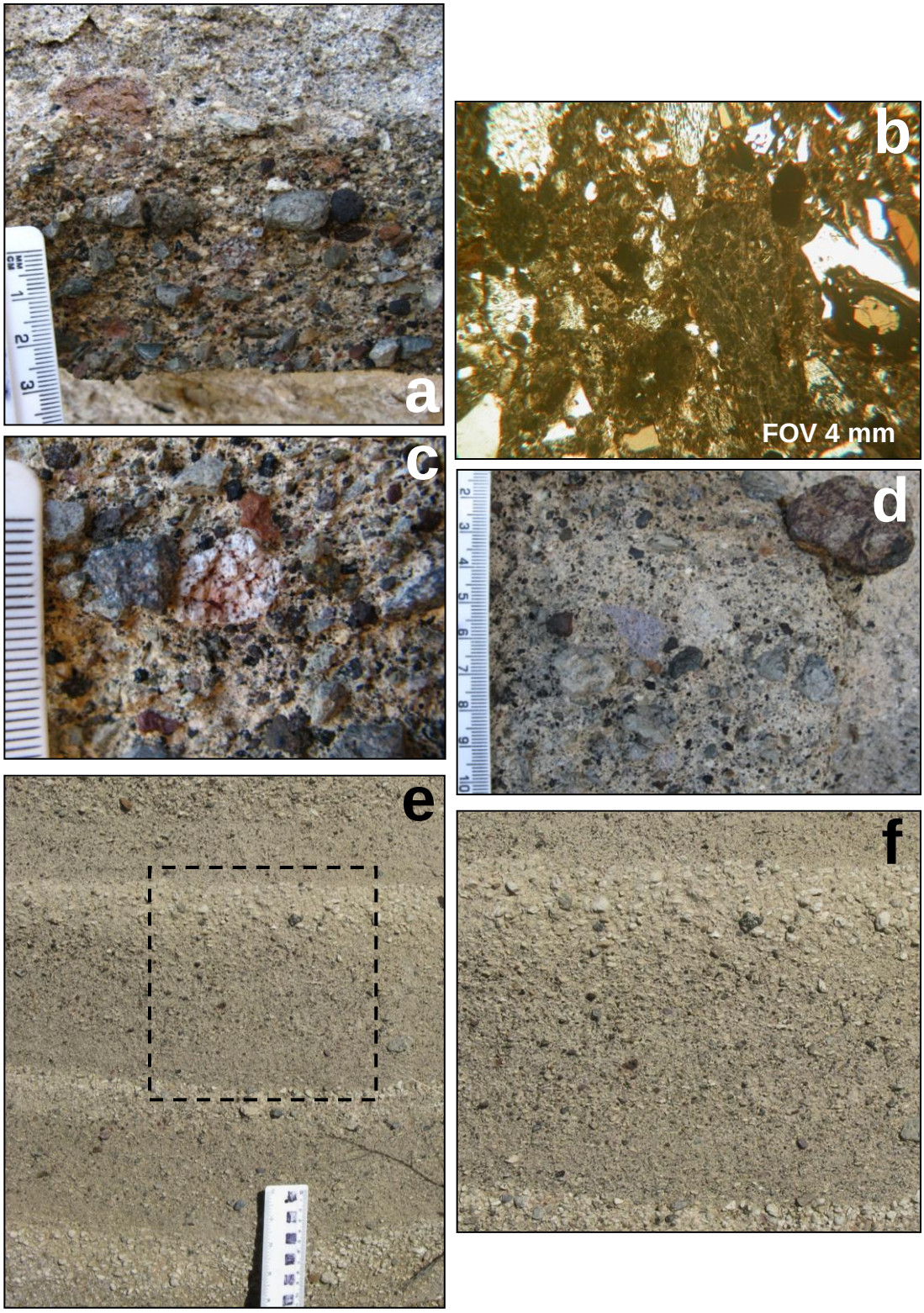

Figure 4.13 (a) The lithic-rich base of slcrT in erosive contact with mTacc1 at locality 16. (b) In thin section (ppl), the high concentration of angular lithic and crystal material in slcrT is clear. Clinopyroxene, feldspar and amphibole commonly occur. (c) and (d) slcrT is heterolithic and poorly sorted at its base, containing red and purple altered clasts. (e) Sets of inversely graded pumices occur towards the top of slcrT, shown close-up in box (f).

base of slcrT records waxing energy; material was then deposited as conditions waned. The sets of inversely graded pumice clasts at some localities indicate a pulsatory nature to density current deposition at this time. Scour and graded bedding are discussed further in Chapter 5. Up through the deposit fragmented lithics and crystals become less concentrated, which possibly is an indication that through time the eruption style became magmatic once more, with fewer fragmented lithics entrained at source.

4.2.6 Thin massive ash with small accretionary pellets (mTacc2)

A second mTacc unit occurs above slcrT at localities 16 and 17. The 2 cm thick layer consists of white ash with accretionary pellets <1 cm in diameter. In contrast to the first mTacc layer, where the accretionary pellets are commonly multi-rimmed and could be sampled easily because their exterior was hard, these, when seen in cross section, have a relatively large grey core mostly with only one or two coating layers of white ash. When mTacc2 was sampled, no accretionary pellets survived and sections of them could not be made. The upper part of the ash is overlain by a 1-cm-thick layer of mm-scale lithics with small-scale scour and flame features, in erosional contact with the ash (Fig 4.14). The mTacc2 layer occurs only at the two most northerly outcrops. At southern outcrops, the freshly exposed contact between slcrT and the facies above shows no evidence of fine ash or a concentration of accretionary pellets (see Section 4.3.1).

Interpretation

The lithic-poor, thin ash unit atop the slcrT ignimbrite is interpreted to record ash deposition during a temporary pause in lapilli-tuff deposition. The origin of this ash is discussed in Chapter 5. The less well-formed accretionary pellets indicate that, relative to the stage represented by the first mTacc layer, there was less time between pellet formation and accretionary pellet deposition. The sedimentation of this ash is not ubiquitously recorded across the DH wall; either the ash layer was scoured in southern parts by subsequent currents, or the current persisted in southern parts of the DH area while ash was being deposited to the north. This has implications for the designation of flow units in the proximal zone (see Chapter 5).

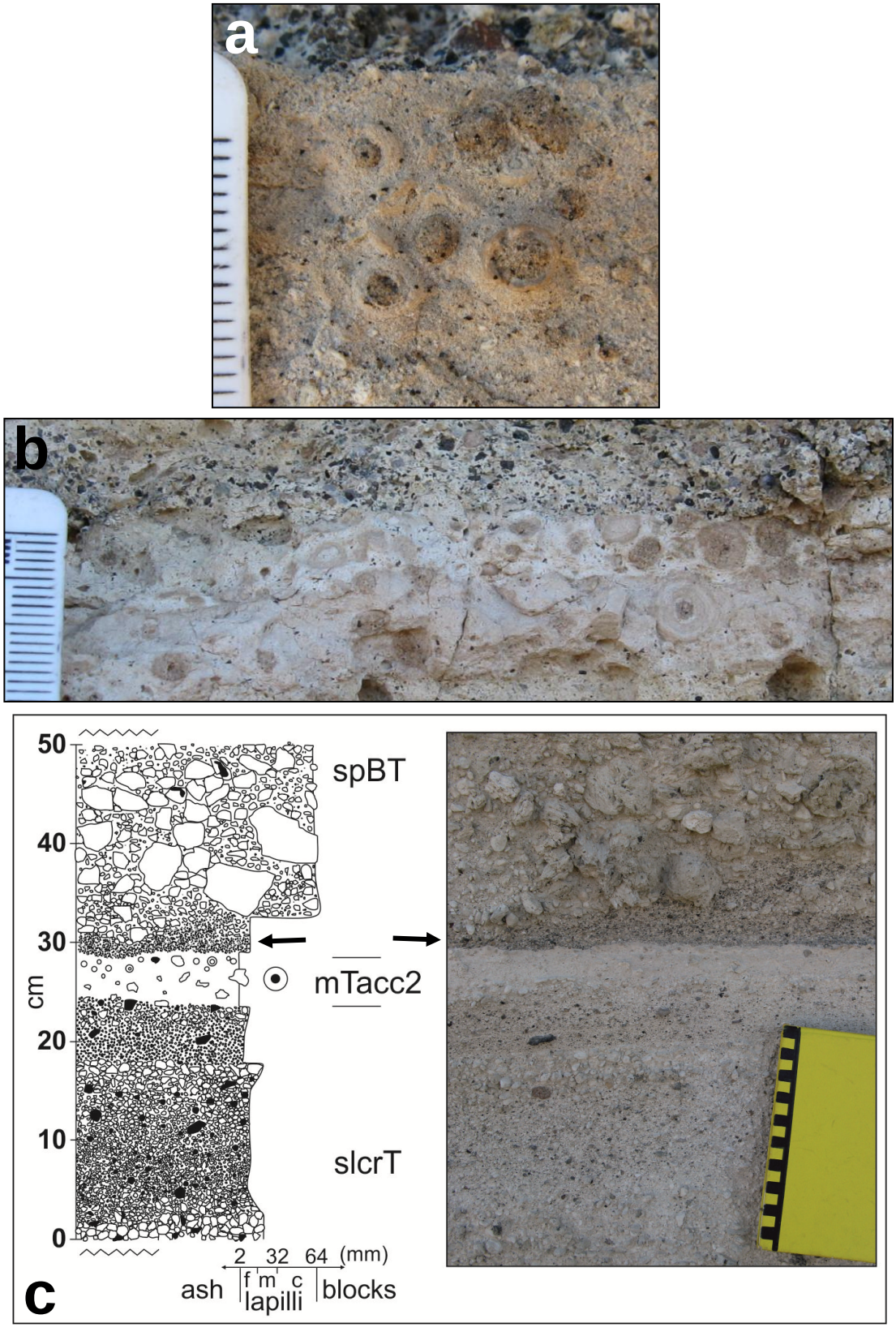

Figure 4.14 (a) In contrast to the accretionary pellets in mTacc1, mTacc2 accretionary pellets have a relatively large grey ash core and few concentric rims of paler ash. (b) mTacc2 lies at the top of slcrT and is in erosive contact with the unit above. (c) Mini-log of mTacc2 at locality 17. Note the layer of fine-grained lithics that occurs at the base of spBT (arrows).

4.2.7 Stratified pumice block tuff (spBT)

A poorly sorted, stratified tuff rich in pumices 0.5-30 cm in diameter overlies slcrT. The spBT lithofacies is ≤2 m thick and consists of pumice-rich beds separated by layers of fine-grained matrix ≤10 cm thick. The unit contains accretionary pellets <2 cm in diameter and scarce lithic lapilli >1 cm in diameter.

Pumice beds vary in thickness from 5-80 cm, both laterally across the DH wall and radially into the cliff face, and they display planar and low-angle cross bedding. They are typically massive, but at one locality contain internal stratification (Fig. 4.15). Pale-green to cream pumices are locally clast-supported and frequently contain discrete 'blebs' of dark grey-black material (a characteristic of Poris pumices also noted by Edgar *et al.* (2007) and discussed further in Chapter 6). Pumices ≤2 cm in diameter are slightly rounded, while larger clasts (2-30 cm) are sub-angular to angular. Where relatively fresh, these larger clasts are evidently mainly of the pale-green pumice type (Fig 4.15). The largest blocks (15-30 cm in diameter) are commonly banded, with streaking of black, green, and cream glass; they show no evidence of ballistic impact onto the material beneath.

Matrix material comprises ash, crystal fragments and lithics ≤5 mm in diameter. Fine-grained beds can be subtly stratified and are commonly in scour contact with pumice beds below (Fig. 4.15).

Interpretation

Plinian fall deposits mantle topography and are typically rich in well sorted, angular pumice clasts, while PDC deposits are commonly laterally variable, poorly sorted and matrix-supported, containing pumices rounded by abrasion and reworking during transport. Thus the spBT unit is interpreted to be a hybrid deposit resulting from multiple depositional processes. The sub-angular pumice lapilli imply fallout from a Plinian plume into a PDC, while the fine-grained material and smaller sub-rounded pumices record transport in the current from source. Local zones of clast-supported pumices indicate a higher influence from Plinian fallout in these areas, and the occurrence of stratified and cross stratified beds, and of stratified clasts within beds, reflects unsteadiness and tractional processes at a current flow-boundary zone.

The very large pumice blocks suggest ballistic input, but the lack of impact features implies that the blocks fell into currents and were transported along with smaller clasts before deposition.

There is no evidence that Plinian deposition ceased completely at any time during the Poris eruption; at times of ignimbrite deposition fallout material may have become entrained in PDCs and difficult to distinguish in the deposit. However, the angular fallout-derived pumices of spBT are considerably coarser than those of the Plinian lithofacies at the base of the Poris succession and the hybrid nature of the unit is therefore unambiguous. The cause of this coarsening of Plinian pumices is uncertain, but it may be connected to the phreatomagmatic episode that preceded the deposition of spBT. The lithic-rich nature of the slcrT facies below indicates considerable removal of rock from the source area, implying substantial vent widening. This may have led to shallower and lessened fragmentation. Experimental studies (Dufek and Manga, 2011) indicate that eruption of large pumice clasts (>10 cm) can reflect relatively shallow levels of fragmentation within the volcanic conduit. Conversely, or in addition, it may be that the wind dispersal direction of Plinian material changed during the eruption, leading to the deposition of the coarsest proximal fallout material in different sectors at different times. The presence of accretionary pellets in this lithofacies, following their occurrence in discrete ash beds lower in the succession, indicates that they were continually generated in the proximal zone.

Hybrid units are fairly common. Valentine and Giannetti (1995) described laterally variable pyroclastic beds that contain sub-angular pumices not abraded by lateral transport, at Roccamonfina in Italy, and interpreted them to result from the interaction of simultaneous fallout and 'surge' events. The Bishop Tuff in California includes fall deposits containing cross bedding and rounded clasts, which Wilson and Hildreth (1998) interpreted as fall material re-deposited by strong air currents associated with coeval PDCs. Similar units occur at Pantelleria volcano, Italy (Rebecca Williams, pers. comm., 2009) and at Los Humeros, Mexico (Mike Branney, pers. comm., 2011).

4.2.8 Stratified to diffuse stratified to massive tuff variably rich in lithics (s-ds-mlLT)

This unit consists of variable ignimbrite lithofacies that are linked here according to their stratigraphic position between the stratified block tuff below and a lithic-rich layer of tuff above. The overlying lithic rich layer, described in Section 4.2.9, has an erosional basal contact across much of the DH wall and s-ds-mlLT is preserved at only a few localities (see Fig. 4.1).

The tuff contains pumice clasts typically ≤4 cm in diameter with subordinate lithic clasts of various lithologies. Stratification and the relationship with spBT below change across the cliff. In the north at locality 17, stratified tuff ≤ 2 m thick occurs above spBT, comprising 4 beds of inversely graded pumices clasts ≤3 cm in diameter overlain by 3 beds of finer pumices ≤1.5 cm in diameter. Here the stratified facies has an irregular upper contact with the erosive lithic-rich layer above and is separated from spBT below by a 'mat' of reworked pumices (Fig. 4.16).

In the centre of the DH wall, at locality 10, ~30 cm of stratified tuff overlain by massive tuff with some diffuse stratification is in gradational contact with spBT. Beds of pumice block tuff develop from sLT beds over 4 metres distance, longitudinally from source. As a result the spBT lithofacies thickens *into* the cliff; localities 9 and 9a are set farther back on the DH slope and record spBT in a higher position, a result of this thickening (Fig. 4.3).

In the south at the same stratigraphic position, diffusely stratified tuff truncates a spBT pumice bed with internal stratification (locality 5, see Fig 4.15f), while stratified tuff is not present above spBT at localities 1, 2 and 3; the unit is massive and locally lithic-rich.

This unit records the cessation of deposition of *coarse* pumice from fallout in the DH area along with the onset of more typical ignimbrite deposition. This may have been due to a stronger tendency towards fountaining of the eruptive column with less input from Plinian fallout, or it may reflect a change in fragmentation style in the conduit.

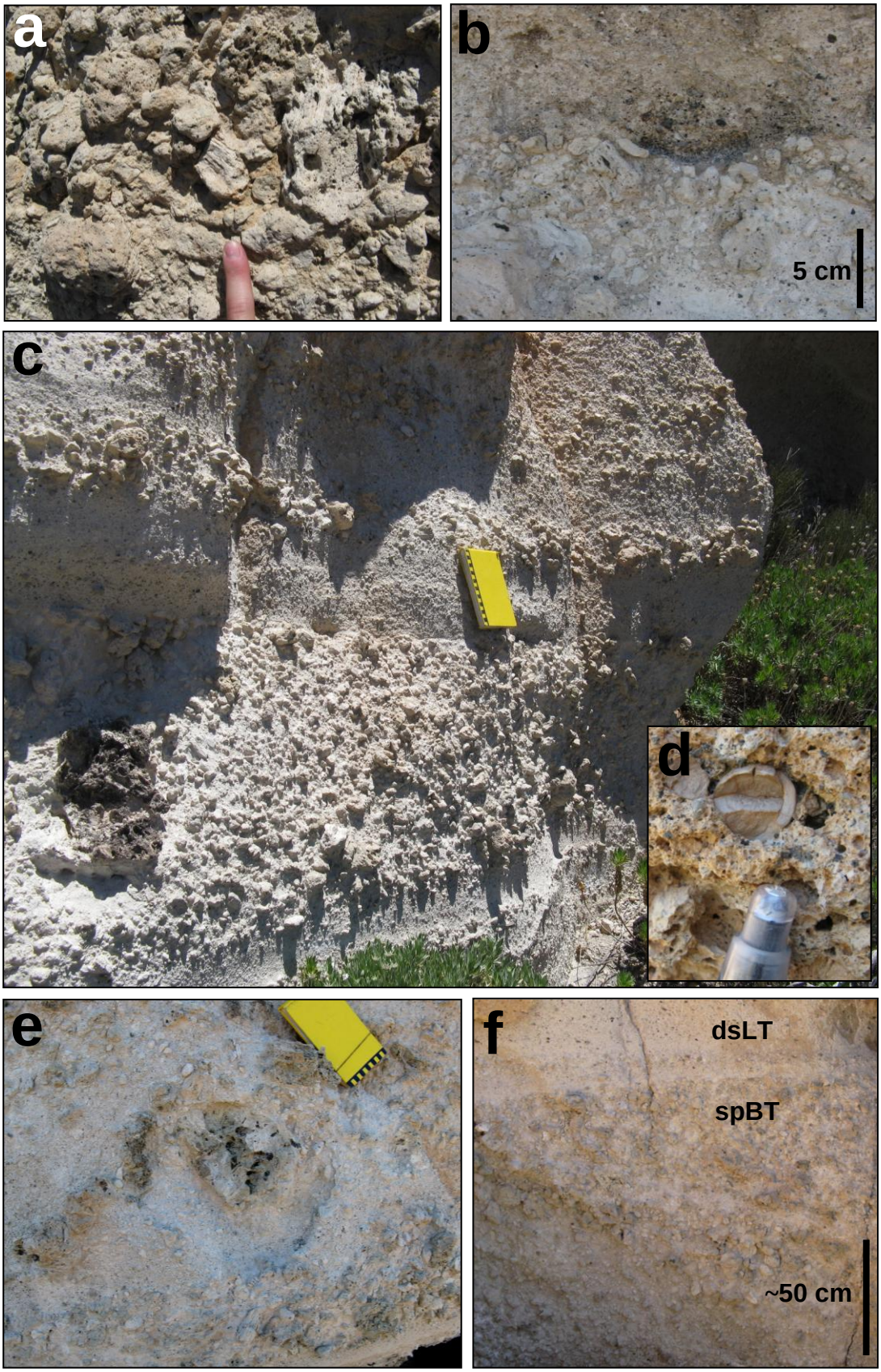

Figure 4.15 Stratified pumice block tuff. (a) spBT is locally clast supported. (b) Lithic fragments are commonly concentrated at the base of fine-grained beds, here seen in scour contact with the pumice bed below. (c) spBT pumice beds separated by fine-grained beds at locality 10. Note large mafic pumice in left of image. (d) Broken accretionary pellet in spBT. (e) Pale green, angular pumice clasts together with smaller, cream, rounded clasts. (f) Stratification of clasts within a pumice bed at locality 5 (current direction is into page). The finer-grained bed above truncates the stratification.

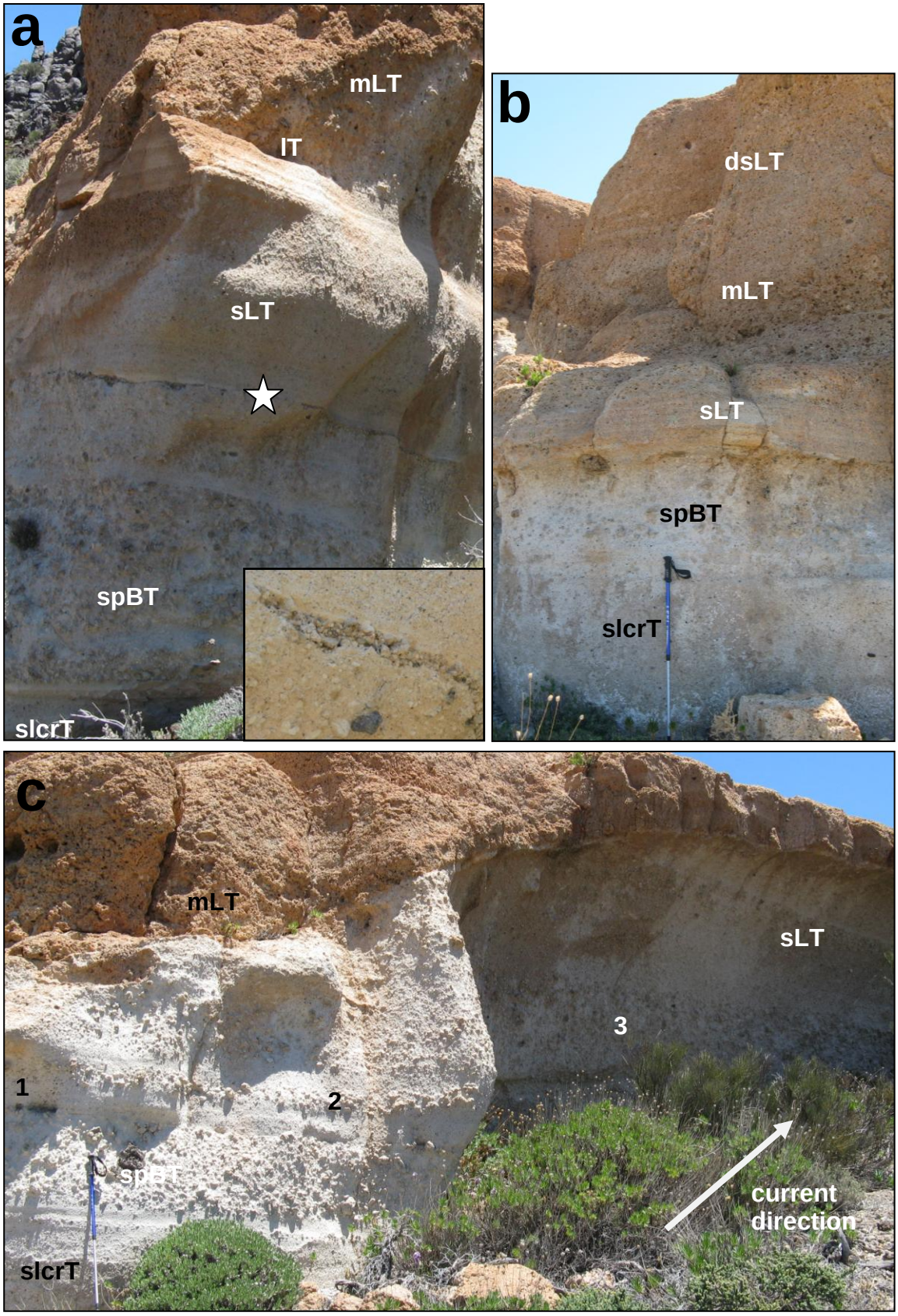

Figure 4.16 (a) At locality 17 stratified tuff occurs above spBT and is scoured into by lithic-rich tuff above. A 'mat' of reworked pumices separates spBT and sLT (star) and is shown in closeup. (b) and (c) The stratification above spBT is different at locality 10. In cross section (b), sLT, mLT and dsLT occur above spBT (with no lT layers). In a cut perpendicular to current direction (c) the gradational nature of the contact is seen. Points 1, 2 and 3 are at the same stratigraphic level. 1=sLT. 2= thin bed of spBT develops. 3= bed of spBT has thickened to ~1 m. Above, massive lapilli tuff becomes stratified into the outcrop.

Interpretation

The gradational contact between spBT and the stratified material above at locality 10 implies that there was no hiatus in current deposition in the central area of the wall at this time; changes in input from source and current unsteadiness created the observed succession of lithofacies. However, the layer of reworked pumices in the north records a temporary hiatus here, while the truncating contact at locality 5 indicates that currents were locally erosive. This non-uniformity across the DH exposure is also reflected in the variation from stratified to diffusely stratified to massive, indicating laterally changing depositional steadiness. The structure of the current(s) active across the DH wall at this time is unclear due to the effects of subsequent scour and a lack of connecting exposure. This group of lithofacies may reflect one large current, or the deposits of more than one current. Proximal lateral non-uniformity is discussed in Chapter 5.

4.2.9 Lithic-rich layers of tuff (lT)

Discrete layers of lithic-rich tuff (lT), ≤10 cm thick, occur throughout the proximal Poris stratigraphy and comprise poorly sorted, heterolithic clasts typically <8 cm in diameter. Lithologies include fine-grained lava or hypabyssal intrusive rock, syenite, scoria, pale green welded ignimbrite and green-black obsidian. Purple, red and brown altered clasts are common (Fig 4.17). The lithics are poorly sorted and are largest (≤15 cm in diameter) at localities 9 and 13. A single, unusually large lithic, >30 cm diameter, occurs at the same stratigraphic height as an lT layer at locality 4.

In the south, where outcrops are closely spaced, three lT layers can be correlated across 10 outcrops, whereas in the north fewer lT layers occur and larger zones of non-exposure make correlation difficult (see Figs. 4.2 to 4.4). At localities 3, 3a and 4, lithic-rich layers pinch out and reappear farther along the outcrop. Lithic layers are absent at locality 10.

The lowermost of the Poris lT layers traces a significant scour into underlying lithofacies (see Fig 4.1). At several exposures spBT is removed partly or completely; at locality 7, mLT above the scour is rich in pumice blocks as a result of

erosional incorporation (up-current) from below. Although the succeeding lithic layers within the upper Poris stratigraphy are planar across much of the wall, they are also locally associated with erosion; three lithic rich layers are seen in scour contact with each other at locality 8. The implications of this erosion are discussed in Chapter 5.

Load structures, ranging from 5 cm to 1 m in apparent width, are commonly associated with the lithic-rich layers. Multiple lithic-rich load structures occur and are truncated by planar horizons of tuff at locality 3a. Flame structures are rarer and two types occur: relatively lithic-poor mLT forms a flame structure next to a lithic-rich load at locality 3, whereas a striking lithic-rich flame structure stretches >3 m up from a planar lithic-rich layer into the overlying mLT at locality 17 (see Chapter 5 for further discussion of these features).

Interpretation

The lT layers indicate either an increase in lithic supply to currents at source, or a temporary increase in deposition of lithics due to changing current conditions, or both. The coincidence of lithic-rich layers with scours implies temporary waxing of the current; large and dense clasts are transported farther and finer material is eroded. Simultaneously, finer material that previously would have been deposited here overpasses this area to become deposited in more distal reaches. The 'pinching-out' of lithic-rich layers implies non-uniformity, with development of thalwegs along which the effects of temporary waxing were more pronounced. Lithic material within these thalwegs is deposited following the erosion (see Chapter 5). The recurring lithic layers may represent incremental dilation of faults within the edifice, leading to periodic input of wall rock into the erupted material (e.g. Kokelaar, 2007). Such subtle changes in lithic concentration may not be unambiguously preserved in distal zones due to substrate erosion during PDC transport.

Figure 4.17 (overleaf) Lithic-rich layers. (a) Two lT layers at locality 6a. (b) lT layer in erosive contact with sLT at locality 17. Lithics pinch out to the left. (c) Rare exposure of relatively fresh lT at locality 1. (d) Colour-coded lithology photomap of (c). Dark green = green and black obsidian. Pale green = pale green ignimbrite clasts similar in nature to the welded ignimbrite of the Guajara Formation. Pale pink = syenite, altered to a reddish colour in places. Grey = fine grained clasts likely to be lavas or hypabyssal intrusive rock. Dark purple = red and purple altered clasts, most of which are lava/hypabyssal rock. Brown = Yellowish-brown altered clasts. Black = scoria. White = pumice. Pen lid is 4 cm long.


a
b
c
d

4.2.10 Massive lapilli tuff (mLT)

Poorly sorted, matrix-supported, massive lapilli tuff (mLT) makes ≤9 m of the proximal Poris ignimbrite succession. Cream, sub-rounded to sub-angular pumice lapilli, typically ≤4 cm but sparsely ≤30 cm in diameter, occur with sub-angular to angular lithic clasts ≤3 cm in diameter in an ashy matrix containing sub-mm lithics and crystal fragments. Lithic clasts are similar lithologies to those present in lT. Banded pumices, which occur rarely throughout the lower Poris lithofacies, occur infrequently throughout the mLT (Fig 4.18). This lithofacies constitutes the upper part of the cliff outcrops and is thus consistently heavily altered with a recess-weathered, cemented orange surface. This alteration effect, which is variable, renders quantitative granulometric study impossible.

Massive tuff with elutriation pipes (mLTpip)

Pipe-shaped zones of fines-poor tuff occur within the mLT facies at localities 3 and 3a. The pipes are ≤4 cm wide, 5-50 cm long, occur in groups and locally contain clast-supported lapilli (Fig. 4.18 c and d). Where the outcrop presents a cross-section perpendicular to current direction, at locality 3a, the pipes are near-vertical. However, where pipes are exposed dissected roughly in the direction of flow at the north face of outcrop 3, they are vertical near the base and sheared towards 124° (ESE) towards the top.

Interpretation

At this stage of the eruption deposition was mainly relatively steady, with general absence of turbulence towards the lower flow boundary. Massive lapilli tuff records deposition from a well developed granular-fluid flow boundary zone, where supply equals or is greater than deposition and there is thus a strong tendency to deposit. Sustained high-mass-flux fountaining seems probable. Steady deposition was intermittently disturbed by current waxing, with the arrival of lithics and localised erosion and bypass, before waning to more uniform conditions.

Fine particles entrained by gas became elutriated upwards following their deposition, creating vertical pipes in the deposit that were sheared by an over-riding current. The shear orientation indicates at least the local flow direction at that time, towards

the southeast. These features only occur in certain areas, and are considered further in Chapter 5 below.

4.2.11 Stratified lapilli tuff (dsLT, sLT, (ds)LT)

Zones of stratification occur in the upper part of the succession at various points across the DH wall (Fig. 4.1). At some locations the stratification is diffuse, occurring as subtly finer layers of tuff that are most easily identified at weathered surfaces; these are laterally discontinuous and cannot be traced along an outcrop. At localities 1, 2, 11 and 14, between the first and second lithic-rich tuff layers within the mLT, the stratification is defined by sequences of inversely graded pumices that range from <1 mm in diameter to 2 cm. At locality 14 the second lT layer steeply truncates this stratification (Fig. 4.18 e and f).

Interpretation

The diffusely stratified tuff that occurs locally within mLT reflects temporary, non-uniform, unsteadiness in current conditions. The inverse grading of pumices at some localities represents current unsteadiness too, and may reflect pulsatory deposition (see Chapter 5). The truncation of stratified layers by the lithic-rich material without load- or shear-related deformation implies that stratified material was less fluidal than mLT on deposition, probably somewhat better sorted and conceivably aggraded more slowly.

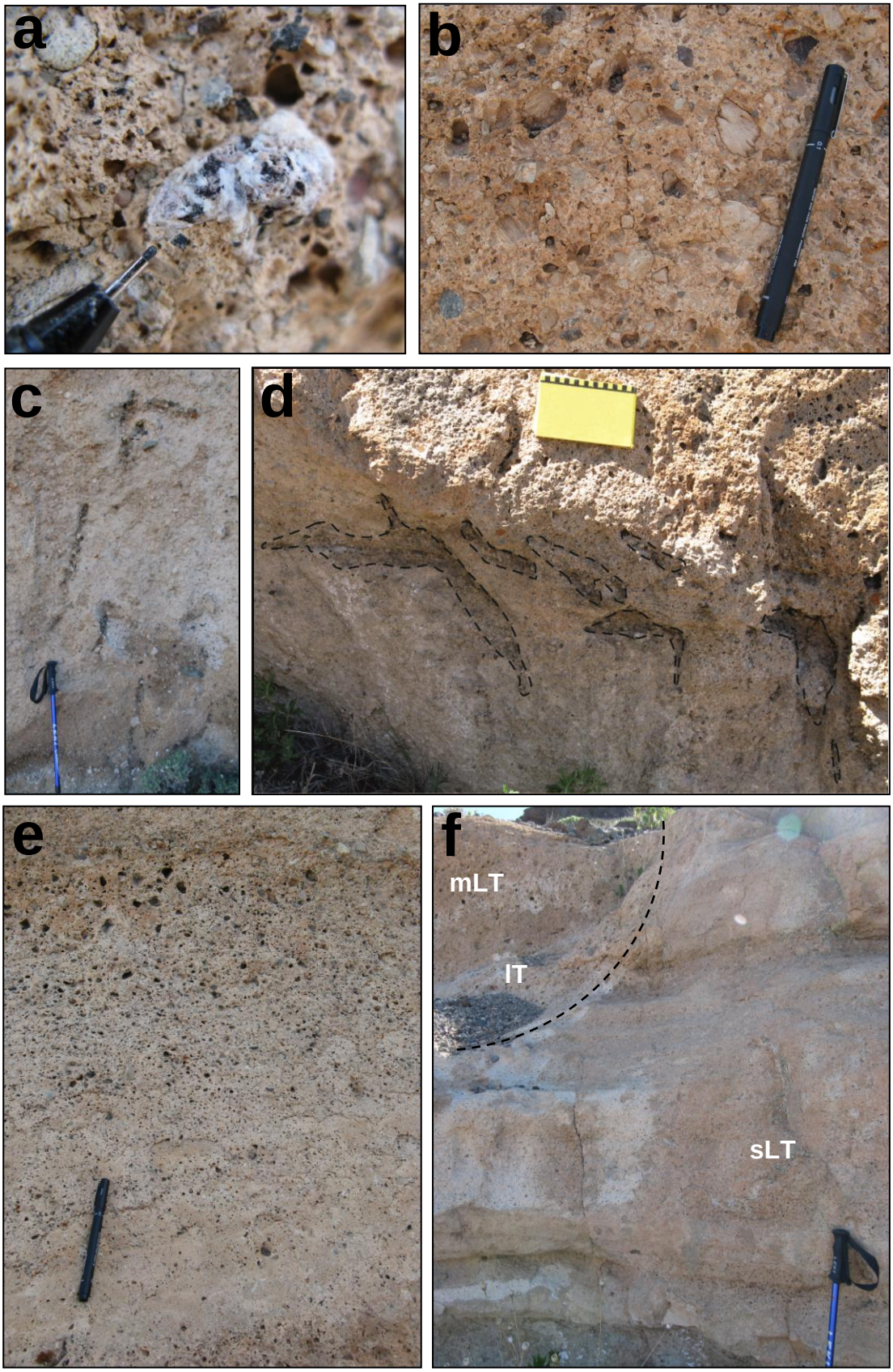

Figure 4.18 (a) Syenite clast in mLT. (b) Weathered, orange surface of mLT, typical of appearance at most outcrops. (c) Elutriation pipes at locality 3a (current direction into page). (d) Sheared elutriation pipes (marked out with dashed lines) at locality 3. (e) sLT in the form of inversely graded pumices at locality 1. (f) Lithic-rich layer truncates sLT at locality 14.

4.2.12 Breccia rich in black and banded pumice blocks (splBr)

The uppermost lithofacies of the succession is a matrix-supported, poorly sorted, subtly stratified breccia with a lithic-block layer at its base and lithic-poor, pumice-block-rich zones >1 m above this (see logs of Fig 4.4). Pumice clasts range from ~1 cm to ≤120 cm in diameter and mostly have sub-angular and contorted shapes. Cream, green and black pumices rich in white tabular feldspars occur alongside banded clasts that contain all three types. Lithics range from mm-scale to ≤50 cm in diameter, are sub-rounded to angular and comprise lithologies similar to those in the lower Poris lithofacies: fine grained lavas or hypabyssal rocks (some with spallation textures), highly vesicular scoria, altered pink, purple and brown clasts and green welded tuff (Fig. 4.19).

The breccia occurs in scree directly above the flat top surfaces of cliff outcrops and is best exposed in the northern part of the wall. The mLT-splBr contact is marked by an increase in pumice lapilli size, a subtle matrix colour change from cream to beige, and the occurrence of a lithic-block layer ≤60 cm thick. At localities 20, 18, and 10, where the top and bottom contacts of the breccia are exposed, the facies is respectively 9 m, 10 m and 8 m thick and is capped by a brown soil 38 cm thick and overlain by the Sabinita pumice deposit (see Fig. 4.1). Evidence of the continuation of the breccia across the southern part of the DH wall occurs above locality 8, where the upper contact of plBr is exposed in a gully ~5 m above the cliff outcrop. Black pumices occur commonly in scree above the main Poris outcrops.

A previously unreported Poris exposure occurs in a gully south of Montaña el Cerrillar, trending SE-NW. The splBr breccia here occurs in a cliff section >30 m wide on the north side of the gully, unconformably alongside a pyroclastic sequence of unknown age exposed at the gully mouth (the Plinian fall, yellow stratified tuff and grey unit annotated in Fig 4.20c).

In the gully, the base of splBr is covered by thick vegetation and the lower Poris lithofacies are not exposed. The distinct basal lithic boulder layer seen elsewhere along the DH wall is not present, possibly due to this poor exposure at the base. The breccia is stratified here; in the central part of the cliff a 1-m-thick lithic-rich zone

containing clasts ≤10 cm in diameter occurs at the base and is overlain by a pumice-rich zone where large pumice blocks >30 cm in diameter are locally concentrated (Fig 4.20e). The thickness of the breccia varies across the cliff; in the central part of the gully ~5 m of splBr is exposed, but this lessens to just 20 cm at the southeastern end, where the unit is overlain by a 5-m-thick bedded sedimentary sequence (Fig 4.20f). A black scoria unit dipping at 12/118 NW overlain by a blocky lava flow caps the deposits exposed in the gully.

Interpretation

This facies is interpreted to record the climax of the Poris eruption. The spallation features and evidence of alteration in the lithic blocks at the base of the unit indicate a deep, conduit origin, implying significant destruction of the walls of the active magmatic system. The lithic-rich currents generated during this climactic collapse are likely to have been widely erosive, creating a relatively planar upper surface to the mLT facies below. The energetic, lithic-rich currents produced during this phase may have largely bypassed the proximal zone towards the distal area, but evidence of this bypass is not found in the poorly preserved DH splBr exposures.

The high concentrations of black and banded pumices within splBr signify a change in the plumbing of eruption; a secondary magma batch became more extensively tapped as a result of the disturbance and collapse of the subterranean system and so more mafic clasts entered the PDCs. The increase in clast size may be a result of conduit destruction creating a wider vent thereby weakening the jet and lowering the explosivity of the eruption, or could be a result of the greater density of these clasts making them more robust and resistant to abrasion and breakage than the less-dense cream pumice types. As in spBT, there is no evidence of ballistic impact, but many of the larger clasts may have followed ballistic trajectories before entering PDCs.

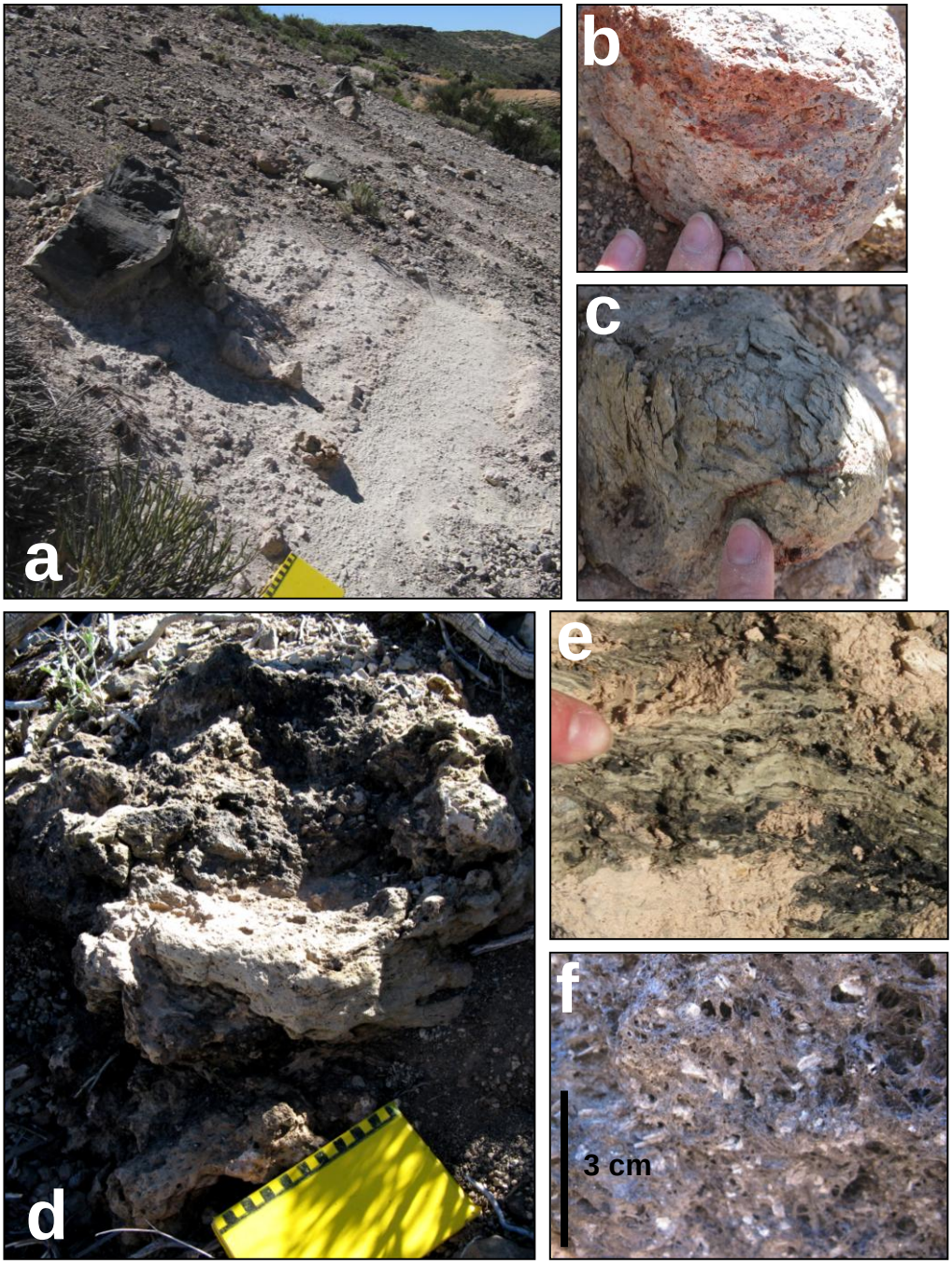

Figure 4.19 Stratified pumice-block breccia. (a) Change of grainsize at contact with mLT at locality 13. Note the position of flat surface of cliff outcrop in distance. (b) Pink altered lithic at base of the unit. (c) Spallation texture in lithic block. (d) Single in-situ banded pumice clast >70 cm in diameter poorly exposed in scree above locality 12. (e) Banded glass in pumice clast. (c) Black pumice with coarse tabular feldspars.

Figure 4.20 (overleaf) (a) Gully west of Montaña el Cerrillar contains the best exposure of splBr. (b) Gully exposure. Locations of photos (d),(e) and (f) are shown. (e) Sketch of key features. Note the unconformity beneath thick scree and vegetation. Units to the left of plBr are not Poris lithofacies; their age is unknown. (d) Black and banded pumice blocks >1 m occur in splBr. (e) splBr is subtly stratified; a bed rich in pumice blocks overlies a lithic-rich bed. (f) At the head of the gully splBr is overlain by 5-m-thick sedimentary sequence that does not occur in the main DH wall. The Sabinita pumice deposit does not occur here; a scoria fall deposit similar to that seen above the Sabinita in the DH wall caps the succession.

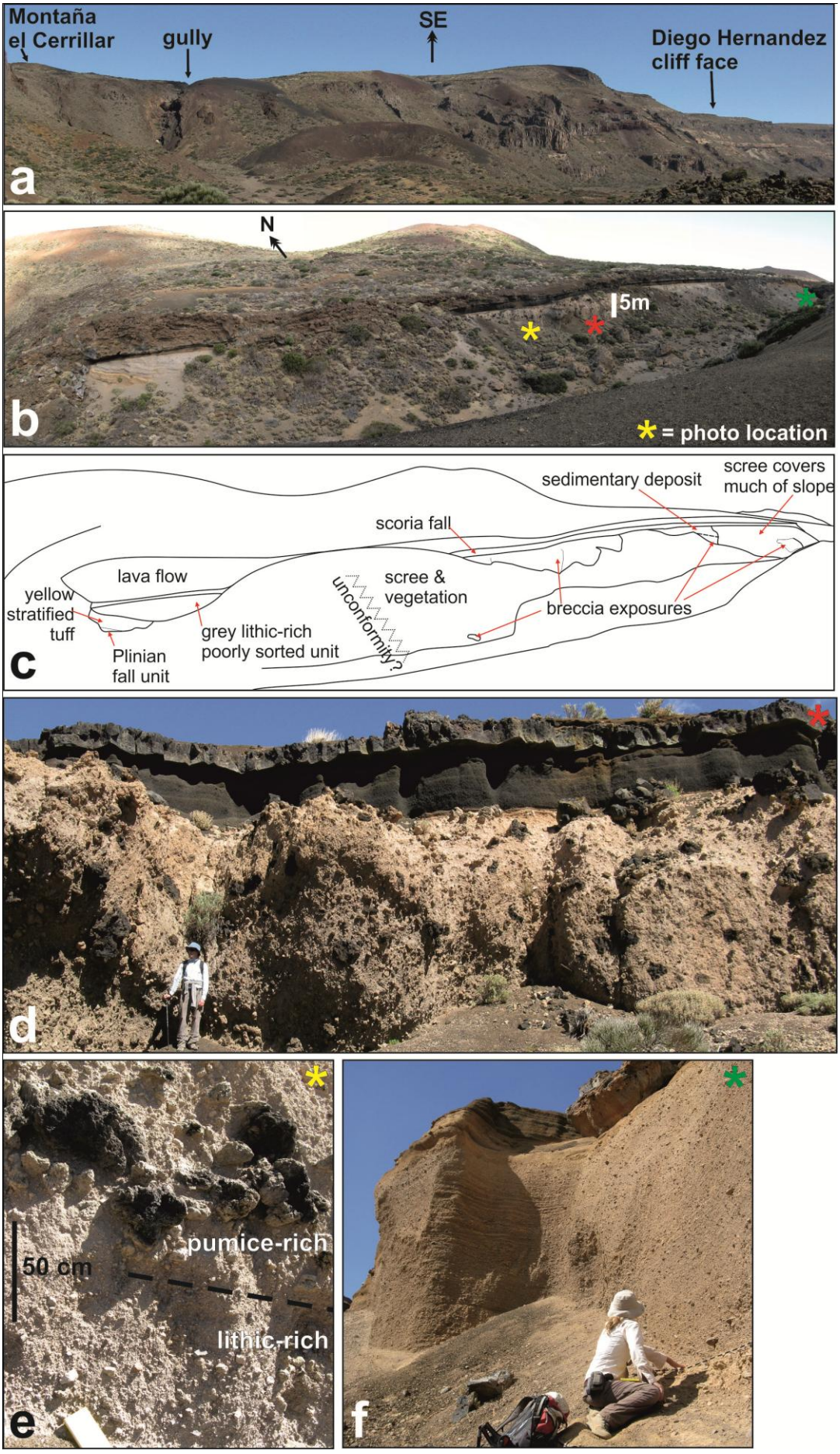
Montaña
el Cerrillar
gully
SE
Diego Hernandez
cliff face
a
N
5m
b
* = photo location
sedimentary deposit
scree covers
much of slope
scoria fall
lava flow
yellow
stratified
tuff
Plinian
fall unit
grey lithic-rich
poorly sorted unit
unconformity?
scree &
vegetation
breccia exposures
c
d
50 cm
pumice-rich
lithic-rich
e
f

4.3 Summary

The proximal Poris succession comprises 11 different lithofacies recording Plinian deposition, topographic interaction, phreatomagmatism, hybrid interaction, non-uniform ignimbrite sedimentation and climactic collapse.

In the following chapter, the architecture of these lithofacies is considered and a detailed interpretation of Poris proximal processes is presented.

Chapter Five

Architecture: proximal processes in time and space

5.1 Introduction

The term 'architecture' refers to the overall structure of an ignimbrite or ignimbrite succession, including the thickness, distribution, and arrangement of lithofacies in relation to coeval deposits, e.g. fallout tephras, substrate and topography (Branney and Kokelaar, 2002). Understanding the architecture of proximal lithofacies is crucial to understanding the near-vent dynamics and behaviour of pyroclastic density currents, and coeval fallout, in both time and space.

This chapter reports and discusses the architecture of the lower lithofacies (//bpL to slcrT), then the middle lithofacies (spBT to mLT) and finally the upper lithofacies (splBr) that record the Poris eruption; it is dependent upon the interpretations made in Chapter 4. These divisions reflect the early phases, main stage, and climax of the eruption respectively. No single outcrop in the Diego Hernandez wall exhibits the full Poris stratigraphic thickness (shown in Fig. 4.1). Across the wall vertical, lateral and radial changes in lithofacies characteristics and thickness occur and are indicators of unsteadiness, non-uniformity, scour, bypass, hiatus and the nature of palaeotopography. At some outcrops, the lower lithofacies are not exposed. Lithofacies changes are mapped in cross-section (Fig. 5.1). Before presenting the deposit architecture, substrate, bypass and hiatus recognition are discussed.

5.2 Substrate and pre-Poris landscape

When considered across the entire Diego Hernandez wall, the Poris stratigraphy is surprisingly consistent; lithofacies can be traced and correlated over 2 kilometres of exposure (see Figs 4.2-4.4). This level of consistency would not necessarily be expected proximally. The lack of welded lithofacies at the study site implies relatively low deposition temperatures; this may indicate that the DH deposits were not in very close proximity to their eruptive source, as compared, for example, with the prominently welded Guajara units, which must have been relatively close to their vent(s) (Joan Martí, pers. comm., 2010).

All of the Diego Hernandez pyroclastic deposits occur within a 'palaeovalley' of uncertain origin (discussed in Chapter 2), bounded by the Risco Verde escarpment to the south and somewhere amidst monogentic vents of the Cordillera Dorsal to the north. This valley had a shallow gradient and conceivably was part of an outer-flank setting; bedding structures within the Poris succession display a subtle dip of just ~2º ESE consistently across the DH wall, evidence that the underlying lavas formed a relatively flat topography prior to the eruption. Figure 5.2 is a schematic view of the possible setting of the Diego Hernandez study site at the time of the Poris eruption.

5.3 Bypass

The nature of deposition from pyroclastic density currents is essentially linked to large amounts of material bypass. Any point in an ignimbrite records deposition from the PDC flow-boundary zone at a certain place at a certain time (see Branney and Kokelaar 2002); material higher in the current does not deposit there and thus overpasses. In distal areas, there is evidence that a significant amount of Poris density current material bypassed the coastal zone and was deposited in the ocean (see Chapter 2; Brown and Branney, 2004a; Brown and Branney, 2004b). Although the record of this process is cryptic, it is clear that bypass has also been important in the proximal zone. A considerable part of the lithofacies record present elsewhere in the DH wall is missing at localities 9, 10, 11 and 14, indicating that significant bypass occurred here.

Figure 5.1 (overleaf fold-out and large A2 map in back pocket) Mapped lithofacies architecture of the proximal Poris succession. Boxes on the top photo correlate with the close-ups below. Due to perspective change, the scale differs slightly between boxes. Enlargements of key features are shown for log locations 11 and 16. The map of Las Cañadas shows location of the boxes. Areas of non-exposure are not enlarged. Field and digitised log locations are shown. Relationships between exposures are inferred where possible. (1= Brown et al., 2003; 2= Edgar et al., 2007).

Figure 5.1 (at end of digital document)

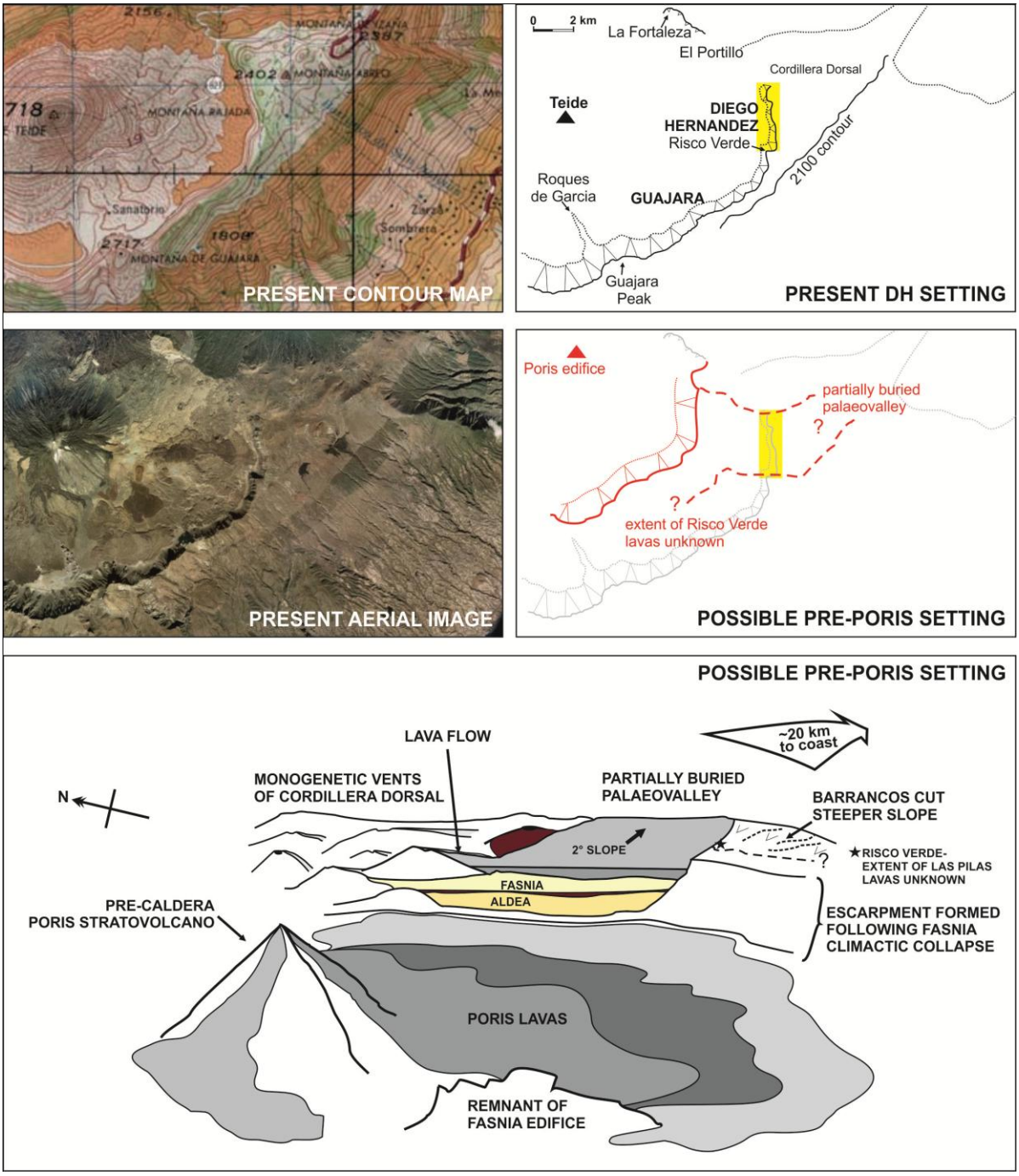

Figure 5.2 Possible pre-Poris setting for the DH location. The lack of welded ignimbrite in the DH deposits and flat substrate beneath the proximal Poris ignimbrite indicates that the DH wall was once part of a flank setting, set back from the vent by perhaps up to 10 km. The Fasnia climactic collapse would have created a topographic barrier that acted as an obstacle during the first part of the Poris eruption. The DH location was only exposed following further collapses (Poris, La Caleta, Abrigo) and degradation.

5.4 Hiatus recognition

Previously, abrupt changes in bedding, grading and pumice concentration have been used to distinguish deposits of discrete pyroclastic currents, or 'flow-units' (e.g. Sparks *et al.*, 1973). More recently it has been suggested that evidence for a hiatus in current activity is needed to delimit flow units, because bedding and grading changes could simply reflect current unsteadiness (Branney and Kokelaar, 2002). Plinian fallout layers, evidence of secondary reworking or soil within an ignimbrite sequence would provide robust evidence for a hiatus. Ash layers correlated across large distances within ignimbrite have been interpreted to indicate deposition of 'co-ignimbrite ash' after passage of a pyroclastic density current (e.g. Sparks and Walker, 1977; Sigurdsson and Carey, 1989; Pittari *et al.*, 2006) and these have been used to define flow units in the distal Poris succession (Brown and Branney, 2004b). It is important to distinguish between no current activity at all, i.e. a fundamental hiatus, and temporarily redirected current that would form a local hiatus. Evidence of hiatus in the proximal Poris record is typically laterally impersistent and ambiguous regarding cessation or redirection of current activity (Fig 5.3). The discrimination of flow units in the proximal environment is thus somewhat arbitrary; near to source, more than at medial or distal locations, a hiatus in one place may merely reflect momentary lateral redirection of a current owing to rapid changes at the vent or in local topography. Thus, in this study, depositional architecture is not discussed in terms of 'flow units' but rather in terms of episodes of deposition, non-deposition, and/or erosion in time and space.

5.4.1 Ash layers in the proximal Poris succession

The mTacc1 facies overlying //spLT is the only ash layer that is continuous across the entire Diego Hernandez Poris outcrop (Fig 5.3). This lithofacies association records the partial blocking of a density-stratified PDC in the near-vent zone (see Section 4.2.3), conceivably by a degraded caldera wall created during the Fasnia eruption. The upper part of the PDC surmounted the obstacle and became re-stratified; it did not have the competence to transport pumice and lithic lapilli, but was able to rework the Plinian substrate via tractional processes and deposit small pumice clasts (//spLT). The uppermost, dilute part of the system was ash-rich, and ash and accretionary pellets that formed in both the volcanic plume and the PDC

were deposited following the passage of the lower part of the stripped current. (Fig. 4.11).

It is known that ash aggregates can form quickly; AP1 aggregates were deposited within five minutes of the start of the 1990 eruption of Sakurajima volcano in Japan (Gilbert and Lane, 1994). In 1997, two Vulcanian explosions at Soufriere Hills volcano, Montserrat produced an ashfall with a peak accumulation rate of 0.5-1.2 x 10^{-3} kg m^{-2} s^{-1} (Bonadonna *et al.*, 2002b). The ash fallout was accompanied by the sedimentation of AP1 aggregates up to 4 mm in diameter, ~7 km from the vent, which began 15 minutes after the onset of the eruptions and lasted for 10-30 minutes. The deposition at this location was believed to be derived from a combination of both the vertical plume and the co-ignimbrite cloud (Brown *et al.*, in press), which is the same origin envisaged for the mTacc1 ash. It is difficult to estimate a timescale for the deposition of mTacc1, due to an unknown degree of coalescence, compaction, and subsequent scour, but it seems conceivable that the unit represents a hiatus in flow of tens of minutes, possibly hours (Jennie Gilbert, pers. comm., 2012).

A second mTacc layer (mTacc2), described in Section 4.2.6, separates slcrT from spBT at localities 16 and 17 in the north. This ash layer is not found elsewhere on the wall and at locality 2 the slcrT is clearly in direct contact with spBT with no sign of scour (Fig. 5.4). Another discontinuous stratified ash layer, <5 cm thick, occurs at locality 1 in the south, immediately overlain by the second lT layer. Rounded accretionary pellets <5 mm in diameter are distinguishable in the heavily weathered bed (Fig. 5.4). The overlying lithic-rich layer can be traced across nine adjacent outcrops, but the ash layer does not continue.

It is possible that each of these impersistent ash layers represents a widespread hiatus in PDC activity, allowing ash and ash agglomerates to be deposited from a co-ignimbrite cloud or from the margins of the Plinian plume. The ash layers were then mostly eroded by subsequent currents. The laterally continuous lT layer on top of the ash layer at locality 1 would be consistent with an episode of scour in the DH wall. Alternatively, these ash beds may record temporary local hiatus due to thalweg migration or momentary waning conditions. At locality 2 slcrT beds coarsen upwards and grade into spBT beds, which is clear evidence of sustained deposition at

this location. The discontinuous ash layers are found at the northern and southern margins of the Diego Hernandez palaeovalley, and this may be a sign that a single density current migrated slightly north and south during the eruption. Such local hiatuses would have allowed ash and ash agglomerations falling out from the Plinian column in the proximal region to become registered in the deposit, forming a discontinuous layer. The lack of exposure in the central area makes confident interpretation of such discontinuous layers difficult.

In the lowermost mTacc1 layer accretionary pellets are well developed, have multiple rims (AP2 in Brown *et al.*, in press), are up to 2 cm in diameter and show evidence of deformation. The accretionary pellets in mTacc2 are smaller, consist of fewer concentric rims and are less brittle. The ash agglomerates in the third ash bed are far smaller and less well defined. This variation suggests that ash aggregation became less efficient as the eruption progressed. The significance of ash aggregates in the Poris eruption is considered further in Chapter 7.

Figure 5.3 (overleaf) Hiatus recognition in the proximal Poris succession. Features that traditionally may have been used to delineate flow units are here found mostly to reflect changing conditions at the depositional flow-boundary zone during ignimbrite sedimentation. Ash layers may reflect temporary hiatuses in deposition from currents.

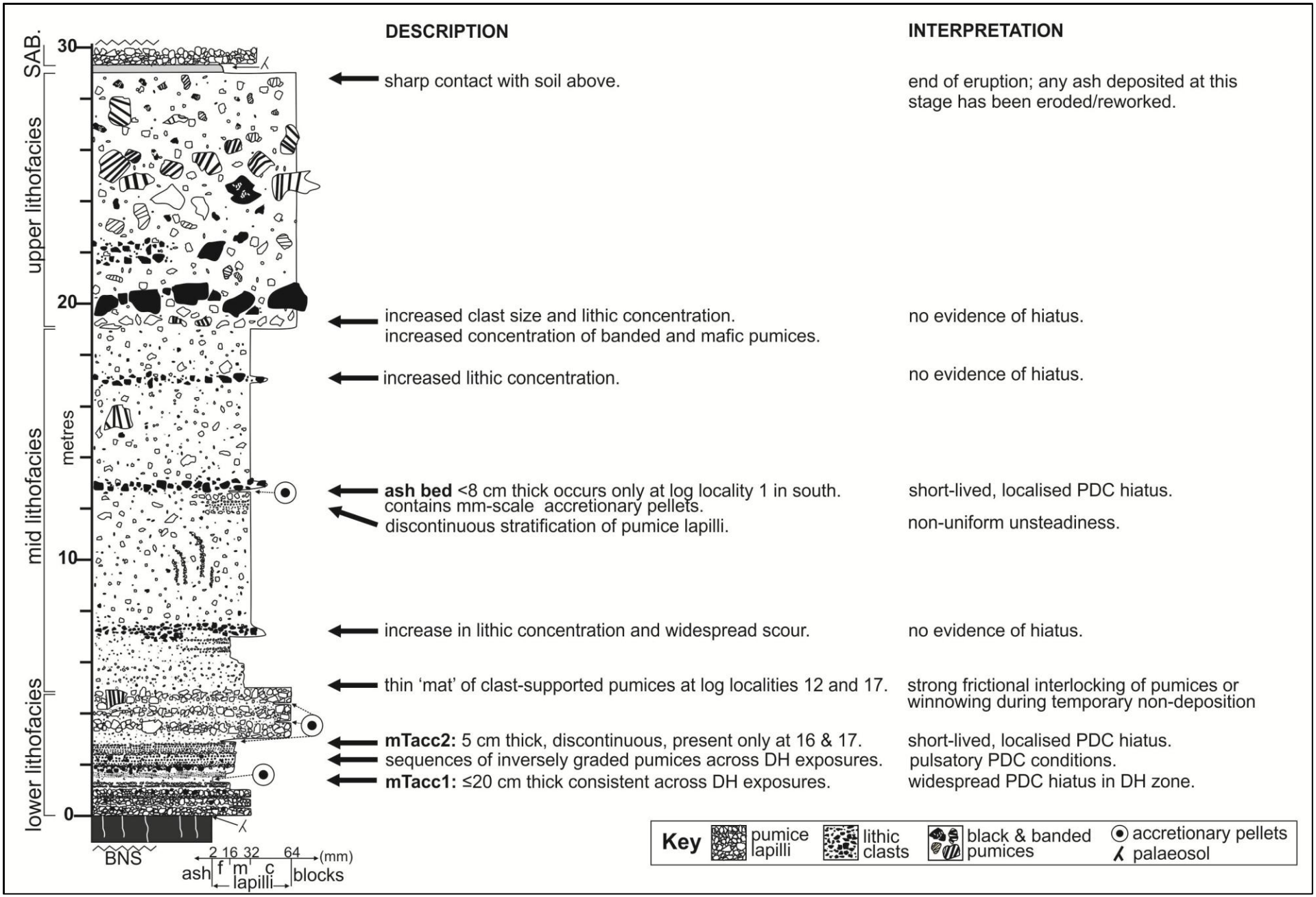
SAB.
upper lithofacies
mid lithofacies
lower lithofacies
30
20
10
0
metres
BNS
2 16 32 64 (mm)
ash f m c blocks
lapilli
DESCRIPTION
INTERPRETATION
sharp contact with soil above.
end of eruption; any ash deposited at this stage has been eroded/reworked.
increased clast size and lithic concentration.
increased concentration of banded and mafic pumices.
no evidence of hiatus.
increased lithic concentration.
no evidence of hiatus.
ash bed <8 cm thick occurs only at log locality 1 in south.
contains mm-scale accretionary pellets.
discontinuous stratification of pumice lapilli.
short-lived, localised PDC hiatus.
non-uniform unsteadiness.
increase in lithic concentration and widespread scour.
no evidence of hiatus.
thin 'mat' of clast-supported pumices at log localities 12 and 17.
strong frictional interlocking of pumices or winnowing during temporary non-deposition
mTacc2: 5 cm thick, discontinuous, present only at 16 & 17.
sequences of inversely graded pumices across DH exposures.
mTacc1: ≤20 cm thick consistent across DH exposures.
short-lived, localised PDC hiatus.
pulsatory PDC conditions.
widespread PDC hiatus in DH zone.
Key
pumice lapilli
lithic clasts
black & banded pumices
accretionary pellets
palaeosol

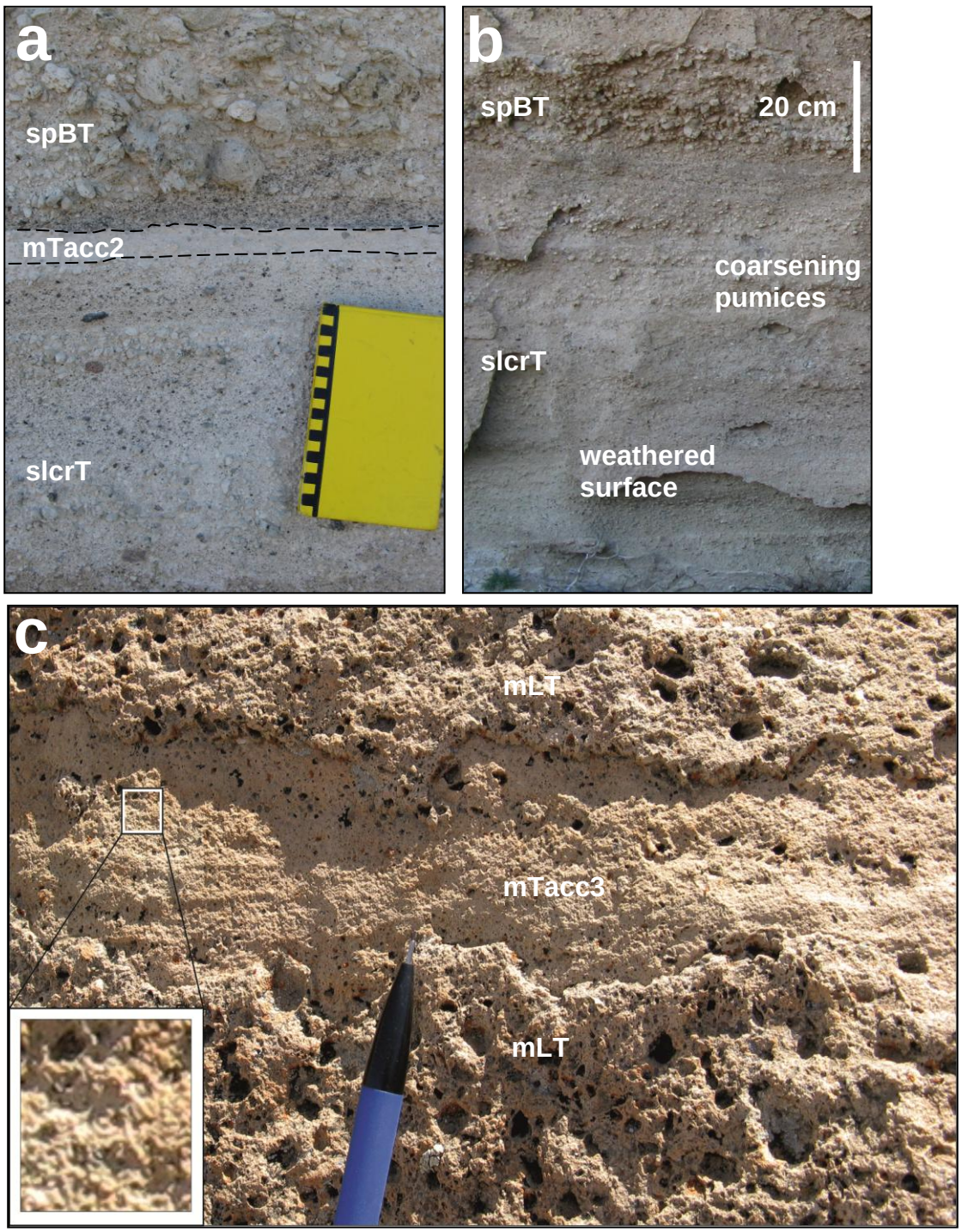

Figure 5.4 Discontinuous ash layers in the DH wall. (a) mTacc2 at locality 17 in the north (outlined). (b) There is no sign of mTacc2 between slcrT and spBT in the south at locality 2. (c) Laterally discontinuous ash bed at locality 1. The ash contains little or no pumice lapilli, which form recess-weathered holes in the surrounding mLT. The ash bed contains diffuse stratification to the left of the image and rounded mm-scale ash agglomerations (zoomed box).

5.4.2 Graded bedding

In the 'standard ignimbrite flow unit' model (Sparks *et al.*, 1973; Sparks, 1976) a relatively well sorted 'surge deposit' (layer 1) is overlain by a basal fine-grained, inversely graded division (2a) succeeded by a poorly sorted massive division with inverse coarse-tail graded pumices and normal coarse-tail graded lithics (2b), and an upper ash layer (3). The proximal Poris deposits do not fit this model. Most stratified tuff across the DH wall occurs as matrix-supported beds of inversely graded pumices that pass laterally into mLT in adjacent exposures. The most distinctive example of graded bedding occurs in slcrT, where stacked beds of tuff display coarse-tail grading of pumices. There is no ash or evidence of hiatus between beds. This stacking of graded beds is interpreted to record pulsatory flow that waxed and waned in competence rather than recording numerous flow units (discussed further below).

5.4.3 Pumice 'mats'

Clast supported, thin 'mats' of pumice <30 cm across occur at log localities 12 and 17 (see Fig 4.14). These rare features are discontinuous and may reflect winnowing of fines and reworking during temporary periods of non-deposition from currents. Another possibility is that brief episodes of strong frictional interlocking between pumices during deposition created pumiceous concentrations that 'locked up' and deposited; a process similar to the way in which pumiceous levèes form.

5.5 Lower lithofacies architecture (//bpL to spBT)

5.5.1 Plinian deposition

The Poris eruption began with deposition from a Plinian plume, a process that typically results in the mantling of topography with a consistent thickness of pumice lapilli. However, significant thickness variations occur in northern exposures of proximal Poris Plinian material. The undulose and gradational contact between pL and //spLT at log locality 11 is evidence that erosion and reworking by subsequent currents modified the Plinian layer. Although subsequent density current activity prevented fallout from being clearly recorded, there is no reason to suppose that Plinian deposition halted completely at any stage of the eruption.

5.5.2 Topographic interaction

The //spLT and mTacc facies record the passage of a dilute PDC with tractional processes at the flow-boundary zone, followed by the deposition of agglomerated ash. These are interpreted to reflect the presence of a large density stratified current in the proximal zone. This current became topographically constrained closer to the source, so that only the uppermost parts travelled across the DH area. The thickness of the two units varies and the pumice layers in //spLT cannot be correlated with confidence from one exposure to another (see Fig. 4.7); this variation reflects non-uniformity in the degree of substrate reworking, changing supply of material to the depositional flow boundary zone, and erosion to a variable depth by the subsequent current.

5.5.3 Phreatomagmatism and pulsatory flow

The increase of lithic and crystal material in the succession at this stage, up to 40% in slcrT compared to just 5% in mTacc, records an increase in lithic input at source due to phreatomagmatic explosivity. The occurrence of coarse-grained lithics that are altered syenite suggests that phreatomagmatism involved magmatic interaction with the hydrothermal system at depth, rather than interaction with water-saturated material in the vent region.

Either as a result of continued topographic blocking or initially fully dilute conditions, the first register of phreatomagmatism in the DH area is a crystal-rich cross stratified tuff (xscrT) deposited by a low-concentration density current. Subsequently, waxing conditions and concentrated flow are recorded at the DH location. The stratified lithic- and crystal-rich facies (slcrT) is associated with the erosion of the underlying divisions; the mTacc1 layer is absent at some localities where lithic-rich material fills scour surfaces (see Fig 5.5). The scour contact into the ash unit is commonly very sharp, indicating that the ash was not loose but had become fairly cohesive prior to the erosion. Following current waxing and erosion, the slcrT facies was deposited as the current waned slightly and/or became overloaded at source and therefore reduced in capacity. The relationship between current waning and lithic deposition is considered below in Section 5.6.2.

Beds of tuff with coarse-tail inverse grading of pumices, which vary in number and thickness across the wall, record pulsatory unsteadiness during the deposition of slcrT. At locality 17 graded beds in slcrT are capped by an ash layer (mTacc2), evidence that, locally, flow stopped completely. The graded beds may therefore reflect pulsatory conditions during waning flow. Evidence of this is seen higher up in the succession, and is discussed in Section 5.6.

Spontaneously developed roll waves, which are shock-like disturbances that travel faster than the material in the flow (Balmforth and Mandre, 2004 and references therein), have been observed in debris-flow flume experiments (e.g. Johnson *et al*. in press) and are inferred to form stratification bands and also regularly stacked and thin pumiceous layers in some ignimbrites (e.g. Mount St. Helens July 22nd and August 7th 1980 deposits; Pete Kokelaar, pers. comm., 2011). Roll waves are not well understood in PDCs, but their pulsatory passage could well be a contributing factor in the development of regularly repetitious graded layers in ignimbrites.

5.5.4 Hybrid deposition

Following the phreatomagmatic episode, a localised temporary hiatus in ignimbrite sedimentation is recorded by a discontinuous ash layer at locality 17 (see Section 4.3.2 above). The overlying hybrid spBT facies records the resumption of magmatic activity, addition of coarser pumice clasts to the Plinian plume, and an increased input of Plinian and ballistic material into density currents. The thickness, bedding and internal stratification of this lithofacies vary across the DH wall.

The bedding changes within spBT indicate unsteadiness in the flow boundary zone during deposition, although the exact nature of this unsteadiness is unclear; pumice blocks and lapilli were periodically prevented from reaching the deposit surface,

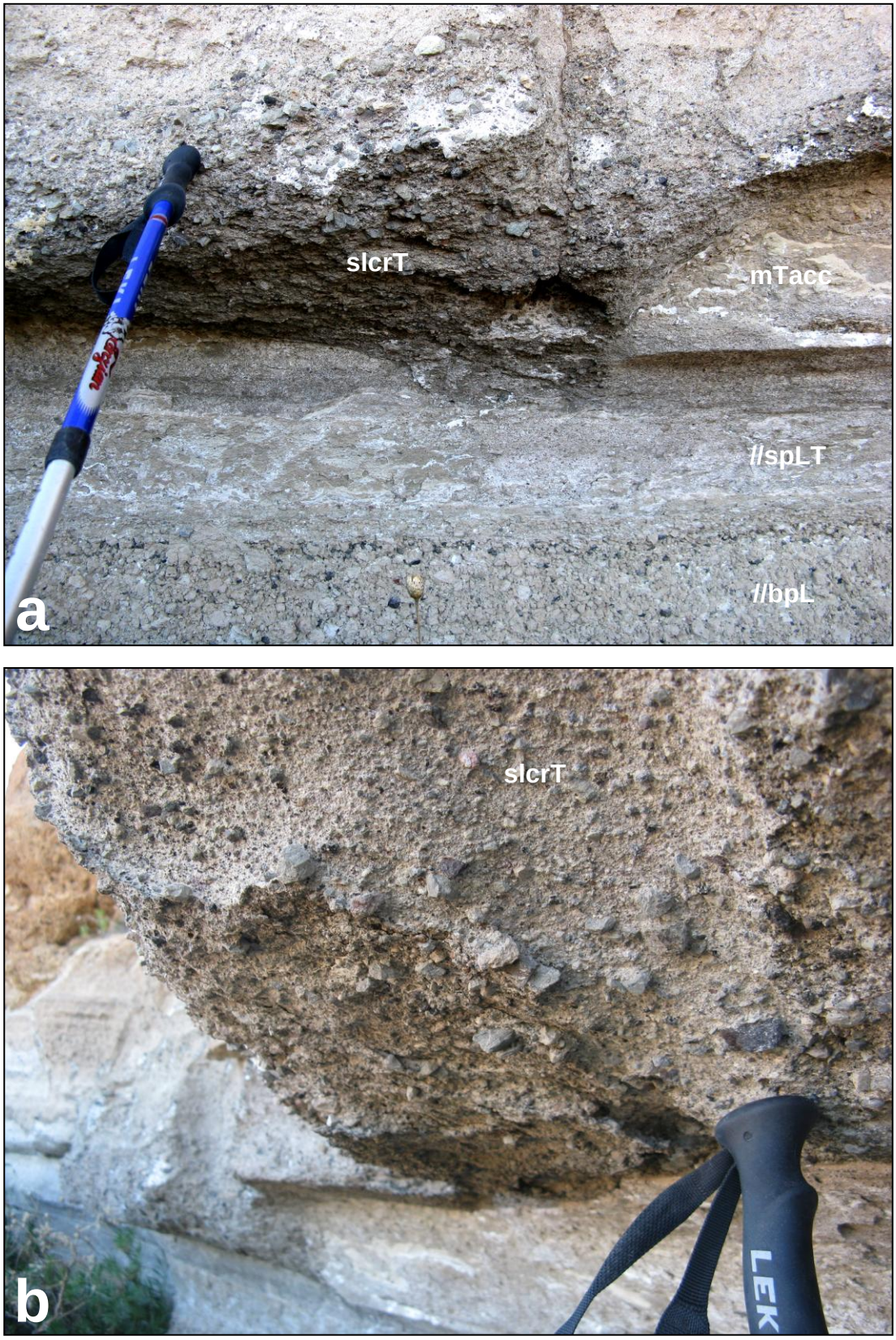

Figure 5.5 (a) slcrT in erosive contact with mTacc at locality 16. mTacc is removed completely as a result of scouring here. (b) A close-up of the lithic-rich nature of the base of slcrT. Walking stick handle is 10 cm.

allowing the deposition of dominantly fine-grained layers of variable thickness. It is difficult to imagine a mechanism whereby changes at source caused this variation. The varying nature of the pumiceous beds, from clast-supported to matrix-supported, indicates variable segregation in the depositional flow boundary zone, possibly with variable elutriation of fines in the supply of material down towards the lower flow boundary.

Beds became subtly cross-stratified at low angles as a result of migrating bedforms at the depositional flow boundary zone. The clarity of cross-stratification is non-uniform across the DH wall. Pumice blocks up to 40 cm in diameter, derived from ballistic fallout into the current(s), are sporadically present across the exposure of spBT and do not appear to be concentrated in any one area.

The hybrid lithofacies is exposed in a vent-radial section at locality 10, providing a small-scale 3D view of architectural changes. Stratified lapilli tuff grades into coarse spBT beds radially and the spBT unit therefore thickens into the cliff. This could be a local disturbance; the lack of substantial medial Poris exposure makes meaningful interpretation impossible.

5.5.5 Small-scale faulting

At the centre of the locality 2 exposure a segment of lithofacies is downfaulted, by 67 cm on the southern side and 62 cm on the northern side. The apparent dips of the faults on either side of the downthrown section are 42º on the southern side and 62º on the northern side (Fig. 5.6). The bedding in slcrT and spBT at the base of the outcrop clearly marks the faults, but the trace is less distinct in the mLT and lT facies above. The area affected by the faulting is <5 m wide and there is no sign that the faults continue into the lavas exposed in the cliffs below the outcrop. The fault traces indicate that material was well-cemented at the time of the deformation. There is no evidence of faults at other exposures in the proximal succession; if they existed hidden beneath scree, they could only be of limited offset because exposed beds show no large displacement. The small faults may have formed during structural disturbances associated with Caleta or Abrigo caldera collapses, or may record a minor event not related to a large eruption.

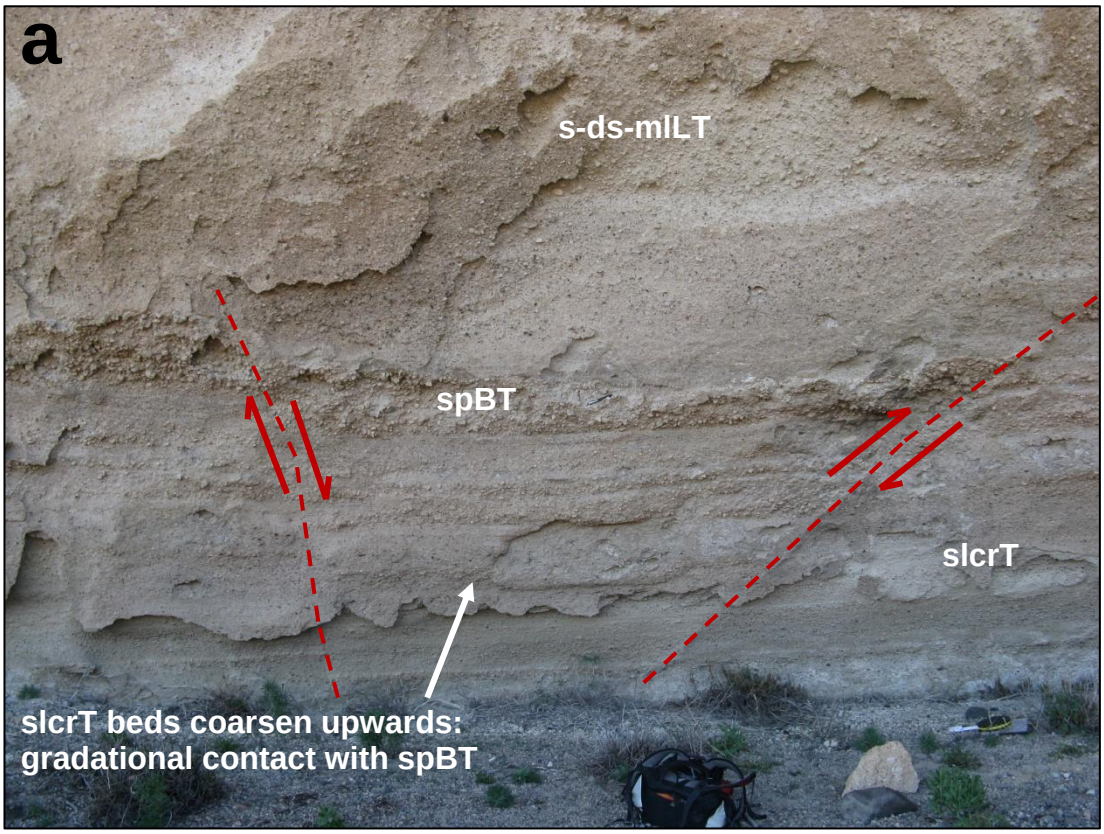

Figure 5.6 Downfaulted segment of outcrop at locality 2. (a) Bed displacement clearly seen in lower lithofacies. Note the gradational contact between slcrT and spBT at this location. (b) The (southern) fault trace is sharply defined, implying that the faulting occurred after lithification.

5.6 Mid lithofacies architecture (sLT, dsLT, mLT, lT)

5.6.1 Discontinuous stratification and the number of coeval currents

Following the cessation of phreatomagmatism and coarse pumice input, density currents began to deposit less well stratified, poorly sorted, matrix-supported ignimbrite. Laterally discontinuous stratification in the form of grainsize changes and graded beds occurs within ignimbrite at a number of exposures, passing laterally into mLT in adjacent outcrops. Two depositional possibilities could account for this variability. It could reflect lateral non-uniformity of the flow-boundary zone of a single, large current. Subtle changes in substrate and topography can locally dampen turbulence at the base of a PDC, affecting the thickness of the granular-fluid flow boundary zone and thus controlling the structure of the deposited material (Branney and Kokelaar, 2002) (Fig. 5.7). In the same way, the subtle zones of diffusely stratified tuff that occur throughout the mLT lithofacies reflect transient unsteadiness at the base of the current.

An alternative possibility would be that numerous relatively uniform currents were simultaneously depositing in the DH area, creating different zones of stratified and massive tuff. However, there is no evidence for multiple contemporaneous currents, such as might be distinguished by laterally equivalent deposits with contrasting lithics or pumices, mixed in places, and there is no need to invoke them. Stratified tuff occurs at the same levels in the stratigraphy in both northern and southern outcrops and non-uniformity of a single current flow boundary zone is the simplest interpretation, consistent with the wall-wide variations above and below. Above spBT, discontinuous stratification occurs beneath the first lithic-rich tuff layer (s-ds-mlLT) and also beneath the second lithic-rich tuff layer (prominent at log localities 1 and 14) (see Section 4.2.11). This correlation of the material based upon the position of the lithic-rich layers supports the inference of deposition from a single large current.

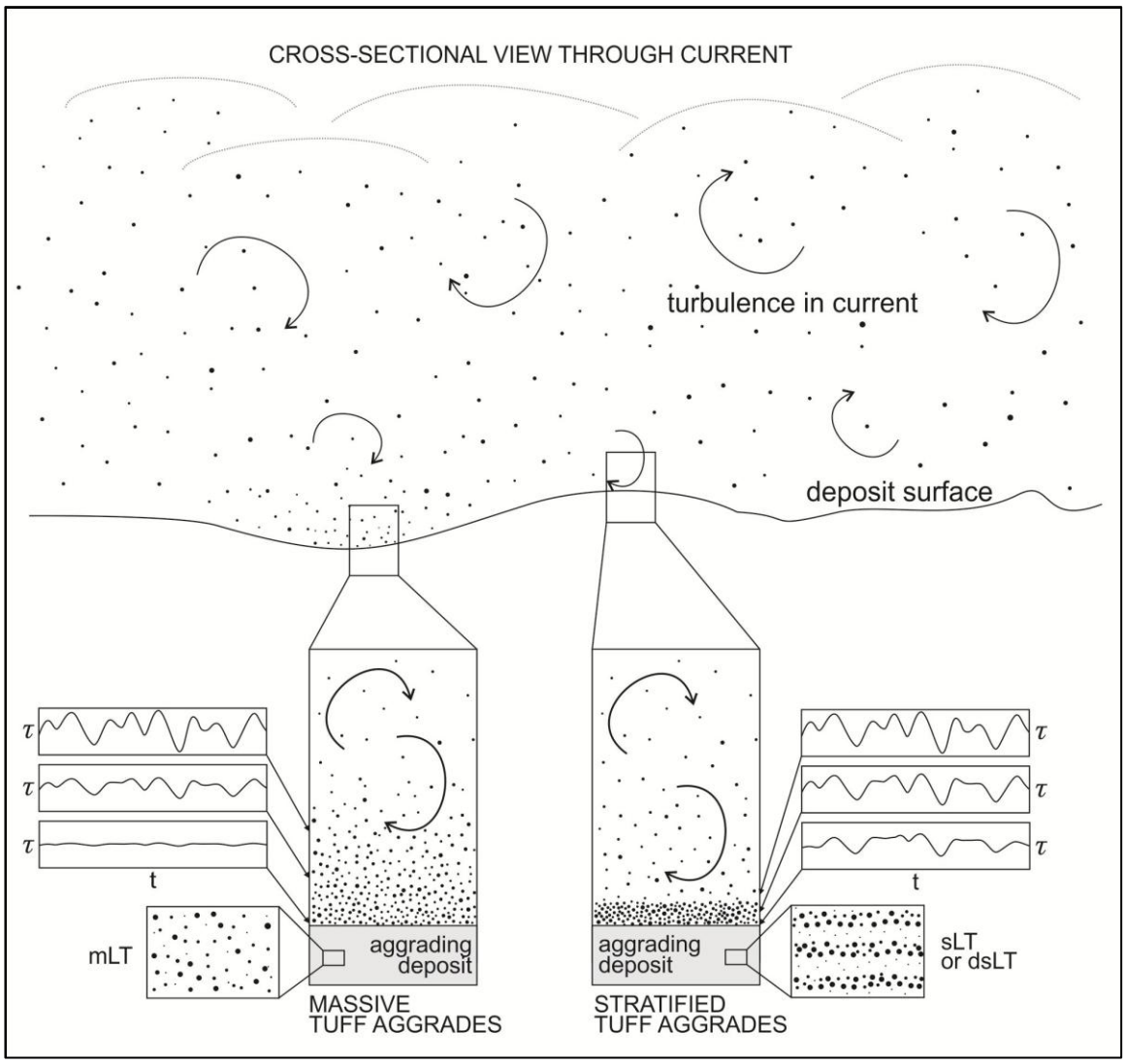

Figure 5.7 Subtle changes in substrate and topography can locally dampen turbulence at the base of a current, affecting the thickness of the granular-fluid based flow boundary zone and thus controlling the structure of the deposited material. (Adapted from Branney and Kokelaar, 2002). Graphs of τ/t show how shear stress fluctuates through time at different heights within the FBZ in each scenario.

5.6.2 Lithic-rich layers

Evidence of scour

Large- and small-scale features of scour and erosion are common across proximal Poris exposures and are typically associated with increases in the abundance of lithic clasts (lT layers) and/or grainsize (splBr). The reworking of //bpL pumices at the base of the succession is the exception to this rule of association and is an indication that the loosely compacted Plinian substrate was susceptible to erosion by even dilute parts of density-stratified pyroclastic currents.

The most widespread scour feature in the proximal Poris succession is that associated with the first lithic-rich tuff layer, which is in erosional unconformable contact with subjacent lithofacies at many exposures (see Fig 5.1). Other erosional features are related to slcrT, which occupies scours into mTacc1 (described above), and the second lithic-rich tuff layer, which marks striking local scour features at localities 6 and 14 (Fig. 5.8). In the northern part of the wall, which is due east of the present El Teide stratovolcano, scour structures associated with slcrT and lT(2) record current-directional azimuths of 071° and 080° respectively. Poris bedding in the DH wall typically dips at only ~2º in a radial (downstream) direction, but scour surfaces can dip at substantially greater angles, such as at locality 12 where a lT layer cuts sLT at 20º in the downstream direction (091º E).

Evidence of bypass is typically cryptic throughout the succession, but it is represented in the lithic-rich layers that 'pinch' in and out of mLT across an exposure (see Fig. 4.15b). This feature can be a result of erosion by subsequent currents (as appears to be the case at locality 6), or, where it occurs with no sign of succeeding scour (locality 3a, see Fig 5.12) could be evidence of non-uniform bypass and loading-related lithic capture.

Episodes of current waxing and increased lithic input occurred during the deposition of mLT. It is inferred that such episodes resulted from volcanotectonic fault dilation within the edifice with incremental internal collapse, leading to increased eruptive mass flux (Kokelaar, 2007). Consequent current waxing would then have led to erosion and scour into just-deposited material, while lithic-rich material bypassed.

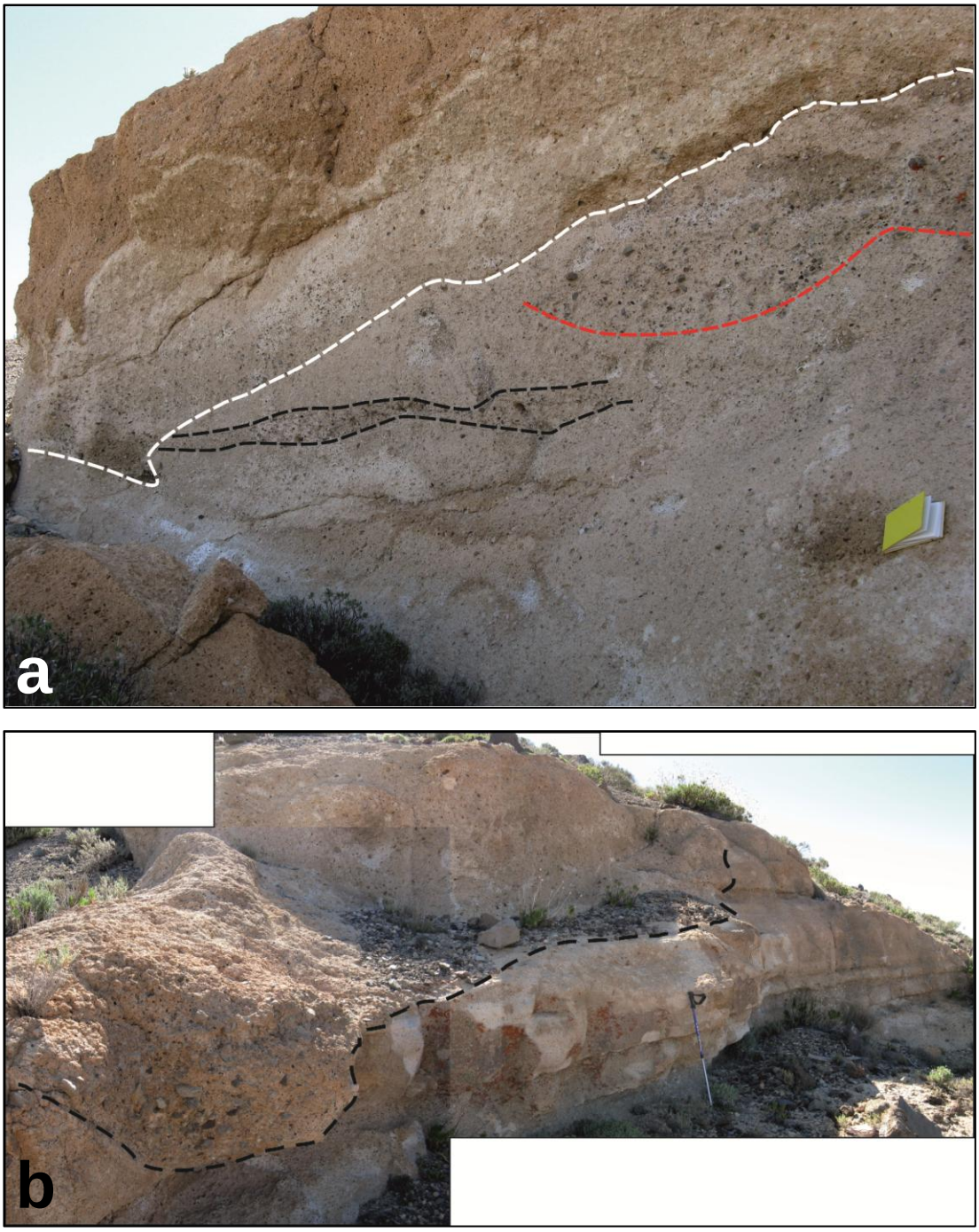

Figure 5.8 Scour features associated with lithic-rich layers of tuff. (a) At locality 6, at least 3 zones of lithics are in erosional contact with each other, at the stratigraphic position of the second and third lithic-rich layers of tuff. (b) At locality 14, the second lithic-rich tuff layer truncates a zone of stratified beds of graded tuff.

This would have persisted until the current waned and some of the breccia was deposited, filling the scours and forming a more extensive layer. As the current waned further the lithic supply dwindled, possibly reflecting decreasing input at source, and relatively steady sedimentation recommenced with mLT deposition (Fig. 5.9a).

At localities 1 and 14, the second lithic-rich layer overlies tuff displaying grading stratification. As discussed above for the slcrT lithofacies, it may be that graded beds form as the current undergoes unsteady waning, possibly as a result of the passage of roll waves. At locality 1, an ash layer occurs between graded beds and the lithic-rich layer. This appears to be evidence that, locally, flow stopped temporarily after the deposition of graded beds. It is suggested here that the occurrence of lithic-rich layers records a new pulse of material and an increase in current energy following pulsatory waning (Fig 5.9b). This is different from the traditional idea that graded stratified beds occurs at the base of a massive division (e.g. layer 2a of Sparks, 1976).

Imbrication

Imbrication of clasts is typically unclear in Poris deposits, mostly a result of transverse exposures and case-hardened surfaces. However at one radial-to-vent exposure at locality 16 subtle imbrication of lithic clasts can be discerned in the first lithic-rich tuff layer, giving an indication of current direction. Lithics are imbricated at <45º (dipping upstream) on a surface striking 088º E (Fig. 5.10).

Stratified lithic-rich tuff

At locality 3, the second lithic-rich tuff layer is stratified; strata dip at an angle of 32º upstream (122º SE), and individual clasts are not imbricated. (Fig 5.11). The Poris lT layers are typically planar with only very subtle diffuse stratification, and this unusual exposure may record locally non-uniform, chaotic deposition, possibly with changing current thalweg.

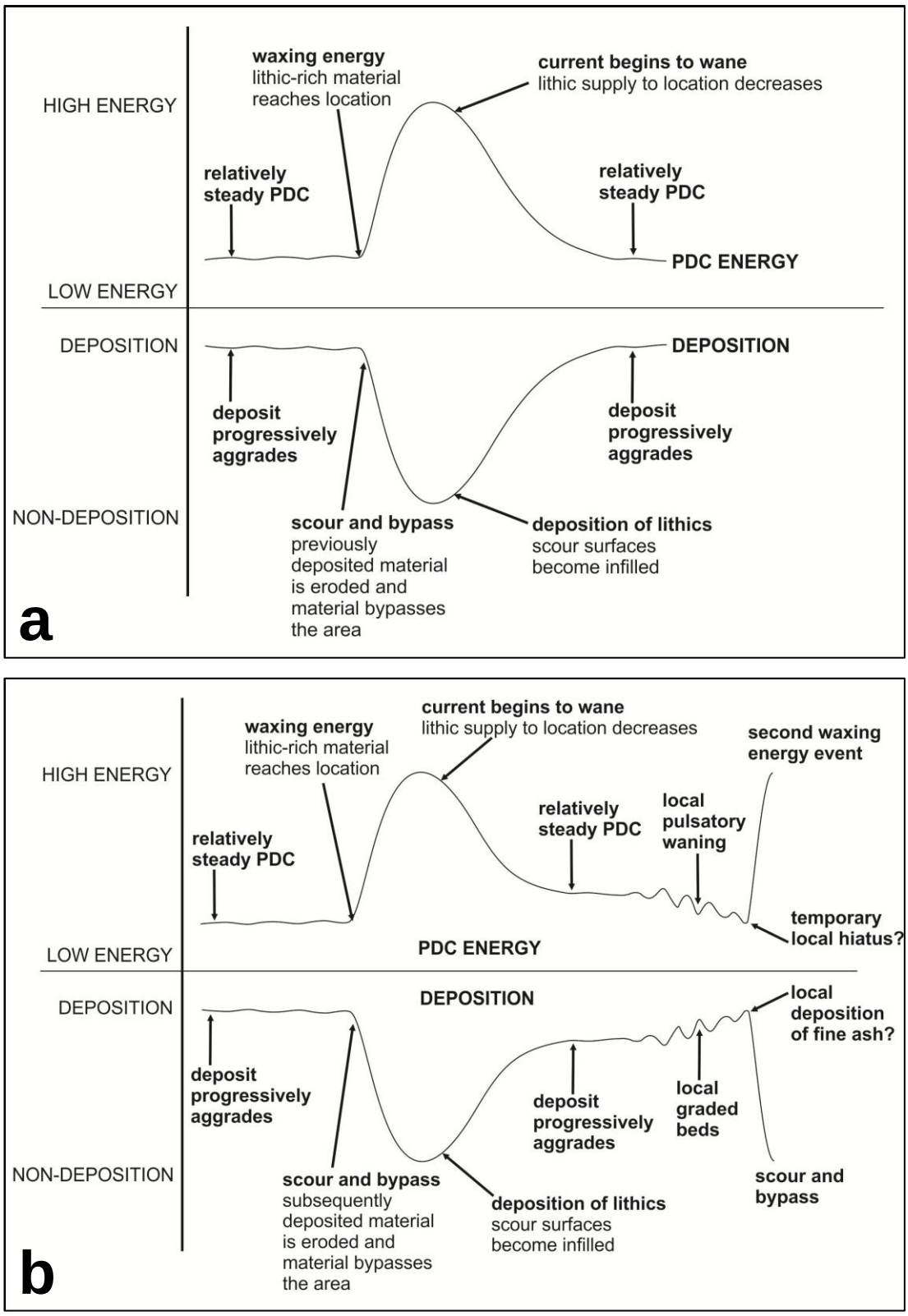

Figure 5.9 (a) PDC energy vs. deposition schematic diagram to illustrate the processes occurring during the deposition of the lT layers. (b) Modified diagram to illustrate the possibility that the graded stratification seen in slcrT and beneath the second lithic rich tuff layer occurs as currents wane unsteadily.

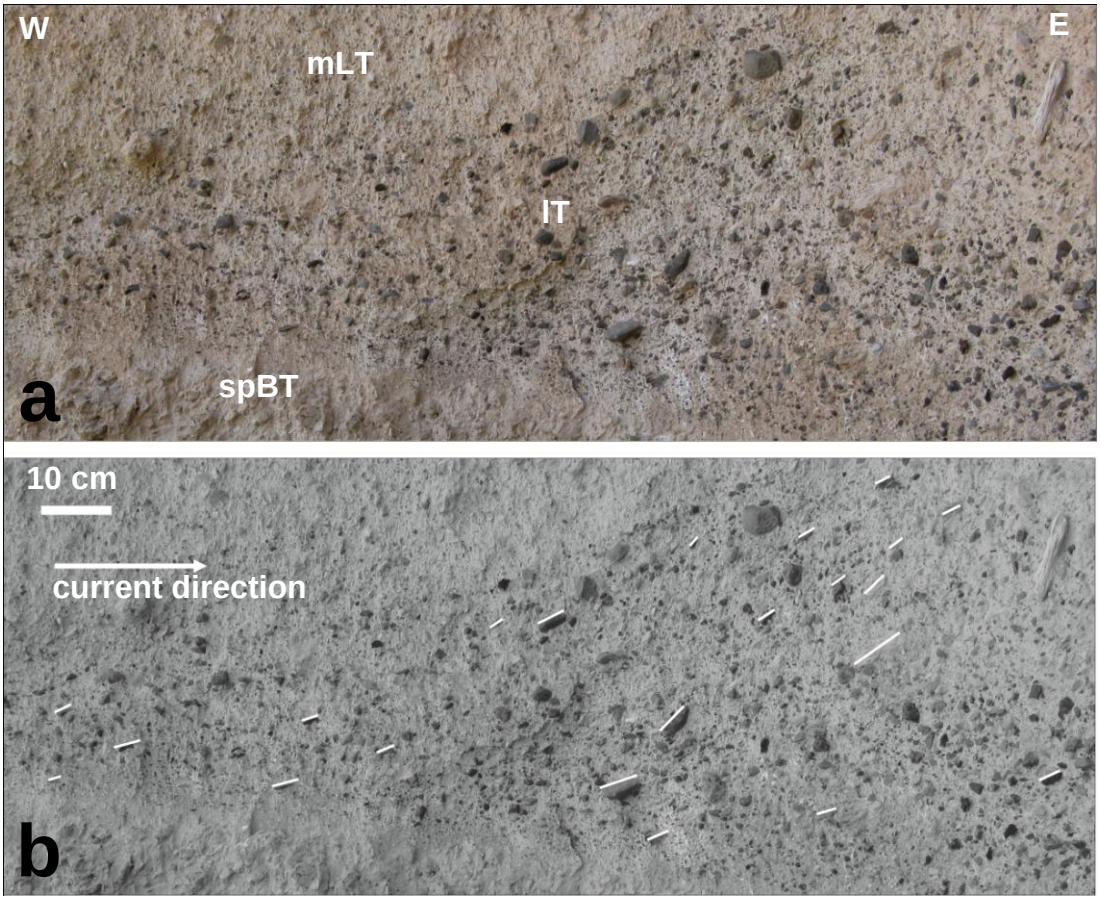

Figure 5.10 Imbrication in the proximal Poris succession (a) First lithic-rich tuff layer overlying spBT at locality 16. (b) Greyscale image of (a) mapped to show imbrications of clasts.

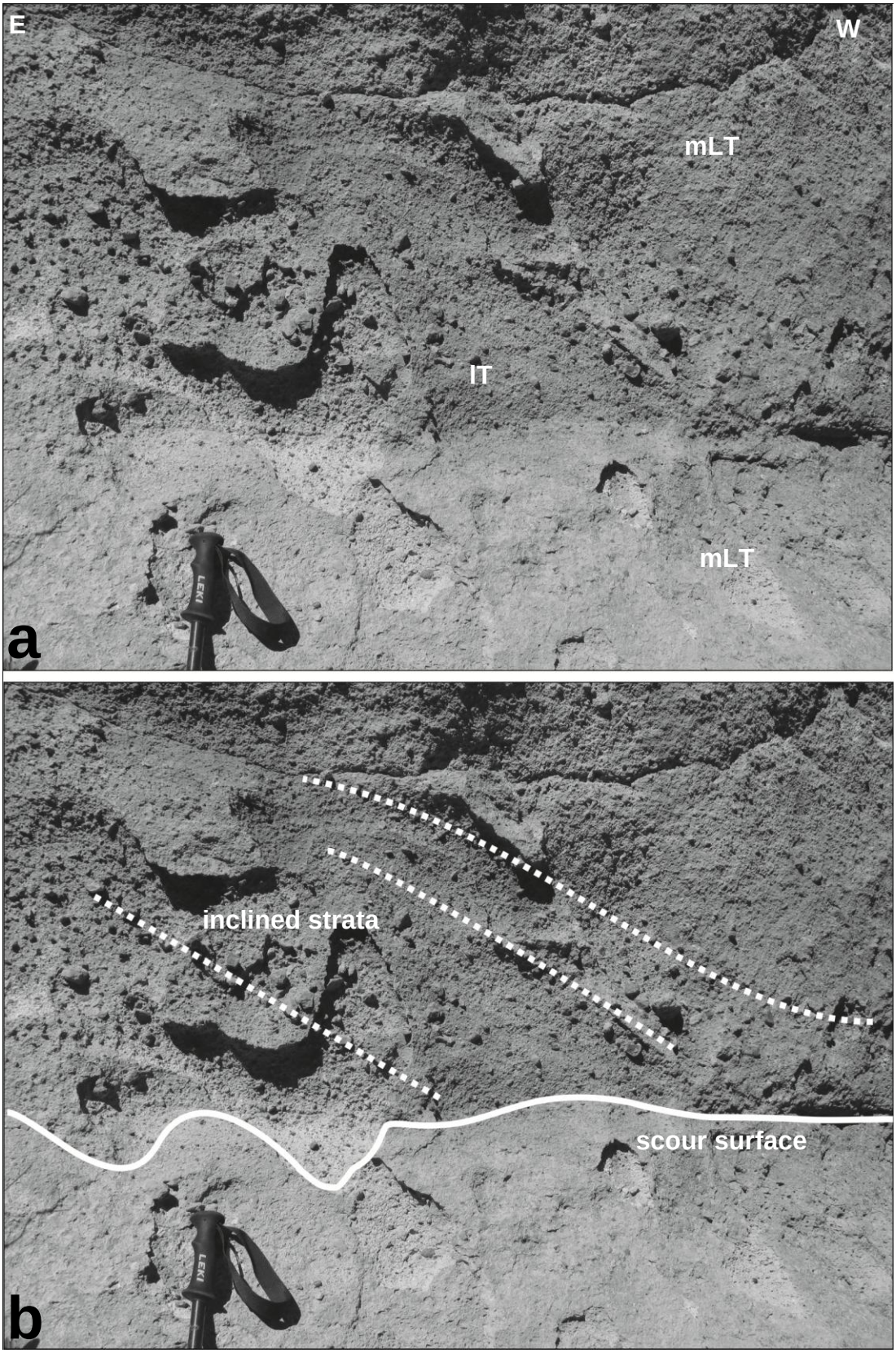

Figure 5.11 Subtle cross-stratification in lithic-rich tuff. (a) Contact between mLT and the second lT layer at locality 3. (b) Mapped to highlight stratification.

5.6.3 Distribution of load, flame and elutriation structures

Load structures are common at southern localities 2, 3 and 3a. Clast-rich, bulbous zones of lithics encroach down into the mLT below from relatively planar layers of lithic-rich tuff; some have a sharp contact with the mLT above. The largest examples are at locality 3a, where a lT layer forms load structures that are > 1 m wide and pinch out laterally into mLT (Fig. 5.12).

Distinctive flame structures are exposed at locality 16 in the north and at locality 3 in the south (Fig 5.13). At the former, a lithic-rich flame extends 2 m vertically up into the overlying mLT from a planar layer of lithic-rich tuff that occupies scours into underlying spBT. At locality 3, lapilli tuff forms a distinct wave shape, sheared upwards between two lithic-rich lobate load structures. Similar flame features are seen on a smaller scale at locality 17, where mm-scale lithics are displaced up into overlying spBT (see Fig 4.14c).

Load and flame structures form within an ignimbrite during or just after deposition from a PDC; they develop as Rayleigh-Taylor instabilities between an upper, denser deposit and an underlying less dense deposit or substrate (Branney and Kokelaar, 2002). Load structures form where lithic-laden currents pass over loosely compacted material that aggraded quickly; the lithic clasts are not adequately supported and sink into the 'fluffy', degassing deposit below. Material from below can become displaced upwards, forming flame features between lithic lobes. Flames may be created solely by shearing flow across a previous deposit, somewhat akin to the development of Kelvin-Helmholz instabilities (Rowley *et al.*, 2011).

During the Poris eruption the mLT lithofacies remained very loosely packed ('fluffy') and fluidal in some places following deposition, at least locally, so that at times of heightened lithic input the deposit surface could not adequately support the clasts and yielded to the load, in places becoming sheared downstream. Such deformation may have been common during ignimbrite emplacement, but the interactions would not be recognised where the involved materials were visually identical (Rowley *et al.*, 2011). The deformation associated with the lT layers is

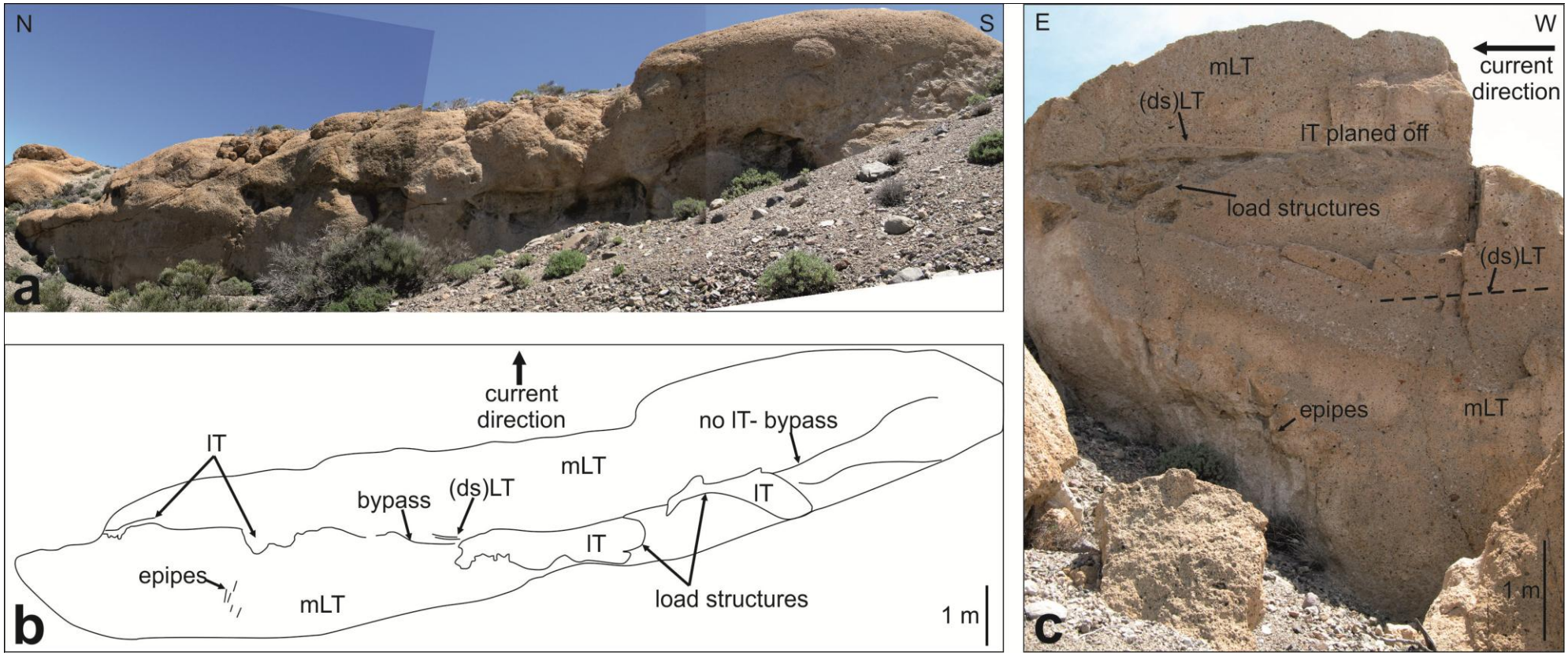

Figure 5.12 Load structures associated with the second lithic-rich tuff layer in southern outcrops. (a) and (b) Locality 3a. Lithic-rich load features pinch out southwards into bypass surfaces. At the northern end of the exposure, the lT layer reappears. (c) Locality 3, north face of exposure. The same layer of lT here appears to have been planed off by subsequent currents; the load structure has a flat top, unlike those at locality 3a.

Figure 5.13 (overleaf) (a) and (b) Localities 16 (foreground) and 17 (behind), photomapped to show lithofacies architecture and flame structures. (c) Close-up of flame structures at locality 16. (d) Distinctive load and flame structures occur at locality 3 (west face), shown in close-up in (e). Black arrows show current direction.

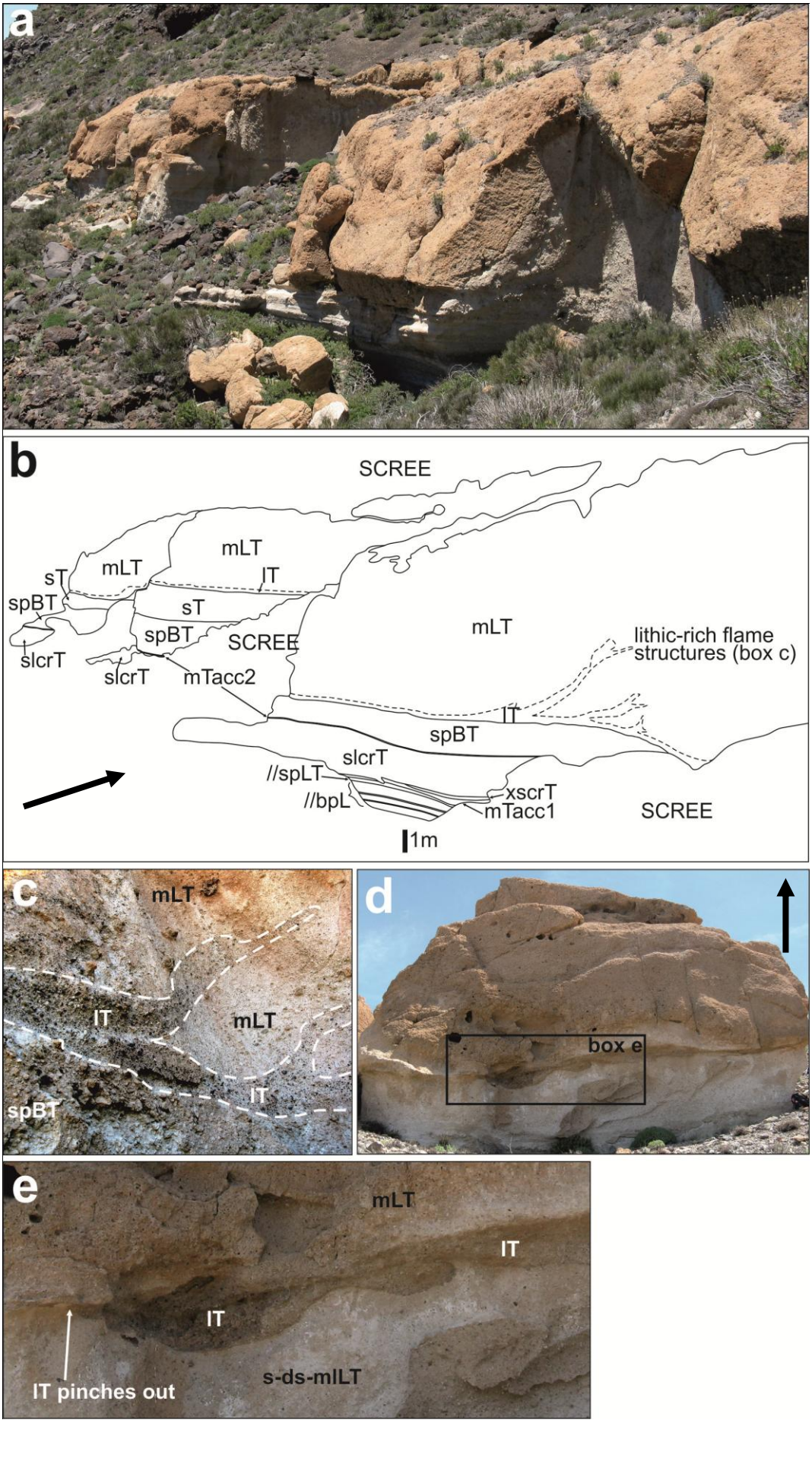
a
b
SCREE
mLT
mLT
IT
sT
spBT
sT
spBT
SCREE
slcrT
slcrT
mTacc2
mLT
lithic-rich flame
structures (box c)
IT
spBT
slcrT
//spLT
//bpL
xscrT
mTacc1
SCREE
1m
c
mLT
IT
mLT
IT
spBT
d
box e
e
mLT
IT
IT
s-ds-mlLT
IT pinches out

clearly recorded because of the lithic content. It is conceivable that the ignimbrite was not necessarily so massive upon deposition, but became so after mixing and slumping. A massive division can give a false impression of current steadiness when the current has a strong tendency to deposit.

The elutriation pipes described above in Section 4.2.10 are evidence that ignimbrite segregated during degassing and compaction soon after deposition. The deflection of some indicates that the ignimbrite remained fluidal at this stage and was sheared by subsequent flow.

The pipes are exposed at localities 3 and 3a, in the zone of mLT above the first lithic-rich layer (see Fig. 5.12), but are unknown elsewhere along the DH wall. The most prominent load structures are also concentrated in this part of the wall, at the same stratigraphic level as the pipes. This apparent coincidence might result from favourable weathering to reveal the pipes, but it may indicate that at this stage of the eruption PDCs travelling across this area were depositing particularly gas-rich and loosely consolidated material, forming a more 'fluidal' ignimbrite here (graded stratified tuff was being deposited at localities 1 and 14 at this stage). The fluidal state may reflect a current interaction with topography; for example, nearby blocking against a scarp would cause dramatic loss of capacity and consequent exceptional sedimentation.

The change in deposition in this area may have been a result of temporary topographic changes in the substrate. Between localities 3 and 4 there was significant scour at this time of depositional history (see Fig. 5.1), which may have resulted in the depositional flow boundary having been thicker in this zone. This layer would have dampened turbulence and been dominated by fluid escape.

5.7 Upper lithofacies architecture (splBr)

5.7.1 Breccia thickness

The uppermost breccia has a marked thickness change across the DH exposure. It is 8-10 m thick in northern and central areas, but just 5-6 m thick at southern outcrops.

The thickness change may reflect a change in PDC flow direction at this stage of the eruption; a shift in direction from east to north-eastwards could explain why the Cerrillar gully, north of the DH wall, apparently contains the breccia alone, without the lower Poris lithofacies. However, there is no other evidence for a change in current direction and it is possible that relatively thin lower Poris lithofacies were deposited in the gully, but are now hidden beneath scree there and/or were completely removed by erosive flows produced during the latter stage of the eruption.

The breccia thickness change across the DH wall conceivably is a result of post-Poris erosion, but exposure is not good enough to establish this. Following the Poris eruption the northern deposits may have been relatively sheltered from erosion by the Cordillera Dorsal monogentic vents (see Fig 5.2).

5.7.2 Climactic currents and the shape of Poris outcrops

The flat upper surface of the cliff exposures containing the mid-lower lithofacies implies that climactic currents produced soon after catastrophic collapse of the Poris edifice were strongly erosive. Whereas the within-exposure lithofacies boundaries are rarely consistent in height from locality to locality, the contact between mLT and splBr is sharp and planar across all exposures, creating the 'flat top'. The presence of a layer of lithic blocks along this consistent upper mLT surface indicates that similar processes to those occurring during the deposition of lT lower in the stratigraphy were operating at this stage, but on a more dramatic scale (see Fig. 5.9). Lithic-rich, erosive flows eroded the substrate and mainly bypassed the proximal zone; during waning, bed-load lithic blocks were deposited, being too large to be transported far, and the splBr unit was aggraded.

The morphology of the Poris cliff outcrops is unusual; the Fasnia and Aldea deposits below both form consistently planar exposures across the cliff, yet there are degraded channel-like gaps between the rounded Poris exposures (particularly visible between localities 16 and 17 and at southern outcrops (Fig. 5.1). Although at first these were thought perhaps to reflect channelised scour during the climactic phase of the Poris eruption, there is no unconformable infill corresponding to the gaps and the

lithofacies continue uninterrupted beneath the scree. This is clearly seen in Figure 4.19a, where the contact between splBr and mlT is planar between rounded cliff outcrops. The morphology is therefore interpreted to result from post-Poris degradation; caldera collapse has occurred at least twice in the Cañadas area since the Poris eruption, during the Abrigo and the La Caleta eruptions, and mass wasting degradation must have followed these collapses and is ongoing today.

In the main DH wall there is a distinct change in morphology between the rounded cliff exposures of the mid-lower lithofacies and the overlying splBr facies, which is set back in scree slopes. Only in the relatively sheltered Cerrillar gully is splBr freshly exposed in a cliff. Seemingly splBr has been weathered and eroded more than the lower lithofacies. This may be because the uppermost lithofacies, splBr, formed the post-Poris surface and was therefore more exposed to weathering; it may also have been relatively permeable and subject to degradation by leaching and/or freeze-thaw.

5.7.3 Breccia stratification

The subtle stratification present in the breccia, distinguished as a lithic-rich zone overlain by a pumice-rich zone, is here interpreted to be a result of changing supply at source. Following collapse of the Poris edifice, as a result of dilation of internal faults and disruption of the hydrothermal system surrounding the Poris magma chamber, high quantities of lithic-rich material of highly variable composition entered a climactic density current. Disruption of the vent, and/or the opening of additional vents, may have led to decreased explosivity, column failure, and increased but lower fountaining. At first, the lithic-rich currents mainly bypassed the proximal zone, but as the current waned and lost competence lithic-rich material was deposited. At source, lithic input to currents began to decrease and pumices input increased, possibly related to the additional tapping of a second magma (see Chapter 6). This material was deposited as currents waned.

5.8 Clast size and lithic concentration in proximal zone

Variations in lithic concentration in the proximal zone give a relatively unambiguous indication of supply changes from the source vent as the eruption progressed.

Similar changes in the distal ignimbrite record can be more ambiguous; the proportion of 'accidental' lithics picked up by the flow during transport is difficult to determine. Edgar (2002) reports an influx of black alkali basalt lava clasts in an exposure of distal Poris ignimbrite at La Mareta; the clasts are proposed to be derived from the erosion of a nearby scoria cone during the flow of Poris PDCs.

Similarly, the size of pumice clasts in the proximal area can be assumed to give a more realistic view of ejected clast size than those present in the distal zone, because clast breakage during transport increases with time. In the proximal pumice block breccia clasts reach over 1 m in diameter, but distally no clasts larger than 40 cm are reported.

5.9 Conclusions: proximal record of Poris processes

The characteristics and architecture of the Poris lithofacies exposed in the Diego Hernandez wall record a complex progression of proximal processes during the Poris eruption. This proximal record is summarised here. A full eruption model, taking into account the geochemistry and correlation with distal lithofacies, is presented in Chapter 7.

The Poris eruption began with pumice fallout from a Plinian plume, with some interaction from dilute density currents (//bpL). Activity precursory to this is not recorded at Diego Hernandez exposures. Following a period of widening of the obsidian-dominated vent, a density stratified pyroclastic current formed and became partially restricted by topography in the near-vent zone. The upper dilute part of the current surmounted the obstacle, eroding and reworking the Plinian substrate and depositing stratified layers (//spLT). Ash deposition from a hybrid plume, incorporating the main plume and the co-ignimbrite cloud, took place after the lower part of the stripped PDC passed by; accretionary pellets that had formed by lofting, circulating, and accreting ash layers in the density stratified PDC and the volcanic plume were deposited along with agglomerated ash (mTacc). This ash layer therefore represents a hiatus in energetic PDC activity *at this location.*

Phreatomagmatic activity then began and ignimbrite rich in finely fragmented crystals and lithics with some plutonic input was deposited. Initially, a dilute PDC with tractional flow-boundary conditions deposited cross stratified tuff (xscrT), possibly reflecting continued topographic blocking. Subsequently, possibly following topographic modification, conceivably substantial burial, a waxing PDC scoured into previously deposited material, with much of the material bypassing to lower slopes. As intensity waned, the current lost capacity and began to deposit; lithic-rich material became concentrated along scour surfaces. As waning progressed and lithic supply decreased the deposit became less lithic-rich. Unsteady pulsatory waning created stacked graded stratification, and in the north of the DH location a short lived local hiatus allowed ash and accretionary pellets from the margins of the Plinian column to form a deposit layer.

A return to magmatic activity was marked by increased intensity in Plinian deposition and ballistic ejection. An influx of coarse Plinian fallout and ballistics into PDCs resulted in the deposition of a hybrid lithofacies (spBT). The current had non-uniform, unsteady conditions, and migrating bedforms created some low-angle cross-stratification. At this point, the proportion of erupted mingled and 'blebbed' pumices increased (discussed in Chapter 6).

As coarse pumice input ceased, deposition of ignimbrite from the sustained current continued. In some areas the unsteadiness that created the stratification in the hybrid lithofacies persisted, and stratified and diffusely stratified tuff was deposited (s-ds-mLT).

As ignimbrite continued to be deposited, internal destabilisation of the edifice began, with incremental dilation of faults and disruption of the hydrothermal system. As this occurred, influxes of lithic-rich material sporadically arrived at the DH location accompanied by temporary waxing PDC conditions. During current waxing, previously deposited tuff was eroded and transported away from the site. As conditions waned, well defined lithic-rich tuff layers were deposited and in some places became loaded into the material below. Two waxing episodes are recorded at most outcrops, with a third episode recorded in southern exposures. Between the first and second episodes, the flow boundary zone of the density current was highly non-

uniform across the DH wall; graded stratified beds were deposited in some zones while fluidal ignimbrite was increasingly loaded and elutriated at others.

Following this main phase of ignimbrite sedimentation, a final episode of climactic destabilisation occurred and faulting within the edifice led to the major disruption of the hydrothermal system. Highly erosive waxing currents, rich in conduit-derived hydrothermally altered lithics, arrived at the DH location and scoured across the massive lapilli tuff substrate below at a consistent level, forming a relatively planar contact. Much of the material bypassed to lower slopes, but, as currents waned and lost capacity, lithics were deposited to form a layer of boulders.

Large, contorted, banded, black and cream pumice blocks entered currents and became subtly stratified upon deposition, possibly recording 'rafts' of large pumices locking together. It is unclear if the large pumice entered the current via fountaining, ballistic input or fallout.

Chapter Six

Pumice analysis and proof of Poris

6.1 Introduction

Previous studies have considered in detail the geochemistry and petrogenesis of Diego Hernandez deposits (see Wolff et al., 2000; Bryan et al., 2002; Edgar et al., 2002; Edgar et al., 2007), but geochemistry has not previously been used as a tool to compare and correlate proximal and distal Poris lithofacies. In this chapter a small-scale analytical study of Poris pumices from the Diego Hernandez wall and the coastal Bandas del Sur zone is presented. Key features of Poris geochemistry are reported, the age of the lithofacies studied is verified by comparison to previously published data, and stratigraphic geochemical variation is discussed.

6.2 Sample collection

Pumice samples were collected from fresh exposures of each of the proximal Poris lithofacies (described in Chapter 4), and from the La Caleta Formation (see Fig 3.1). Ash from mTacc layers 1 and 2 was also sampled, but only pumices were geochemically analysed. Samples were taken from locations in the north (logs 11, 13, 16 and 17), centre (log 10) and south (log 5) of the DH wall, and from the exposure at El Cerrillar. Distal pumice samples were collected from documented Bandas del Sur Poris localities (Brown, 2001; Brown *et al.*, 2003; Brown and Branney, 2004b). In the case of spBT, mLT, splBr and distal Member 1, pumices were sampled from different exposures of the same lithofacies across the study area, to compare lateral variation. Table 6.1 is a full sample list and Figure 6.1 shows sample locations.

The majority of samples are of cream pumices, although black, green and mingled clasts were sampled where present. The grain-size of pumices sampled ranged from 2 - 30 cm in diameter. For spBT and splBr, samples containing different clast sizes were obtained to allow comparison.

Sample	Lithofacies	Location	XRF	EPMA	Section
Proximal					
FSS1†	bpL bed 1: cream	Locality 16	X		
FSS2	bpL fall bed 5: cream	Locality 16	X	X	X
FSS3	slcrT: cream	Locality 17	X		
FSS4	spBT: cream <2cm	Locality 10	X		
FSS5	spBT: cream >2 cm	Locality 5	X	X	X
FSS6	spBT: cream with blebs (cream analysed)	Locality 17	X		X
FSS6a	spBT: bleb material from FSS6	Locality 17	X		
FSS7	spBT: dark green	Locality 16	X		X
FSS8	s-ds-mLT: cream	Locality 17	X		
FSS9	mLT: south cream	Locality 5	X		
FSS10	mLT: cream with blebs (cream analysed)	Locality 16	X	X	X
FSS11	mLT north: cream	Locality 17	X	X	X
FSS12	splBr just above contact with mLT: cream	Locality 13	X		
FSS13	splBr at contact with mlt: mingled black	Locality 13	X		
FSS14	splBr: cream, grey and pale green <3 cm	Cerrillar	X	X	X
FSS15	splBr: dark green	Cerrillar	X	X	X
FSS16	splBr: black	Cerrillar	X		
FSS17	splBr 15 cm below palaeosol: black	Locality 13	X		
FSS18	splBr at upper contact: cream	Locality 10	X		
FSS19ǂ	La Caleta pumices from ig 8m above Sabafo	Trench 1	X		
EX1	splBr: mingled green and black	Locality 13			X
EX2	splBr: black phenocryst-rich pumice	Locality 10		X	X
EX3	splBr: cream phenocryst-rich pumice	Locality 13		X	X
EX4	xscrT: bulk cemented tuff	Locality 11			X
Distal					
DIST1	Hidalga (1): Plinian- W. lower lobe: cream	Spooky Dog	X	X	X
DIST2	Hidalga (1): Plinian- W. lower lobe: cream	Tajao Road section	X		
DIST3	Hidalga (1): Plinian- E. upper lobe: cream	Guimar-Arafo road	X	X	X
DIST4	Hidalga(1): upper lobe: inflated cream	Guimar-Arafo road	X		
DIST5	Magua (3): ignimbrite above DIST1: cream	Spooky Dog	X		
DIST6	Rio (7): ignimbrite beneath lBr: cream	Tajao Road section	X	X	X
DIST7	Rio (7): ignimbrite beneath lBr: black	Tajao Road section	X		
DIST8	Tamadaya (8): ig above lBr: cream	Poris Quarry	X	X	X
DIST9	Tamadaya (8): ig above lBr: black	Poris Quarry	X		
DIST10	Tamadaya (8): above lBr: mingled black	Poris Quarry	X	X	X
DIST11	Guimar (9): fallout at top of sequence: cream	Guimar-Arafo road	X		
DIST12	Guimar (9): fallout at top of sequence: black	Guimar-Arafo road	X	X	X
DIST13	Caballos (5): fallout unit: cream	Guimar-Arafo road	X	X	X

Table 6.1 Colour, sample location and lithofacies information of the distal and proximal samples analysed in this study (locations shown on Fig. 6.1). Crosses denote whether samples were processed into beads and pellets for XRF, made into grain mounts for EPMA and/or made into polished sections for optical analysis. Distal Member names and numbers (in parentheses) are used after Brown and Branney (2004). Distal zoned fallout at the top of the Poris sequence is described in Brown (2001). Proximal samples were collected in June and October 2009 by NS. Distal samples were collected in December 2009 by PK and MB.
† FSS1 was affected by clay-alteration (explained in text).
ǂ FSS19, from La Caleta Formation, is the only sample NOT from the Poris Formation.

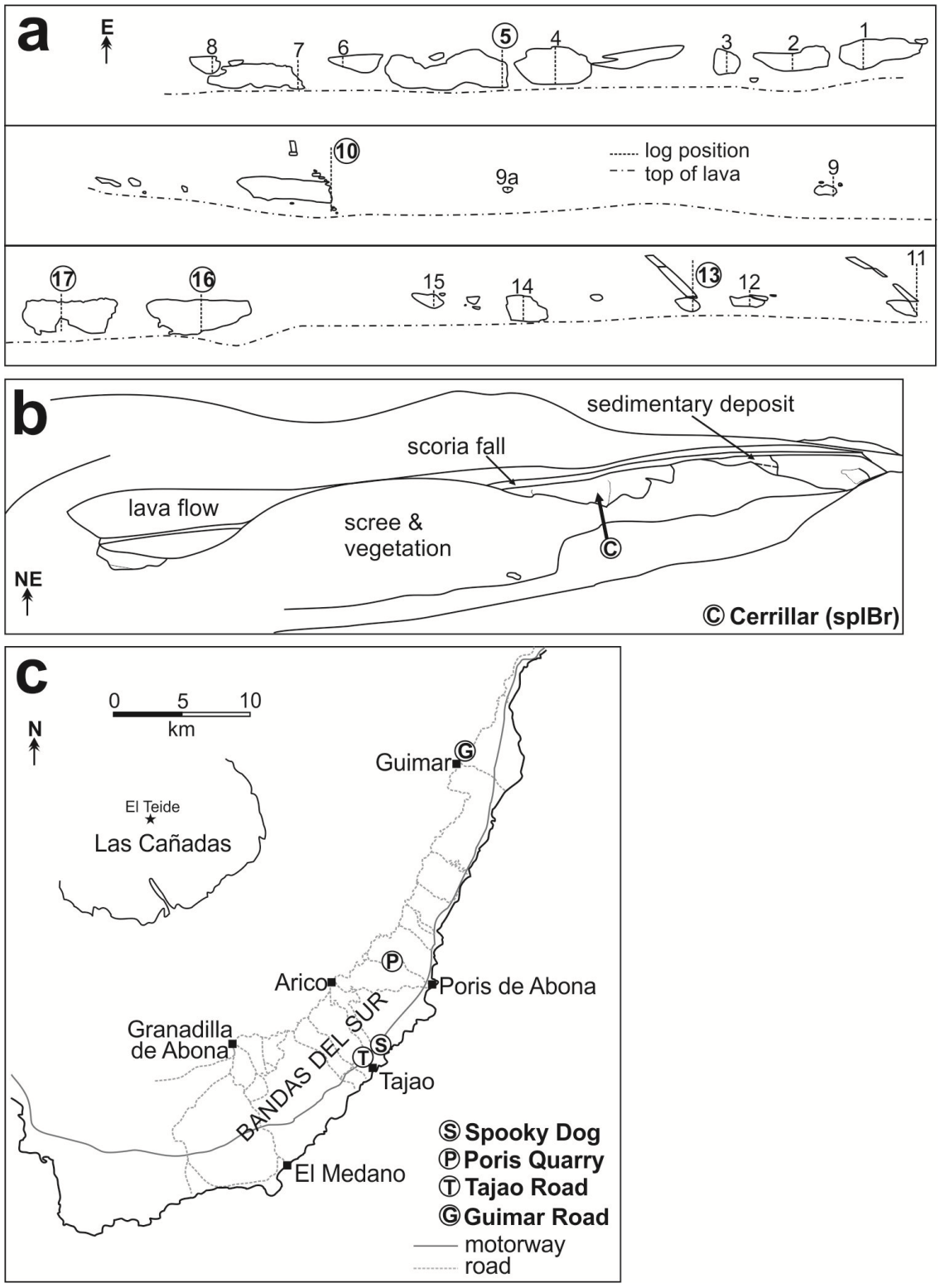

Figure 6.1 Sample locations for (a) the Diego Hernandez wall, (b) the gully at El Cerrillar, and (c) the Bandas del Sur in southeast Tenerife. Numbers represent log localities. Sample points are designated by circles and bold font. See Brown and Branney (2004b) for full detail of all distal Poris localities. See Chapter 4 for fuller details of proximal locations and logs, and Table 6.1 for corresponding sample names.

6.3 Optical analysis

Thin sections of pumice clasts from distal and proximal deposits (final column in Table 6.1), were analysed with the petrological microscope. Additional sections of bulk material from xscrT, slcrT and splBr were made.

The degree and nature of glass vesicularity in Poris pumices varies widely (Fig. 6.2). In cream pumice clasts, vesicle shapes are irregular (6.2a), regular and rounded (6.2b), or highly elongated and aligned tubular (6.2c). Some pumices appear 'inflated', having large voids within. Cream pumice is commonly crystal-poor. Sample FSS15, a dark green pumice from splBr, contains more crystals than the cream type and has irregular vesicularity (6.2d). A black pumice sampled from splBr contains dark brown glass with larger and more irregular vesicles than occur in the cream or green varieties (6.3e).

Black pumices are typically more crystal-rich (up to ~30 % crystals) than cream pumices (~5%) (6.2f); feldspar, amphibole, and clinopyroxene phenocrysts occur, along with opaque oxides (6.2g, h, i). Euhedral feldpsars are present, but many plagioclase crystals display disequilibrium textures, such as sieve textures and embayment, indicative of resorption (6.2g). Some feldspars are compositionally zoned. Anhedral amphiboles also show evidence of embayment and disequilibrium, whereas clinopyroxene crystals tend to be more euhedral. Bright blue crystals of nosean-haüyne are visible but sparse in hand specimens of all three colour variants; they were not identified in thin section (see Section 6.6 for mineralogical analysis).

Interpretation

The varying nature of cream-pumice vesicularity suggests variability of vesiculation and fragmentation of Poris pumices. High vesicularity and a lack of phenocrysts is interpreted to indicate rapid rise of magma with little volatile loss (Heiken and Wohletz, 1985); this may be the case for the cream Poris pumice population. The highly elongate vesicles in some tubular pumices indicate stretching during laminar conduit flow of the viscous magma (Heiken and Wohletz, 1985). The more irregular vesicularity of the black-pumice population suggests that this magma type

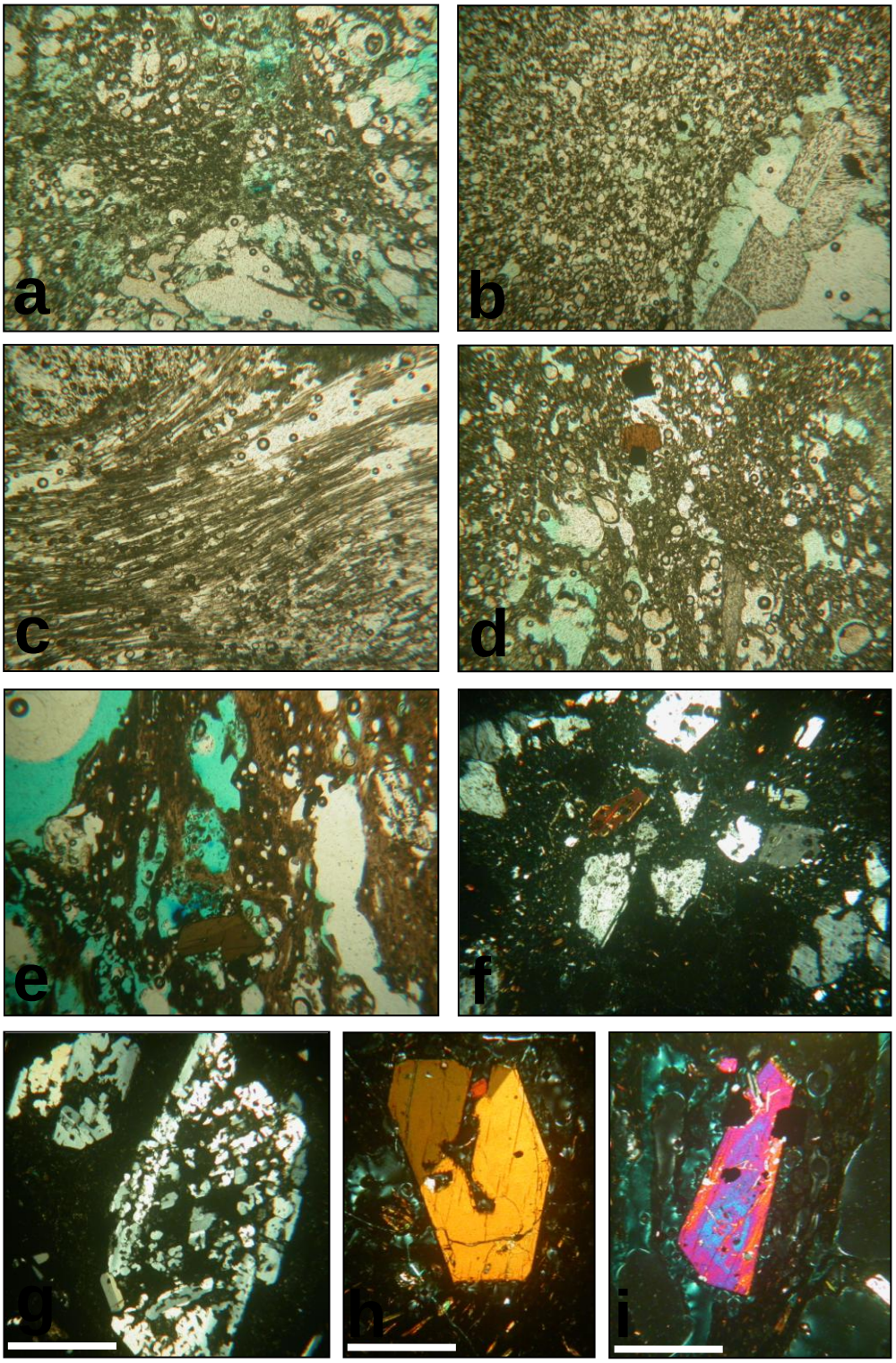

Figure 6.2 Optical analysis of Poris pumices [4 mm FOV in a-f]. (a) Irregular sub-rounded vesicles in a proximal Plinian pumice (PPL). (b) Tight, regular vesicularity in a cream pumice from spBT, with an anhedral feldspar in lower right (PPL). (c) Elongate, tubular vesicles in a distal Plinian pumice (PPL). (d) Amphibole, feldspar and opaque oxide crystals in a green pumice (PPL). (e) Brown glass containing relatively large, irregular vesicles from a black proximal splBr pumice (PPL). (f) Crystal-rich black pumice; sample DIST10 (XPL). (g) Feldspar showing disequilibrium textures in a bulk tuff sample of splBr (XPL). Original euhedral form is locally preserved with evidence of either extreme resorption or an element of skeletal growth. (h) Embayed, twinned amphibole in black pumice DIST10 (XPL). (i) Clinopyroxene phenocryst in splBr black pumice (XPL) [1 mm scale bar].

experienced less simple shear, possibly due to differences in temperature, chemistry and volatile content, and hence rheology. This black material is concentrated in the upper parts of the succession, possibly indicating that the nature of explosivity changed during the course of the eruption as magma rheology changed.

The plagioclases with disequilibrium and resorption textures may reflect heating episodes and/or mixing with a more mafic magma. Such features in plagioclases from Teide lavas have been interpreted to indicate the presence of a 'large, bipolarly-zoned' chamber beneath Mt. Teide that experiences infrequent influxes of mafic melt (Kouli and St. Seymour, 2006).

6.4 Diverse mingling textures

Two styles of mingling occur in the sampled Poris pumices. One style consists of sub-angular to sub-rounded discrete fragments of pumiceous black material within a pumice clast. These features, referred to as 'blebs' by Edgar *et al.* (2002), are commonly less vesicular and more crystal-rich than the host pumice (Fig. 6.3). The contact between the two pumice types is sharp. Blebs occur in pumices *throughout* the Poris succession, but are more readily detected where pumice clasts are larger, such as in the spBT lithofacies. Bleb material was extracted from a spBT pumice for geochemical analysis (sample FSS6a), the results of which are presented in Section 6.5 below. Blebs are clearly visible in cream pumices, but they also occur in dark green and black varieties (see Fig. 6.3d).

The second style is a more fluidal mingling where boundaries between magmatic components, commonly green and black, are less distinct. The contacts between these different components appear stretched and elongate in hand specimen, often emphasised by the presence of elongated vesicles; they are clearly seen in thin section (Fig 6.4). The intimate nature of this mingling renders mechanical separation of the different glass types for XRF analysis unfeasible, but a thin section comparison indicates that the components evident in the mingled clasts are the same as those that constitute unmingled green and black pumices.

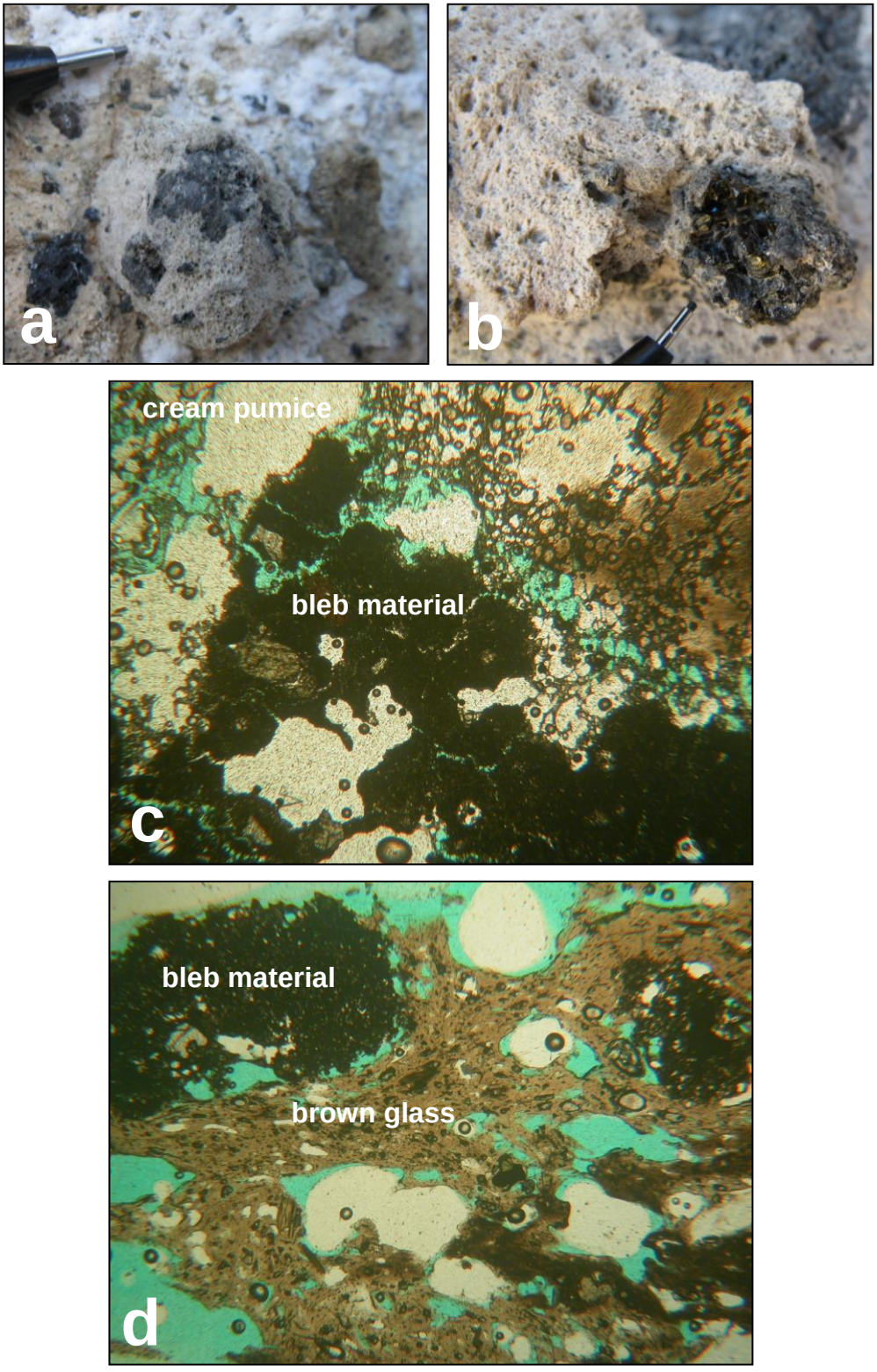

Figure 6.3 Bleb-type mingling in Poris pumices. FOV of thin sections is 4 mm. (a) Dark grey bleb in spBT pumice at log 1. (b) Crystal-rich bleb in spBT pumice at log 10. (c) Black bleb material in cream spBT pumice. (d) Discrete black blebs within brown glass in EX2, a black phenocrystic pumice clast.

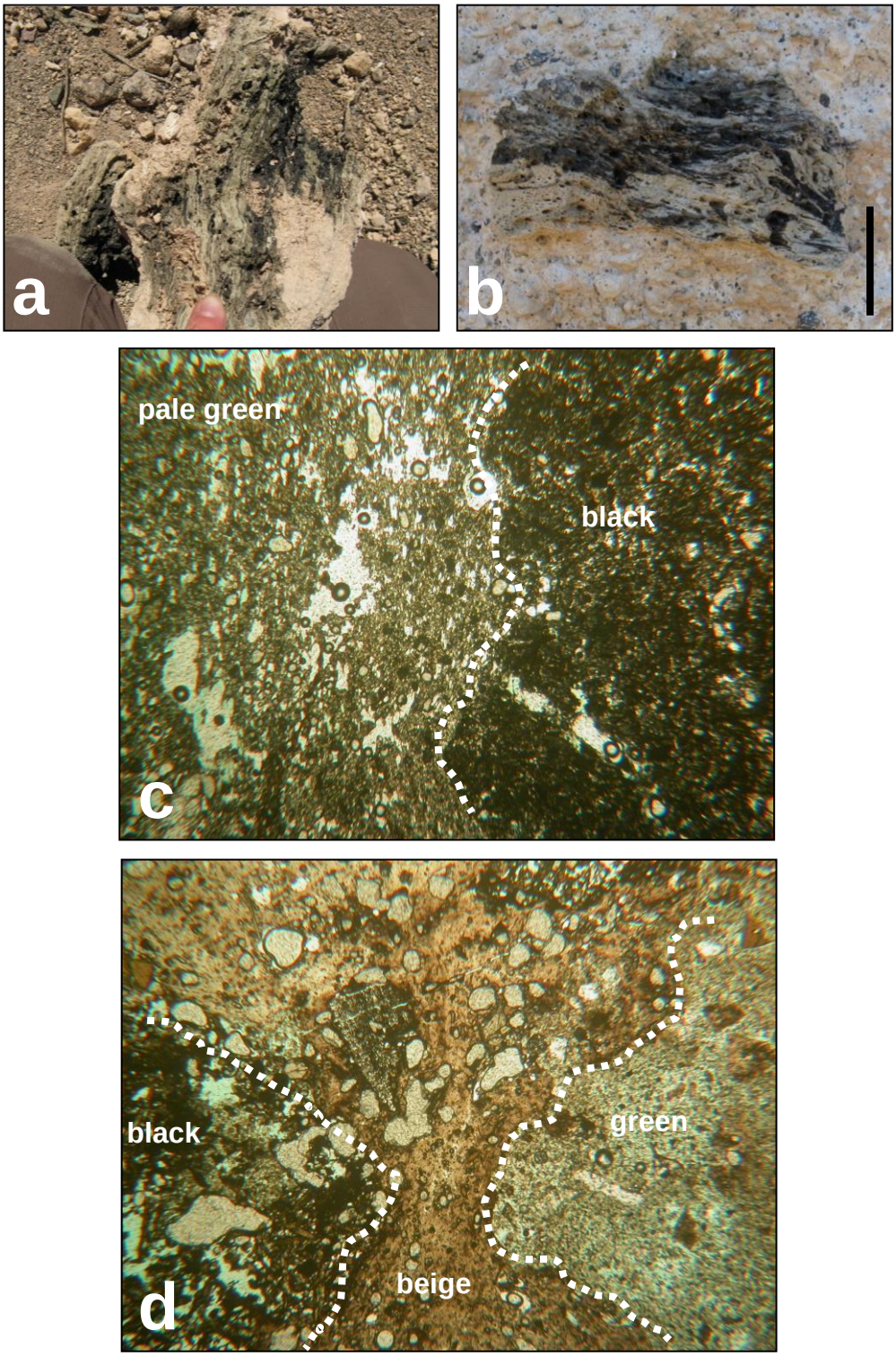

Figure 6.4 Fluidal-type mingling in Poris pumices. (a) Mingled pumice block from splBr at log 13. (b) Mingled pumice lapilli in mLT at log 10 (1 cm scale bar). (c) Contact between glass types in EX1, the mingled clast shown in (a). (d) Mingling in distal black pumice DIST10.

Interpretation

The evidence of mingled magmas early in the Poris succession (mingled clasts occur in the opening-phase Poris Plinian) indicates that (at least) two magma types were available throughout the entire recorded Poris eruption. The magma represented by black material, however, becomes notably more prevalent in the late-phase deposits. The different types of mingling indicate that interaction between the different magmas was non-uniform. Complete mixing, evidence of which cannot be seen in the clasts, may have occurred. The poor vesicularity of the blebs suggests that these were relatively volatile-poor, possibly originating from a different zone in the magma 'chamber', so that they did not become expanded, 'stretched out', and more thoroughly mingled with the host magma. Alternatively, they may represent relatively degassed magma that resided in another 'chamber' through which the main stage magma passed.

6.5 X-Ray Fluorescence analysis (XRF)

During X-ray fluorescence analysis a geological sample is radiated and emits characteristic secondary X-rays that are measured to provide bulk-rock geochemical data. In this study XRF was chosen in preference to single-grain tephra analysis methods, such as laser ablation ICP-MS, so new data could be compared with the previous XRF studies of Tenerife ignimbrites (Brown, 2001; Bryan *et al.*, 2002; Edgar *et al.*, 2007). Analysis was carried out at Leicester University on a PANanalytical Axios-Advanced XRF spectrometer.

6.5.1 Sample preparation

For each sample, a single pumice clast >5 cm in diameter was prepared for analysis. Multiple pumices were used for samples where clast size was <5 cm. Pumices were first cleaned of adhering ash and weathered 'rind' material. Those containing dark blebs were separated to analyse either pale or dark material. Samples were crushed with an engineering fly press to gravel size and milled with an agate planetary mill to <50 μm. Fusion beads and pellets were created from the powders (see Appendix for procedures). During pellet making, sample FSS1 (//bpL bed 1), cracked and reacted with the glue, indicating significant alteration to clay (pers. comm. XRF technician

Rob Kelly, 2010). This sample later gave anomalous results indicative of weathering (see Section 6.5.2).

6.5.2 Results

Major and trace element analyses were obtained for each sample: Beads were analysed and results reported for SiO_2, Al_2O_3, TiO_2, Fe_2O_3, MgO, CaO, K_2O, MnO, SO_3 and P_2O_5, and pellets for Ba, Ce, Co, Cr, Cs, Cu, Ga, La, Mo, Nb, Nd, Ni, Pb, Rb, Sc, Sr, Th, U, V, Y, Zn and Zr. The results are presented in Table 6.2.

Proof of Poris

Proximal and distal samples from this study lie in the same fields on a Zr-Nb co-variation plot (Fig. 6.5), confirming that the deposits sampled at the Diego Hernandez wall and the Bandas del Sur can be counterparts recording the same eruption. The data match well with previous geochemical analyses of Poris material from Brown (2001) and Edgar *et al*. (2002). Assuming that these correlations are robust, this verifies the age of the deposit studied; the Poris Formation has been $^{39}Ar/^{40}Ar$ dated at 273 ka (Brown *et al.*, 2003). The analysis of pumice sampled from the proximal ignimbrite overlying the Poris and believed to be La Caleta (see Chapter 3) plots within the La Caleta data field reported by Edgar *et al*. (2007).

Key features of juvenile composition

Four different magmatic compositional components are present in the Poris ignimbrite succession (Figs 6.6 and 6.7). The majority of the samples analysed are a **high-Zr phonolite**, typically containing 1100-1360 ppm Zr, 54-57% SiO_2, and 13-15% total alkalis. Three proximal splBr samples are a **low-Zr phonolite**, containing 500-800 ppm Zr, 56-57% SiO_2, and 12-13% total alkalis. Three proximal splBr samples and two distal breccia samples are a **low-Zr tephriphonolite** containing 510-740 ppm Zr, 52-57% SiO_2, and 10-13% total alkalis. The most mafic component analysed is a **low-Zr phonotephrite**, containing the lowest Zr concentrations (460-630 ppm), notably less SiO_2 (48-50%), and lower total alkalis (8-10%). A bleb in a spBT pumice and two distal samples analysed were of this latter composition.

Table 6.2 (i) XRF analyses [FSS1† = anomalous results due to alteration to clay]

	High-Zr Phonolite											
	Proximal											
Lithofacies	bpL	bpL	slcrT	spBT	spBT	spBT	spBT	sLT	mLT	mLT	mLT	splBr
Sample	FSS1†	FSS2	FSS3	FSS4	FSS5	FSS6	FSS7	FSS8	FSS9	FSS10	FSS11	FSS12
Colour	cream	cream	cream	cream	cream	cream	green	cream	cream	cream	cream	cream
Major elements												
SiO_2	50.6	56.5	55.5	56.2	55.9	56.4	56.9	57.8	57.0	57.5	57.2	55.9
TiO_2	0.51	0.46	0.84	0.67	0.81	0.62	0.94	0.44	0.56	0.61	0.50	0.43
Al_2O_3	24.0	19.8	19.6	19.7	19.9	19.9	19.8	20.3	20.1	20.3	20.1	20.5
Fe_2O_3	3.29	2.82	3.76	3.36	3.77	3.21	3.96	2.81	3.05	3.27	2.92	2.86
MnO	0.208	0.178	0.179	0.177	0.176	0.181	0.179	0.184	0.177	0.192	0.180	0.180
MgO	0.300	0.220	0.619	0.425	0.583	0.303	0.648	0.088	0.240	0.305	0.163	0.074
CaO	0.824	1.06	2.14	1.75	1.81	1.38	2.24	0.90	1.22	1.38	1.05	0.79
Na_2O	5.77	8.09	8.17	7.82	7.75	8.43	8.81	8.53	8.49	9.23	8.47	7.66
K_2O	5.02	5.71	5.30	5.54	5.17	5.52	4.96	5.51	5.37	5.19	5.41	5.42
P_2O_5	0.062	0.064	0.167	0.113	0.138	0.109	0.179	0.046	0.087	0.117	0.066	0.036
SO_3	0.051	0.073	0.088	0.062	0.075	0.057	0.108	0.030	0.050	0.058	0.040	0.036
Trace elements												
Ba	26.7	120.2	395.7	347.5	424.5	247.1	610.3	84.4	307.6	178.4	73.1	92.4
Ce	202.3	175.5	182.0	171.9	173.9	175.6	190.3	168.5	170.9	174.0	167.5	174.0
Cl	24220	5509	5084	5798	3998	3383	2960	3880	3499	3318	6039	3502
Co	3.54	3.12	5.40	2.76	3.03	2.90	5.46	2.83	2.89	4.83	2.45	2.15
Cr	16.5	<0.6	<0.6	14.1	<0.6	<0.6	<0.7	<0.6	<0.6	<0.6	17.0	<0.6
Cs	6.08	4.49	7.03	3.99	5.87	7.62	4.74	6.97	6.81	5.07	6.41	9.19
Cu	11.5	6.62	5.70	<0.4	<0.5	<0.4	2.57	<0.4	<0.4	1.80	0.69	<0.4
Ga	53.7	33.9	31.9	31.4	32.1	32.8	32.0	33.6	32.1	33.8	33.4	35.5
La	109.4	112.0	112.5	110.9	108.5	112.6	110.4	113.7	113.0	109.8	109.8	117.9
Mo	3.95	5.56	6.05	5.53	6.33	5.85	6.40	6.08	5.97	6.11	5.93	5.43
Nb	273.8	240.4	224.3	224.7	223.9	231.5	222.5	241.8	236.2	238.9	238.6	245.6
Nd	49.1	44.0	52.1	46.6	48.2	44.4	57.6	38.2	42.6	40.6	38.8	43.1
Ni	2.43	2.02	0.75	0.86	1.62	<0.5	<0.6	<0.5	<0.5	<0.5	<0.5	<0.5
Pb	26.6	19.2	17.1	135.8	17.3	18.3	143.0	19.9	21.6	18.1	19.1	39.2
Rb	122.4	193.9	176.1	180.8	170.5	191.4	167.6	209.3	191.2	200.9	205.8	201.8
Sc	2.02	1.55	1.09	1.81	1.67	<1.1	2.07	1.38	<1.1	1.50	<1.1	<1.0
Sr	108.1	79.9	306.5	199.1	242.5	155.0	327.3	57.1	143.9	142.5	57.7	43.8
Th	43.0	37.2	30.4	32.7	30.5	32.9	29.2	36.0	33.7	34.9	36.7	37.6
U	6.60	9.40	8.39	8.10	8.23	8.83	6.65	9.33	8.70	9.10	9.24	9.87
V	23.6	30.3	54.1	44.6	52.7	39.8	60.0	30.3	36.9	41.4	30.7	25.7
Y	58.7	26.5	28.6	26.6	27.2	24.9	30.5	22.9	25.5	24.7	22.9	25.5
Zn	128.8	110.2	109.1	107.2	108.7	106.7	108.2	109.7	109.4	111.7	109.0	114.0
Zr	1538.2	1317.7	1129.6	1167.2	1142.9	1220.9	1076.4	1328.9	1242.6	1282.0	1314.8	1355.7

Table 6.2 (ii) XRF analyses

	High-Zr Phonolite					Low-Zr Phonolite		
	Distal					Proximal		
Lithofacies	Mem. 1	Mem. 1	Mem. 7	Mem. 8	Mem. 11	splBr	splBr	splBr
Sample	DIST2	DIST3	DIST6	DIST8	DIST11	FSS14	FSS15	FSS18
Colour	cream	cream	cream	cream	cream	cream	green	cream
Major elements								
SiO_2	55.2	54.7	55.8	54.5	54.3	57.6	56.6	57.9
TiO_2	0.37	0.41	0.40	0.62	0.52	0.47	0.94	0.73
Al_2O_3	19.3	19.1	19.6	18.9	19.0	20.7	20.2	19.3
Fe_2O_3	2.60	2.68	2.67	3.11	2.94	2.94	4.02	2.95
MnO	0.174	0.174	0.177	0.169	0.173	0.184	0.181	0.147
MgO	0.226	0.550	0.175	0.919	0.554	0.121	0.678	0.350
CaO	0.740	1.89	0.951	3.29	2.88	0.940	2.18	1.38
Na_2O	8.73	8.10	8.66	8.10	7.90	8.22	7.64	7.12
K_2O	5.24	5.74	5.46	5.23	5.69	5.52	4.98	5.73
P_2O_5	0.034	0.057	0.041	0.132	0.102	0.052	0.204	0.105
SO_3	0.115	0.088	0.075	0.088	0.092	0.039	0.071	0.059
Trace elements								
Ba	48.6	38.3	60.2	271.9	132.8	945.7	750.2	624.1
Ce	157.4	158.8	165.2	166.5	168.2	204.2	184.6	179.3
Cl	17788	3743	6476	3176	3480	1284	985	2045
Co	1.60	3.09	3.29	3.50	3.35	1.17	<1.1	<1.1
Cr	21.3	<0.6	<0.6	<0.6	<0.6	24.1	<0.6	<0.6
Cs	7.86	5.85	3.68	5.69	5.64	<1.7	4.59	3.33
Cu	3.91	8.07	4.18	5.94	7.81	<0.4	<0.4	<0.4
Ga	31.3	31.8	33.6	29.6	30.4	25.5	22.6	25.1
La	105.9	111.8	113.4	107.4	117.9	109.1	98.4	102.6
Mo	5.77	5.81	6.08	5.99	5.57	7.01	7.09	5.40
Nb	231.2	233.7	240.6	218.5	213.3	179.4	146.8	207.3
Nd	35.3	36.7	38.6	46.7	47.9	74.9	69.0	55.4
Ni	1.85	1.19	<0.5	0.88	1.27	<0.5	<0.5	<0.5
Pb	18.5	22.1	19.3	16.4	18.6	8.00	7.05	12.8
Rb	197.4	205.1	206.9	176.1	182.0	101.7	88.6	140.2
Sc	<1.0	1.61	1.55	<1.1	<1.1	2.03	1.48	1.17
Sr	29.9	72.1	48.7	220.6	139.3	170.0	74.9	143.1
Th	35.2	35.4	36.7	30.2	31.7	13.5	10.6	21.5
U	8.43	8.46	9.53	7.38	8.08	3.07	2.87	5.44
V	25.8	27.3	25.3	40.1	35.5	47.6	39.1	38.7
Y	21.2	23.2	23.4	25.3	24.5	37.1	32.3	33.5
Zn	104.6	117.0	108.3	101.3	104.9	97.6	84.7	83.3
Zr	1291.9	1304.8	1332.7	1139.5	1148.6	680.7	537.3	827.8

Table 6.2 (iii) XRF analyses

	Low-Zr Tephriphonolite					Low-Zr Phonotephrite		
	Proximal			Distal		Proximal	Distal	
Lithofacies	splBr	splBr	splBr	Mem. 8	Mem. 8	spBT	Mem. 7	Mem. 11
Sample	FSS13	FSS16	FSS17	DIST9	DIST10	FSS6a	DIST7	DIST12
Colour	mingled	black	black	black	mingled	bleb	black	black
Major elements								
SiO_2	53.5	56.3	52.4	53.3	56.4	50.5	49.0	48.2
TiO_2	1.86	1.18	1.87	2.08	1.39	2.33	2.63	2.92
Al_2O_3	18.9	20.0	18.7	19.0	19.3	18.3	17.8	17.4
Fe_2O_3	6.13	4.59	6.57	6.65	4.80	7.55	8.35	9.30
MnO	0.172	0.180	0.186	0.181	0.161	0.196	0.193	0.197
MgO	1.79	0.966	2.12	2.07	1.19	2.55	3.04	3.77
CaO	4.66	2.83	4.77	5.63	3.50	6.37	7.34	7.98
Na_2O	6.33	7.38	6.55	6.68	7.61	6.31	6.02	5.23
K_2O	3.79	4.72	3.75	3.51	4.67	3.37	2.76	2.73
P_2O_5	0.507	0.282	0.486	0.593	0.371	0.770	0.815	0.915
SO_3	0.136	0.088	0.077	0.215	0.174	0.194	0.278	0.179
Trace elements								
Ba	1488.4	1886.8	950.4	1889.7	1290.5	1017.7	1518.8	1079.0
Ce	205.0	177.7	191.9	204.4	201.2	202.9	193.2	188.5
Cl	1220	913	1540	1174	1502	1683	3534	1152
Co	12.0	3.34	11.7	10.50	7.51	14.6	17.2	19.4
Cr	<0.7	<0.7	3.64	6.12	5.36	<0.7	39.7	13.1
Cs	<1.7	<1.7	4.47	<1.8	<1.7	2.52	<1.8	<1.9
Cu	3.89	<0.4	6.89	9.58	8.26	5.01	14.8	17.6
Ga	25.8	21.4	27.8	23.4	24.7	25.3	23.4	22.1
La	149.4	94.1	103.6	102.8	107.8	103.0	95.8	93.4
Mo	4.50	7.14	4.71	5.61	6.18	6.28	5.31	4.82
Nb	178.2	138.4	183.6	163.5	186.8	165.2	142.9	137.1
Nd	100.0	68.4	70.7	84.7	73.4	83.7	89.1	79.8
Ni	<0.6	<0.5	5.70	1.34	<0.6	<0.6	4.36	9.25
Pb	9.22	6.84	10.4	6.94	9.26	10.0	5.75	5.78
Rb	88.7	79.7	106.9	74.8	103.2	87.6	59.9	61.5
Sc	5.75	<1.1	5.32	6.69	3.90	8.25	9.94	10.80
Sr	813.1	244.5	801.4	1092.4	563.8	1069.4	1285.3	1175.5
Th	15.0	9.89	18.9	11.4	15.5	14.7	9.6	9.22
U	4.34	2.14	5.54	3.31	4.45	4.43	2.30	2.56
V	106.3	47.3	108.9	118.2	84.3	148.4	163.3	186.0
Y	47.0	31.9	38.4	42.0	38.0	39.6	41.4	40.7
Zn	99.5	85.9	103.5	95.0	92.1	109.0	100.4	102.6
Zr	610.3	510.1	737.1	524.6	656.9	624.5	468.7	462.0

Table 6.2 (iv) XRF analyses

	High-Zr Tephriphonolite- altered?				La Caleta
	Distal				Proximal
Lithofacies	Mem. 1	Mem. 1	Mem. 3	Mem. 5	Caleta mLT
Sample	DIST1	DIST4	DIST5	DIST13	FSS19
Colour	cream	cream	cream	cream	cream
Major elements					
SiO_2	55.4	53.3	51.9	53.2	57.0
TiO_2	0.38	0.41	0.40	0.54	0.55
Al_2O_3	19.4	18.7	18.7	18.4	20.0
Fe_2O_3	2.64	2.61	2.61	2.94	2.86
MnO	0.158	0.169	0.163	0.167	0.152
MgO	0.464	0.526	0.424	0.966	0.222
CaO	1.09	3.14	4.71	3.72	1.17
Na_2O	7.63	8.00	7.50	7.51	6.48
K_2O	4.77	5.62	5.01	5.55	5.45
P_2O_5	0.034	0.079	0.075	0.099	0.056
SO_3	0.027	0.077	0.093	0.233	0.021
Trace elements					
Ba	17.9	83.5	57.7	180.8	272.7
Ce	155.2	156.7	154.6	164.0	118.7
Cl	6367	3478	6293	3593	2340
Co	2.12	1.35	2.33	4.45	3.30
Cr	<0.6	<0.6	<0.6	10.0	<0.6
Cs	7.28	4.98	5.26	5.74	3.09
Cu	4.08	6.08	4.02	8.51	<0.4
Ga	31.9	31.5	31.5	30.2	29.4
La	100.9	111.7	103.7	110.9	79.2
Mo	5.54	5.82	5.69	5.92	5.25
Nb	226.6	227.8	220.0	216.7	158.4
Nd	34.2	37.9	34.7	43.9	27.9
Ni	<0.5	1.66	<0.5	2.52	<0.5
Pb	18.1	19.1	17.8	19.4	13.4
Rb	185.1	199.6	184.3	183.6	161.7
Sc	<1.0	<1.1	3.34	2.39	<1.0
Sr	42.3	110.0	90.4	193.9	103.1
Th	36.4	34.8	33.7	31.6	25.4
U	7.76	8.67	13.34	8.66	5.66
V	22.5	27.6	26.6	35.0	28.6
Y	19.7	24.4	25.1	24.5	14.3
Zn	102.8	114.0	104.5	109.9	82.4
Zr	1332.6	1257.2	1280.9	1163.1	991.9

Associating chemistry with pumice colour is not straightforward in the Poris Formation. All of the high-Zr analyses were from cream pumice samples, whereas cream, green, black and mingled varieties of low-Zr types occur. All phonotephrite analyses were from black pumices (Table 6.2), but the spBT green pumice FSS7 contains high Zr and is relatively silicic, whereas a similar looking green pumice block from splBr (FSS15) is more like the black FSS16 sample in Zr content. Sample FSS14, a mix of cream, grey and pale green pumice clasts <3 cm in diameter, contains less Zr than the black clast FSS17.

Phonolite, tephriphonolite, and phonotephrite are compositional fields typical of Tenerife ignimbrites (e.g. Wolff *et al.*, 2000). However, post-depositional hydration of pumices can cause alkalis to be leached from felsic glass (Scott, 1971), and may render TAS classification unreliable. On a TAS plot of the pumices analysed in this study (Fig. 6.6), the clustering of data in the three fields suggests that, on the whole, alteration effects have been minimal. However, four cream pumice samples from the lower distal stratigraphy (DIST 1, 4, 5 and 13) fall in the tephriphonolite field with lower SiO_2 than would typically be expected. The appearance of this possible fifth, (cream) tephriphonolite, magmatic component may be an artefact of post-depositional modification. Closer to the sea, where there is extensive diagenetic case-hardening reflecting groundwater-table migrations, the distal deposits may have undergone alteration that has subtly affected major element chemistry. None of the cream proximal samples are tephriphonolites. Following the method of Edgar *et al.* (2002), Zr is used as a key index element for geochemical variation in this study, because it is incompatible in the Tenerife magma series and immobile during hydrous alteration (Wolff *et al.*, 2000; Edgar *et al.*, 2002). The zirconium concentration of cream tephriphonolite pumices closely matches that of cream phonolite pumices from the same stratigraphic position, indicating that alteration has not affected this trace element (distal Plinian samples, Fig. 6.8). Therefore it is seems probable that the cream tephriphonolite pumices originally were phonolite.

The presence of two petrogenetically distinct Poris magma series, one with higher and one with lower Zr (Fig. 6.7), has been reported previously (Edgar *et al.*, 2002) and is discussed more fully in Chapter 7.

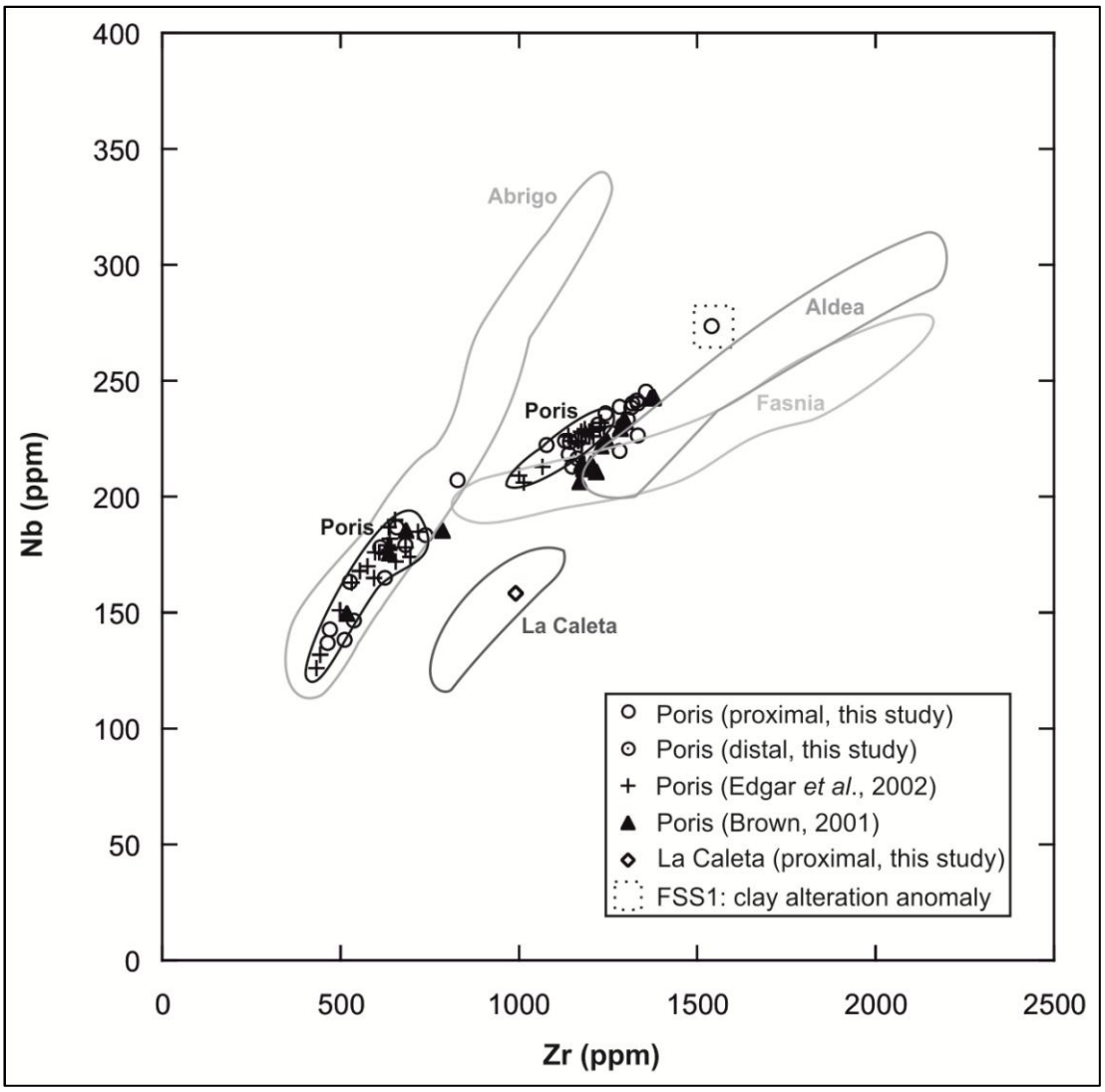

Figure 6.5 Proof of Poris. Proximal and distal pumice compositions determined in this study correlate well, confirming that the outcrops sampled are counterparts from the same eruption. The fields shown on the graph represent geochemical data from Diego Hernandez aged ignimbrites, adapted from Figure 6 of Edgar *et al.* (2007). There is some overlap between eruptions, but the results from this study fall within (or very close to) the Poris fields from Edgar *et al.* (2007) and correlate with Poris analyses from Edgar *et al.* (2002) and Brown (2001). Note that stratigraphic evidence indicates that the samples analysed during this study caanot be from the Abrigo eruption (see Chapter 3). The proximal La Caleta sample from this study plots within the field of La Caleta. The anomalous sample FSS1, from the base of the Poris, is significantly altered to clay (see text) and is thus omitted from subsequent plots.

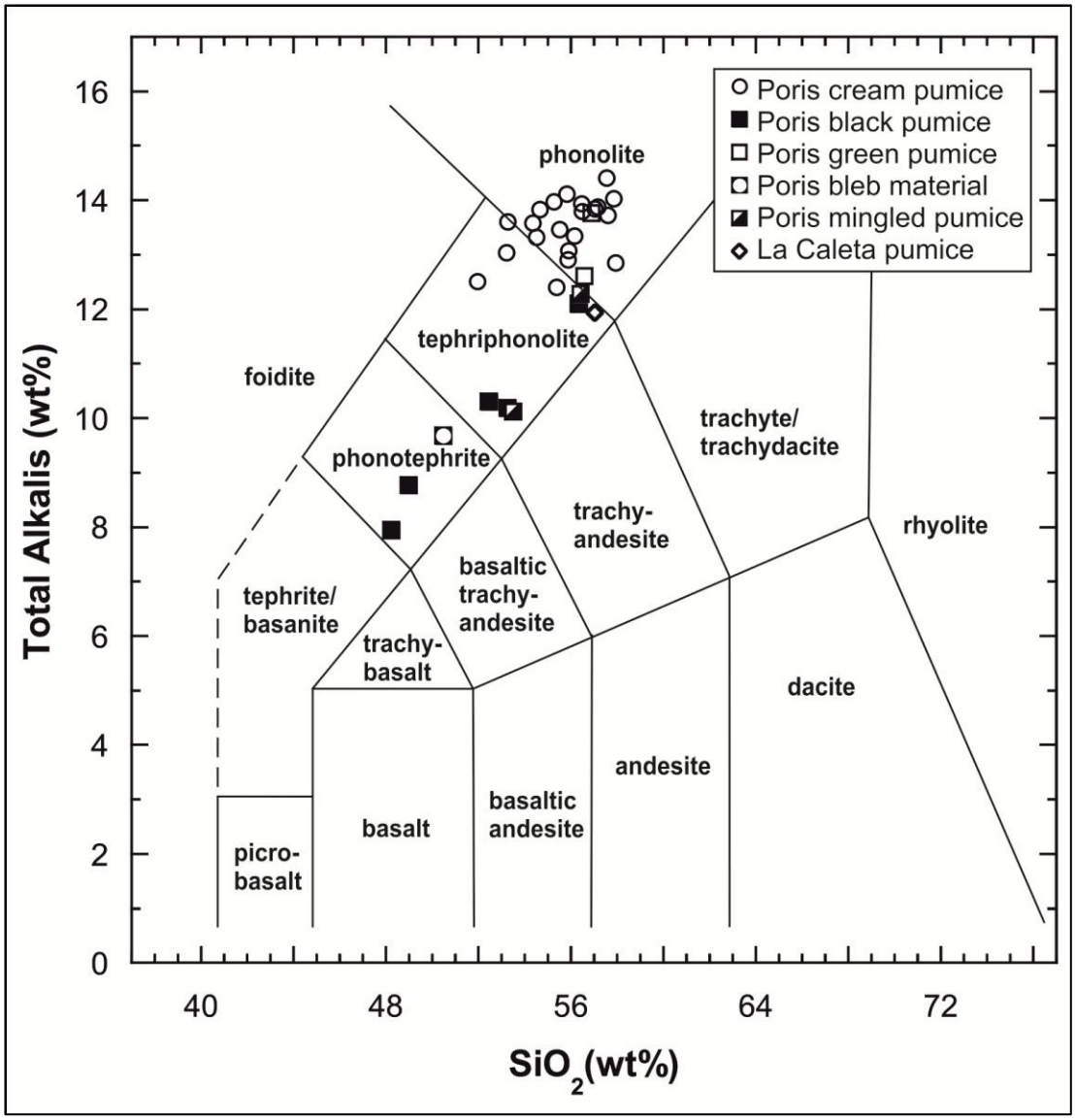

Figure 6.6 TAS classification diagram for pumices analysed in this study. The samples all plot within the expected fields of phonolite, tephriphonolite and phonotephrite, indicating that alkali leaching in Poris pumices is not a large problem.

Figure 6.7 (overleaf) (a) Nb-Zr covariation of Poris samples tagged according to TAS classification. Two magma series with petrogenetically distinct evolutionary trends occur; (i) high Zr-phonolite and tephriphonolite (cream), and (ii) low-Zr phonolite, tephriphonolite, and phonotephrite. The mingled pumice samples plot in the low-Zr group, indicating that they predominantly comprise this magma type. (b) Close up showing the analytical uncertainty bars of 2 samples, the small scale of which illustrates that the analyses show real compositional variation.

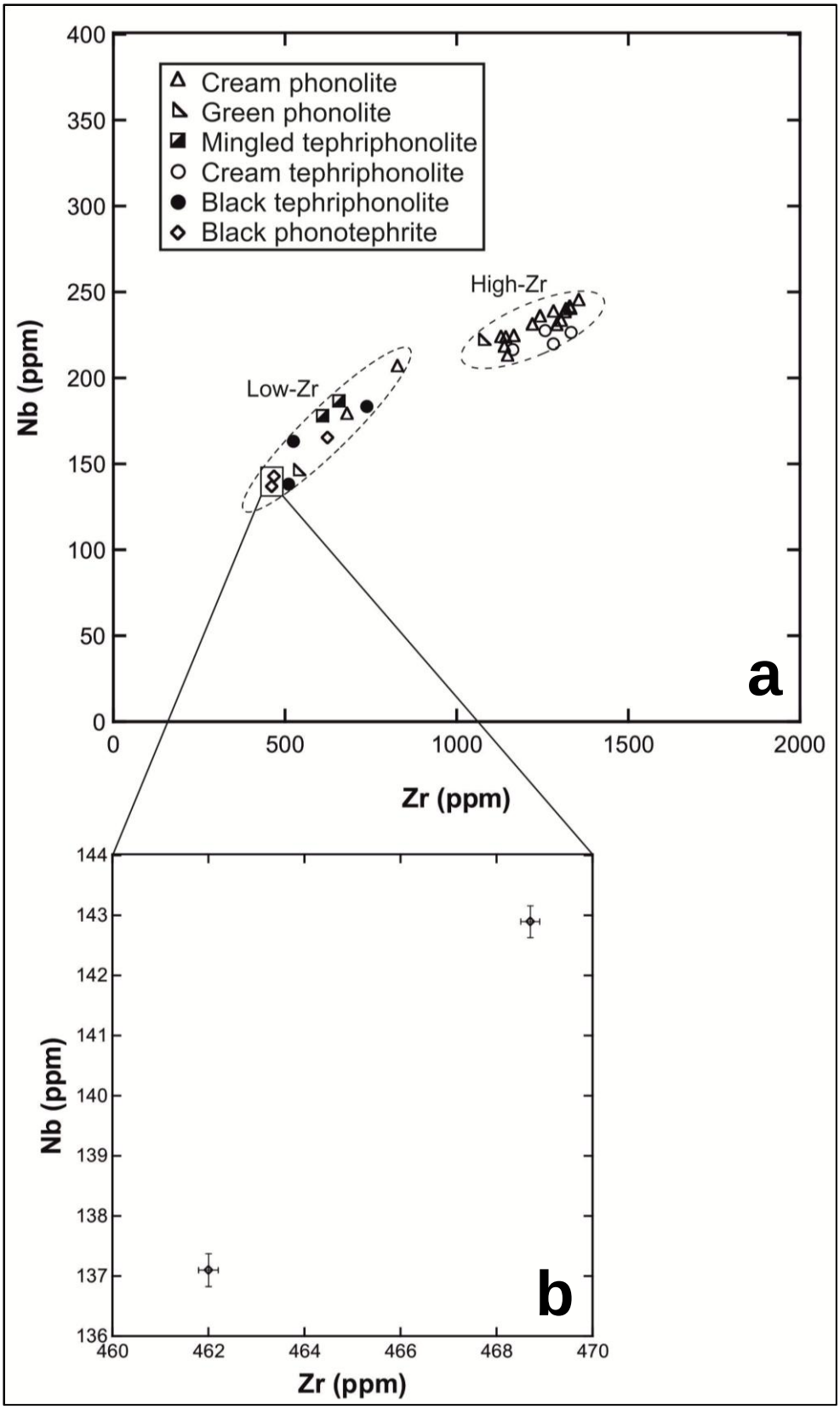
Cream phonolite
Green phonolite
Mingled tephriphonolite
Cream tephriphonolite
Black tephriphonolite
Black phonotephrite
High-Zr
Low-Zr
Nb (ppm)
Zr (ppm)
a
b

Geochemical Variation

All the pumices analysed from the lower Poris succession are of the high-Zr magma type, whereas pumices sampled from the upper breccia lithofacies, in both proximal and distal areas, are an assortment of high- and low-Zr phonolite, tephriphonolite and phonotephrite. The occurrence of mingling (e.g. phonotephrite bleb sample FSS6a) throughout the succession indicates that the low-Zr magma type was available throughout the eruption, before becoming prevalent in the eruptive material during the final stages. The physical explanation for this is discussed in Chapter 7. The two cream pumice samples from above the lithic-block layer in proximal splBr are of the low-Zr type, whereas the cream pumices sampled from the distal breccia are not; however, there are too few samples to make a petrogenetic comment.

There is a subtle change in cream pumice chemistry in lower to mid Poris stratigraphy, as well as the large-scale geochemical variation prominent in the upper part (labelled on Fig 6.8). Proximal high-Zr pumices from //bpL, s-ds-mlLT, mLT, and the base of splBr contain >1240 ppm Zr. However, at slcrT and spBT there is a distinct decrease in Zr concentration, where pumices contain 1076-1221 ppm Zr. In distal samples, cream pumices from Members 1, 3 and 7 contain >1240 ppm zirconium. DIST 13, from the Caballos fall unit in the lower stratigraphy, contains only 1163 ppm Zr. Cream pumices from distal Members 8 and 9 also have this slightly lower Zr content (<1200 ppm). These series trends are matched by other trace elements, which behave in a coherent fashion; Zr variation is shown alone on Figure 6.8 for clarity. These changes are relatively minor, and, given the small sample set, may have little statistical validity; however, such subtle variations do provide additional information that is considered in correlating between proximal and distal lithofacies (see Chapter 7).

Figure 6.8 (overleaf) Geochemical variation diagrams showing changes in Zr concentration throughout the proximal and distal Poris. The location of data points corresponds to the sample positions within the succession. The proximal general vertical section is from this study and the distal GVS is from Brown and Branney (2004). All geochemical data are from this study. Note the different scales on the logs, and the differences in proximal and distal stratigraphy. Correlation of the sequences is discussed in Chapter 7. Note that at the labelled subtle 'dogleg' in the trend, Zn, U, Th, Rb, Nb and Ga decrease along with Zr, whereas increases occur in FeO, MgO, Y, V, Sr, and Nd concentrations.

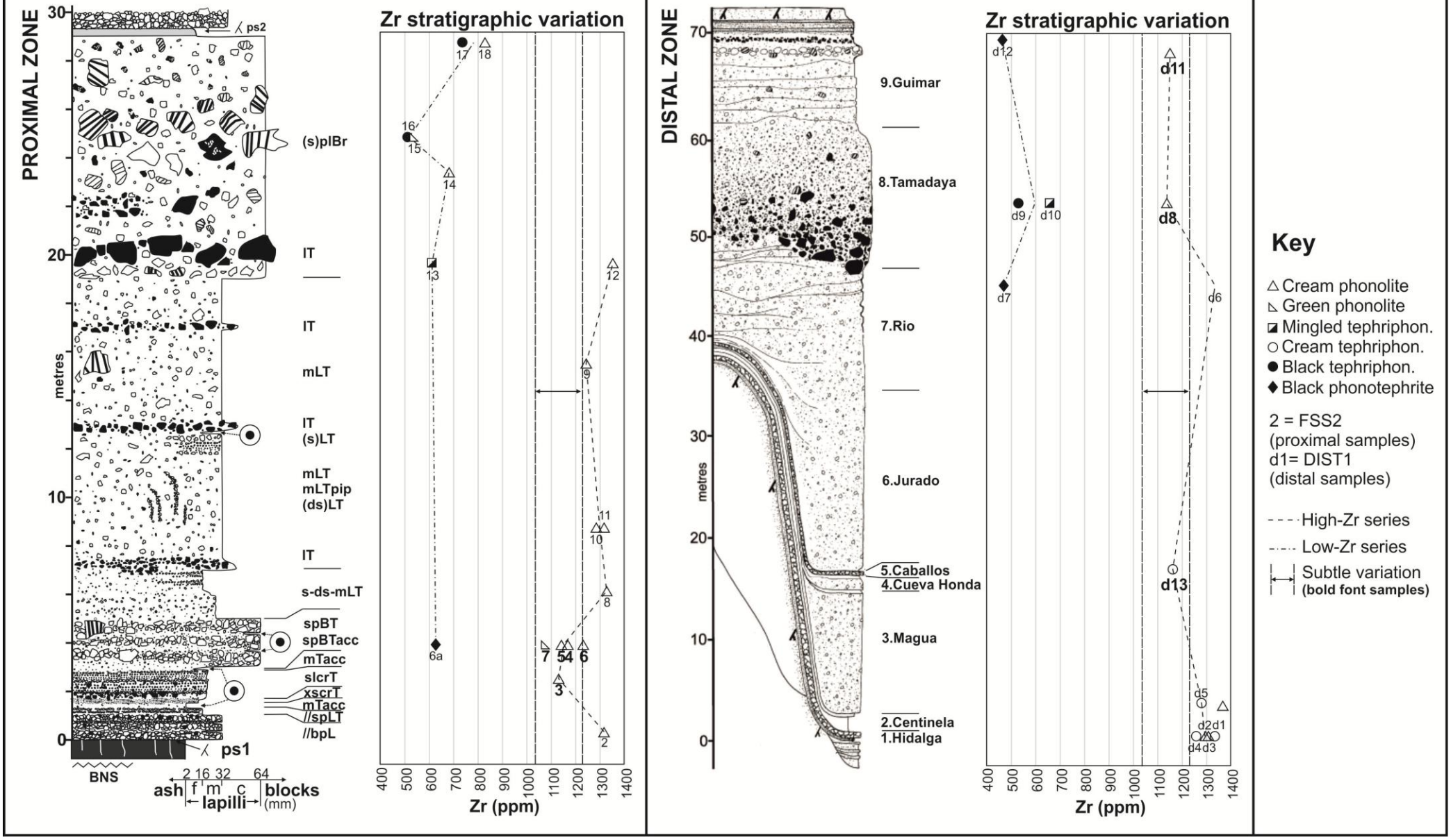
PROXIMAL ZONE
metres
ps2
(s)plBr
IT
IT
mLT
IT
(s)LT
mLT
mLTpip
(ds)LT
IT
s-ds-mLT
spBT
spBTacc
mTacc
slcrT
xscrT
mTacc
//spLT
//bpL
ps1
BNS
ash
f
m
c
lapilli
2 16 32 64
blocks
(mm)
Zr stratigraphic variation
Zr (ppm)
DISTAL ZONE
9.Guimar
8.Tamadaya
7.Rio
6.Jurado
5.Caballos
4.Cueva Honda
3.Magua
2.Centinela
1.Hidalga
Zr stratigraphic variation
Zr (ppm)
Key
Cream phonolite
Green phonolite
Mingled tephriphon.
Cream tephriphon.
Black tephriphon.
Black phonotephrite
2 = FSS2
(proximal samples)
d1= DIST1
(distal samples)
High-Zr series
Low-Zr series
Subtle variation
(bold font samples)

Pumices were analysed from multiple exposures of spBT, mLT, splBr and the distal Plinian unit to assess any geochemical variability within lithofacies. Pumices from the distal Plinian unit are grouped closely (D1-D4 on Fig 6.8) as are proximal samples 9-11 from mLT. There is more variability in spBT; samples FSS4 and FSS5 are similar in Zr content, whereas FSS6 is slightly higher. This sample contained prominent bleb material that was carefully extracted for separate analysis and found to be of phonotephrite composition (6a, Fig 6.8); it may plot higher than FSS4 and FSS5 because the effect of mingling was removed. Evidence of bleb-type mingling is commonly found in hand specimens from the spBT facies, and samples 4 and 5 may have contained cryptic mingling that was not removed. Sample FSS7, lower than 4, 5 and 6, is a green pumice. It is conceivable that increased mingling and mixing between low-Zr phonotephrite and high-Zr phonolite at this stage of the eruption caused the dogleg in the high-Zr series. This scenario may also explain the doglegs present in the distal trend (D11, D8, D13, Fig. 6.8), and is discussed below in Chapter 7.

In the upper part of the succession, the black pumices DIST9 and DIST10 are from the same height and location, but differ, containing 525 ppm and 657 ppm Zr respectively. DIST10 contains streaks of green glass, whereas DIST9 contains no evidence of mingling (Fig 6.9). FSS13, a mingled sample close to the lithic concentration in the proximal zone, contains 610 ppm Zr. The degree of internal fluidal-type mingling, even if subtle to the eye, appears to affect the bulk geochemistry of black pumices, just as the black bleb-type mingling within predominantly cream pumices affects the geochemical trend in spBT.

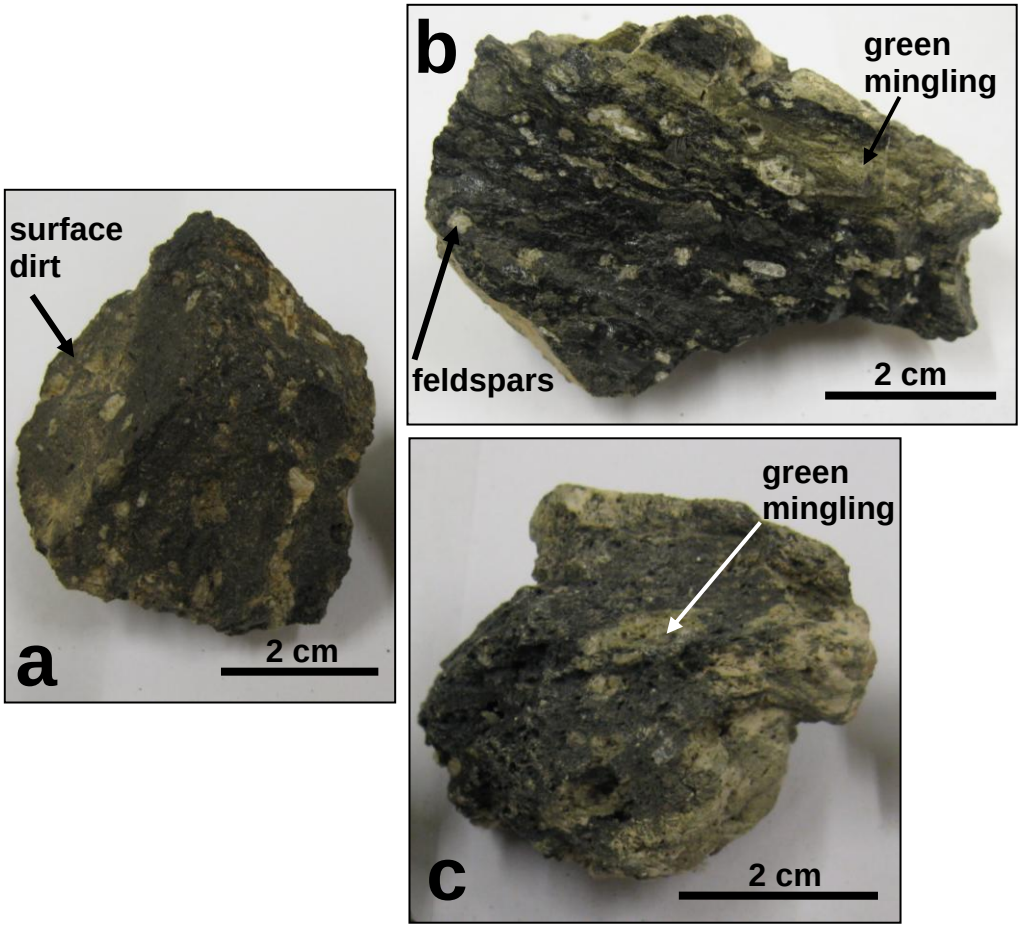

Figure 6.9 (a) Black phenocrystic pumices with little evidence of magma mingling (DIST9), although cryptic mixing cannot be ruled out. (b) Distal black pumice contains streaks of green pumice (DIST10). (c) Proximal black pumice showing mingling (FSS10).

6.5.3 Precision and accuracy

During XRF analysis, standard reference materials were analysed to gauge accuracy and precision for the technique. Each standard was analysed multiple times throughout the sample runs, to provide reproducibility measurements (% standard deviation). The mean result was then compared to the published standard values (from Govindaraju, 1994, the Geological Survey of Japan, and the University of Leicester) to give an indication of accuracy. A phonolite standard was not available, but the rhyolite standard analysed provided relative accuracy results of +/-1.57% for Nb and 0.19% for Zr. On average, for 8 standards of various geological materials analysed, Zr precision was to within 0.26% and relative accuracy 3.36%, and Nb precision was 0.43% and relative accuracy 2.68%. Trace element data for the rhyolite standard JR3 are shown in Table 6.3a, and major element data for BCS375, a soda feldspar standard, are shown in Table 6.3b (see appendix for the full accuracy and precision dataset).

Relative counting statistic error (%CSE) values are commonly used in XRF analysis to give an indication of instrumental analytical uncertainty (Nick Marsh, pers. comm., 2012). This uncertainty is negligible; when multiplied by 3 and plotted as 3σ error bars on the data, the bars are only seen clearly when enlarged (Fig. 6.7). If the accuracy data for the rhyolite standard were used to create error bars for the Poris data, the potential variability would be similarly low, indicating that the geochemical variation observed in the Poris stratigraphy is real and not a result of spread in the data.

Element (ppm)	Published Data	Run 1	Run 2	Run 3	Run 4	Run 5	Mean	std. dev.	%std. dev. (precision)	Absolute error	Relative accuracy (%)
Mo	0.49	-0.43	-0.23	-0.38	-0.27	-0.25	-0.31	0.09	27.75	-0.80	164.23
Nb	564	572	573	572	573	573	573	0.24	0.04	8.59	1.52
Zr	1675	1672	1671	1672	1672	1672	1672	0.39	0.02	-3.25	0.19
Y	166	174	174	174	174	174	174	0.12	0.07	8.18	4.93
Sr	10.4	10.2	10.6	10.5	10.1	10.2	10.3	0.21	2.00	-0.05	0.50
Rb	453	473	471	471	471	470	471	0.85	0.18	18.42	4.07
Ga	36.6	38.1	38.8	38.5	37.5	39.0	38.4	0.62	1.62	1.77	4.83
Zn	209	193	194	193	193	194	193	0.37	0.19	-15.61	7.47
Cu	2.9	0.8	1.3	1.5	1.9	1.5	1.4	0.39	27.58	-1.49	51.23
Ni	1.6	3.6	4.7	4.4	3.7	6.7	4.6	1.25	27.04	3.03	189.58
Co	0.98	3.20	1.79	2.56	1.82	2.61	2.39	0.59	24.81	1.41	144.38
Cr	3.5	-1.5	-2.4	-0.1	-1.6	-0.9	-1.3	0.83	64.66	-4.79	136.89
V	4.2	1.2	1.5	1.8	1.7	0.6	1.4	0.49	35.82	-2.84	67.56
Sc	0.50	-0.31	0.73	1.39	0.03	-0.17	0.33	0.71	213.71	-0.17	33.22
Ba	65.8	50.2	48.2	46.7	50.4	45.5	48.2	2.15	4.45	-17.60	26.75
La	179	158	158	158	160	157	158	1.04	0.66	-21.03	11.75
Ce	327	312	312	309	310	310	311	1.48	0.47	-16.26	4.97
Nd	107	105	105	105	106	105	105	0.36	0.35	-1.80	1.68
Pb	32.8	36.1	36.2	37.4	37.4	37.4	36.9	0.7	1.82	4.08	12.44
Th	112	114	114	114	114	114	114	0	0.14	1.89	1.69
U	21.1	21.4	21.6	21.8	21.8	21.4	21.6	0.2	0.94	0.51	2.43

Table 6.3a Trace element precision and accuracy data from JR3, a rhyolite powder standard. Published values are from the Geological survey of Japan, courtesy of Nick Marsh at Leicester University. See appendix for full standard dataset.

Element (wt%)	Published data	Run 1	Run 2	Run 3	Run 4	Run 5	Run 6	Run 7	Run 8	Run 9	Run 10	Run 11	Run 12	Mean	std. dev.	%std. dev. (precision)	Absolute error	Relative accuracy (%)
SiO_2	67.10	66.82	66.72	66.49	66.42	65.77	66.44	66.43	66.42	66.89	66.16	67.00	66.66	66.518	0.336	0.51	-0.58	0.87
TiO2	0.38	0.37	0.37	0.37	0.37	0.37	0.37	0.37	0.37	0.37	0.36	0.38	0.37	0.370	0.004	0.97	-0.01	2.75
Al_2O_3	19.80	20.18	20.10	20.03	20.06	19.84	20.13	20.08	20.05	20.16	19.97	20.34	20.20	20.095	0.124	0.62	0.30	1.49
Fe2O3	0.12	0.12	0.12	0.12	0.11	0.12	0.12	0.12	0.12	0.12	0.11	0.11	0.11	0.116	0.002	1.88	0.00	3.66
Mno	0.00	0.01	0.01	0.01	0.01	0.01	0.01	0.01	0.01	0.01	0.01	0.01	0.01	0.006	0.001	9.53	0.00	84.66
MgO	0.50	-0.23	-0.22	-0.23	-0.20	-0.20	-0.21	-0.21	-0.18	-0.20	-0.23	-0.24	-0.25	-0.216	0.021	9.52	-0.72	143.10
CaO	0.89	0.85	0.84	0.84	0.85	0.85	0.85	0.85	0.84	0.84	0.84	0.84	0.83	0.843	0.007	0.84	-0.05	5.30
Na_2O	10.40	10.49	10.51	10.48	10.45	10.32	10.51	10.48	10.46	10.51	10.47	10.64	10.58	10.492	0.076	0.73	0.09	0.89
K_2O	0.79	0.77	0.76	0.76	0.76	0.76	0.76	0.75	0.76	0.76	0.75	0.76	0.76	0.759	0.004	0.52	-0.03	3.87
P2O5		0.02	0.02	0.02	0.02	0.02	0.02	0.02	0.02	0.02	0.02	0.02	0.02	0.020	0.002	10.23		
SO_3		0.06	0.06	0.06	0.06	0.06	0.06	0.06	0.06	0.06	0.06	0.00	0.00	0.049	0.024	48.51		
Total		99.46	99.30	98.95	98.90	97.92	99.03	98.95	98.92	99.54	98.53	99.84	99.28					

Table 6.3b Major element precision and accuracy data from BCS375, a soda feldspar standard. Published values are from Govindaraju (1994), courtesy of Nick Marsh at Leicester University. See appendix for full standard dataset.

6.6 Electron microprobe analysis

During electron probe microanalysis (EPMA), a solid material is bombarded by an accelerated and focused electron beam. Each element generates emissions of a characteristic wavelength, which are detected by an X-Ray spectrometer and translated into element concentrations and distribution patterns (Gill, 1997). In this study, EPMA was used to analyse the crystal chemistry of 15 pumice samples (see EPMA column in Table 6.1). Mineral analyses were obtained at the University of Leicester using carbon-coated polished grain mounts on a JEOL JXA-8600S electron microprobe with an accelerating voltage of 15 kV, a probe current of 30 nA, and a beam diameter of 10 microns. Characteristic peak intensities were measured during 20 second count times, with 10 seconds at each of the background positions selected on either side of the peak. Quantitative background-corrected results were standardised against a combination of synthetic materials and well characterised natural minerals (see Appendix for list) and corrected for matrix effects using a ZAF correction procedure. Minimum detection limits were calculated as 3 standard deviations above background and typically range from 0.02 wt% for Na_2O to 0.05 wt% for FeO and NiO.

6.6.1 Sample preparation

Pumice clasts were crushed with an agate pestle and mortar, and crystals were handpicked using an optical microscope. The remaining material was then sieved and the 100-300 μm fraction underwent sodium polytungstate heavy liquid separation, to separate minerals and glass. Grain mounts, comprising handpicked crystals, crystals 100-300 μm, and pure glass 100-300 μm, were produced for each sample. See Appendix for grain mount preparation technique.

6.6.2 Results

A suite of major elements was obtained for each crystal analysed; SiO_2, TiO_2, Al_2O_3, Cr_2O_3, FeO, MnO, MgO, CaO, Na_2O, K_2O, and NiO. Results were then grouped by mineral type. Alkali feldspars were encountered most commonly during the analysis, while nosean-haüyne and olivine were sparse. Average compositions for each mineral group are shown in Table 6.4 (see Appendix for complete lists). The totals

	(wt%)	SiO_2	TiO_2	Al_2O_3	Cr_2O_3	FeO	MnO	MgO	CaO	Na_2O	K_2O	NiO	Total	Or	Ab	An
Alkali feldspar (n=147)	**mean**	64.43	0.09	19.42	0.01	0.53	0.03	0.03	0.85	6.94	6.23	0.01	98.56	35.59	60.28	4.12
	sd	1.91	0.18	1.50	0.01	1.08	0.06	0.13	0.65	0.87	1.58	0.01	2.03			
	%rsd	2.97	194.91	7.73	162.18	202.05	244.23	419.50	76.58	12.61	25.36	150.91	2.06			
Plagioclase (n=47)	**mean**	54.12	0.15	27.07	0.01	0.59	0.02	0.05	9.59	5.58	0.72	0.01	97.90	4.02	48.84	47.15
	sd	3.22	0.24	2.61	0.01	0.43	0.07	0.04	3.01	1.62	0.91	0.01	1.70			
	%rsd	5.96	161.91	9.63	167.09	72.07	320.83	82.18	31.34	29.02	125.70	198.58	1.74			
Titanomagnetite (n=71)	**mean**	0.43	13.55	3.35	0.75	69.37	1.51	3.43	0.08	0.07	0.04	0.02	92.61			
	sd	1.77	4.38	2.96	3.76	8.83	1.06	2.44	0.21	0.16	0.16	0.04	3.04			
	%rsd	414.69	32.33	88.50	501.29	12.72	70.53	71.03	248.47	231.38	356.03	156.38	3.29			
Amphibole (n=65)	**mean**	38.89	6.33	12.77	0.01	10.53	0.22	12.43	11.97	2.75	0.96	0.01	96.87			
	sd	1.08	0.50	0.87	0.01	1.03	0.10	0.73	0.60	0.26	0.16	0.01	1.29			
	%rsd	2.77	7.85	6.81	145.00	9.78	46.33	5.87	4.98	9.31	16.82	161.54	1.33			
Pyroxene (n=62)	**mean**	47.56	2.20	5.00	0.01	7.86	0.39	12.29	22.31	0.90	0.02	0.01	98.54			
	sd	2.48	1.05	2.30	0.02	1.26	0.30	0.85	0.46	0.41	0.03	0.02	1.33			
	%rsd	5.21	47.86	45.95	156.82	16.09	76.61	6.93	2.08	45.46	186.84	162.51	1.35			
Biotite (n=17)	**mean**	37.06	6.52	13.93	0.01	12.66	0.43	14.28	0.20	0.97	8.26	0.01	94.33			
	sd	1.83	1.81	2.98	0.01	1.73	0.18	2.01	0.47	0.13	0.86	0.02	1.29			
	%rsd	4.95	27.76	21.43	153.51	13.69	42.39	14.09	234.57	13.19	10.45	130.87	1.37			
Ilmenite (n=16)	**mean**	0.01	46.23	0.50	0.02	44.05	1.27	5.16	0.07	0.04	0.01	0.00	97.36			
	sd	0.04	4.15	0.42	0.02	3.98	0.70	1.47	0.06	0.07	0.02	0.01	1.32			
	%rsd	288.25	8.98	83.66	116.28	9.03	55.27	28.46	84.68	193.40	200.15	231.24	1.35			
Titanite (n=12)	**mean**	29.09	35.80	1.00	0.00	1.73	0.11	0.03	26.60	0.09	0.01	0.01	94.47			
	sd	0.32	0.54	0.10	0.00	0.15	0.02	0.03	0.49	0.04	0.01	0.02	0.93			
	%rsd	1.11	1.51	9.69	346.41	8.59	21.68	103.83	1.86	46.10	128.55	144.62	0.98			
Nosean (n=8)	**mean**	39.35	0.01	31.16	0.01	0.26	0.02	0.00	5.43	16.90	1.08	0.00	94.22			
	sd	1.51	0.02	1.13	0.01	0.04	0.02	0.00	1.02	1.63	0.47	0.01	3.14			
	%rsd	3.83	189.03	3.63	137.33	15.52	111.98	282.84	18.82	9.63	43.27	241.80	3.33			
Hauyne (n=2)	**mean**	36.54	0.05	28.49	0.00	0.43	0.02	0.22	10.76	13.94	0.93	0.00	91.37			
	sd	1.51	0.07	0.49	0.00	0.21	0.02	0.06	0.63	0.26	0.17	0.00	0.62			
	%rsd	4.13	141.42	1.74		49.34	82.22	24.96	5.84	1.85	18.45		0.68			
Olivine (n=3)	**mean**	38.85	0.02	0.02	0.03	17.35	0.24	42.53	0.29	0.03	0.00	0.14	99.51			
	sd	0.22	0.02	0.02	0.03	0.42	0.01	0.32	0.04	0.02	0.00	0.01	0.79			
	%rsd	0.57	97.31	124.90	127.11	2.41	5.28	0.75	13.02	89.89		8.32	0.80			

Table 6.4
Average compositions of Poris pumice phenocrysts analysed by EPMA. Mean feldspar compositions are shown in terms of albite (Ab), orthoclase (Or) and anorthite (An).

for some mineral groups are quite low, particularly the anhydrous minerals; this could be a result of a number of factors, such as poor polish, the beam hitting cleavage planes or points close to a rim, 'mixed' analyses due to contacts not normal to the surface, or instrumental error (Rob Wilson, pers. comm., 2012). Furthermore, some minerals, such as titanomagnetite, may produce low totals due to an unreported ferric iron phase.

The Poris phenocryst assemblage consists of alkali feldspar, plagioclase, kaersutite (amphibole), diopside (pyroxene), titanomagnetite, titanite (sphene), biotite, ilmenite, nosean-haüyne and rare olivine. Some minerals are more prevalent in one pumice type than another, for example 14 of the 17 biotites sampled were from low-Zr pumices and 13 of the 14 titanites analysed were from high-Zr cream phonolite pumices, but this may be an effect of sampling.

Cream pumices contain a wide range of feldspar mineralogies, from bytownite through to sanidine, whereas black and green pumices contain predominantly sanidine and anorthoclase; only a few plagioclase feldspars were analysed in black and mingled pumices (Fig. 6.10). The green splBr pumice FSS15 is rich in anorthoclase. A petrological study of the Bandas del Sur deposits by Bryan *et al.* (2002) reports feldspar compositions from the 668 ka Arico ignimbrite that are tightly clustered in the anorthoclase field, and from the 600 ka Granadilla ignimbrite that are clustered in the anorthoclase and oligoclase fields (ages from Brown *et al.*, 2003); the Poris analyses are more widely spread than the patterns observed in these older deposits.

Results show that there is no clear link between mineral composition and stratigraphy in the Poris Formation. Amphibole, biotite, and pyroxene analyses show little overall compositional variation (Figs 6.11-6.13). The pyroxenes are diopsides, which is the predominant pyroxene in Bandas del Sur ignimbrites (Bryan *et al.*, 2002). A wide variation of titanomagnetite composition occurs, but there is no apparent systematic variation with stratigraphic height in either proximal or distal samples (Fig 6.14). There are too few analyses of nosean, haüyne and olivine to aid

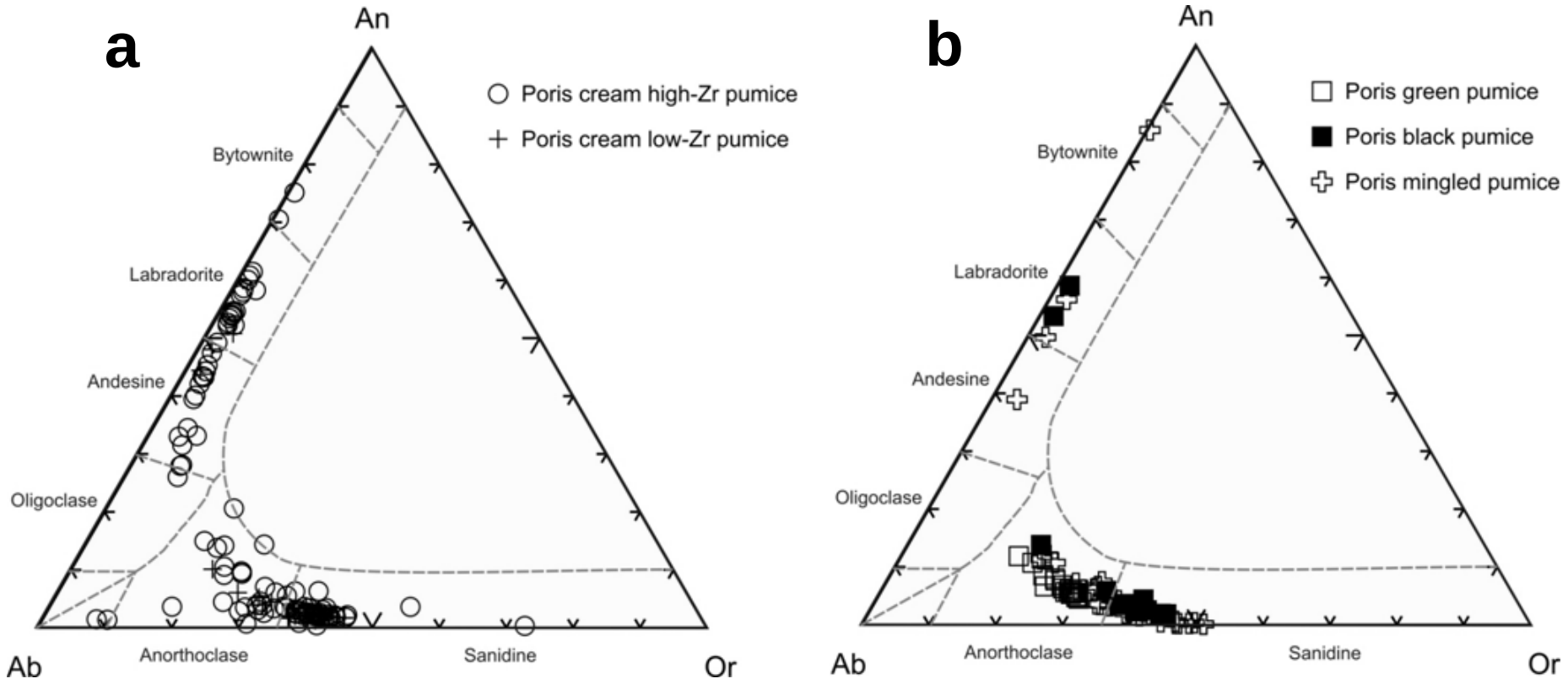

Figure 6.10 Comparative tri-plots showing feldspar composition in Poris pumices. Ab = albite; An = anorthoclase; Or = orthoclase. (a) Cream pumices contain a wide range of feldspar compositions, with both plagioclase and alkali feldspar varieties. (b) Green, black and mingled pumices contain a far more restricted range of feldspar copmpositions. Mingled pumices contain some plagioclase crystals, but only two plagioclases were encountered in the analysis of black pumices. No plagioclases were analysed in the green pumice sampled.

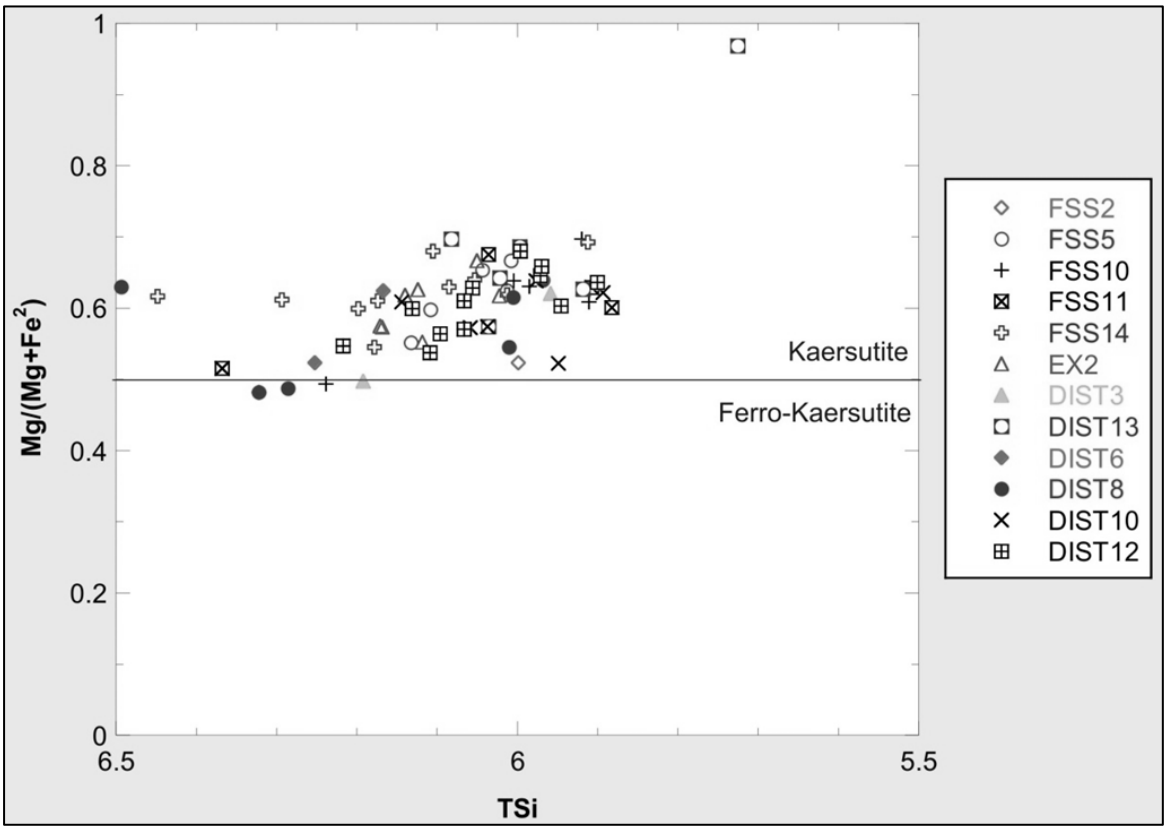

Figure 6.11 Amphibole compositions in Poris pumices, plotted as described in Bryan *et al*. (2002). There is no obvious variation with stratigraphy in the data. Sample names correspond to Table 6.1.

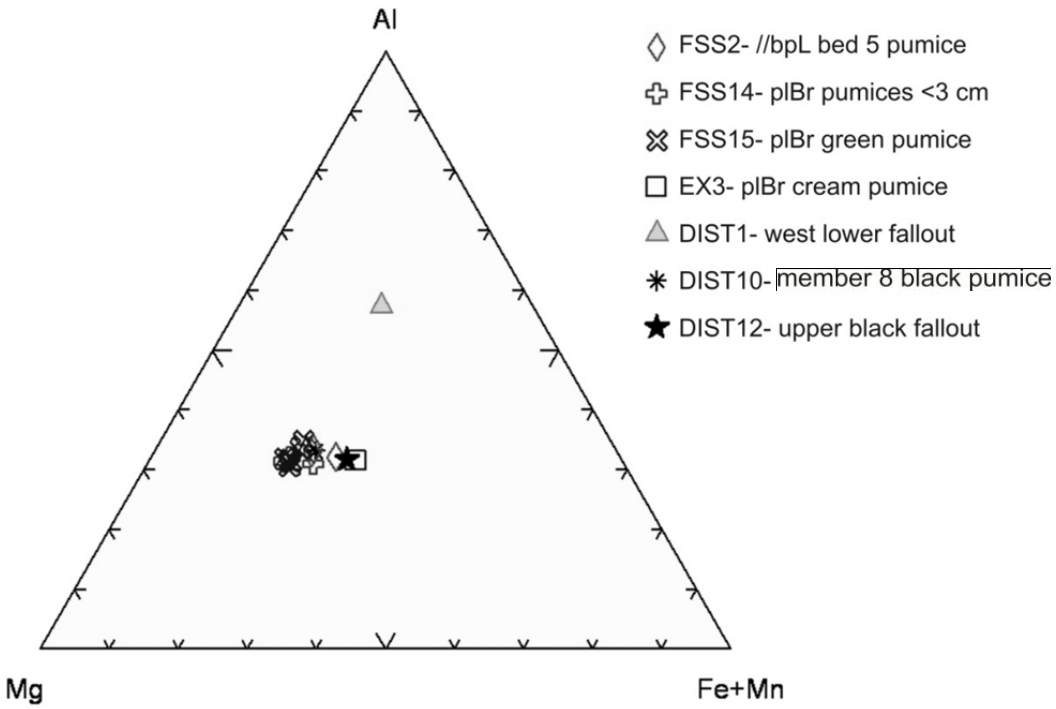

Figure 6.12 Biotite compositions in Poris pumices, plotted as shown in Bryan *et al.* (2002). Biotites were found in only 7 of the samples, and were most common in the green pumice analysed. The anomaly DIST1 may be a result of the electron beam exciting more than one mineral.

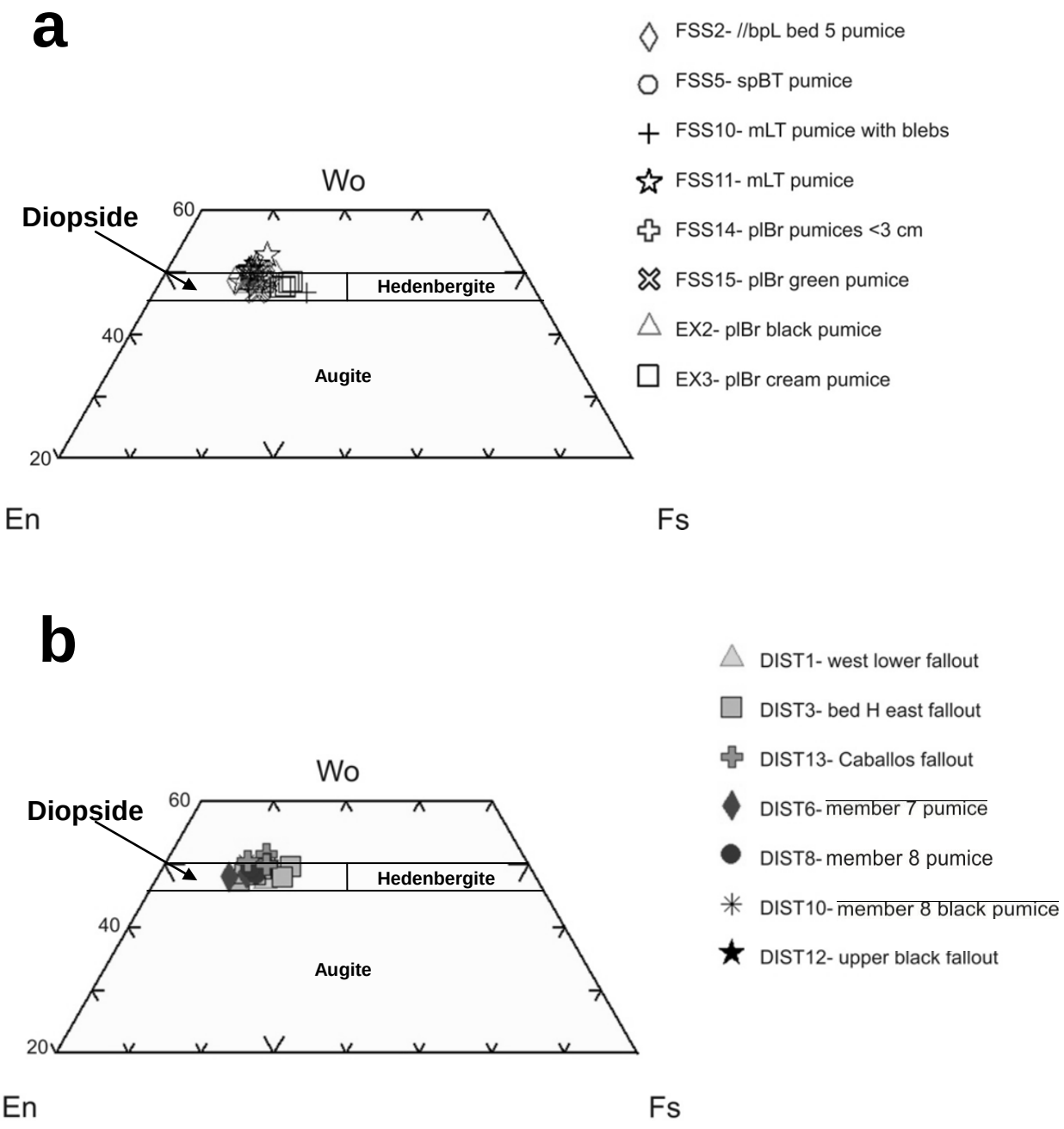

Figure 6.13 Pyroxene compositions in proximal (a) and distal (b) Poris pumices, expressed as the wollastonite-enstatite-ferrosilite system. There is a very little compositional variation; analyses are closely clustered in or near the diopside field (after Morimoto, 1988).

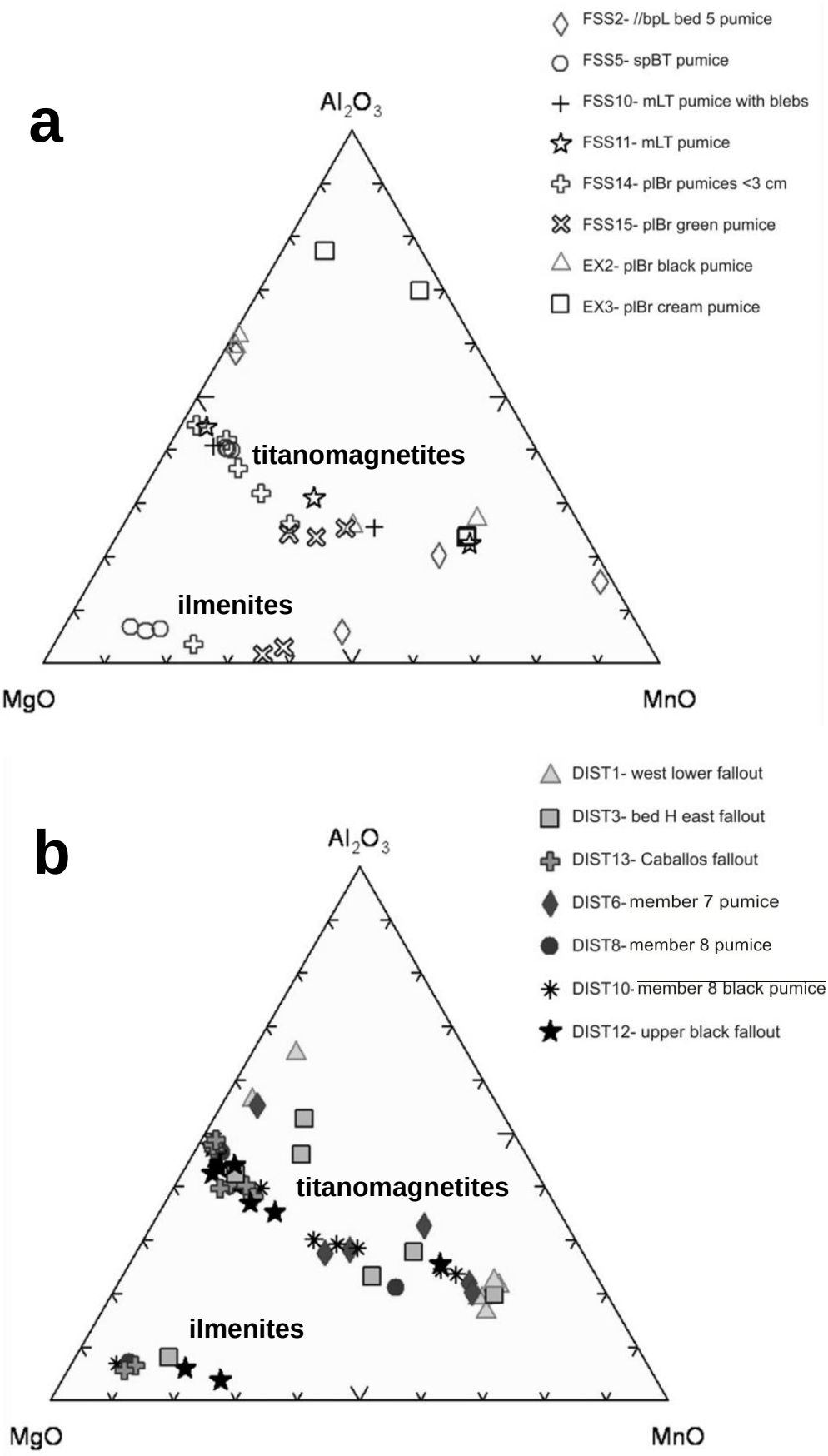

Figure 6.14 Titanomagnetite and ilmenite minor element compositions in (a) proximal and (b) distal Poris pumices, plotted as shown in Bryan *et al.* (2002).

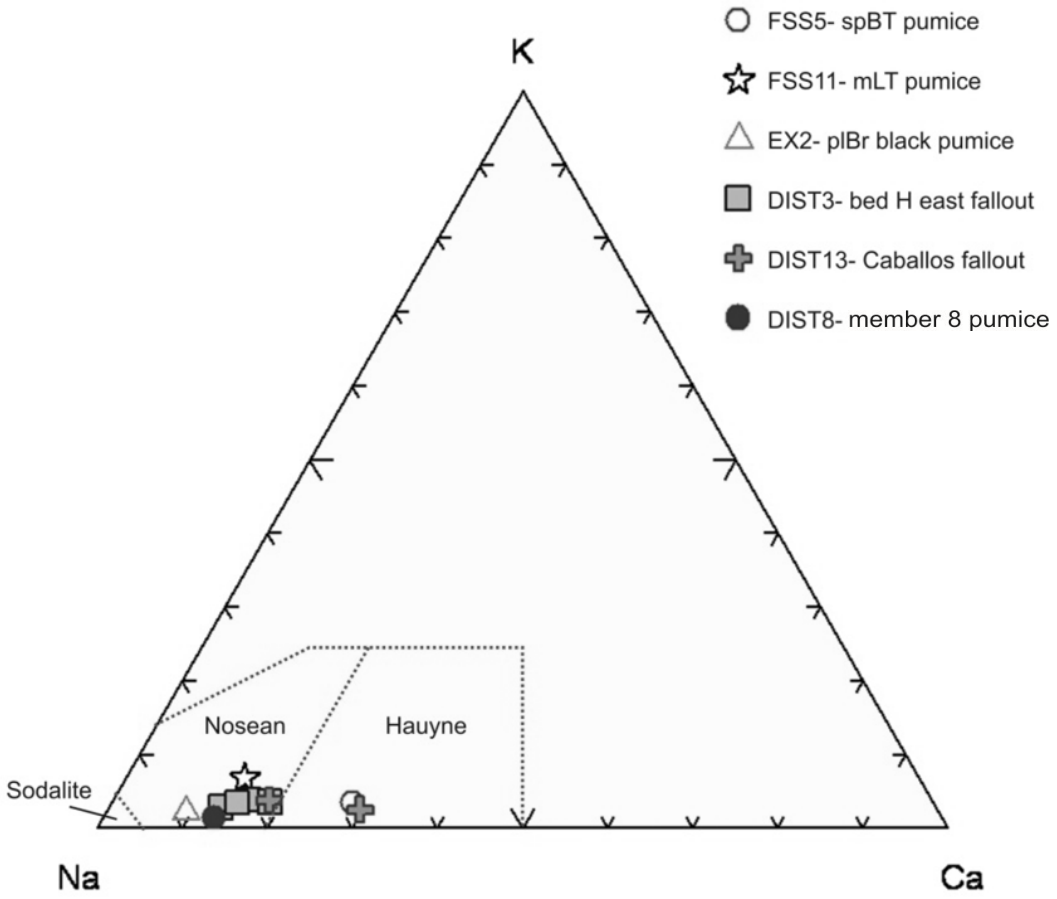

Figure 6.15 Haüyne and nosean compositions in Poris pumices. Field boundaries after Bryan *et al.* (2002), from Lessing and Grout (1971). The only two haüyne analyses are from the proximal hybrid unit and the distal Plinian unit (see Chapter 7 for discussion of lithofacies correlation)

correlation between proximal and distal stratigraphy; the only two haüyne analyses are from the proximal hybrid unit and the distal mid-stratigraphy Plinian unit (the 'Caballos Member' of Brown and Branney, 2004) (Fig 6.15). The link between these units is discussed in Chapter 7. The low number of analyses of haüyne and nosean crystals may not be a true representation of their occurrence; the low density of these feldspathoids (~2.4 gm/cc) may have caused them to become preferentially depleted during the heavy mineral separation process and extracted along with the glass.

6.7 Discussion

6.7.1 Chemical variation

A significant feature revealed by the bulk analyses of Poris pumice is the duality of the magmatic system; there are two petrogenetically distinct magma series. The lower part of the succession is dominated by high-Zr pumice, while in the upper part low-Zr pumices become more abundant. Colour is not necessarily indicative of pumice composition, although all black pumices analysed are of the low-Zr magma type.

Small-scale variation exists within the high-Zr series. A 'dogleg' occurs in the pumice data plots at slcrT and spBT in the proximal zone, and a similar feature occurs at the mid-stratigraphy Plinian unit (the 'Caballos' of Brown and Branney, 2004), and at the top of the sequence, in the data from the distal area.

The occurrence of magma mingling textures, as both discrete blebs and more diffuse fluidal forms, is evidence that the two Poris magma series were connected. The subtle changes in geochemistry described above are most simply reconciled with variable interaction between the two magmas at different stages of the eruption. The slcrT lithofacies was deposited following phreatomagmatic explosions (see Chapter 4) that may have changed the plumbing system, leading to the eruption of pumices with decreased Zr content at this level and in the spBT lithofacies above. The change back to higher Zr concentrations in the mLT facies may indicate that less mingling and mixing occurred at this stage, following the return to magmatic conditions. Following caldera collapse, the sub-volcanic structure was sufficiently

modified to allow the large-scale tapping of the low-Zr magma, allowing substantial mingling of the two magma types. The physical aspects of these events, and their relevance to lithofacies correlation with the distal record, are discussed further in Chapter 7.

6.7.2 Mineralogy

This study finds that the same crystal *assemblage* occurs in both low-Zr and high-Zr Poris pumices: alkali feldspar + plagioclase + kaersutite + diopside + titanomagnetite + ilmenite + titanite + nosean-haüyne +/- olivine. This crystal assemblage similarity is conceivably an artefact of cryptic mixing between the two magma series. Relative modal abundances of the crystals in the two types have not been determined; to do this would be a non-trivial exercise beyond the scope of this work. Poris crystal chemistry shows little variability with stratigraphic height, in both the proximal and the distal successions, indicating that the eruption tapped magmas with similar phases throughout.

Bryan *et al.* (2002) report that phonolite pyroclastic deposits of the Bandas del Sur contain: alkali feldspar + biotite + sodian diopside + titanomagnetite + ilmenite + nosean-haüyne + titanite + apatite. These findings broadly fit with this study, although a direct comparison of Poris data is problematic because the units referred to by Bryan *et al.* (2002) as the Poris, La Mareta, Upper Grey and Pedrigal ignimbrites have subsequently been all deemed to be parts of the Poris succession (Brown *et al.*, 2003; Edgar *et al.*, 2007) (see Fig. 2.11).

Edgar *et al.* (2002) report that Poris phonolite pumices contain alkali feldspar, biotite, clinopyroxene, iron-titanium oxides, and titanite, and that black pumices contain kaersutite, plagioclase, clinopyroxene, and Fe-Ti oxides. This bimodal mineralogy is not found in this study. The paucity of plagioclase crystals in low-Zr pumices reported here conflicts with the results of Edgar *et al.* (2002); this may be a chance effect of crystal sample selection during analysis, or possibly an artefact of the mineral density-separation process.

Chapter Seven

A new model for the 273 ka Poris eruption

Correlation of a proximal ignimbrite with its distal counterpart

7.1 Introduction

Previous workers have devised eruption models for the Poris event (Edgar *et al.*, 2002; Brown and Branney, 2004b), but these studies do not fully consider the proximal record, or account for changes in lithofacies with distance from the vent. The investigation of proximal Poris lithofacies architecture presented in Chapters 4 and 5 sheds light on the near-vent processes operating during the eruption, and the analysis of pumice from distal and proximal deposits, reported in Chapter 6, proves that they are counterparts. In this chapter, proximal lithofacies are correlated and compared with their distal counterparts, and a coherent model for the Poris eruption and depositional processes is presented.

7.1.1 Previous Poris stratigraphic schemes

The Poris ignimbrite succession, originally also known as the 'Lower Grey ignimbrite' (e.g. Bryan *et al.*, 1998a), has been investigated in detail in two previous studies. Edgar *et al.* (2002) describe exposures across the island, including one proximal location, and the Poris 'Member' is subdivided into 12 units; unit A surge, unit B Plinian fall, unit C surge, the Manteca ignimbrite, unit D Plinian fall, unit E surge, the Abona, Quinta, and Mareta ignimbrites, units F and G Plinian fall, and the Confital ignimbrite. The proximal location of Edgar *et al.* (2002) appears to be locality 16 in this thesis (see Fig 4.4). Brown and Branney (2004b) describe Poris exposures solely within the Bandas del Sur and, using a lithofacies approach, divide the Poris 'Formation' into 10 'Members': Hidalga, Centinela, Magua, Cueva Honda, Caballos, Jurado, Rio, Tamadaya, Guimar, and Cuerva.

7.1.2 Correlating stratigraphy

Due to the dynamic nature of sustained pyroclastic density currents, physical similarities between ignimbrite lithofacies are unlikely to represent temporal correlation; lithostratigraphy does not necessarily equate to chronostratigraphy.

Branney and Kokelaar (2002) coined the term 'depochron' to describe a notional surface within an ignimbrite sheet connecting clasts deposited at the same moment in time, but over large distances, with a lack of connecting exposure and significant changes in outcrop appearance, depochrons can be difficult to establish. 'Entrachrons', notional surfaces connecting the lowermost clasts that were entrained into current together at the same instant in time (Branney and Kokelaar, 2002), may be clearer; for example, the increased influx of more mafic pumice material towards the end of the Poris eruption formed an entrachron. The entrachron for this mafic influx need not occur in the same lithofacies in proximal and distal zones; this would depend on the conditions of the flow boundary zone of the PDC at each location.

When using geochemical data from previous studies for correlation, several issues must be considered. The analytical uncertainty in data from Brown (2001) and Edgar *et al.* (2002) is not known (it is negligible for this study; see Section 6.3). The datasets are small and not all units have been sampled. Furthermore, the exact locations and stratigraphic heights of the sampling are unknown. Although the analysis by Brown, like this work, was carried out at Leicester University, the work by Edgar was done elsewhere, adding the possibility of instrumental differences. Nevertheless, the comparison of overall stratigraphic trends is useful and is thus undertaken here with caution.

7.2 A new model for the 273 ka Poris eruption

In this section physical characteristics of proximal and distal deposits are compared and correlated, geochemical evidence is considered, and a new eruption model for the Poris event is presented. Table 7.1 is a summary of the physical features of the lithofacies deposited during each phase, and Figure 7.1 illustrates the physical correlations made between the different stratigraphic schemes. Figure 7.2 is a compilation of Poris geochemical data showing Zr concentrations during each phase, and Figure 7.3 is a schematic representation of the new eruption model. Correlations are explained in the text.

Phase	Processes	Proximal record	Distal record	Physical correlation
8	**Waning PDC and fallout**	splBr	Units F and G (1) Uppermost part of Guimar Member (2)	The lack of a proximal correlative may be due to post-eruption reworking. Alternatively, it may indicate that PDC flow ceased distally before it did proximally, as PDC run-out distance decreased.
7	**Waning conditions** and mafic influx	splBr	Mareta (1) Guimar (2)	Mafic and banded pumices significantly increase in abundance at this point in both the proximal and the distal record (increased-mafic entrachron).
6	**Caldera collapse** and lithic influx creates waxing PDC conditions	lT at base of splBr	Quinta (1) Tamadaya (2)	The lithic-block entrachron occurs at this point in both the proximal and the distal record. The relatively thin layer in the proximal zone indicates a significant amount of bypass across the near-vent zone.
5	**Main stage of PDC bypass, scour and deposition** with periodic lithic influx	mLT lT s-ds-mlLT	Upper part of Abona (1) Rio and underlying Jurado (2)	The s-ds-mlLT facies is interpreted to be the deposit of a non-uniform, unsteady current, as is the Jurado (2). The upper part of the Abona contains subunits bounded by lithic breccia layers, similar to the proximal lT layers. Evidence of scour and bypass occurs in both proximal and distal lithofacies.
4	**Hybrid fall and flow** occurs proximally. Coarse Plinian input and ballistic activity.	spBT(acc)	Unit D fallout overlain by Unit E 'surge' (1) Cueva Honda ignimbrite overlain by Caballos fallout (2)	spBT is a uniquely proximal lithofacies with characteristics indicating fall, flow and ballistic processes. Both spBT and the Caballos contain distinctive pale green pumices. Unit E contains AP2 pellets and ballistic pumice bombs.
3	**Phreatomagmatism** creates pulsatory explosions and highly fragmented lithic material	mTacc2 slcrT xscrT	Manteca (1) Magua (2)	slcrT is a uniquely proximal lithofacies. The Magua Member is the distal counterpart; both slcrT and the Magua ignimbrite are grey, and the Magua contains the distinctive grey accretionary pellets found in mTacc2.
2	**First density stratified PDC** becomes partly blocked proximally	mTacc1 //spLT	Unit C 'surge' (1) Centinela (2)	Both proximal and distal units overlie the Plinian deposit below with no evidence of a time break. AP2 pellets occur in both the Centinela and mTacc1.
1	**Plinian deposition** with dilute pyroclastic currents	//bpL	Unit B fallout (1) Hidalga (2) Unit A ash (1)	Green obsidian fragments occur in both proximal and distal fallout. Lithofacies are physically similar in proximal and distal zones.

Table 7.1 Summary of the correlation between the new investigation of the proximal Poris record and the previously published studies of the distal record. (1) is Edgar *et al*. (2002) and (2) is Brown and Branney (2004).

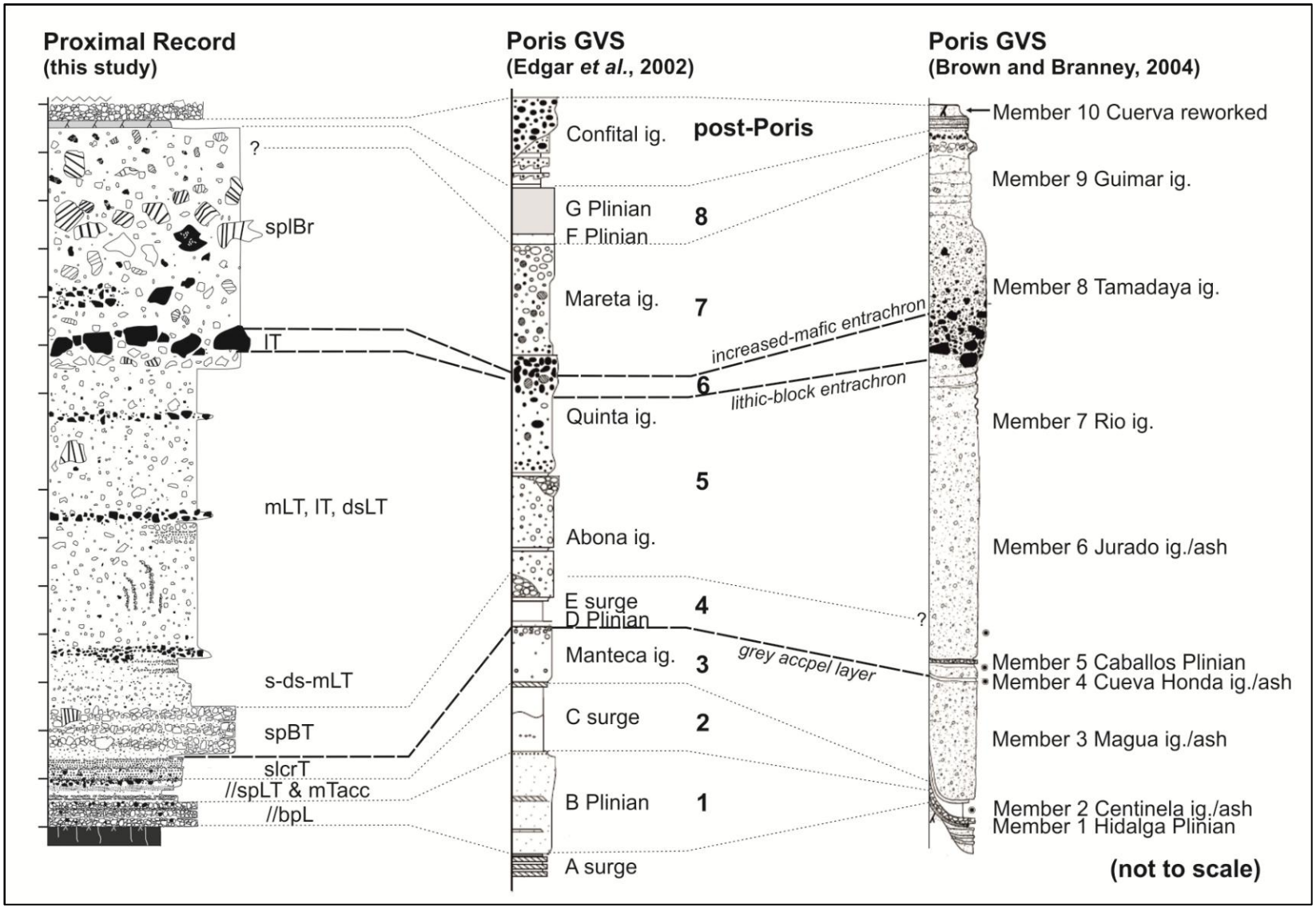

Figure 7.1
Proposed physical correlation between proximal findings of this study and previously published Poris stratigraphic schemes. Bold numbers relate to eruption phases summarised in Table 7.1. See text for full explanation.

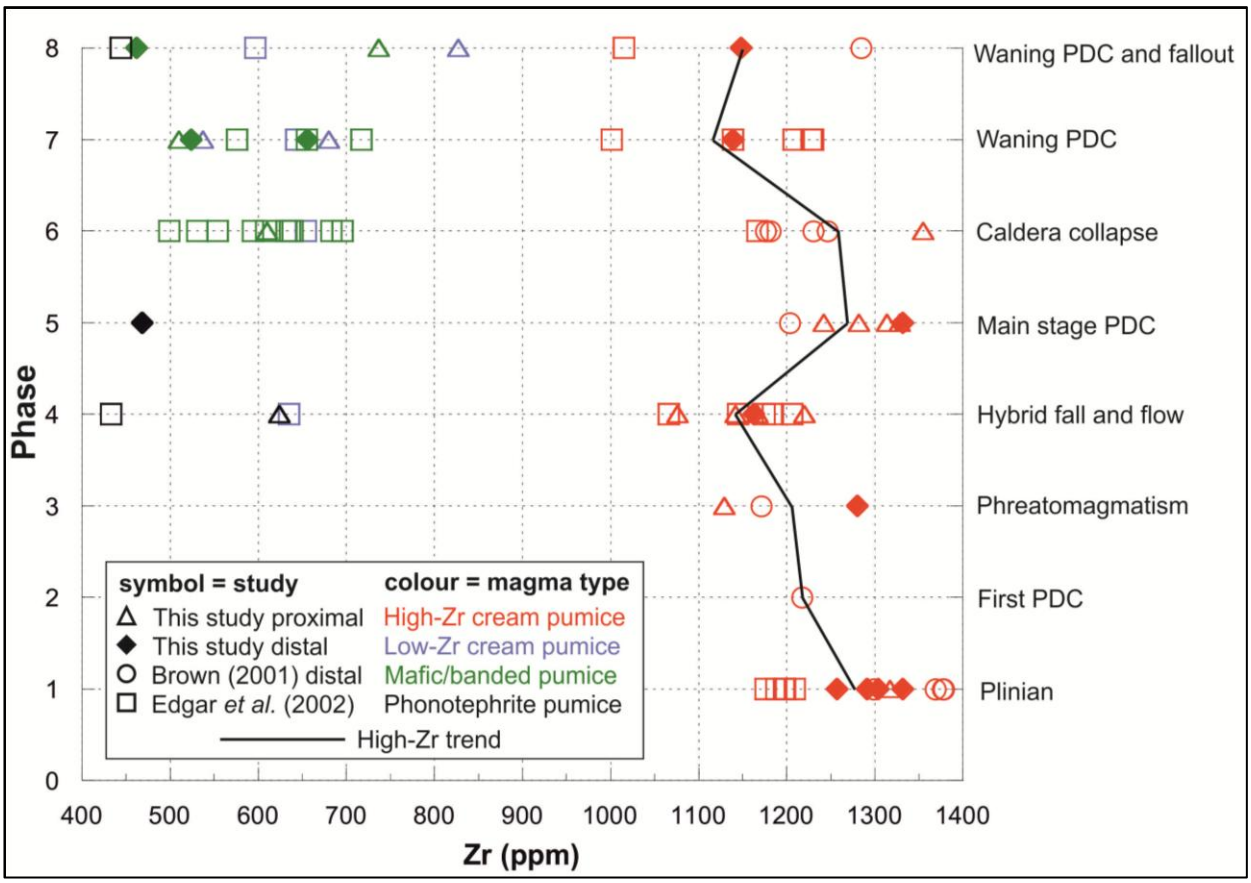

Figure 7.2 Zirconium variation with stratigraphic height for samples from this study along with those from Brown (2001) and Edgar *et al.* (2002). Only high-Zr data from Brown (2001) are plotted. Based on the physical correlations described in Table 7.1, data plotted at each phase are:
1 = Plinian (this study), Unit B (Edgar), Hidalga (this study; Brown).
2 = Centinela (Brown).
3 = slcrT (this study), Magua (this study; Brown).
4 = spBT (this study), Abona (Edgar), Caballos (Brown).
5 = s-ds-mlLT (this study), mLT (this study), Jurado (Brown), Rio (this study)
6 = base of splBr (this study), Tamadaya lBr (Brown), Quinta (Edgar)
7 = splBr (this study), Tamadaya [above lBr] (this study), Mareta (Edgar)
8 = top contact of splBr (this study), Guimar (this study, Brown), Units F and G (Edgar)
[At phase 8, waning stage fallout is the uppermost distal Poris deposit. Proximally, there is no upper fallout recorded, therefore pumice analyses from the uppermost part of splBr are plotted here at phase 8 for comparison].

Figure 7.3 (at end of digital document)

7.2.1 Phase 1: Plinian deposition

Proximal record

A parallel-bedded pumice lapilli facies (//bpL) overlies pre-Poris basanite lavas (Wolff *et al.*, 2000) across the DH wall, ranging from 10 cm – 1 m in thickness. An ash bed and a bed of rounded, smaller pumices occur interspersed with three clast supported fallout layers; the unit contains abundant dark green obsidian fragments.

Distal record

Brown and Branney (2004b) report that the Plinian deposit (the 'Hidalga') consists of 8 distinct beds of pumice (B, D, E, G and H) and ash (A, C and F). Beds A-G are exposed in southeast Tenerife whereas Bed H occurs at Guimar in the east; the authors propose that upper parts of the Plinian column were influenced by different wind conditions and thus had a more easterly dispersal than lower parts. Edgar *et al.* (2002) state that the Poris fallout deposit (Unit B) is thickest on the Cordillera Dorsal (2 m), and propose an eastwards Plinian dispersal from the north-eastern part of Las Cañadas.

Physical correlation

No Poris deposits occur between the pre-Poris lavas and //bpL, therefore the precursory distal ash unit 'A' (Edgar *et al.*, 2002; Brown and Branney, 2004b) has no proximal correlative. The ash is thickest in south-eastern coastal exposures (Edgar *et al.*, 2002) and may not have been deposited in the eastern DH zone.

The ash layers recognised between fallout layers by Brown and Branney (2004b) may correlate to beds 2 and 4 in the proximal //bpL facies. However, the deposition of such ash is likely to depend upon temporary, local hiatus in Plinian fallout, so the proximal and distal occurrences may not be *temporal* correlatives. There is no proximal record of the coarser pumice facies described as Unit H by Brown and Branney (2004b), but the upper part of the proximal Plinian unit has been reworked and this material may have been removed from the proximal record. The dark green obsidian chips common throughout the proximal //bpL facies are markedly concentrated at the base of a distal Plinian exposure near Tajao (Richard Brown, pers. comm., 2011).

Geochemical evidence

Proximal and distal Plinian pumices analysed in this study contain 1257 to 1332 ppm Zr. The range of compositions found by Brown (2001) is slightly higher (1299 – 1378 ppm) and that by Edgar *et al.* (2002) lower (1176 – 1209ppm). In EPMA analyses, biotites are uncommon, but they occur in both proximal and distal pumices from the Plinian unit (this may be a sampling effect).

Interpretation

The eruption began with formation of a dilute ash cloud, deposition from which is recorded in the southeast. A Plinian plume developed and pumice deposition commenced, along with lithic material derived from the obsidian-rich vent zone. The concentration of obsidian chips at the base of the deposit at Tajao could reflect subtle differences in terminal fall velocity between pumice and lithic clasts. Dilute pyroclastic clouds formed and the atmosphere in the near-vent zone became laden with ash. During temporary local hiatuses in pumice deposition, ash and small sub-rounded pumices became deposited as layers between Plinian beds. The hiatuses may reflect changes in wind direction.

There are several possible explanations for the lack of ash aggregates in the deposits at this stage. If ash deposition was due to flushing by rainfall, any wet aggregates would have coalesced, leaving no record. If dry ash aggregates fell from the ash cloud/s, they may have disaggregated on impact with the coarse pumice-strewn ground. Alternatively, ash aggregation may not have commenced at this early stage in the eruption, but ash deposition without aggregation is difficult to envisage unless the atmosphere was still, which seems unlikely.

7.2.2 Phase 2: First pyroclastic density current

Proximal record

Stratified layers of Plinian-population pumices, and smaller, rounded pumices, within tuff (//spLT) are in erosional contact with the Plinian deposit. The //spLT facies is overlain by a white ash layer, <20 cm thick, containing both AP1 unstructured ash pellets and AP2 accretionary pellets ≤1.5 cm (mTacc1) in a matrix

of smaller, millimetre-scale pellets. The layer varies in thickness due to an erosional contact with the deposit above.

Distal record

Edgar *et al*. (2002) describe Unit C as comprising three ash beds that occur variably at different Poris exposures. C1 is described as diffusely stratified with up to 100% accretionary lapilli at some locations, C2 as grey and erosive with fewer accretionary lapilli, and C3 as rich in sub-millimetre lithics and with pinch and swell structures.

Brown and Branney (2004) describe this part of the distal stratigraphy differently. On the Plinian deposit are the Centinela, Magua, and Cueva Honda Members, described as ignimbrites with associated ash layers reflecting flow units 1, 2 and 3 of the eruption. The lowermost of these ignimbrites, the Centinela, is described as a vitric tuff containing 'accretionary lapilli' (AP2 of Brown *et al.*, in press) and fine ash made up of ash pellets < 2 mm, overlain by a layer of framework supported AP1 pellets ≤15 mm in diameter (Brown, 2001).

Physical correlation

Unit C described by Edgar *et al.* (2002) is interpreted as a record of phreatomagmatic "base surges", based upon the wide dispersal and the presence of abundant accretionary lapilli. The reported beds have characteristics similar to //spLT, mTacc1 and xscrT at locality 16 in the DH wall, but a different mechanism for their deposition is proposed here.

There is no closely similar correlative for the //spLT lithofacies; distally, Plinian clasts are matrix supported in the Centinela ignimbrite above (Figure 8 of Brown and Branney, 2004b), but a lithofacies containing *stratified* pumice layers is not reported.

The description of the Centinela Member closely matches that of mTacc1 in the DH wall, apart from the nature of the ash aggregates. In the proximal layer, AP1 and AP2 pellets of a similar size occur together, matrix-supported in ash. This is unlike the distal clast-supported AP1 pellet layer.

Interpretation

A pyroclastic density current was generated by fountaining of the eruption column following widening of the obsidian-rich vent. It quickly became density stratified and was partly blocked by pre-Poris caldera topography in the proximal zone. The upper, dilute part surmounted the topographic obstacle. This stripped current did not have the competence to support lapilli-sized clasts, but was able to roll, saltate and rework Plinian pumice lapilli from the underlying substrate. A stratified ignimbrite veneer was thus deposited in the DH zone. After this current passed by, a hiatus in energetic PDC deposition occurred and ash aggregates were deposited from a hybrid ash cloud that included the fringes of the main Plinian column and the co-ignimbrite cloud. Multi-rimmed accretionary pellets that had been formed in the density stratified PDC became deposited along with unstructured ash pellets.

The lower, granular-fluid part of the partly blocked PDC was redirected, and re-stratified en route to the coastal zone where it deposited valley-fill ignimbrite in topographic lows and lapilli-poor veneers on topographic highs. Multi-rimmed AP2 ash aggregates that formed in the density stratified PDC were deposited along with ignimbrite. After the current had passed by, a layer of clast-supported AP1 pellets formed by deposition from the co-ignimbrite cloud. The presence of such a layer distally but not proximally may indicate that ash pellets were relatively abundant in the co-ignimbrite cloud by the time the current had reached the coast, or that in the proximal region depositional conditions were wetter and the unstructured pellets were insufficiently hardened to form such a layer here. Alternatively, any clast-supported ash pellet layer in the proximal zone may have been eroded by the subsequent PDC (discussed further in Section 7.3.2).

7.2.3 Phase 3: Phreatomagmatism

Proximal record

A thin, cross-stratified, fine-grained tuff (xscrT) is in erosive contact with mTacc1. This is overlain and scoured into by a stratified tuff rich in small crystals, altered lithics (including plutonics), and pumice clasts (slcrT). This is grey at the base due to a high lithic content and paler towards the top. Laterally variable inverse grading of pumices occurs in slcrT across the DH wall, and in the north this stratification is

capped by a 5-cm-thick ash layer containing accretionary pellets (mTacc2). These pellets are distinctive; they are small (<1 cm), with grey cores and less brittle rims than those found elsewhere in the proximal and distal successions

Distal record

The 'Manteca' ignimbrite of Edgar *et al.* (2002) overlies Unit C; an erosive-based unit in the proximal log is described and interpreted as a 'ground surge' deposit. In the study by Brown and Branney (2004b) the Magua Member overlies the Centinela; it is a veneer and valley-filling massive lapilli tuff overlain by an ash pellet layer, interpreted to record a topography-surmounting PDC that spread over a wide area. The mLT facies of the Magua Member is grey, and contains grey accretionary pellets (Brown, 2001).

Physical correlation

The lithic-rich, grey, stratified tuff is a uniquely proximal lithofacies; no reported distal lithofacies has similar characteristics. The grey colour of the Magua Member of Brown and Branney (2004b) is an indication that it may be the distal counterpart of slcrT. The small, grey accretionary pellets are a distinctive marker feature; their presence in both the Magua ignimbrite and the proximal mTacc2 layer (Fig 7.4) is further evidence of a correlation between these units.

Geochemical evidence

Samples FSS3 and DIST5 from slcrT and the distal Magua deposit are not a close match; they contain 1129 ppm Zr and 1280 ppm Zr respectively. However, DIST5 is one of the distal clasts that has been affected by alteration; it contains lower SiO_2 and higher CaO than any other cream pumice analysed (51.9 wt% and 4.7 wt% respectively compared to typical ranges of 53-57 wt% and 0-3 wt%). The Magua analysis from Brown (2001) contains 1171 ppm Zr and is a closer match with the slcrT sample from this study.

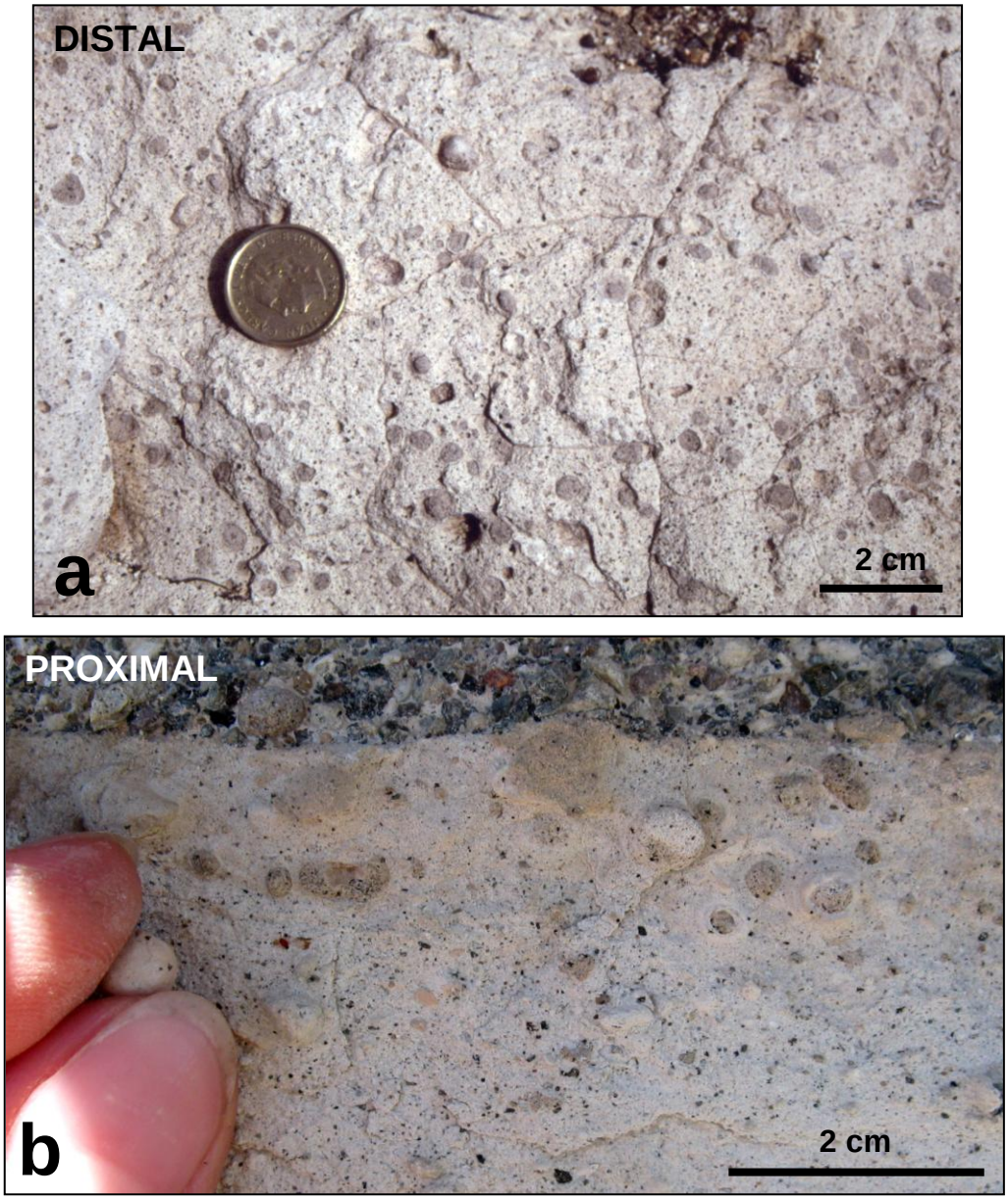

Figure 7.4 (a) Accretionary pellets with dark cores in the distal zone, on Tajao Road, stratigraphically below the Caballos Plinian unit (photograph courtesy of Rich Brown). (b) Accretionary pellets with dark cores in proximal zone, at log 17, stratigraphically below spBT hybrid lithofacies. The pellets in both the distal and proximal zones are very similar in colour, size and morphology; ash cores are <1 cm in diameter, smoothly irregular in shape rather than perfectly spherical.

Interpretation

Interaction between magma and water, possibly at depth, led to phreatomagmatic explosivity. Lithic material from the conduit and vent zone became finely fragmented and entered a pyroclastic density current. Topographic blocking may have continued for a time in the proximal zone, causing only the uppermost, dilute parts of the density current to be recorded in the DH wall (xscrT). When the topography became sufficiently buried, a granular fluid, concentrated flow was able to reach the study area. In the proximal region, the PDC was erosive and lithic-rich, creating distinct proximal lithofacies, but by the time it reached the distal flanks it had shed much of the lithic load and deposited more typical mLT. On distal topographic highs between barrancos, ignimbrite veneer was deposited (Brown and Branney, 2004b).

Ash aggregation was ongoing in the proximal region at this time. Highly fragmented fine-grained lithic material entered the plume as a grey ash, and ash aggregates containing grey ash cores formed. The irregular, contorted nature of the accretionary pellets at this stage, compared to those lower in the stratigraphy, may indicate that the pellets underwent less 'baking' within the plume and/or PDC. Conceivably, phreatomagmatic conditions may have caused a drop in temperature of the erupted material, contributing to this effect (discussed further in Section 7.3.2).

7.2.4 Phase 4: Hybrid fall and flow

Proximal record

A locally clast-supported, stratified pumice-block tuff containing AP2 accretionary pellets <20 mm (spBT(acc)) overlies slcrT and mTacc2 in the DH wall. Pumices are typically <10 cm diameter and commonly contain dark blebs. Pumice blocks up to 30 cm diameter occur and contain evidence of magma mingling. Larger pumices are pale greenish-cream, and more contorted and angular than the cream lapilli <2 cm diameter. Fines-rich layers separate pumice-rich beds, with evidence of internal scour. Rare low-angle cross-stratification occurs and pumice beds pinch out across exposures. In southern DH outcrops, spBT grades up from slcrT.

Distal record

Edgar *et al*. (2002) report that in the distal zone, above the 'Manteca', a Plinian fall deposit (Unit D) is overlain by a diffusely stratified 'surge' deposit (Unit E) containing white ash, coarse accretionary pellets, and inflated pumice 'bombs' up to 26 cm in diameter. The 'Abona' ignimbrite overlies these units. In the proximal log of their study, the Abona directly overlies the Manteca ignimbrite.

Brown and Branney (2004b) report a veneer and valley-fill ignimbrite atop the Magua Member, known as the 'Cueva Honda', which is overlain by a Plinian fallout unit, the Caballos Member. The Caballos contains pale green pumice lapilli.

Physical correlation

No closely similar correlative of the spBT lithofacies is reported in distal exposures; it is an exclusively proximal lithofacies. Edgar *et al.* (2002) describe the 'pumiceous base' of the Abona in their proximal log, but do not report the locally clast-supported nature of the lithofacies or the hybrid nature of the pumice clasts. The authors propose that the Manteca ignimbrite is stratigraphically related to the Unit D fallout layer, a relationship not supported by evidence gathered in this study.

It is proposed here that spBT is a hybrid lithofacies that temporally correlates with multiple distal units. The pale green pumices present in spBT are also reported in the distal Caballos Plinian unit. The occurrences of accretionary pellets and inflated pumice blocks in the distal stratified ash 'Unit E', atop the distal Plinian, are distinctive features of spBT; furthermore, spBT has a fines-rich matrix, abundant in the stratified fine-grained layers between pumiceous beds. The rounded pumices present in spBT are clasts typical of PDC deposits; therefore the distal Cueva Honda and Abona units may be ignimbrite correlatives of the hybrid lithofacies.

Geochemical evidence

Samples from slcrT, spBT and the Caballos all contain less Zr than samples from the opening Plinian event (~1200ppm Zr compared to ~1400 ppm). Nb and Rb follow the Zr trend and Nd behaves inversely. When phenocryst data are grouped by eruption phase, subtle variation in chemistry is found in titanomagnetites; those from

spBT and the Caballos contain more TiO_2, Al_2O_3 and MgO, and less FeO and MnO, than those from other samples (Table 7.2)

Interpretation

Following the phreatomagmatic phase, the eruption reverted to magmatic. Coarse Plinian pumices fell close to the vent, and interplay between ballistic, fallout and PDC activity occurred in the proximal zone (as discussed in Houghton *et al.*, 2004). Distally, fallout mixed with PDCs and was deposited as part of mLT lithofacies (e.g. Abona/Cueva Honda). When a hiatus in flow occurred, a clast-supported fallout layer was deposited (unit D/Caballos), followed by an ash layer containing inflated pumices up to 26 cm in diameter (unit E). The hiatus that occurred distally at this stage is not recorded proximally. There is, however, evidence that the density current active proximally at this time was unsteady and non-uniform; fine-grained ash and crystal layers deposited between pumice block rich beds reflect variations in flow-boundary zone conditions.

The influx of pale green pumice and change in bulk pumice chemistry at this stage may reflect the tapping of a different zone of the magma system during and following the phreatomagmatic explosion(s). A subtle change in plumbing may be responsible for the increased abundance of mafic blebs in spBT pumices, and for the variation in titanomagnetite composition.

Implications

Brown and Branney (2004b) describe the Poris eruption in terms of a series of 4 distinct flow units. However, in the DH wall, slcrT and spBT are separated by an ash layer in the north but are gradational in the south, and there is no evidence of flow hiatus between spBT and s-ds-mlLT above. Proximally, there is only definitive evidence of two flow units, separated by the mTacc1 lithofacies. This relationship indicates that hiatus varies spatially; as a sustained current waxes and wanes, pyroclastic flow may stop completely in distal reaches while it continues close to the source. Thus, hiatuses that are recorded distally may not occur proximally, and the number of flow units recorded in the two zones will differ (see Chapter 8).

Phase		SiO_2	TiO_2	Al_2O_3	Cr_2O_3	FeO	MnO	MgO	CaO	Na_2O	K_2O	NiO	Total
1	Mean	1.29	11.22	2.44	0.72	70.23	2.20	1.88	0.20	0.18	0.11	0.02	90.48
(n=15)	Stdev	3.31	5.90	2.84	2.68	11.11	1.61	1.94	0.36	0.32	0.27	0.04	3.38
4	Mean	0.16	15.97	4.68	0.02	66.35	0.79	5.40	0.14	0.04	0.00	0.03	93.57
(n=10)	Stdev	0.38	0.78	1.56	0.02	4.21	0.29	1.25	0.30	0.04	0.01	0.02	2.16
5	Mean	0.02	13.03	2.76	0.03	73.18	1.81	2.95	0.02	0.03	0.01	0.02	93.86
(n=12)	Stdev	0.04	2.93	2.09	0.03	6.40	0.86	1.99	0.02	0.04	0.01	0.03	1.45
7	Mean	0.35	13.58	3.30	1.68	68.56	1.44	3.26	0.05	0.04	0.05	0.02	92.33
(n=25)	Stdev	1.41	4.73	3.87	5.96	10.14	0.79	2.69	0.05	0.04	0.16	0.05	2.61
8	Mean	0.04	15.38	4.29	0.01	68.45	0.96	4.95	0.02	0.04	0.01	0.02	94.17
(n=9)	Stdev	0.10	2.38	1.91	0.01	6.55	0.58	2.03	0.02	0.06	0.01	0.02	4.20

Table 7.2 Average titanomagnetite compositions grouped by eruption phase. Phase 4 titanomagnetites have the highest TiO_2, Al_2O_3 and MgO, and the lowest Feo and MnO.

7.2.5 Phase 5: Main stage of PDC bypass, scour and deposition

Proximal record

Up to 2m of stratified to diffusely stratified, locally lithic-rich tuff (s-ds-mlLT) overlies spBT and is overlain by 10-12 m of massive lapilli tuff (mLT) with zones of diffuse stratification (dsLT). Layers of lithic-rich tuff (lT), typically less than 20 cm thick and with associated load and flame structures, mark scour and bypass surfaces. Localised zones rich in elutriation pipes occur in southern part of wall (mLTpip).

Distal record

The 'Jurado Member' (Brown and Branney, 2004b) contains variably stratified lithofacies, and is interpreted as the deposit of an unsteady PDC. The overlying 'Rio Member' is interpreted to record a rapid increase in the area inundated by the PDC as the eruption waxed; it overlaps all preceding members in the distal zone and reaches up to 20 m in thickness.

The upper part of the distal 'Abona' ignimbrite described by Edgar *et al*. (2002) contains 'lithic concentration zones at various levels'.

Physical correlation

The s-ds-mlLT proximal facies is vertically and laterally variable, indicating that this phase began with turbulent, unsteady, non-uniform flow-boundary zone conditions. The distal Jurado ignimbrite (Brown and Branney, 2004b) may be a distal counterpart deposit.

The widespread and thick nature of the Rio Member/Abona makes this unit a likely counterpart of the mLT/lT proximal lithofacies, which contain evidence of considerable bypass to distal slopes. The 'subunits' bounded by fines-enriched layers or thin lithic 'ground-surge' deposits described in the Abona by Edgar *et al.* (2002) may be correlatives of the proximal lT layers.

The presence of Poris material on the sea floor off Tenerife (Schmincke and Sumita, 1998) implies that bypass over distal slopes also took place, and this seems most likely to have occurred at this waxing stage of the eruption.

Geochemical evidence

Results from this study show similar Zr results for proximal s-ds-mLT, mLT, and distal Rio Member pumices. FSS8, 9 10, 11, and DIST6 have Zr concentrations of 1242 -1332 ppm Zr. However, results from previous studies are more widely spread (Fig. 7.2). This may reflect the greater area and thickness covered by these distal ignimbrites, with fuller representation of the erupted products, and thus the greater potential for inter-unit geochemical variation. It may also reflect the waxing nature of the eruption at this stage, with incorporation of magma from deeper parts of the sub-volcanic system, i.e. deeper draw-down (e.g. Blake and Ivey, 1986).

Interpretation

After coarse Plinian fallout ceased, a sustained pyroclastic density current with non-uniform and unsteady flow-boundary zone conditions deposited variably stratified lithofacies. Structural instabilities in the conduit-vent region developed, with periodic waxing mass flux and entrainment of lithics into the current. The PDC scoured into and bypassed over previously deposited units and a relatively small amount of material is recorded proximally (the amount eroded during the climactic event is unknown). Up to 30 m thickness of ignimbrite is recorded distally, and a substantial amount of pyroclastic material bypassed into the sea.

7.2.6 Phase 6: Caldera collapse and waxing PDC

Proximal record

A lithic-block layer, <1.5 m thick, occurs at the base of splBr. Blocks are ≤1 m in diameter and include a wide variety of lithologies. The contact between mLT and the base of splBr is planar and distinct due to an increase in pumice size, an increased occurrence of mafic pumice, and a matrix colour change from cream to pinkish-beige.

Distal record

Edgar *et al.* (2002) describe the 'Quinta' ignimbrite, which overlies the Abona, as tan in colour, with a high lithic content and prominent banded pumice. Brown and Branney (2004b) refer to this ignimbrite as the 'Tamadaya Member', and report lithic breccia (mlBr) and lithic-rich ignimbrite (mlLT) facies with a pink-weathering

matrix. Load and flame structures involving underlying ignimbrite are common, and the unit is up to 15 m thick. The Tamadaya is in gradational contact with the unit above (Brown and Branney, 2004b).

Physical correlation

The high lithic content, increase in mafic pumice, and matrix colour change are distinguishing features that suggest that the distal deposit counterpart to the lithic-block layer in the DH wall is the Quinta/Tamadaya. The relatively thin proximal lithic-block layer implies considerable bypass across the DH zone at this time. The lower splBr contact is sharp in the proximal zone, whereas distally load and flame features are common at this contact. This implies that the lithic-rich PDC was highly erosional in the near-vent zone, creating a relatively planar surface, whereas distally material 'piled up' on top of previously deposited 'fluffy' ignimbrite, and sank into it. The lithic influx recorded in the upper part of both the proximal and the distal successions is here interpreted as an entrachron (see Fig 7.1).

Geochemical evidence

Cream pumices at the base of the proximal splBr, and from the distal lithic-breccia lithofacies, have a spread of Zr contents between 1150-1400 ppm. The mafic samples analysed from these sites contain 500-700 ppm Zr.

Feldspar compositions differ between the cream and black pumices. Black pumices are rich in anorthoclase and sanidines whereas cream pumices contain a larger range of compositions, including bytownite, labradorite, andesine and oligoclase, as well as sanidine and anorthoclase. As discussed in Chapter 6, the rarity of plagioclases in the black pumices reported here conflicts with previously published work.

Interpretation

After the ejection of large volumes of magma during Phase 5, a critical extent of magma evacuation was reached. The ‘chamber’ roof collapsed, and large faults dilated, disrupting the surrounding hydrothermal system. Conduit-derived, hydrothermally altered lithic blocks entered the unstable eruptive jet(s) and the

waxing pyroclastic density current became lithic-rich. As caldera collapse ensued, the mafic magma was more extensively tapped.

7.2.7 Phase 7: Waning PDC and mafic influx

Proximal record

A poorly-exposed, 10-m-thick, stratified pumice-block breccia, rich in banded and black pumice blocks ≤1.5 m in diameter, is present atop mLT across the DH wall (splBr). A key exposure of this breccia occurs in a gully next to Montaña El Cerrillar. Excepting the lithic-block layer at its base (described above), lithic clast size is similar to that seen in the mLT. Stratification is variable and is distinguished by the changing abundance of pumice blocks; some zones have greater concentrations of large pumices whereas others are richer in lithics.

The 'Abona' is the uppermost ignimbrite in the proximal log reported in Figure 4 of Edgar *et al.* (2002). A lithic-block layer above it is interpreted to be part of the distal Quinta ignimbrite, but the extent of the proximal pumice-block breccia lithofacies is not described, and the Poris exposure in the Cerrillar gully is not reported.

Distal record

Edgar *et al.* (2002) describe the 'Mareta' ignimbrite, in gradational contact with the Quinta, as having a relatively low lithic content and abundant banded pumice ≤50 cm in diameter. Brown and Branney (2004b) describe the 'Guimar' Member as a waning-phase ignimbrite containing both phonolitic and tephriphonolitic banded pumice.

Physical correlation

The increase in mafic pumice content as the lithic breccias grade up into mLT in the distal stratigraphy is interpreted as a correlative entrachron for the increase of mafic pumices in the proximal splBr. Brown and Branney (2004b) report a thickness of 10 m for the Guimar ignimbrite (see Fig. 7.1), similar to that recorded proximally in splBr.

Geochemical evidence

During phases 6 and 7 the chemical composition of the low-Zr pumice remains similar, in the range of 500-700 ppm Zr. Low-Zr phonolites are found both proximally (this study) and distally (Edgar *et al.*, 2002). The Nb/Zr covariation plot (Fig 6.7) illustrates that the low-Zr magma type is petrogenetically distinct from the high-Zr type; the geometry of magma storage is unclear, but the occurrence of mingled pumice throughout the Poris succession suggests the reservoirs of the two magmas were persistently connected.

Interpretation

Following the climactic explosions and caldera collapse, a phase characterised in the proximal zone by considerable erosion and non-deposition, proximal deposition began again as the pyroclastic density current waned in energy. The similarity in thickness between the proximal and distal correlatives at this stage may be coincidence (the thickness removed during post-Poris reworking is unknown), but it could be an indication that aggradation was persistent in the proximal zone during this waning phase. The lack of coarse pumice blocks in distal exposures is most likely to be due to breakage during transport across the volcanic flanks.

7.2.8 Phase 8: Waning PDC and fallout

Proximal record

The stratified pumice-block breccia is the final deposit recorded proximally. A soil 38 cm thick occurs atop splBr in the DH wall, and 5 m of stratified pumice-rich gravels overlie the unit in the Cerrillar gully. It is conceivable that any lithofacies deposited following splBr were removed by erosion.

Distal record

At Guimar, a zoned fallout unit consisting of cream pumices overlain by black pumices occurs at the top of the Poris succession (Brown, 2001; Edgar *et al.*, 2002; Pete Kokelaar, pers. comm., 2010) (Fig 7.5). The fallout is known as Units F and G in Edgar *et al.* (2002), and it is the uppermost part of the Guimar Member of Brown and Branney (2004b).

Physical correlation

The distal fallout layer has no proximal counterpart although it may temporally correlate with the upper parts of splBr.

Geochemical evidence

Low-Zr phonolite occurs in both the uppermost proximal splBr pumices and in the distal fallout layer.

Cream pumices show a spread of Zr concentration in Phases 7 and 8, from 1000 - 1300 ppm. These uppermost analyses also show the largest spread in the Zr content of the low-Zr pumices, from 440 - 850 ppm (Fig 7.2).

Interpretation

Pyroclastic current activity ceased in the distal zone and Plinian fallout tephra was deposited. Plinian deposition may have been ongoing throughout the Poris eruption, only being recorded during a significant hiatus in flow, in Phase 4 and when distal PDC activity ceased at the end of the eruption. Alternatively, Plinian activity may have ceased following Phase 4 and restarted towards the end of the eruption. The opening of vents during the caldera collapse could well have led to temporary failure to form a buoyant eruption plume.

The lack of a proximal physical correlative to the distal fallout layer could be due to post-eruption sedimentary reworking, but it may reflect continuation of pyroclastic density current activity in the proximal zone after flow had ceased in the distal zone. As the current waned, regressive deposition of tuff may have occurred as the flow run-out distance diminished; Plinian pumices would have fallen into the current in the proximal zone and would not have been recorded as a fallout layer.

The geochemical variability evident in the closing stages of the eruption indicates that mingling and cryptic mixing between the two magmas became more significant as the mafic magma was tapped in larger quantities.

7.2.9 Reworking

Edgar *et al.* (2002) describe a further ignimbrite, the 'Confital', on top of the fallout units. The exposure of this unit, in the Guimar valley, has since been reinterpreted as reworked pumices and slopewash (The Cueva Member of Brown and Branney, 2004b; Pete Kokelaar, pers. comm., 2010) (Fig 7.5). Edgar *et al.* (2002) report that a clast-supported facies of the Confital is discontinuously exposed in the Diego Hernandez wall, but the location of the exposure is not described and the deposit may be a poor exposure of splBr.

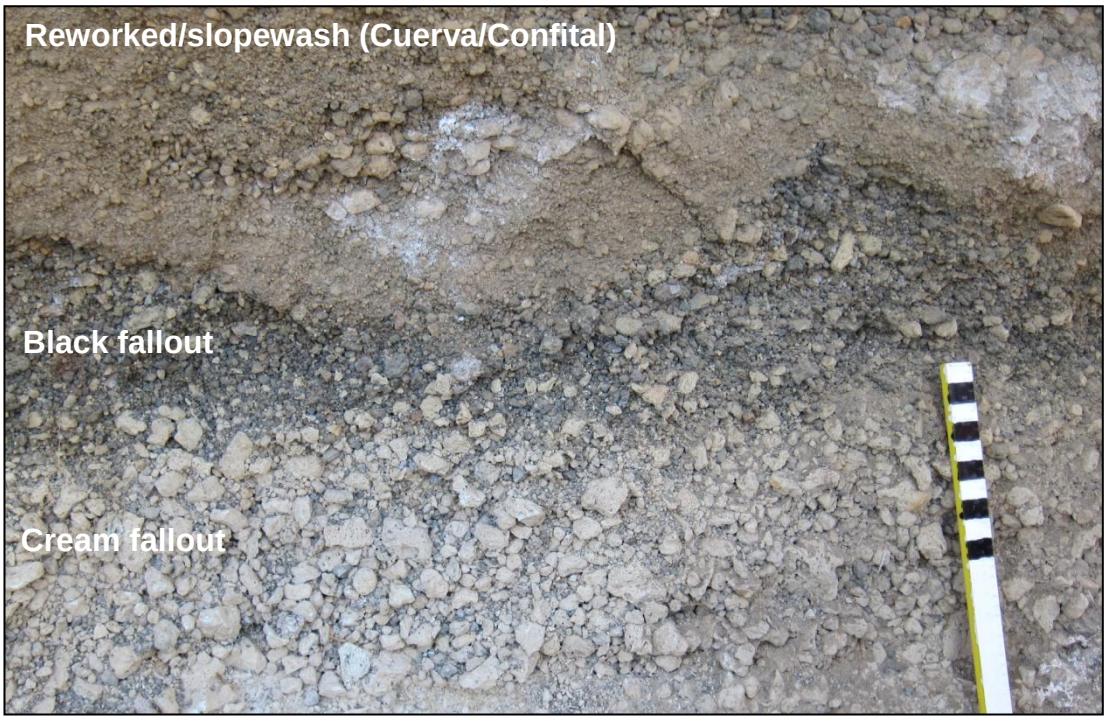

Figure 7.5 The top of the distal Poris succession at Guimar. A zoned fallout unit is overlain by brown slopewash material rich in Poris pumice clasts (photograph courtesy of PK, scale in cm).

7.3 Discussion

7.3.1 The role of topography

Topographic changes from near-vent to distal locations have a crucial effect on the dynamics of the PDC and the architecture of the lithofacies deposited. Near-vent caldera topography caused the first density current generated during the Poris eruption to be recorded in the DH wall merely as a thin veneer; lapilli tuff was deposited here only once the topography had been infilled and surmounted, an event recorded by the slcrT lithofacies.

Distally, topography played an important role in determining the outcrop variability; barrancos and ridges that dominate the present Tenerife landscape are believed to have been closely similar in style to the pre-Poris landscape, resulting in the ignimbrite veneer and valley-fill ignimbrite lithofacies distributions described by Brown and Branney (2004b). Distally, where ignimbrite exposure continues over a large area and topography varies across relatively short distances, lateral changes in the lithofacies succession, such as splay and fade stratification, occur at the transition from topographic high to topographic low (Branney and Kokelaar, 2002; Brown and Branney, 2004b). In the DH area such features do not occur in the Poris ignimbrite, partly perhaps because the topography in this zone, downstream of the Fasnia caldera wall, was of low slope with limited relief (see Fig. 5.2).

7.3.2 Ash aggregates in the proximal and distal record

Accretionary pellets are present in many lithofacies of the Poris succession, illustrating the importance of particle agglomeration in 'flushing' ash from the atmosphere during volcanic eruptions. There has been much debate concerning ash aggregation and several models have been proposed for the formation of accretionary pellets, both within the plume and within density stratified PDCs (see Section 1.4 and Brown *et al.*, in press). Large variation in ash aggregate morphology as a function of distance from source indicates that there are multiple aggregation pathways (Brown *et al.*, in press).

Brown and Branney (2004b) report that in distal Tenerife multi-rimmed AP2 pellets <15 mm in diameter occur in mLT deposits, capped by a fallout layer of unstructured

AP1 pellets. Only very small AP1 pellets, <2 mm in diameter, occur amidst the fine ash in the mLT units. On topographic highs, these deposits become thin ignimbrite veneers, and the mLTacc does not contain pumice and lithic lapilli. This lithofacies association is interpreted to reflect formation of AP1 pellets in the co-ignimbrite plume, which may then fall into the current and accrete rims to become AP2 pellets. The pellets rain out over topographic highs and lows to become deposited in ignimbrite. After the current has passed by, the remaining AP1 pellets in the co-ignimbrite plume fallout to form a clast-supported overlying layer (Brown *et al.*, 2010).

In the proximal zone, accretionary pellets do not occur in the same lithofacies association. No fallout layers of clast-supported AP1 pellets occur, and in mTacc1, thin section analysis of ash aggregates sampled shows that AP1 and AP2 pellets of a similar size (≤15 mm) occur together, supported by a fine-grained ash matrix that in places appears to consist of mm-scale ash pellets.

The difference in the occurrence of ash aggregates in proximal deposits is here interpreted to reflect hybrid aggregation processes. Distally, the PDC is the main source of ash. Proximally, the atmosphere around the plume above the vent is likely to be ash-laden, with plenty of scope for circulation towards and away from the hot plume axis, and electrically charged. Also, the availability of water is a control on ash aggregation, and water in the eruption plume can originate from volatiles in the magma, entrainment of moist tropospheric air, and through phreatomagmatism (Brown *et al.*, in press and references therein). It seems likely that in the near-vent region ash aggregation would have been ongoing in both the plume *and* within density currents, leading to various types of accretionary pellets becoming intermixed within the DH deposits.

There are several possibilities for the lack of AP1 fallout layers in the proximal zone. They may have been eroded by subsequent currents, but even at locality 16 where erosion is minimal between xscrT and mTacc1 there is no sign of a fallout layer. Alternatively, their absence may indicate that proximal conditions are not conducive to the formation of such layers. Following the passage of the main part of the first PDC, there was deposition of a mixture of ash, AP1 and AP2 aggregates, most

probably from a hybrid plume, to form mTacc1; the hybrid plume did not have an uppermost part that exclusively contained AP1 pellets, so no fallout layer of them alone was deposited.

A lack of significant hiatus in flow is given as the reason for the lack of ash pellet fall layers within the final flow unit of the distal stratigraphic scheme of Brown and Branney (2004b). In the DH zone, the mTacc2 and the third ash bed record highly localised, possibly short-lived, hiatus in PDC activity; perhaps the lack of ash pellet fallout layers above them reflects that there was not enough time for one to be deposited.

The change from the brittle, white, spherical accretionary pellets present in Phase 2 deposits to the grey, smaller, smoothly irregular pellets present in Phase 3 is here interpreted to reflect phreatomagmatism at this stage of the eruption. The fine fragmentation of lithic material caused an influx of grey ash into the eruptive plume. Some of this material agglomerated to form the grey central 'nucleus' particle of the accretionary pellets. The surrounding paler rims (Fig 7.4) suggest that by the time ash layers had begun accreting to the grey core, much of the lithic-rich ash had been shed from the plume. The fewer rims, and irregular nature of the grey accretionary pellets may indicate that the phreatomagmatic PDC was relatively cool and the cloud less turbulent, possibly due to increased water content; the circulation and 'baking' of accretionary pellets was therefore less effective. Accretionary lapilli in spBTacc in the DH wall (Phase 5) are brittle, relatively large, and do not have grey cores (see Fig 4.13d), indicating that when magmatic conditions resumed, ash aggregation changed back to the style experienced during Phase 2 of the eruption.

7.3.3 Poris petrogenesis: two magma series

The petrology and geochemistry of Diego Herrnandez deposits has been reported in several studies (Wolff, 1985; Wolff *et al.*, 2000; Edgar *et al.*, 2002; Edgar *et al.*, 2007). Each ignimbrite-forming eruption of the Diego Hernandez episode has a distinct Nb/Zr covariation signature (Fig.7.6), reflecting the relative incompatibility of Zr and the influence of titanite on the enrichment of Nb during phonolite petrogenesis (see Wolff *et al.*, 2000). The compositional duality found in the Poris

succession, recording contemporary eruption of two discrete magmas, also occurs in the Aldea, Fasnia, Caleta and Abrigo ignimbrites, as well as in some more minor deposits such as the Sabinita (Edgar *et al.*, 2007).

The high-Zr and low-Zr phonolite magmas that remained available to varying degrees throughout the Diego Hernandez episode are not thought to be related by any simple evolutionary mechanism (Edgar *et al.*, 2007). It has been suggested that the coexistence of the two separate magma chambers throughout this period, some 300 ka, is unlikely; the persistence of the distinct magmas may instead reflect repeated melting of different protoliths, with repeated fractionation of the magmas, following the caldera collapse and structural changes associated with each major eruption (Edgar *et al.*, 2007).

The new proximal findings from the Poris succession do not conflict with the previous studies; although there was a relatively large influx of the low-Zr magma in the closing stages of the eruption, it was available throughout the eruption, particularly evident in the blebs and mingled ballistics in Phase 4 deposits. Poris caldera collapse did not simply trigger the opening of a new vent to a different magma chamber, but subtly changed the plumbing of a complicated internal system.

7.3.4 The timing and cause of phreatomagmatism

Large accretionary pellets can form in the ash clouds of phreatomagmatic eruptions, where a considerable amount of water may be incorporated into the column (Brown *et al.*, in press). However, as discussed above, the moisture needed for ash aggregation to occur need not come from a phreatomagmatic eruption; non-phreatomagmatic, PDC-generating dome collapses at Unzen produced accretionary lapilli-rich deposits (Watanabe *et al.*, 1999).

Edgar *et al.*, (2002) interpret an ash layer containing accretionary pellets, Unit C (equivalent to mTacc1), as indicating phreatomagmatism at this stage of the eruption. This is refuted by Brown and Branney (2004b), who suggest that Poris ash layers

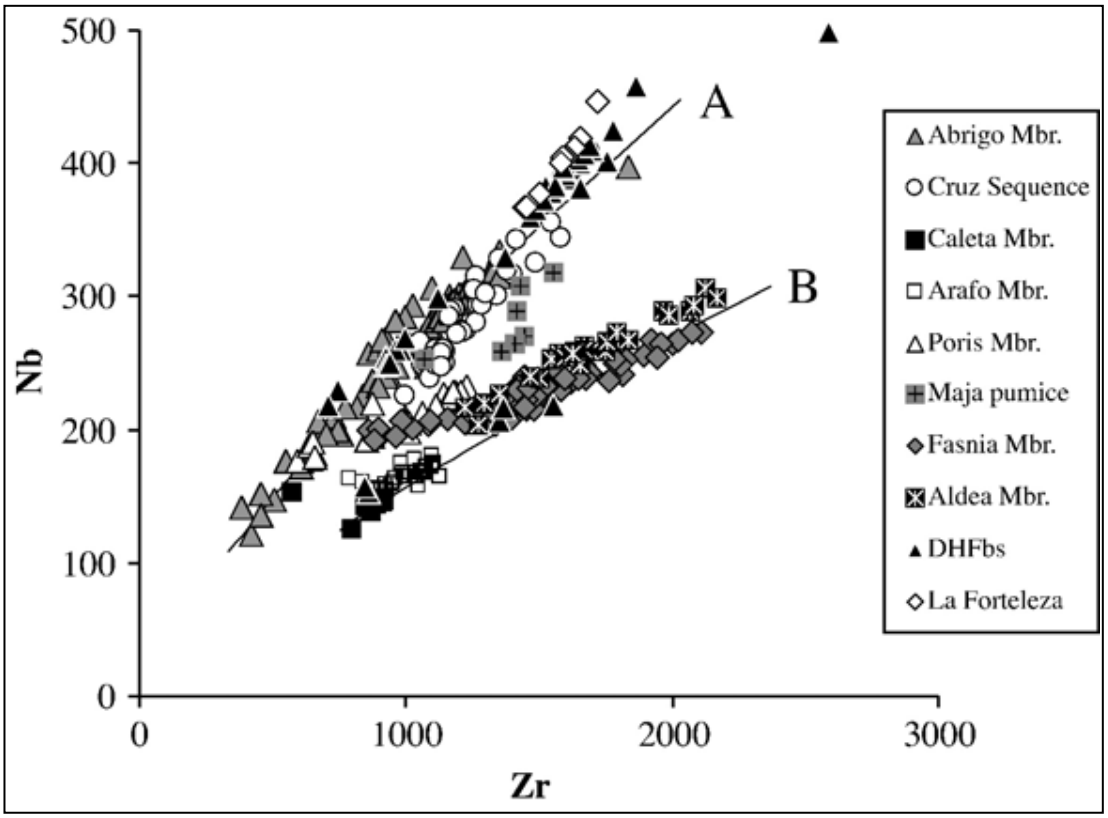

Fig 7.6 Nb/Zr covariation for phonolitic components of Diego Hernandez episode eruptions. A and B are Rayleigh Fractionation curves for two *different* starting compositions, both with 1% titanite in the fractionating assemblage (taken from Edgar *et al.*, 2007, adapted from Wolff *et al*., 2000, see papers for full explanation of data plotted).

with accretionary lapilli are ignimbrite veneers deposited by density stratified PDCs on topographic highs.

This new proximal investigation finds that the fine fragmentation of lithics, the altered heterolithic population, and the evidence of pulsatory waxing and waning in slcrT, offer strong evidence of phreatomagmatism during Phase 3 of the eruption. It is proposed here that although phreatomagmatism *may* have begun before this stage, during the deposition of //spLT/mTacc1, the presence of accretionary pellets is not conclusive evidence of this.

The source of the water that causes phreatomagmatic explosions is, in general, commonly unclear. Edgar *et al.* (2002) suggest that a shallow lake in the vent region is the most likely scenario. However, the pre-Poris environment may have been similar to the present; there is no lake in the current Cañadas basin, except for the ephemeral shallow ponds that form after heavy rainfall. The presence of a wide range of lithics in the slcrT deposit, including plutonic syenite, indicates that the phreatomagmatic source may have been within the volcanic aquifer, which was breached during the initial Plinian eruption. This would account for the excavation of deep, altered rocks during this phase of the eruption. It is not clear, in any case, how lake water alone can become profoundly reacted with a high mass flux eruptive jet; aquifer or hydrothermal system sources are most likely to be involved (pers. comm., Pete Kokelaar, 2012).

A grey, obsidian-rich tuff ring deposit at the base of the Diego Hernandez wall has similar structural features to the Poris slcrT lithofacies, with variable thin layers of graded tuff. The tuff ring lithic content, however, is different; altered and plutonic lithologies are rare. Whereas the Poris eruption involved the disruption of the internal hydrothermal system, the magma-water interaction that created the older tuff ring eruption apparently occurred at a shallower level (see Appendix 1).

7.3.5 Duration and volume

Brown and Branney (2004b) suggest that there is no evidence in the distal Poris succession for significant pauses during the eruption, and that the Poris event was

sustained over a period of hours to days rather than months to years. Findings from the proximal deposits support this hypothesis; there is no evidence of remobilisation or reworking of deposits within the succession.

It is difficult to estimate how long different phases of the eruption would have lasted. The main- and waning-phase ignimbrite deposits in the Diego Hernandez wall are of similar thickness, but this is no indication of the relative time taken to deposit. The main-phase deposits contain bypass surfaces that may represent minutes or hours of PDC activity. The climactic stage of the eruption, recorded proximally as the lithic-block layer, may have been relatively brief or may have been prolonged; there is no way of knowing.

The occurrence of hybrid deposits proximally, and the evidence that Plinian material entered currents and was deposited along with ignimbrite distally, implies that isopach maps of fallout unit thickness would be an unreliable tool for estimating total Plinian deposition during the Poris eruption. Furthermore, the considerable evidence of PDC bypass across proximal *and* distal zones suggests that it would be unfeasible to use ignimbrite volumes to determine actual, as opposed to minimum, erupted volume.

Edgar *et al.* (2002) propose a DRE volume of 3-4 km^3 for the eruption, but it has since been suggested that this figure could be considerably more, on account of the unknown extent of bypass of PDC material into the ocean (Brown and Branney, 2004a; 2004b). It has been suggested that the true volume may be 30-40 km^3 DRE (Brown and Branney, 2004b), which would be consistent with the order of size of caldera that could be accommodated within Las Cañadas. The deposit onland, to an extent, records slope and area; there is no recorded deposition on mid-flank regions, or on steep coastal reaches formed by lavas where coastal fans cannot accumulate.

7.3.6 Insights into Poris caldera collapse

The lithic-rich breccias in the distal Quinta/Tamadaya ignimbrites is clear evidence of a major structural change in the closing stages of the Poris eruption, which prompted a large influx of lithics into the eruption column. Doubtless some of the

lithics within the distal breccias were picked up from the substrate during flow, but the presence of altered and plutonic lithics is strong proof that the lithic influx records a major stage of Poris caldera collapse (Edgar *et al.*, 2002).

In the proximal zone, evidence of caldera collapse is rather more subtle. The presence of discrete lithic-rich layers within the mLT facies below the pumice-block breccia indicates that, periodically, large concentrations of lithics were entrained in PDCs. Close to the vent, there would have been less time and space for PDCs to entrain rocks from the substrate, so changes in lithic concentration are more indicative of subterranean processes. The lithic layers are commonly associated with evidence of bypass, so the true amount of lithics present in the current at the time cannot be known. It is proposed here that structural instabilities and incremental collapse, conceivably of a piecemeal nature, began to occur earlier in the Poris eruption than previously believed, but that this process is only clearly recorded proximally, where subtle changes in lithic concentration can be interpreted more directly. The lithic-block layer at the base of splBr, which correlates with the widespread distal lithic breccias, reflects the *climactic* collapse that began when a critical level of magma evacuation was reached and large parts of the chamber roof foundered.

7.3.7 The location of Poris exposure

It is important to consider the context of the Diego Hernandez exposures. The proximal lithofacies architecture presented here is a local snapshot, giving an insight into the processes occurring in a *particular sector* during the eruption. No other proximal exposures of the Poris ignimbrite succession have been found, but if they did exist they may display a different set of lithofacies. Changes in dispersal direction, topography and substrate around the vent would contribute to variability in proximal lithofacies in different sectors.

There is a dearth of medial exposures of Diego Hernandez pyroclastic deposits. Furthermore, the many Cordillera Dorsal lava flows and scoria layers on the flanks east of the DH wall make stratigraphic identification there of the few exposed deposits very difficult without geochemical analysis or dating. Medial and more

vent-radial exposures of Poris deposits would add to the eruption history, possibly shedding more light upon the bypass and hiatus issues; but at the time of writing it appears that these aspects of the story will remain missing.

Most of the reported distal Poris exposures are in the southeast Bandas del Sur zone, and authors have used those to infer direction of PDC flow and dispersal directions of Plinian fallout (e.g. Edgar *et al.*, 2002). It seems likely that the distribution of distal deposits has a direct relationship with the pre-Poris caldera-wall topography, which would have influenced PDC flow directions; for example, it could be inferred that the pre-Poris caldera was closed topographically to the north, because otherwise Poris density currents would have drained in this direction as well as to the south.

It has been suggested, based upon onshore deposits, that during eruptions of the Diego Hernandez episode pyroclastic density currents mainly moved towards the southeast of Tenerife from the central Cañadas zone (Edgar *et al.*, 2007). However, because material bypassed into the ocean in the Bandas del Sur region, where the coastal slopes are the least steep on Tenerife, and, because there are few or no deposits in steeper medial reaches above Bandas del Sur where currents must have passed, it is conceivable that pyroclastic density currents moved in other directions away from the vent, and that these are not registered in subaerial deposits because of erosion or non-deposition (Brown and Branney, 2004a).

It may be that Poris deposits elsewhere on the island have been eroded or destroyed during subsequent structural events such as lateral collapse, giving a misleading view of PDC flow direction. New research by Davila-Harris *et al*. (submitted) implies that many more landslides may have occurred on Tenerife during the past than previously thought. The authors propose the occurrence of a landslide in the Abona region (see Fig 2.1) not associated with a sector collapse scar of the scale of Guimar and La Orotava. The 'Abona Member' debris avalanche deposit, dated at 733±3 ka and therefore >400 ka years older than the Poris eruption, is enclosed by ignimbrites of the same age and is interpreted to reflect landsliding during the Helecho eruption in response to oversteepening of a phonolite lava dome. The evidence for this is solely geological, and not based upon geomorphology or offshore deposits, and though the event can be dated precisely using sanidines from phonolite blocks within the

deposit, the structural effects and extent of the slide are cryptic. Any valley created during the slide has since been buried by subsequent volcanism. Such landslides would significantly modify the local topography as well as eroding previously deposited material. It has been suggested that ignimbrites are sectoral in their exposure across Tenerife because of progressive changes in the landscape, rather than as a result of eruptive variations at source; the Abona landslide may have been responsible for the channelling of subsequent density currents to the southeast Bandas del Sur region (Davila-Harris *et al.*, submitted).

The work presented here should be viewed in context; Poris exposures studied in this thesis and by previous workers record an eruption and associated phenomena that varied significantly in time and space. The exact volume of Poris material that bypassed into the ocean during the eruption is unknown; the amount of the on-land Poris record lost to erosion is also unknown.

Chapter Eight
Synthesis and further work

This study has applied the lithofacies architecture approach of Branney and Kokelaar (2002) to investigate proximal deposition from pyroclastic density currents and to correlate the proximal record of an ignimbrite-forming eruption with its distal counterpart. In this chapter, key findings are discussed and potential sites for further study of proximal deposition are outlined.

8.1 Proximal lithofacies architecture

Uniquely proximal lithofacies identified in the Diego Hernandez exposures of the Poris succession include a hybrid unit, a lithic-rich phreatomagmatic deposit, and a pumice-block breccia. These are not recorded distally, and their characteristics reveal near-vent processes that study of the coastal region alone could not. Ignimbrite veneer lithofacies with associated accretionary pellets occur in both the proximal and the distal zone, but represent different environments of deposition; proximally, the lithofacies records interaction of density stratified currents with significant caldera topography, whereas distally the units are formed as a result of PDC interaction with localised ridges and valleys.

Proximally, the paucity of intervening ground where PDCs could entrain lithics from the substrate prior to sedimentation creates a depositional record sensitive to changes in lithic input at source. Evidence for incremental destabilisation prior to climactic caldera collapse is thus recorded proximally, as discrete lithic-rich layers of tuff. Similarly, the lack of opportunity for substantial clast abrasion within any flow prior to proximal sedimentation means that the grain-size of near-vent deposits is likely to be more representative of the size of the material erupted than is the case for distal deposits. The large pumice blocks ejected during the final stages of the eruption are preserved in the proximal record but not distally.

The architecture of the proximal Poris deposits is consistent with deposition from a density stratified pyroclastic current onto a fairly planar substrate within the Diego Hernandez palaeovalley; this was down-stream of a significant caldera topographic

barrier that is inferred to have become buried as the eruption progressed. Relatively minor topographic modification would have occurred during the eruption, as the density current(s) scoured into previous deposits to different levels, affecting subsequent deposition; in the southern exposures, where the first lithic-rich tuff layer occupies deep scours, the overlying ignimbrite is relatively rich in elutriation pipes and load structures. Outside of the Diego Hernandez palaeovalley, depositional conditions varied; a different sequence is recorded at the gully near Montaña el Cerrillar, where only the final pumice-block breccia occurs. In the lower Diego Hernandez wall, the 319 ka Aldea ignimbrite (Edgar *et al.*, 2007) contains large and complex scour features (see Appendix 1). This succession was deposited onto a substrate that varied in topography across the wall, partly due to the irregular top surface of a tuff ring; the contrast between Aldea and Poris scour features is further evidence of the important control of topography upon ignimbrite architecture.

Stratification in the proximal zone is somewhat different from that which occurs distally. Laterally variable, discontinuous, inversely graded tuff is common in DH exposures. In the distal zone, diffuse and splay-and-fade stratification is common, particularly in the transition zone between valley fill and veneer lithofacies (Brown and Branney, 2004b). The creation of stratification within ignimbrites is a non-trivial issue and the causes of this variability are not completely understood. The degree of non-uniformity within the flow-boundary zone and the nature of substrate topography are crucial factors. This work indicates that across a relatively low-gradient substrate, pulsatory waning and waxing of the current may play a crucial part in the creation of deposit stratification. The mechanisms of such pulsatory conditions at the flow boundary zone are unclear, but within relatively thin flows, or in thin granular-fluid basal zones, they may reflect the spontaneous generation of roll waves.

8.2 The nature of Poris pyroclastic density currents

Brown and Branney (2004b) report that the distal Poris ignimbrite succession is composed of four flow units, delineated by ash fallout layers, and they propose that at least four sustained and widespread PDCs were generated during the eruption. However, the proximal record comprises only two flow units delineated by the

intervening mTacc1 lithofacies, which records a widespread hiatus in the passage of PDCs. Localised ash layers at higher levels in the proximal succession record only local hiatus in ignimbrite deposition. Nevertheless, correlation between the distal and proximal records indicates that all the units recorded distally have a proximal *temporal* counterpart, if not a physically similar counterpart.

This study proposes that the Poris eruption may have involved only *two* density-stratified pyroclastic currents; the first relatively small, the second large and sustained (Fig. 8.1). The periodic waning of the large, second current led to two widespread hiatuses in the distal zone while deposition continued proximally. Waning occurred following the phreatomagmatic phase when ash fallout was deposited and also following the hybrid phase when a Plinian fallout bed was deposited distally. During these waning events, proximal deposition was particularly unsteady; stratification formed and some evidence of localised hiatus is recorded. Periodic waning may have continued further into the eruption, but the run-out distance of the current was such that no further hiatuses were recorded in the Bandas del Sur. Waxing of the current was accompanied by an influx of lithics at ≥5 points during the eruption (slcrT lithics at phase 3, at least three lithic-rich layers of tuff in phase 5, and the lithic block layer of phase 6) (Fig. 8.1). During the final waning of the eruption, the run-out distance of the density current gradually decreased and Plinian deposition was recorded in some distal zones.

The characteristics of proximal Poris lithofacies reflect conditions at the base of the pyroclastic density currents during deposition. At first, the Diego Hernandez zone was part of a topographic high and the parts of the first current that surmounted it were fully dilute, turbulent and with traction at the base. At the same time, diverted lower parts of the same PDC had granular-fluid basal parts and continued to form over-riding low-concentration parts. As the eruption progressed and the topography became modified, the concentration gradient at the current-deposit interface became more gradational as granular-fluid based deposition occurred in the DH zone.

Figure 8.1: Schematic diagram to show the nature of pyroclastic density current deposition during the Poris eruption. Plinian deposition is inferred and included for completeness; it is not known whether Plinian fallout persisted throughout the entire eruption. No scale is implied; in reality, distal deposits are far greater in thickness than proximal units due to the effect of bypass. Eruption phases correspond to those described in detail in Chapter 7.

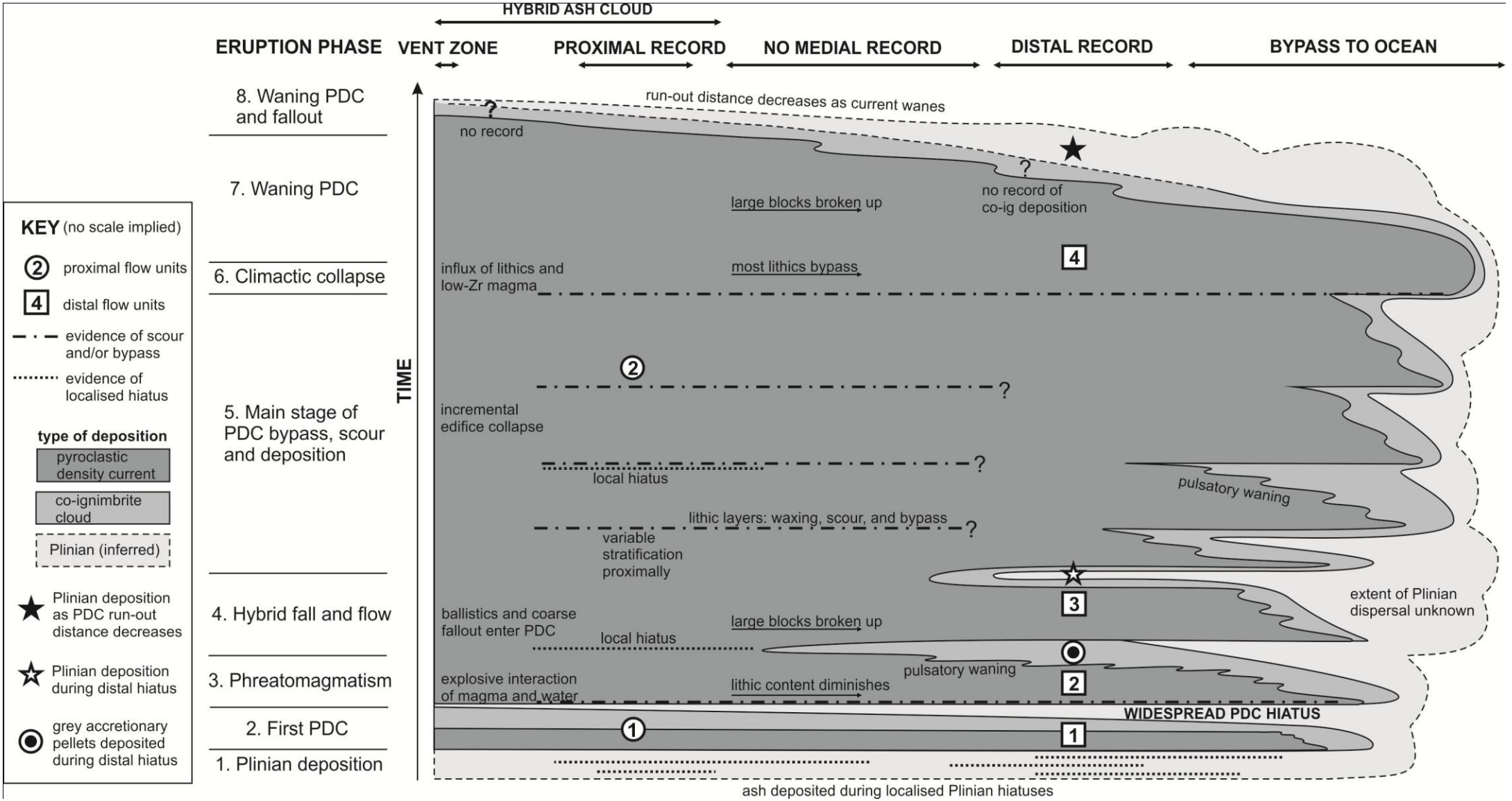
HYBRID ASH CLOUD
ERUPTION PHASE
VENT ZONE
PROXIMAL RECORD
NO MEDIAL RECORD
DISTAL RECORD
BYPASS TO OCEAN
8. Waning PDC and fallout
7. Waning PDC
6. Climactic collapse
5. Main stage of PDC bypass, scour and deposition
4. Hybrid fall and flow
3. Phreatomagmatism
2. First PDC
1. Plinian deposition
TIME
KEY (no scale implied)
proximal flow units
distal flow units
evidence of scour and/or bypass
evidence of localised hiatus
type of deposition
pyroclastic density current
co-ignimbrite cloud
Plinian (inferred)
Plinian deposition as PDC run-out distance decreases
Plinian deposition during distal hiatus
grey accretionary pellets deposited during distal hiatus
run-out distance decreases as current wanes
no record
large blocks broken up
no record of co-ig deposition
influx of lithics and low-Zr magma
most lithics bypass
incremental edifice collapse
local hiatus
pulsatory waning
lithic layers: waxing, scour, and bypass
variable stratification proximally
extent of Plinian dispersal unknown
ballistics and coarse fallout enter PDC
large blocks broken up
local hiatus
pulsatory waning
explosive interaction of magma and water
lithic content diminishes
WIDESPREAD PDC HIATUS
ash deposited during localised Plinian hiatuses

Subtle topographic variations and changes in substrate as a result of scour and infill were ongoing during the eruption, causing unsteadiness and lateral non-uniformity in flow boundary conditions. These processes combined with the larger-scale patterns of current waxing and waning created the variable stratification in the deposits.

8.3 How proximal was the Diego Hernandez wall at 273 ka?

Features typically associated with near-vent volcanic deposition such as intense welding (Carey *et al.*, 2008a, b), evidence of conduit structures (Soriano *et al.*, 2006) and spatter-type ejecta (Mellors and Sparks, 1991) are not recorded in the Poris lithofacies exposed in the Diego Hernandez wall. Fire-fountaining during Plinian eruptions may create welded deposits that occur a few kilometres from source (Capaccioni and Cuccoli, 2005), and although welded units are reported in the Guajara and Ucanca sections of the Cañadas wall (Martí *et al.*, 1990), eutaxitic textures and evidence of rheomorphic flow are not found in the Fasnia, Aldea, or Poris ignimbrite exposures. It appears that there is not enough of a compositional difference between the Ucanca, Guajara and Diego Hernandez magmas to suggest that differing rheologies and eruption styles led to the presence or absence of welding (pers. comm.., Joan Martí, 2010). Therefore, although the ignimbrites are proximal compared to those in the Bandas del Sur, the Diego Hernandez wall may not have been 'under the fountain', very close to the vent, during these eruptions.

It has been suggested that the Guajara and Ucanca vents were located in the southern part of the current Cañadas depression, whereas the Aldea, Fasnia and Poris vents were located farther north, closer to the present La Fortaleza escarpment (Fig 8.2). This isolated outcrop is interpreted as a caldera-wall segment and it contains welded deposits believed to be of early DH age (pers. comm., Joan Martí, 2010). The Roques de Garcia, a pre-Ucanca (1.69 Ma) formation densely intruded with dykes (Martí *et al.*, 2010) may represent part of the plumbing system of a pre-DH (>500 ka) edifice (see Chapter 2). Structural changes in the volcanic plumbing of the area following the climactic Granadilla eruption at 600 ka (Brown *et al.*, 2003), may have caused vent migration following the Guajara episode of volcanism.

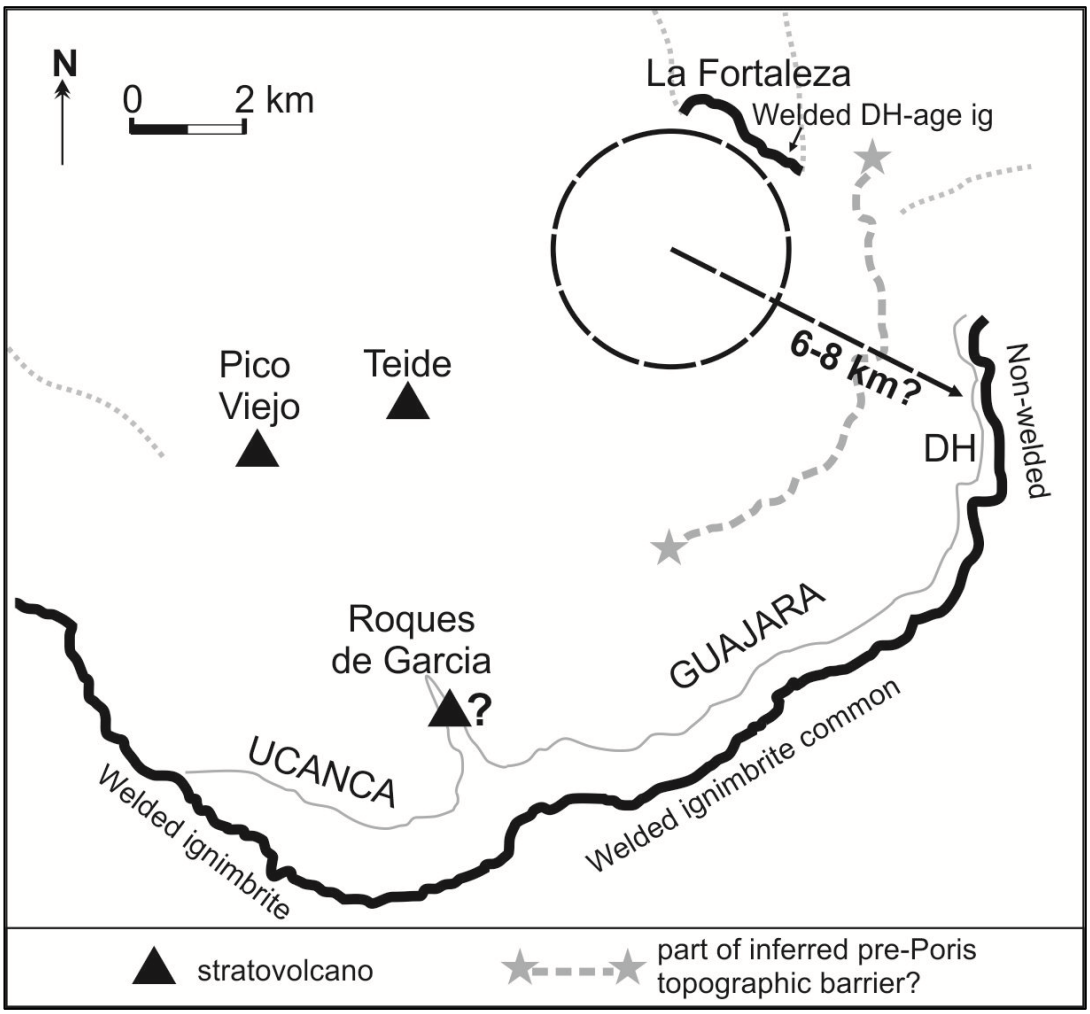

Figure 8.2 Possible source location of the Diego Hernandez aged pyroclastic units (160-400 ka) (circle), based upon occurrence of welded ignimbrite of Diego Hernandez age in the La Fortaleza escarpment (Joan Martí, pers. comm.., 2010). The predominance of welded ignimbrite in the Ucanca and Guajara sectors of the wall indicate that the source vent was farther south when these units were deposited.

Information collected from scours and sheared elutriation pipes in DH Poris deposits (this study) records current directions of 071-080 º in northern units and 124º ESE in southern units, conceivably indicating that Poris PDCs spread radially across the area from a northwesterly source. This does not match well with a source of Poris close to La Fortaleza, but PDCs are likely to have been constrained by topography and channelled through the Diego Hernandez 'palaeovalley', so to use the scour and shear orientations strictly as an indication of source location is unwarranted. Furthermore, evidence of non-uniform deposition across the DH wall (see Chapter 5) suggests that current direction information from any one location is unlikely to be representative of the PDC(s) as a whole.

8.4 The significance of ignimbrite correlation

The most significant finding of the correlation of the proximal and distal records is the new information concerning the number of pyroclastic density currents that were generated during the Poris eruption (discussed above). Density currents are the most deadly volcanic hazard, and information concerning their frequency and behaviour during past eruptions may be of use when planning for mitigation of risks due to future explosive eruptions on Tenerife. That currents were partly blocked by near-vent topography may also be significant for planning, as similar effects due to the Cañadas landscape may be anticipated during future eruptions. The opening to the north due to the Icod collapse could conceivably lead to a very different coastal distribution of ignimbrite during future eruptions.

Another issue highlighted by this research is the lack of 'typical' Plinian deposition in the proximal region, owing to hybrid processes and reworking. The reworking of the Plinian substrate by the first PDC led to irregular thickness of the fallout deposit, the original extent of which is unknown. The spBT lithofacies is a reflection of the occurrence of hybrid processes at a time when fallout pumices were coarse enough to be recognised, but it is unclear how much Plinian material fell out into the currents during PDC flow to become deposited along with mLT. The deposition of Plinian material during phase 4 in the distal zone led workers to suggest the "brief re-establishment" of a Plinian column (Brown and Branney, 2004b), but the findings of proximal hybrid deposits in the DH zone are an indication that Plinian deposition

may have played a larger part in the Poris eruption than was previously recognised. This work highlights the fact that the use of isopach maps in the distal zone to ascertain Plinian thickness and therefore total Plinian volumes for very large eruptions that involve widespread PDCs can only ever provide a minimum estimate, as the amount of Plinian fallout deposited along with PDC material to form mLT cannot be quantified.

Evidence of widespread scour and bypass has been reported in distal reaches by previous workers (Brown and Branney, 2004b). This study finds that proximal non-deposition and bypass are also significant, perhaps reinforcing the point that recorded ignimbrite volumes can only give a bare minimum estimate of the material actually erupted.

8.5 Further work

This work represents a step towards a more coherent understanding of how density currents progressively deposit in time and space, but more work is needed to better understand ignimbrite correlations across large distances, and the significance of these correlations in relation to eruption volume, bypass and non-deposition, and the movement of density currents across topography. These issues have knock-on effects for hazard analysis and risk mitigation planning, particularly with respect to the timing of ash aggregate deposition and the flow-stripping of PDCs.

Proximal to distal correlations have been attempted at other locations, such as Campei Flegrei in Italy (Ort *et al.*, 1999), but poor exposure is typically a significant problem. Geochemical analysis is commonly used to correlate between different exposures of an ignimbrite (e.g. de Silva and Francis, 1989) but, where alteration is an issue or stratigraphic geochemical variation is minimal, the lithofacies architecture technique, whereby entrachrons are used to link certain events and therefore certain parts of the record, becomes an invaluable tool.

Tenerife is unlike many locations, in that both proximal and distal outflow sheets are well exposed and relatively easily accessible for study. Further work on the island could include the correlation of proximal Guajara ignimbrite lithofacies with those

exposed at the coastline; the welded facies in the Cañadas wall conceivably represent a more vent-proximal record than that of the Poris Formation and would be invaluable in considering the variability in processes with close proximity to the source region. Such work would also offer the opportunity to compare welded and non-welded proximal evidence of architectural features such as stratification, and scour and bypass surfaces.

This lithofacies architecture method could be applied to other well-exposed ignimbrite sheets with good proximal exposure, such as the Minoan deposit of Santorini. Comparison of studies from multiple volcanoes would enable evaluation of the effects that changes in magma chemistry and topography have upon proximal volcanic processes and the behaviour of pyroclastic density currents in time and space.

References

Ablay, G. and Hürlimann, M., 2000. Evolution of the north flank of Tenerife by recurrent giant landslides. Journal of Volcanology and Geothermal Research, 103(1-4): 135-159.

Ablay, G. and Kearey, P., 2000. Gravity constraints on the structure and volcanic evolution of Tenerife, Canary Islands. Journal of Geophysical Research, 105(B3): 5783-5796.

Ablay, G.J., Ernst, G.G.J., Marti, J. and Sparks, R.S.J., 1995. The ~2?ka subplinian eruption of Montaña Blanca, Tenerife. Bulletin of Volcanology, 57(5): 337-355.

Ancochea, E., Fuster, J.M., Ibarrola, E., Cendrero, A., Coello, J., Hernan, F., Cantagrel, J.M. and Jamond, C., 1990. Volcanic evolution of the island of Tenerife (Canary Islands) in the light of new K-Ar data. Journal of Volcanology and Geothermal Research, 44(3-4): 231-249.

Ancochea, E., Huertas, M.J., Cantagrel, J.M., Coello, J., Fuster, J.M., Arnaud, N. and Ibarrola, E., 1999. Evolution of the Canadas edifice and its implications for the origin of the Canadas Caldera (Tenerife, Canary Islands). Journal of Volcanology and Geothermal Research, 88(3): 177-199.

Anderson, T. and Flett, J.S., 1903. Report on the eruptions of the Soufrière, in St. Vincent, in 1902, and on a visit to Montagne Pelée in Martinique. Royal Society [London] Phil. Trans. Series A Part 1, 200: 353-553.

Andrews, G.D.M. and Branney, M.J., 2011. Emplacement and rheomorphic deformation of a large, lava-like rhyolitic ignimbrite: Grey's Landing, southern Idaho. Geological Society of America Bulletin, 123(3-4): 725-743.

Anguita, F. and Hernan, F., 1975. A propagating fracture model versus a hot-spot origin for the Canary Islands. Earth and Planetary Science Letters, 27: 11-19.

Anguita, F. and Hernán, F., 2000. The Canary Islands origin: a unifying model. Journal of Volcanology and Geothermal Research, 103(1-4): 1-26.

Araña, V., 1971. Litología y estructura del Edificio Cañadas, Tenerife (Islas Canarias). Estudios Geológicos, 27: 95-135.

Araña, V. and Brandle, J.L., 1969. Variation trends in the alkaline salic rocks of Tenerife. Bulletin of Volcanology, 33: 1145-1165.

Balmforth, N.J. and Mandre, S., 2004. Dynamics of roll waves. Journal of Fluid Mechanics, 514: 1-33.

Battaglia, M., 1993. On pyroclastic flow emplacement. Journal of Geophysical Research, 98(B12): 22,269-222,272.

Bear, A.N., Cas, R.A.F. and Giordano, G., 2009a. The implications of spatter, pumice and lithic clast rich proximal co-ignimbrite lag breccias on the dynamics of caldera forming eruptions: The 151 ka Sutri eruption, Vico Volcano, Central Italy. Journal of Volcanology and Geothermal Research, 181(1-2): 1-24.

Bear, A.N., Cas, R.A.F. and Giordano, G., 2009b. Variations in eruptive style and depositional processes associated with explosive, phonolitic composition, caldera-forming eruptions: The 151 ka Sutri eruption, Vico Caldera, central Italy. Journal of Volcanology and Geothermal Research, 184(3-4): 225-255.

Bednarz, U. and Schmincke, H.U., 1990. Evolution of the quaternary mellite-nepheline Herchenberg volcano East Eifel. Bulletin of Volcanology, 52: 426-444.

Blake, S. and Ivey, G.N., 1986. Magma-mixing and the dynamics of withdrawal from stratified reservoirs. Journal of Volcanology and Geothermal Research, 27(1–2): 153-178.

Bonadonna, C., Macedonio, G. and Sparks, R.S.J., 2002a. Numerical modelling of tephra fallout associated with dome collapses and Vulcanian explosions: application to hazard assessment on Montserrat. In: Druit, T.H. and Kokelaar, B.P. (Editors), The

Eruption of Soufrière Hills Volcano, Montserrat, from 1995 to 1999. . Geological Society, London, Memoirs, pp. 517-537.
Bonadonna, C., Mayberry, G.C., Calder, E.S., Sparks, R.S.J., Choux, C.M., Jackson, Lejeune, A.M., Loughlin, S.C., Norton, G.E., Rose, W.I., Ryan, G. and Young, S.R., 2002b. Tephra fallout in the eruption of Soufrière Hills Volcano, Monserrat. In: Druit, T.H. and Kokelaar, B.P. (Editors), The eruption of Soufrière Hills Volcano, Monserrat from 1995 to 1999. . Geological Society, London, Memoirs, pp. 483-516.
Booth, B., 1973. The Granadilla pumice deposit of southern Tenerife, Canary Islands. Proceedings of the Geological Association, 84: 353-370.
Borgia, A., Delaney, P.T. and Denlinger, R.P., 2000. Spreading volcanoes. Annual Review of Earth and Planetary Sciences, 28: 539-570.
Branney, M., 1995. Downsag and extension at calderas: new perspective on collapse geometries from ice-melt, mining, and volcanic subsidence. Bulletin of Volcanology, 57(303-318).
Branney, M.J., 1991. Eruption and depositional facies of the Whorneyside Tuff Formation, English Lake Dustrict- an exceptionally large-magnitude phreatoplinian eruption. Geological Society of America Bulletin, 103(7): 886-897.
Branney, M.J. and Brown, R.J., 2011. Impactoclastic Density Current Emplacement of Terrestrial Meteorite-Impact Ejecta and the Formation of Dust Pellets and Accretionary Lapilli: Evidence from Stac Fada, Scotland. The Journal of Geology, 119(3): 275-292.
Branney, M.J. and Gilbert, J.S., 1995. Ice-melt collapse pits and associated features in the 1991 lahar deposits of Volcán Hudson, Chile: criteria to distinguish eruption-induced glacier melt. Bulletin of Volcanology, 57(5): 293-302.
Branney, M.J. and Kokelaar, B.P., 1992. A reappraisal of ignimbrite emplacement- Progressive aggradation and changes from particulate to non-particulate flow during emplacement of high-grade ignimbrite. Bulletin of Volcanology, 54(6): 504-520.
Branney, M.J. and Kokelaar, B.P., 2002. Pyroclastic Density Currents and the Sedimentation of Ignimbrites.
Branney, M.J. and Kokelaar, P., 1994. Volcanotectonic faulting, soft-state deformation, and rheomorphism of tuffs during development of a piecemeal caldera, English Lake District. Geological Society of America Bulletin, 106(4): 507-530.
Branney, M.J. and Kokelaar, P., 1997. Giant bed from a sustained catastrophic density current flowing over topography: Acatlan ignimbrite, Mexico. Geology, 25(2): 115-118.
Bravo, T., 1952. Aportacion al estudio geomorfologico y geologico de la costa de la fosa tectonica del valle de la Orotava. Bol. R. Soc. Esp. Hist. Nat., Tomo. L.: 1-30.
Bravo, T., 1962. El circo de Las Cañadas y sus dependencias. Bol Esp Hist Nat, 60: 93-135.
Brazier, S., Davis, A.N., Sigurdsson, H. and Sparks, R.S.J., 1982. Fall-out and deposition of volcanic ash during the 1979 explosive eruption of the soufriere of St. Vincent. Journal of Volcanology and Geothermal Research, 14(3-4): 335-359.
Brown, R.J., 2001. Eruption history and depositional processes of the Poris ignimbrite of Tenerife and the Glaramara tuff of the English Lake District. Unpublished PhD Thesis University of Leicester.
Brown, R.J., Barry, T.L., Branney, M.J., Pringle, M.S. and Bryan, S.E., 2003. The Quaternary pyroclastic succession of southeast Tenerife, Canary Islands: explosive eruptions, related caldera subsidence, and sector collapse. Geological Magazine, 140(3): 265-288.
Brown, R.J., Bonadonna, C. and Durant, A.J., in press. A Review of Volcanic Ash Aggregation. Physics and Chemistry of the Earth.
Brown, R.J. and Branney, M., 2004a. Bypassing and diachronous deposition from density currents: Evidence from a giant regressive bed form in the Poris ignimbrite, Tenerife, Canary Islands. Geology, 32(5): 445-448.

Brown, R.J., Branney, M., Maher, C. and Davila-Harris, P., 2010. Origin of accretionary lapilli within ground-hugging density currents: Evidence from pyroclastic couplets on Tenerife. Geological Society of America Bulletin, 122(1/2): 305-320.

Brown, R.J. and Branney, M.J., 2004b. Event-stratigraphy of a caldera-forming ignimbrite eruption on Tenerife: the 273 ka Poris Formation. Bulletin of Volcanology, 66(5): 392-416.

Bryan, S.E., 2006. Petrology and geochemistry of the quaternary caldera-forming, phonolitic Granadilla eruption, Tenerife (Canary Islands). Journal of Petrology, 47(8): 1557-1589.

Bryan, S.E., Cas, R.A.F. and Marti, J., 1998a. Lithic breccias in intermediate volume phonolitic ignimbrites, Tenerife (Canary Islands): constraints on pyroclastic flow depositional processes. Journal of Volcanology and Geothermal Research, 81(3-4): 269-296.

Bryan, S.E., Marti, J. and Cas, R.A.F., 1998b. Stratigraphy of the Bandas del Sur Formation: an extracaldera record of Quaternary phonolitic explosive eruptions from the Las Canadas edifice, Tenerife (Canary Islands). Geological Magazine, 135(5): 605-636.

Bryan, S.E., Marti, J. and Leosson, M., 2002. Petrology and geochemistry of the Bandas del Sur Formation, Las Canadas Edifice, Tenerife (Canary Islands). Journal of Petrology, 43(10): 1815-1856.

Camacho, A.G., Vieira, R. and de Toro, C., 1991. Microgravimetric model of the Las Cañadas caldera (Tenerife). Journal of Volcanology and Geothermal Research, 47(1-2): 75-88.

Cantagrel, J.M., Arnaud, N.O., Ancochea, E., Fuster, J.M. and Huertas, M.J., 1999. Repeated debris avalanches on Tenerife and genesis of Las Canadas caldera wall (Canary Islands). Geology, 27(8): 739-742.

Capaccioni, B. and Cuccoli, F., 2005. Spatter and welded air fall deposits generated by fire-fountaining eruptions: Cooling of pyroclasts during transport and deposition. Journal of Volcanology and Geothermal Research, 145(3–4): 263-280.

Carey, R.J., Houghton, B.F. and Thordarson, T., 2008a. Contrasting styles of welding observed in the proximal Askja 1875 eruption deposits I: Regional welding. Journal of Volcanology and Geothermal Research, 171(1-2): 1-19.

Carey, R.J., Houghton, B.F. and Thordarson, T., 2008b. Contrasting styles of welding observed in the proximal Askja 1875 eruption deposits II: Local welding. Journal of Volcanology and Geothermal Research, 171(1-2): 20-44.

Carey, S. and Sigurdsson, H., 1982. Influence of particle aggregation on deposition of distal tephra from the May 18 1980 eruption of Mount St. Helens volcano. Journal of Geophysical Research, 87(B8): 7061-7072.

Carracedo, J.C., 1994. The Canary Islands: An example of structural control on the growth of large oceanic-island volcanoes. Journal of Volcanology and Geothermal Research, 60(3-4): 225-241.

Carracedo, J.C., 1996. A simple model for the genesis of large gravitational landslide hazards in the Canary Islands. In: McGuire, W.J., Jones, A.P. and Neuberg, J. (Editors), Conference on Volcano Instability on the Earth and Other Planets. Geological Soc Publishing House, London, England, pp. 125-135.

Carracedo, J.C., Day, S.J., Guillou, H. and Pérez Torrado, F.J., 1999. Giant Quaternary landslides in the evolution of La Palma and El Hierro, Canary Islands. Journal of Volcanology and Geothermal Research, 94(1-4): 169-190.

Carracedo, J.C., Day, S.J., Guillou, H., Rodríguez-Badiola, E., Canas, J.A. and Perez Torrado, F.J., 1998. Hotpsot volcanism close to a passive continental margin: the Canary islands. Geological Magazine, 135(591-604).

Cas, R., Porritt, L., Pittari, A. and Hayman, P., 2008. A new approach to kimberlite facies terminology using a revised general approach to the nomenclature of all volcanic rocks and deposits: Descriptive to genetic. Journal of Volcanology and Geothermal Research, 174(1-3): 226-240.

Cas, R. and Wright, J.V., 1987. Volcanic Successions. Chapman & Hall.

Clough, C.T., Maufe, H.B. and Bailey, E.B., 1909. The cauldron subsidence of Glencoe and the associated igneous phenomena. Q. Journal of the Geological Society London, 65: 611-678.

Coates, D., 1977. Landslide Perspectives. Reviews of English Geology, 3: 3-28.

Coello, J., 1973. Las series volcanicas en subsuelos de Tenerife. Estudios Geológicos, 29: 491-512.

Cole, J.W., Milner, D.M. and Spinks, K.D., 2005. Calderas and caldera structures: a review. Earth-Science Reviews, 69(1–2): 1-26.

Cole, P., Guest, J., Duncan, A. and Pacheco, J., 2001. Capelinhos 1957–1958, Faial, Azores: deposits formed by an emergent surtseyan eruption. Bulletin of Volcanology, 63(2): 204-220.

Coppo, N., Schnegg, P.A., Heise, W., Falco, P. and Costa, R., 2008. Multiple caldera collapses inferred from the shallow electrical resistivity signature of the Las Canadas caldera, Tenerife, Canary Islands. Journal of Volcanology and Geothermal Research, 170(3-4): 153-166.

Costa, A., Folch, A. and Macedonio, G., 2010. A model for wet aggregation of ash particles in volcanic plumes and clouds: 1. Theoretical formulation. J. Geophys. Res., 115(B9): B09201.

Dade, W.B. and Huppert, H.E., 1996. Emplacement of the Taupo ignimbrite by a dilute turbulent flow. Nature, 381(6582): 509-512.

Davila-Harris, P., Branney, M. and Storey, M., submitted. Large eruption-triggered ocean-island landslide at Tenerife: on-shore record and long-term effects on hazardous pyroclastic dispersal. Geology.

de Silva, S.L. and Francis, P.W., 1989. Correlation of large ignimbrites — Two case studies from the Central Andes of northern Chile. Journal of Volcanology and Geothermal Research, 37(2): 133-149.

Deplus, C., Le Friant, A., Boudon, G., Komorowski, J.-C., Villemant, B., Harford, C., Ségoufin, J. and Cheminée, J.-L., 2001. Submarine evidence for large-scale debris avalanches in the Lesser Antilles Arc. Earth and Planetary Science Letters, 192(2): 145-157.

Druitt, T.H., 1998. Pyroclastic Density Currents. In: Gilbert, J.S. and Sparks, R.S.J. (Editors), The Physics of Explosive Volcanic Eruptions. Geological Society of London Special Publications, pp. 145-182.

Druitt, T.H. and Bacon, C.R., 1986. Lithic Breccia and Ignimbrite Erupted During the Collapse of Crater Lake, Oregon. Journal of Volcanology and Geothermal Research, 29: 1-32.

Druitt, T.H., Calder, E.S., Cole, P.D., Hoblitt, R.P., Loughlin, S.C., Norton, G.E., Ritchie, L.J., Sparks, R.S.J. and Voight, B., 2002. Small volume, highly mobile pyroclastic flows formed by rapid sedimentation from pyroclastic surges at Soufriere Hills Volcano, Montserrat: an important volcanic hazard. In: Druitt, T.H. and Kokelaar, B.P. (Editors), The Eruption of Soufriere Hills Volcano, Montserrat, from 1995 to 1999. Geological Society of London, pp. 263-279.

Druitt, T.H., Edwards, L., Mellors, R.M., Pyle, D.M., Sparks, R.S.J., Lanphere, M., Davies, M. and Barriero, B., 1999. Santorini Volcano. The Geological Society.

Druitt, T.H. and Sparks, R.S.J., 1982. A proximal ignimbrite breccia facies on santorini , Greece. Journal of Volcanology and Geothermal Research, 13(1-2): 147-171.

Druitt, T.H. and Sparks, R.S.J., 1984. On the formation of calderas during ignimbrite eruptions. Nature, 310(5979): 679-681.

Dufek, J. and Manga, M., 2011. Granular Disruption During Explosive Volcanic Eruptions, IUGG Earth on the Edge, Melbourne, Australia.

Durant, A.J., Rose, W.I., Sarna-Wojcicki, A.M., Carey, S. and Volentik, A.C.M., 2009. Hydrometeor-enhanced tephra sedimentation: Constraints from the 18 May 1980 eruption of Mount St. Helens. J. Geophys. Res., 114(B3): B03204.

Durant, A.J., Villarosa, G., Rose, W.I., Delmelle, P., Prata, A.J. and Viramonte, J.G., in press. Long-range volcanic ash transport and fallout during the 2008 eruption of Chaitén volcano, Chile. Physics and Chemistry of the Earth, Parts A/B/C(0).

Dutton, E.C., 1884. Hawaiian Volcanoes. 4th Annual Report- U.S. Geological Survey, Washington D.C.: 75-219.

Edgar, C.J., Wolff, J.A., Nichols, H.J., Cas, R.A.F. and Marti, J., 2002. A complex quaternary ignimbrite-forming phonolitic eruption: the poris member of the Diego Hernandez Formation (Tenerife, Canary Islands). Journal of Volcanology and Geothermal Research, 118(1-2): 99-130.

Edgar, C.J., Wolff, J.A., Olin, P.H., Nichols, H.J., Pittari, A., Cas, R.A.F., Reiners, P.W., Spell, T.L. and Marti, J., 2007. The late quaternary Diego Hernandez Formation, Tenerife: Volcanology of a complex cycle of voluminous explosive phonolitic eruptions. Journal of Volcanology and Geothermal Research, 160(1-2): 59-85.

Elsworth, D. and Day, S.J., 1999. Flank collapse triggered by intrusion: the Canarian and Cape Verde Archipelagoes. Journal of Volcanology and Geothermal Research, 94(1-4): 323-340.

Elsworth, D. and Voight, B., 1996. Evaluation of volcano flank instability triggered by dyke intrusion. In: McGuire, W.J., Jones, A.P. and Neuberg, J. (Editors), Conference on Volcano Instability on the Earth and Other Planets. Geological Soc Publishing House, London, England, pp. 45-53.

Fisher, R.V., 1966. Mechanism of deposition from pyroclastic flows. Am J Sci, 264(5): 350-363.

Fisher, R.V., 1990. Transport and deposition of a pyroclastic surge across an area of high relief: the 18 May 1980 eruption of Mt. St. Helens, Washington. Geological Society of America Bulletin, 102: 1038-1054.

Fisher, R.V., 1995. Decoupling of pyroclastic currents: hazards assessments. Journal of Volcanology and Geothermal Research, 66: 257-263.

Fisher, R.V., Orsi, G., Ort, M. and Heiken, G., 1993. Mobility of a large-volume pyroclastic flow -- emplacement of the Campanian ignimbrite, Italy. Journal of Volcanology and Geothermal Research, 56(3): 205-220.

Fisher, R.V. and Schmincke, H.U., 1984. Pyroclastic Rocks. Springer, Berlin.

Fisher, R.V. and Waters, A.C., 1970. Base surge bed forms in maar volcanoes. Am J Sci, 268(2): 157-180.

Fouque, F., 1879. Santorin et ses Éruptions. Masson, Paris, 440 pp.

Fuster, J.M., Arana, V., Brandle, J.L., Navarro, M., Alonso, U. and Aparicio, A., 1968. Geología y volcanología de las islas Canarias: Tenerife. CSIC, Madrid: Instituto "Lucas Malladas".

Gardner, J.E., Burgisser, A. and Selling, P., 2007. Eruption and Deposition of the Fisher Tuff (Alaska): Evidence for the Evolution of Pyroclastic Flows. The Journal of Geology, 115: 417-435.

Gilbert, J.S. and Lane, S.J., 1994. The origin of accretionary lapilli. Bulletin of Volcanology, 56(5): 398-411.

Gill, R., 1997. Electron beam methods. In: Gill, R. (Editor), Modern analytical geochemistry. Longman, pp. 215-234.

Girolami, L., Roche, O., Druitt, T. and Corpetti, T., 2010. Particle velocity fields and depositional processes in laboratory ash flows, with implications for the sedimentation of dense pyroclastic flows. Bulletin of Volcanology, 72(6): 747-759.

Glicken, H., 1996. Rockslide-Debris Avalanche of May 18, 1980, Mount St. Helens Volcano, Washington. Open File Report 96-677, US Department of the Interior / USGS.

Global Volcanism Program, 2008. Tenerife: Recent Eruptions Webpage. Smithsonian National Museum of Natural History.

Goff, F., Gardner, J.N., Reneau, S.L., Kelley, S.A., Kempter, K.A. and Lawrence, J.R., 2011. Geologic map of the Valles caldera, Jemez Mountains, New Mexico. New Mexico Bureau of Geology and Mineral Resources.

Gottsmann, J., Camacho, A.G., Marti, J., Wooller, L., Fernandez, J., Garcia, A. and Rymer, H., 2008. Shallow structure beneath the Central Volcanic Complex of Tenerife from new gravity data: Implications for its evolution and recent reactivation. Physics of the Earth and Planetary Interiors, 168(3-4): 212-230.

Govindaraju, K., 1994. Geostandards Newsletter, 18 (Special Issue)(1).

Graup, G., 1981. Terrestrial chondrules, glass spherules and accretionary lapilli from the suevite, Ries Crater, Germany. Earth and Planetary Science Letters, 55(3): 407-418.

Hausen, H., 1956. Contributions to the geology of Tenerife (Canary Islands). Soc. Sci. Fennicae, Comm.Phys.-Mat., 18: 254 pp.

Heiken, G. and Wohletz, K.H., 1985. Volcanic ash University of California Press.

Heiken, G.H., 1971. Tuff Rings: Examples from the Fort Rock-Christmas Lake Valley Basin, South-Central Oregon. J. Geophys. Res., 76(23): 5615-5626.

Heinrichs, T., 1984. The Umsoli chert, turbidite testament for a major phreatoplinian event at the onverwacht/fig tree transition (Swaziland supergroup, Archaean, South Africa). Precambrian Research, 24(3-4): 237-283.

Hobbs, P.V., Lyons, J.H., Locatelli, J.D., Biswas, K.R., Radke, L.F., Weiss, R.R. and Rangno, A.L., 1981. Radar Detection of Cloud-Seeding Effects. Science, 213(4513): 1250-1252.

Hoernle, K. and Schmincke, H.U., 1993. The role of partial melting in the 15-Ma geochemical evolution of Gran-Canaria - A blob model for the Canary hotspot:. Journal of Petrology, 34(3): 599-626.

Holcomb, R.T. and Searle, R.C., 1991. Large landslides from oceanic volcanoes. Marine Geotechnology, 10: 19-32.

Holohan, E.P., Troll, V.R., Walter, T.R., Münn, S., McDonnell, S. and Shipton, Z.K., 2005. Elliptical calderas in active tectonic settings: an experimental approach. Journal of Volcanology and Geothermal Research, 144(1-4): 119-136.

Horwell, C. and Baxter, P., 2006. The respiratory health hazards of volcanic ash: a review for volcanic risk mitigation. Bulletin of Volcanology, 69(1): 1-24.

Houghton, B.F., Wilson, C.J.N., Fierstein, J. and Hildreth, W., 2004. Complex proximal deposition during the Plinian eruptions of 1912 at Novarupta, Alaska. Bulletin of Volcanology, 66(2): 95-133.

Hovey, E.O., 1902. Oberservations on the eruptions of 1902 of La Soufrière, St. Vincent and Mt. Pelée, Martinique. American Journal of Science, 164: 319-350.

Howells, M.F., Leveridge, R., Addison, R., Evans, C.D.R. and Nutt, M.J.C., 1979. The Capel Curig Volcanic Formation, Snowdonia, North Wales; variations in ash-flow tuffs related to emplacement environment. Geological Society, London, Special Publications, 8: 611-618.

Hughes, S.R. and Druitt, T.H., 1998. Particle fabric in a small, type-2 ignimbrite flow unit (Laacher See, Germany) and implications for emplacement dynamics. Bulletin of Volcanology, 60(2): 125-136.

Hürlimann, M., Martí, J. and Ledesma, A., 2004. Morphological and geological aspects related to large slope failures on oceanic islands: The huge La Orotava landslides on Tenerife, Canary Islands. Geomorphology, 62(3-4): 143-158.

James, M.R., Gilbert, J.S. and Lane, S.J., 2002. Experimental investigation of volcanic particle aggregation in the absence of a liquid phase. Journal of Geophysical Research, 107: 2191.

Kennedy, B., Stix, J., Vallance, J.W., Lavallée, Y. and Longpré, M.-A., 2004. Controls on caldera structure: Results from analogue sandbox modeling. Geological Society of America Bulletin, 116(5-6): 515-524.

Kokelaar, B.P. and Moore, I.D., 2006. Classical areas of British geology: Glencoe caldera volcano, Scotland. Keyworth, Nottingham: British Geological Survey.

Kokelaar, P., 2007. Friction melting, catastrophic dilation and breccia formation along caldera superfaults. Journal of the Geological Society, 164: 751-754.

Kokelaar, P. and Romagnoli, C., 1995. Sector collapse, sedimentation and clast population evolution at an active island-arc volcano: Stromboli, Italy. Bulletin of Volcanology, 57(4): 240-262.

Kouli, M. and St. Seymour, K., 2006. Plagioclase microtextures and their importance for magma chamber dynamics - examples from Lesvos, Hellas and Teide, Canary Islands. Neues Jahrbuch für Mineralogie - Abhandlungen, 182(3): 323-336.

Koyaguchi, T. and Woods, A.W., 1996. On the formation of eruption colums following explosive mixing of magma and surface-water. Journal of Geophysical Research, 101(b3): 5561-5574.

Labazuy, P., 1996. Recurrent landslides events on the submarine flank of Piton de la Fournaise volcano (Reunion Island). Geological Society , London, Special Publications, 110: 295-306.

Lacroix, A., 1904. La Montagne Pelée et ses éruptions, Paris, 662 pp.

Lane, S.J., Gilbert, J.S. and Hilton, M., 1993. The aerodynamic behaviour of volcanic aggregates. Bulletin of Volcanology, 55(7): 481-488.

Lane, S.J., James, M.R. and Gilbert, J.S., 2011. Electrostatic phenomena in volcanic eruptions. Journal of Physics: Conference Series, 301(1): 012004.

Le Friant, A., Harford, C.L., Deplus, C., Boudon, G., Sparks, R.S.J., Herd, R.A. and Komorowski, J.C., 2004. Geomorphological evolution of Montserrat (West Indies): importance of flank collapse and erosional processes. Journal of the Geological Society, 161(1): 147-160.

Lessing, P. and Grout, C.M., 1971. Haüynite from Edwards, New York. American Mineralogist, 56(1096-1100).

Lipman, P.W., 1984. The roots of ash flow calderas in western North America- windows into the tops of granitic batholths Journal of Geophysical Research, 89(NB10): 8801-8841.

Lipman, P.W., 1997. Subsidence of ash-flow calderas:relation to cladera size and mangma-chamber geometry. Bulletin of Volcanology, 59(3): 198-218.

Lipman, P.W., 2000a. Calderas. Academic Press.

Lipman, P.W., 2000b. The central San Juan caldera cluster: regional tectonics framework. Special Paper - Geological Society of America, 346: 9-71.

Lipman, P.W., 2000c. The central San Juan caldera cluster: regional volcanic framework. Special Paper- Geological Society of America, 346: 9-71.

Lipman, P.W., Self, S. and Heiken, G., 1984. Caldera and associated igneous rocks-Introduction. Journal of Geophysical Research, 89(NB10): 8219-8221.

Lorenz, V., 1974. Vesiculated tuffs and associated features. Sedimentology, 21(273-291).

Maeno, F. and Taniguchi, H., 2009. Sedimentation and welding processes of dilute pyroclastic density currents and fallout during a large-scale silicic eruption, Kikai caldera, Japan. Sedimentary Geology, 220(3-4): 227-242.

Martí , J., 1998. Comment on "A giant landslide on the north flank of Tenerife, Canary Islands" by A.B. Watts and D.G. Masson. Journal of Geophysical Research, 103(B5): 9945-9947.

Martí, J., Ablay, G., Redshaw, L.T. and Sparks, R.S.J., 1994a. Experimental studies of collapse calderas. Journal of the Geological Society, London, 151: 919-929.

Martí, J., Ablay, G.J. and Bryan, S., 1996. Comment on "the Canary Islands: an example of structural control on the growth of large oceanic-island volcanoes" by J.C. Carracedo. Journal of Volcanology and Geothermal Research, 72(1-2): 143-149.

Marti, J. and Gudmundsson, A., 2000. The Las Cañadas caldera (Tenerife, Canary Islands): an overlapping collapse caldera generated by magma-chamber migration. Journal of Volcanology and Geothermal Research, 103(1-4): 161-173.

Martí, J., Hürlimann, M., Ablay, G. and Gudmundsson, A., 1997. Vertical and lateral collapses on Tenerife (Canary Islands) and other volcanic ocean islands. Geology, 25(879-882).

Martí, J., Mitjavila, J. and Arana, V., 1994b. Stratigraphy, structure and geochronology of the Las Cañadas Caldera (Tenerife, Canary Islands). Geological Magazine, 131(6): 715-727.

Martí, J., Mitjavila, J. and Villa, J., 1990. Stratigraphy and K-Ar ages of the Diego Hernández wall and their significance on the Las Cañadas Caldera formation (Tenerife, Canary Islands. Terra Nova, 2(2): 148-153.

Martí, J., Soriano, C., Galindo, I. and Cas, R., 2010. Resolving problems with the origin of Las Canadas caldera (Tenerife, Canary Island): Los Roques de Garcia Formation-Part of a major debris avalanche or an in situ, stratified, edifice-building succession? In: Groppelli, G. and Viereck-Goette, L. (Editors), Stratigraphy and Geology of Volcanic Areas: Geological Society of America Special Paper 464, pp. 1-20.

Marti, J. and Wolff, J.A., 2000. Introduction: the geology and geophysics of Tenerife. Journal of Volcanology and Geothermal Research, 103(1-4): VII-X.

Masson, D., Watts, A., Gee, M.J.R., Urgeles, R., Mitchell, N.C., Le Bas, T.P. and Canals, M., 2002. Slope failures on the flanks of the western Canary Islands. Earth Science Reviews, 57: 1-35.

Masson, D.G., 1996. Catastrophic collapse of the volcanic island of Hierro 15 ka ago and the history of landslides in the Canary Islands. Geology, 24(3): 231-234.

McGuire, W.J., 1996. Volcano Instability: a review of contemporary themes. In: McGuire, W.J., Jones, A.P. and Neuberg, J. (Editors), Volcano Instability on the Earth and Other Planets: Geological Society Special Publication No. 110, pp. 1-24.

Mellors, R.A. and Sparks, R.S.J., 1991. Spatter-rich pyroclastic flow deposits on Santorini, Greece. Bulletin of Volcanology, 53(5): 327-342.

Milner, D.M., Cole, J.C. and Wood, C.W., 2002a. Asymmetric, multiple-block collapse at Rotorua Caldera, Taupo Volcanic Zone, New Zealand. Bulletin of Volcanology, 64(2): 134-149.

Milner, D.M., Cole, J.W. and Wood, C.P., 2002b. Asymmetric, multiple-block collapse at Rotorua Caldera, Taupo Volcanic Zone, New Zealand. Bulletin of Volcanology, 64(2): 134-149.

Moore, I. and Kokelaar, P., 1997. Tectonic influences in piecemeal caldera collapse at Glencoe Volcano, Scotland. Journal of the Geological Society, 154: 765-768.

Moore, I. and Kokelaar, P., 1998. Tectonically controlled piecemeal caldera collapse: A case study of Glencoe volcano, Scotland. Geological Society of America Bulletin, 110(11): 1448-1466.

Moore, J.G., Clague, D.A., Holcomb, R.T., Lipman, P.W., Normark, W.R. and Torresan, M.E., 1989. Prodigious submarine landslides of the Hawaiian ridge. Journal of Geophysical Research, 94: 17465-17484.

Moore, J.G., Normark, W.R. and Holcomb, R.T., 1994. Giant Hawaiian Landslides. Annual Reviews of Earth and Planetary Sciences, 22(119-144).

Moore, J.G. and Peck, D.L., 1962. Accretionary lapilli in volcanic rocks of the western continental Unites States. Journal of Geology, 70(2): 182-192.

Morgan, J.K., Moore, G.F. and Clague, D.A., 2003. Slope failure and volcanic spreading along the submarine south flank of Kilauea volcano, Hawaii. Journal of Geophysical Research, 108(B9): 2415-2439.

Morimoto, N., 1988. Nomenclature of Pyroxenes. Mineralogy and Petrology, 39(1): 55-76.

Moriya, I., 1980. "Bandaian eruption" and hazards associated with it. Collection of articles in memory of retirement of Prof K Nishimura from Tohoku University: 214-219.

Navarro, M. and Coello, J., 1989. Depressions originated by landslide processes in Tenerife. ESF Meetings on Canarian Volcanism: 150-152.

Neal, V., 1979. New Plymouth, Egmont and Manaia (1st. Ed) [sheets P19, P20, P21], Geological Map of New Zealand. NZ Department of Scientific and Industrial Resources, Wellington.

Oehler, J.-F., Labazuy, P. and Lénat, J.-F., 2004. Recurrence of major flank landslides during the last 2-Ma-history of Reunion Island. Bulletin of Volcanology, 66(7): 585-598.

Oertel, G., 1970. Deformation of a Slaty, Lapillar Tuff in the Lake District, England. Geological Society of America Bulletin, 81(4): 1173-1188.
Ort, M.H., Rosi, M. and Anderson, C.D., 1999. Correlation of deposits and vent locations of the proximal Campanian Ignimbrite deposits, Campi Flegrei, Italy, based on natural remanent magnetization and anisotropy of magnetic susceptibility characteristics. Journal of Volcanology and Geothermal Research, 91(2–4): 167-178.
Ortiz, R., Araña, V., Astiz, M. and Garcia, A., 1986. Magnetotelluric study of the Teide (Tenerife) and Timanfaya (Tanzarote) volcanic areas. Journal of Volcanology and Geothermal Research, 30(3-4): 357-377.
Palacios, D., 1994. The origin of certain wide valleys in the Canary Islands. Geomorphology, 9(1): 1-18.
Perret, F.A., 1924. The Vesuvius eruption of 1906, 151 pp.
Piper, D.J.W. and Normark, W.R., 1983. Turbidite depositional patterns and flow characteristics, Navy Submarine Fan, California Borderland. Sedimentology, 30(5): 681-694.
Pittari, A., Cas, R.A.F., Edgar, C.J., Nichols, H.J., Wolff, J.A. and Marti, J., 2006. The influence of palaeotopography on facies architecture and pyroclastic flow processes of a lithic-rich ignimbrite in a high gradient setting: The Abrigo Ignimbrite, Tenerife, Canary Islands. Journal of Volcanology and Geothermal Research, 152(3-4): 273-315.
Prata, A. and Tupper, A., 2009. Aviation hazards from volcanoes: the state of the science. Natural Hazards, 51(2): 239-244.
Pratt, W.E., 1911. The eruption of Taal volcano, January 30 1911. Phillipines Journal of Science, 6: 63-86.
Reimer, T.O., 1983. Accretionary lapilli in volcanic ash falls: physical factors governing their formation, Coated Grains. Springer-Verlag, Berlin.
Ridley, W.I., 1971. The origin of some collapse structures in the Canary Islands. Geological Magazine, 108: 477-484.
Roche, O., Druitt, T.H. and Merle, O., 2000. Experimental study of caldera formation. J. Geophys. Res., 105(B1): 395-416.
Rodehorst, U., Schmincke, H.U. and Sumita, M., 1998. Geochemistry and Petrology of Pleistocene Ash layers Erupted at Las Canadas Edifice (Tenerife). Proceedings of the Ocean Drilling Program, 157: 315-328.
Romagnoli, C., Kokelaar, P., Casalbore, D. and Chiocci, F.L., 2009. Lateral collapses and active sedimentary processes on the northwestern flank of Stromboli volcano, Italy. Marine Geology, 265(3-4): 101-119.
Rose, W.I. and Durant, A.J., 2011. Fate of volcanic ash: Aggregation and fallout. Geology, 39(9): 895-896.
Rosi, M., 1992. A model for the formation of vesiculated tuff by the coalescence of accretionary lapilli. Bulletin of Volcanology, 59: 429-434.
Rosi, M., Vezzoli, L., Aleotti, P. and De Censi, M., 1996. Interaction between caldera collapse and eruptive dynamics during the Campanian Ignimbrite eruption, Phlegraean Fields, Italy. Bulletin of Volcanology, 57(7): 541-554.
Rowley, P.J., Kokelaar, P., Menzies, M. and Waltham, D., 2011. Shear-Derived Mixing In Dense Granular Flows. Journal of Sedimentary Research, 81(12): 874-884.
Sable, J.E., Houghton, B.F., Wilson, C.J.N. and Carey, R.J., 2006. Complex proximal sedimentation from Plinian plumes: the example of Tarawera 1886. Bulletin of Volcanology, 69: 89-103.
Schmincke, H.U. and Sumita, M., 1998. Volcanic evolution of Gran Canaria reconstructed from apron sediments: synthesis of VICAP project drilling.
Schumacher, R., 1994. A reappraisal of Mount St. Helens' ash clusters- depositional model from experimental observation. Journal of Volcanology and Geothermal Research, 59: 253-260.

Schumacher, R. and Schmincke, H.-U., 1991. Internal structure and occurrence of accretionary lapilli — a case study at Laacher See Volcano. Bulletin of Volcanology, 53(8): 612-634.
Schumacher, R. and Schmincke, H.-U., 1995. Models for the origin of accretionary lapilli. Bulletin of Volcanology, 56(8): 626-639.
Scolamacchia, T., Macias, J.L., Sheridan, M.F. and Hughes, S.R., 2005. Morphology of ash aggregates from wet pyroclastic surges of the 1982 eruption of El Chichón volcano, Mexico. Bulletin of Volcanology, 68: 171-200.
Scott, R.B., 1971. Alkali exchange during devitrification and hydration of glasses in ignimbrite cooling units. Journal of Geology, 79: 100-110.
Scrope, P., 1829. On the volcanic district of Naples. Geological Society of London Transactions, 2: 337-352.
Self, S., 1983. Large-scale phreatomagmatic silicic volcanism: A case study from New Zealand. Journal of Volcanology and Geothermal Research, 17(1-4): 433-469.
Self, S. and Sparks, R., 1978. Characteristics of widespread pyroclastic deposits formed by the interaction of silicic magma and water. Bulletin of Volcanology, 41(3): 196-212.
Sheridan, M.F. and Wohletz, K.H., 1983. Origin of accretionary lapilli from the Pompeii and Avellino deposits of Vesuvius. In: Gooley, R. (Editor), Microbeam Analysis. San Francisco Press, pp. 35-38.
Siebert, L., 1984. Large volcanic debris avalanches: Characteristics of source areas, deposits, and associated eruptions. Journal of Volcanology and Geothermal Research, 22(3-4): 163-197.
Sigurdsson, H. and Carey, S., 1989. Plinian and co-ignimbrite tephra fall from the. Bulletin of Volcanology, 51(4): 243-270.
Sisson, T.W., 1995. Blast ashfall deposit of May 18, 1980 at Mount St. Helens, Washington. Journal of Volcanology and Geothermal Research, 66: 203-216.
Smith, N., Cassidy, J., Locke, C.A., Mauk, J.L. and Christie, A.B., 2006. The role of regional-scale faults in controlling a trapdoor caldera, Coromandel Peninsula, New Zealand. Journal of Volcanology and Geothermal Research, 149(3–4): 312-328.
Smith, R.J. and Bailey, R.A., 1968. Resurgent Calderas.
Smith, R.L., 1960. Ash Flows. Bulletin of the Geological Society of America, 71: 796-842.
Sorem, R.K., 1982. Volcanic ash clusters: Tephra rafts and scavengers. Journal of Volcanology and Geothermal Research, 13(1-2): 63-71.
Soriano, C., Galindo, I., Marti, J. and Wolff, J., 2006. Conduit-vent structures and related proximal deposits in the Las Canadas caldera, Tenerife, Canary Islands. Bulletin of Volcanology, 69(2): 217-231.
Sparks, R.S.J., 1976. Grain size variations in ignimbrites and implications for the transport of pyroclastic flows. Sedimentology, 23(2): 147-188.
Sparks, R.S.J., Bursik, M.I., Carey, S.N., Gilbert, J.S., Glaze, L.S., Sigurdsson, H. and Woods, A.W. (Editors), 1997. Volcanic Plumes. John Wiley & Sons, Chichester, 574 pp.
Sparks, R.S.J., Self, S. and Walker, G.P.L., 1973. Products of Ignimbrite Eruptions. Geology, 1(3): 115-118.
Sparks, R.S.J. and Walker, G.P.L., 1977. The significance of vitric-enriched air-fall ashes associated with crystal-enriched ignimbrites. Journal of Volcanology and Geothermal Research, 2(4): 329-341.
Sperling, F.N., Washington, R. and Whittaker, R.J., 2004. Future climate change of the subtropical North Atlantic: implications for the cloud forests of tenerife. Climate Change, 65(1/2): 103.
Spray, J.G., 1997. Superfaults. Geology, 25(7): 579-582.
Stearns, H., 1925. The explosive phase of Kilauea Volcano, Hawaii, in 1924. Bulletin Volcanologique, 2(2): 193-208.
Sulpizio, R., Bonasia, R., Dellino, P., Mele, D., Di Vito, M. and La Volpe, L., 2010. The Pomici di Avellino eruption of Somma–Vesuvius (3.9 ka <small>BP</small>). Part II:

sedimentology and physical volcanology of pyroclastic density current deposits. Bulletin of Volcanology, 72(5): 559-577.
Taddeucci, J., Scarlato, P., Montanaro, C., Cimarelli, C., Del Bello, E., Freda, C., Andronico, D., Gudmundsson, M.T. and Dingwell, D.B., 2011. Aggregation-dominated ash settling from the Eyjafjallajökull volcanic cloud illuminated by field and laboratory high-speed imaging. Geology, 39(9): 891-894.
Teide Group, 1997. Morphometric study of the northeast and southeast slopes of Tenerife, Canary Islands. Journal of Geophysical Research, 102: 20325-20342.
Textor, C., Graf, H.F., Herzog, M., Oberhuber, J.M., Rose, W.I. and Ernst, G.G.J., 2006. Volcanic particle aggregation in explosive eruption columns. Part I: Parameterization of the microphysics of hydrometeors and ash. Journal of Volcanology and Geothermal Research, 150(4): 359-377.
Thordarson, T., 2004. Accretionary-lapilli-bearing pyroclastic rocks at ODP Leg 192 Site 1184: a record of subaerial phreatomagmatic eruptions on the Ontong Java Plateau. In: Fitton, J.G., Mahoney, J.J., Wallace, P.J. and Saunders, A.D. (Editors), Origin and evolution of the Otong Java Plateau. Geological Society of London, Special Publications, pp. 275-306.
Tibaldi, A., 2001. Multiple sector collapses at Stromboli volcano, Italy: how they work. Bulletin of Volcanology, 63: 112-125.
Tomita, K., Kanai, T., Kobayashi, T. and Oba, N., 1985. Accretionary lapilli formed by the eruption of Sakurajima volcano. Journal of Japanese Association of Mineralogists, Petrologists and Economic Geologists, 80: 49-54.
USGS, 2010. Volcano Hazards Program.
Valentine, G.A., 1987. Stratified flows in pyroclastic surges. Bulletin of Volcanology, 49: 616-630.
Valentine, G.A. and Giannetti, B., 1995. Single pyroclastic beds deposited by simultaneous fallout and surge processes: Roccamonfina volcano, Italy. Journal of Volcanology and Geothermal Research, 64: 129-137.
Verbeek, R.D.M., 1886. Krakatau. Imprimerie de L'Etat, Batavia, Java.
Vieira, R., Toro, C. and Araña, V., 1986. Microgravimetric survey in the Caldera of Teide, Tenerife, Canary Islands. Tectonophysics, 130(1-4): 249-257.
Voight, B., Janda, R.J., Glicken, H. and Douglass, P.M., 1983. Nature and mechanics of the Mount St-Helens rockslide-avalanche of 18 May 1980. Geotechnique, 33(3): 243-273.
von Suchodoletz, H., Faust, D. and Zöller, L., 2009. Geomorphological investigations of sediment traps on Lanzarote (Canary Islands) as a key for the interpretation of a palaeoclimate archive off NW Africa. Quaternary International, 196(1-2): 44-56.
Walker, G.P.L., 1971. Grain-size Characteristics of Pyroclastic Deposits. Journal of Geology, 79(6): 696-714.
Walker, G.P.L., 1983. Ignimbrite types and ignimbrite problems. Journal of Volcanology and Geothermal Research, 17: 65-88.
Walker, G.P.L., 1984. Downsag calderas, ring faults and caldera sizes. Journal of Geophysical Research-Solid Earth, 89(B10): 8407-8416.
Walker, G.P.L., 1985. Origin of coarse lithic breccias near ignimbrite source vents. Journal of Volcanology and Geothermal Research, 25: 157-172.
Walter, T.R. and Troll, V.R., 2003. Experiments on rift zone evolution in unstable volcanic edifices. Journal of Volcanology and Geothermal Research, 127(1-2): 107-120.
Walter, T.R., Troll, V.R., Cailleau, B., Belousov, A., Schmincke, H.U., Amelung, F. and Von der Bogaard, P., 2005. Rift zone reorganization through flank instability in ocean island volcanoes: an example from Tenerife, Canary Islands. Bulletin of Volcanology, 67(4): 281-291.
Warme, J.E., Morgan, M. and Kuehner, H.-C., 2002. Impact-generated carbonate accretionary lapilli in the Late Devonian Alamo Breccia. Special Paper - Geological Society of America, 356: 489-504.

Watanabe, K., Ono, K., Sakaguchi, K., Takada, A. and Hoshizumi, H., 1999. Co-pyroclastic density current ash-fall deposits of the 1991 eruptions of Fugen-dake, Unzen Volcano, Japan. Journal of Volcanology and Geothermal Research, 89: 95-112.

Watts, A. and Masson, D., 1995. A giant landslide of the north flank of Tenerife, Canary Islands. Journal of Geophysical Research, 100(B12): 24487-24498.

Watts, A. and Masson, D., 2001. New sonar evidence for recent catastrophic collapses of the north flank of Tenerife, Canary Islands. Bulletin of Volcanology, 63(1): 8-19.

Watts, A.B. and Masson, D.G., 1998. Reply to comment on "A giant landslide on the north flank of Tenerife, Canary Islands", by J. Marti. Journal of Geophysical Research, 103(B5): 9949-9952.

Wentworth, C.K., 1937. The Diamond Head black ash. Journal of Sedimentary Research, 7(3): 91-103.

Wentworth, C.K. and Williams, H., 1932. The classification and terminology of the pyroclastic rocks. National Research Council Bulletin, 89: 35, 37, 45.

Williams, H., 1942. The geology of Crater Lake National Park, Oregon, with a reconnaisance of the Cascade Range southward to Mount Shasta, 162 pp.

Williams, H., McBirney, A.R. and Lorenz, V., 1970. An Investigation of Volcanic Depressions, Part I: Geologic and Geophysical Features of Calderas, Houston, Texas.

Williams, R., 2010. Unpublished PhD thesis: Emplacement of radial pyroclastic density currents over irregular topography: the chemically-zoned, low aspect-ratio Green Tuff ignimbrite, Pantelleria, Italy. University of Leicester.

Wilson, C.J.N. and Hildreth, W., 1998. Hybrid fall deposits in the Bishop Tuff, California: a novel pyroclastic depositional mechanism. Geology, 26(1): 7-10.

Wilson, J.T., 1963. A possible origin of the Hawaiian Islands. Canadian Journal of Physics, 41: 863-870.

Wilson, L. and Head, J.W., 2007. Explosive volcanic eruptions on Mars: Tephra and accretionary lapilli formation, dispersal and recognition in the geologic record. Journal of Volcanology and Geothermal Research, 163(1-4): 83-97.

Wolff, J., 1985. Zonation, mixing and eruption of silica-undersaturated alkaline magma-a case study from Tenerife, Canary Islands. Geological Magazine, 122: 633-640.

Wolff, J.A., Grandy, J.S. and Larson, P.B., 2000. Interaction of mantle-derived magma with island crust? Trace element and oxygen isotope data from the Diego Hernandez Formation, Las Cañadas, Tenerife. Journal of Volcanology and Geothermal Research, 103(1-4): 343-366.

Woods, A.W., 1993. Moist Convection and the Injection of Volcanic Ash Into the Atmosphere. J. Geophys. Res., 98(B10): 17627-17636.

Woods, A.W., Sparks, R.S.J., Ritchie, L.J., Batey, J., Gladstone, C. and Bursik, M.I., 2002. The explosive decompression of a pressurized volcanic dome: the 26 December 1997 collapse and explosion of Soufrière Hills Volcano, Montserrat. In: Druit, T.H. and Kokelaar, B.P. (Editors), The eruption of Soufrière Hills volcano, Montserrat, from 1995 to 1999. . Geological Society of London Memoirs, pp. 457-465.

Wright, J.V. and Walker, G.P.L., 1977. The ignimbrite source problem: Significance of a co-ignimbrite lag-fall deposit. Geology, 5(12): 729-732.

Wright, J.V. and Walker, G.P.L., 1981. Eruption, transport and deposition of ignimbrite- a case-study from Mexico. Journal of Volcanology and Geothermal Research, 9: 111-131.

Yamamoto, T., Takarada, S. and Suto, S., 1993. Pyroclastic flows from the 1991 eruption of Unzen volcano, Japan. Bulletin of Volcanology, 55: 166-175.

Yancey, T.E. and Guillemette, R.N., 2008. Carbonate accretionary lapilli in distal deposits of the Chicxulub impact event. Geological Society of America Bulletin, 120(9-10): 1105-1118.

Appendix

A1. Study of the lower Diego Hernandez wall

In the lower Diego Hernandez wall, there is evidence of hybrid processes, scour and phreatomagmatism in pre-Poris deposits. Future study of this part of the wall could improve understanding of these processes in the proximal zone; furthermore, comparison with the depositional mechanisms recorded in the Poris deposits may give an indication of how proximal processes changed in the Diego Hernandez zone though time, possibly providing information about structural changes in the area. A reconnaissance of three key deposits was undertaken during this study; their characteristics and potential significance are briefly described here.

A1.1 Introduction to the lower Diego Hernandez wall

Beneath the Poris Formation, two thick pyroclastic successions record the Fasnia (289 ka, $^{40}Ar/^{39}Ar$ dating, Brown *et al.*, 2003) and Aldea (319 ka, $^{40}Ar/^{39}Ar$ dating, Edgar *et al.*, 2007) ignimbrite-forming eruptions. The Fasnia succession occurs beneath the thick lavas at the base of the Poris, and is separated from the Aldea by a distinctive scoria fall unit that can be traced across the DH wall to the prominent red scoria cone halfway up the northern face. The scoria fall unit is primarily black but it has weathered to brown/beige across much of the wall, and has been displaced by more than 30 m at the northern fault that affects all the Diego Hernandez units (Fig A1).

Below the Aldea succession, the DH units are relatively poorly exposed due to vegetation and scree cover. Several alluvial sedimentary deposits occur and are intercalated with lavas and minor Plinian/subplinian pyroclastics. In the centre of the wall a distinctive grey pyroclastic deposit is exposed, above a second buried red scoria cone. Beneath this scoria cone is a well exposed subplinian/sedimentary succession.

A1.2 Subplinian record at the base of the DH wall

The subplinian and sedimentary sequence exposed below the buried scoria cone (box 1 on Fig A1) contains 6 pyroclastic units, each with reworking at the top and evidence of soil formation, two scoria fallout units, one with prominent spatter rags, and the deposits of at least four prolonged periods of sedimentation (Fig. A2).

Pyroclastic units 1-5 are massive, clast-supported, pumice lapillistone facies. They record periods of pumice fallout, possibly from short-lived subplinian eruptions. Each pyroclastic unit grades up into a palaeosol, one of which contains diagenetically compacted pumice clasts. Pyroclastic unit 6 is different to the others: thicker, and intensely stratified. This deposit is interpreted to be a hybrid, reflecting a larger-scale subplinian or small Plinian eruption, where dilute ash-clouds reworked, sorted and stratified Plinian fallout. No ignimbrite lithofacies are recorded in the sequence. The dip of the sequence lessens between Scoria 1 (15º/140 SE) and Pyroclastic unit 6 (8º/156 SE); deposition at this stage occurred on a slope that gradually became shallower as burial continued. Above Pyroclastic unit 6, sedimentary units 3 and 4 have a more subtle dip (4º/130 SE). These units have load structures at their bases, indicating that sedimentation at this stage involved water, possibly in ephemeral channels and ponds. It is conceivable that water reworked the underlying pumice-rich substrate of Pyroclastic unit 6. Sedimentary units 1 and 2, which are clast-rich and poorer in fines than sedimentary units 3 and 4, record dry reworking of pumice-rich material, possibly similar to the mass wasting processes ongoing in Las Cañadas at present.

Figure A1 (overleaf) Features of the lower Diego Hernandez wall. Buried scoria cones and associated scoria fall are shown in orange and red. 1 is a sequence of subplinian, hybrid and sedimentary units, 2 is a tuff ring, and 3 is a scour feature in the Aldea pyroclastic succession. White circles denote further exposures of the tuff ring, traceable below a lava flow. Note the displacement along the normal fault in the north of the wall.

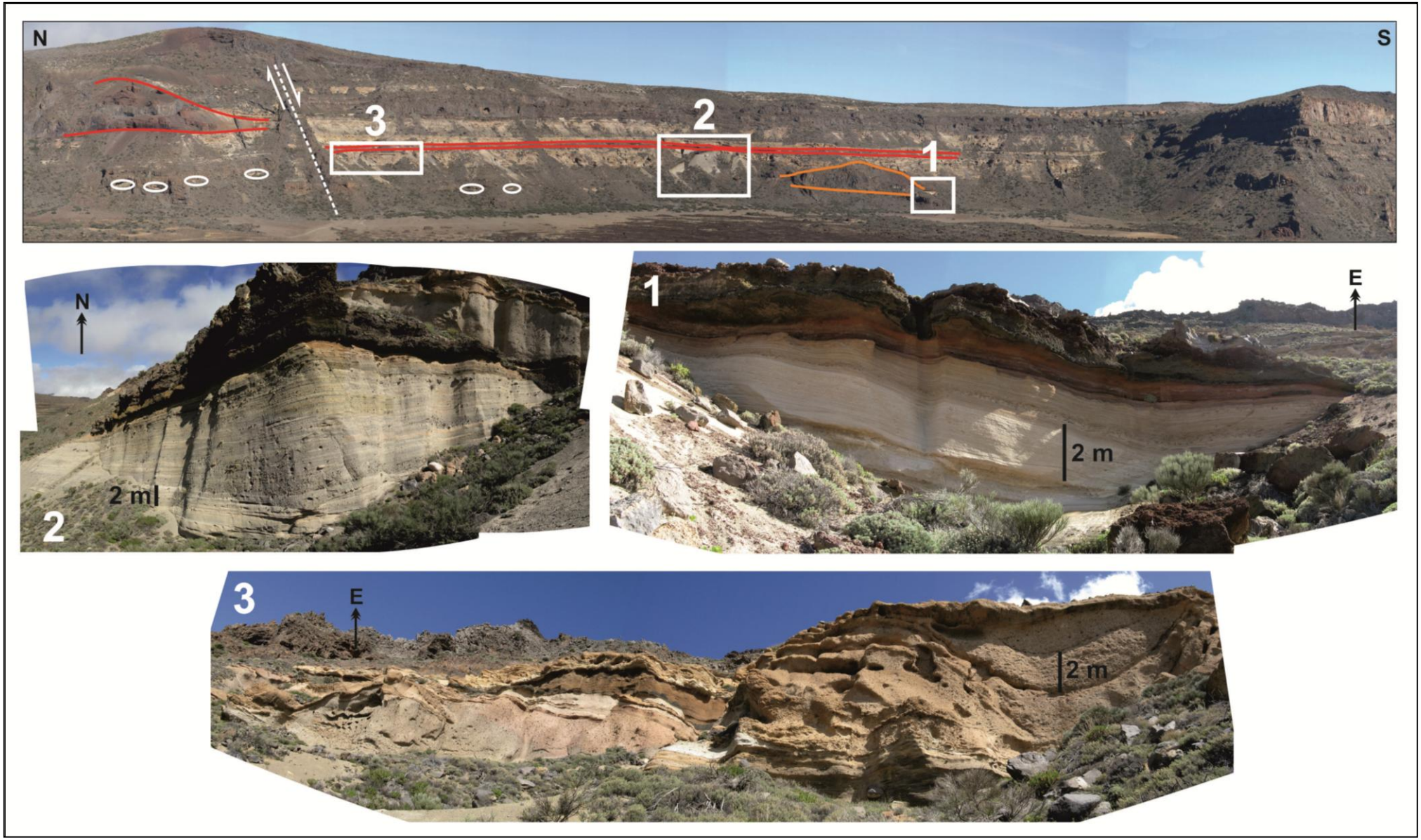
N
S
3
2
1
N
2 m
2
1
E
2 m
3
E
2 m

Significance

This sequence documents changing conditions in Las Cañadas, both in terms of eruption style and sedimentary processes. The latter has implications for the changing structure of the caldera zone and, in the light of the controversial origin of Las Cañadas (see Chapter 2), would be an interesting candidate for further investigation. If the change to water-related reworking is recorded elsewhere in the lower wall, it may be an indication of the presence of water on a large scale. This would suggest a closed depression existed at this time, implying that lateral collapse features were not present in the vicinity.

A1.3 Obsidian-rich tuff ring

In the central part of the lower Diego Hernandez wall a prominent grey unit with a dipping upper surface is exposed. This has been variously described as a pyroclastic surge deposit (Martí *et al.*, 1990) and as pumice-rich gravels (Edgar *et al.*, 2007). Here it is interpreted as a record of tuff ring volcanism.

The unit is exposed between the centre and north of the wall, outcropping beneath a distinctive lava. It is thickest (~10 m) at the main central exposure (Box 2, Fig A1); at other locations, shown in semi-circles in Fig. A1, it is ≤5 m thick. A thin pumice-rich layer at the base of the unit (top of Box 2 in Fig A3), recording an initial fallout stage, and a white ash matrix throughout the unit, very different in nature to the brown soil matrix present in sedimentary units in the lower DH wall, indicates that the material is of volcanic origin.

The unit consists of graded beds, generally with erosive, lithic-rich bases and more pumice rich tops, although grading is often irregular and interrupted. In some areas, bedding is relatively planar, but low-angle cross bedding is common. The lithic population ranges from millimetre-scale fragments to decimetre-scale blocks and includes scoria clasts, fine-grained hypabyssal/lava rocks, and ignimbrite fragments. The predominant lithology is black obsidian, clasts of which are typically ≤7 cm in diameter.

The scour and irregular nature of the cross-bedding in this unit renders determination of original slope direction difficult. Beds dip most steeply at the thickest central outcrop (~18º/315 NW) and less so farther north in the wall (10º/308 NW), indicating that the source vent was located in the vicinity of the present central wall exposure.

Significance

The thin, variable nature of the bedding in the putative tuff ring resembles bedding of the slcrT phreatomagmatic Poris lithofacies described in Chapter 4. The tuff ring lithic content, however, is different; altered and plutonic lithologies are rare. Whereas the Poris eruption involved the disruption of the internal hydrothermal system, the magma-water interaction that created the tuff ring eruption apparently occurred at a shallower level. A detailed comparison of these deposits would reveal how phreatomagmatism changed through the Diego Hernandez volcanic episode; it might reveal more about the proximal processes that occur during different types of phreatomagmatic eruption.

Figure A2 (overleaf) Adjacent to Cueva de Diego Hernandez (a cave at the base of the wall) is a prominent exposure of Plinian fall layers separated by layers of sedimentary reworking (1 in Fig A1). This schematic log depicts the units present. Sed = sedimentary unit, pyro = pyroclastic unit, and scoria = scoria fallout. (a) close-up of pyroclastic unit 6, an intensely-stratified hybrid pyroclastic deposit. (b) diagenetically altered pumices in the palaeosol above pyroclastic unit 5.

Figure A3 (overleaf) Schematic log of the central tuff ring outcrop in the lower DH wall. At the base of the succession, a stratified lapilli tuff is overlain by a black scoria fall layer. The lapill tuff may be a deposit of the 347 ka Roque eruption reported by Edgar *et al.*, 2007. (a) 'Xenoclast' of coarse mLT facies overlain by fine grained tuff enclosed within a pale clast-rich unit below the tuff ring deposit. (b) Diagenetically-flattened pumices within the palaeosol beneath the tuff ring. (c) Bedding structures highlight the pulsatory nature of the tuff ring eruption. (d) The upper part of the tuff-ring exposure is reddish-brown, possibly a result of weathering.

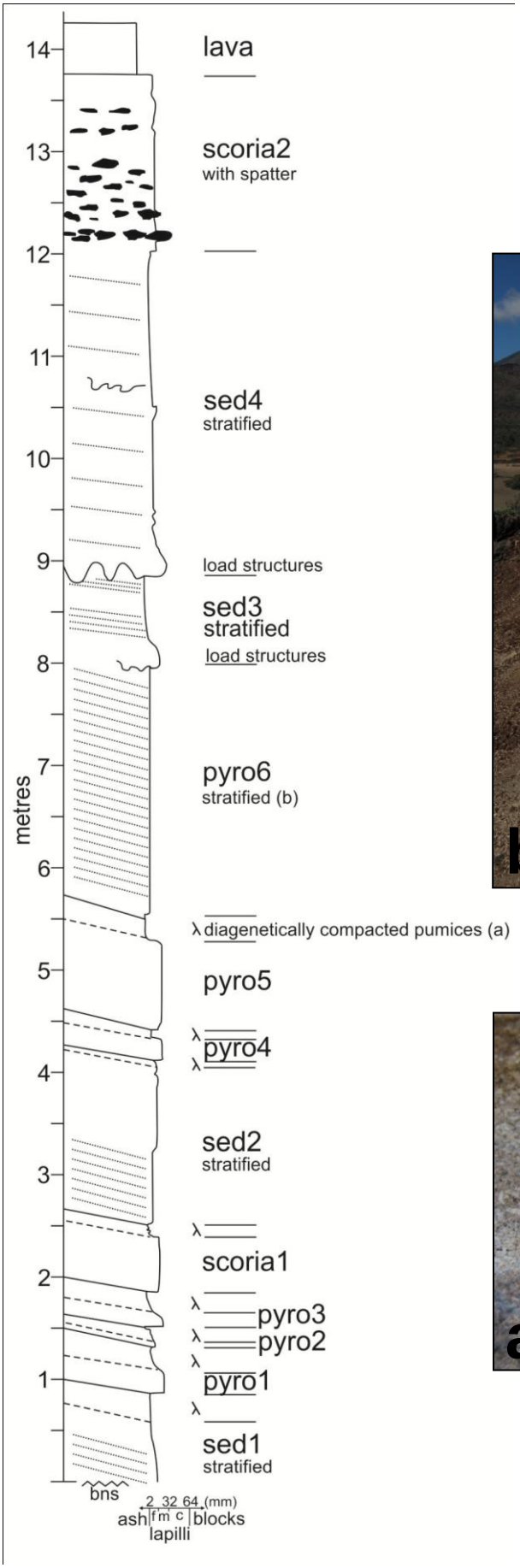
14
13
12
11
10
9
8
7
6
5
4
3
2
1
metres
lava
scoria2
with spatter
sed4
stratified
load structures
sed3
stratified
load structures
pyro6
stratified (b)
λ diagenetically compacted pumices (a)
pyro5
λ pyro4
λ
sed2
stratified
λ
scoria1
λ pyro3
λ pyro2
λ pyro1
λ
sed1
stratified
bns
2 32 64 (mm)
ash f m c blocks
lapilli


b


a

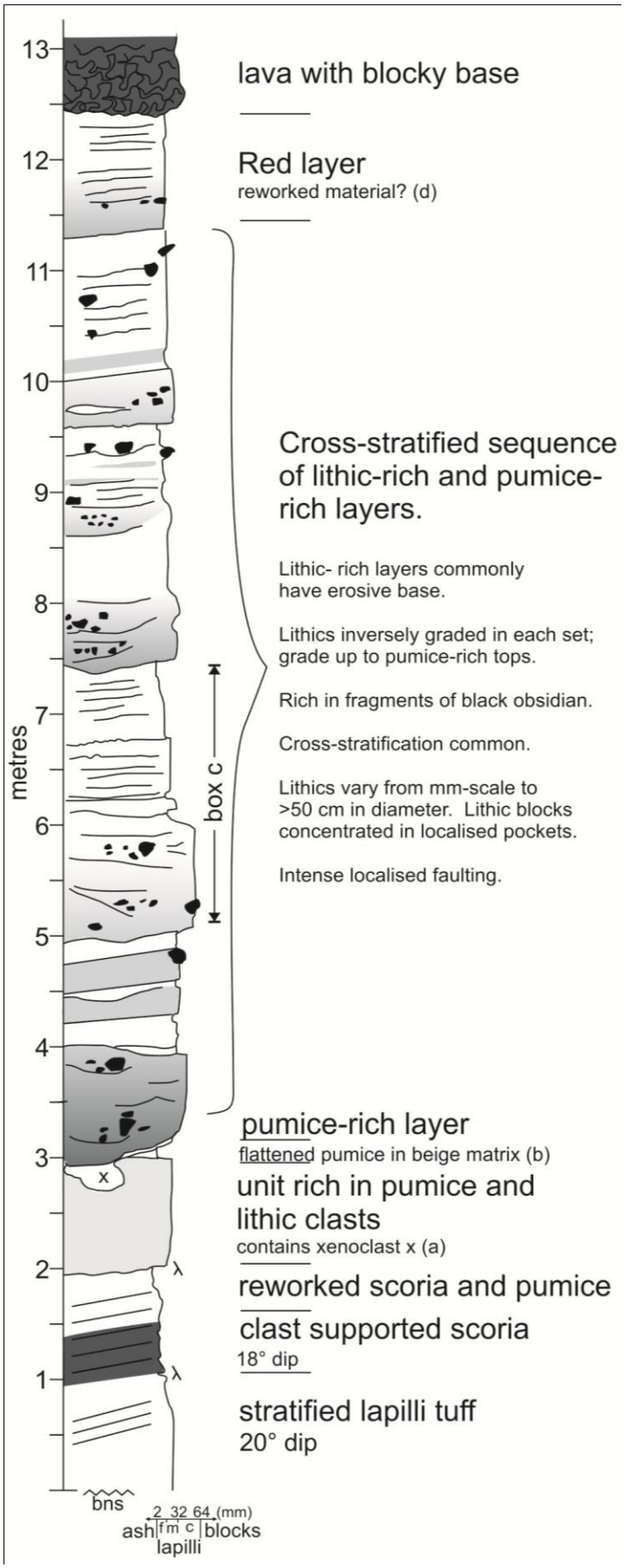
13
12
11
10
9
8
7
6
5
4
3
2
1
metres
box c
x
λ
λ
bns
2 32 64 (mm)
ash f m c blocks
lapilli
lava with blocky base
Red layer
reworked material? (d)
Cross-stratified sequence of lithic-rich and pumice-rich layers.
Lithic- rich layers commonly have erosive base.
Lithics inversely graded in each set; grade up to pumice-rich tops.
Rich in fragments of black obsidian.
Cross-stratification common.
Lithics vary from mm-scale to >50 cm in diameter. Lithic blocks concentrated in localised pockets.
Intense localised faulting.
pumice-rich layer
flattened pumice in beige matrix (b)
unit rich in pumice and lithic clasts
contains xenoclast x (a)
reworked scoria and pumice
clast supported scoria
18° dip
stratified lapilli tuff
20° dip

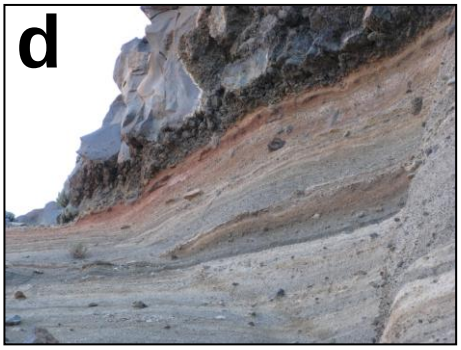
d

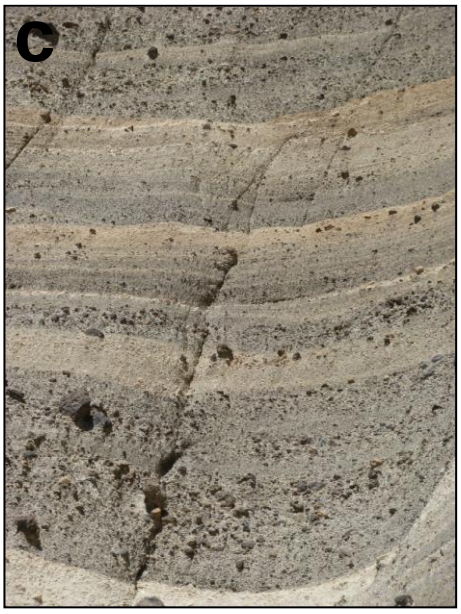
c

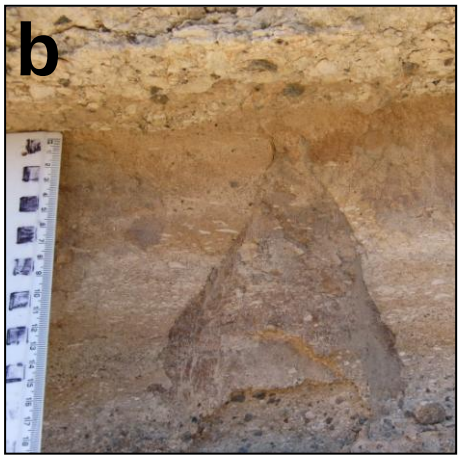
b

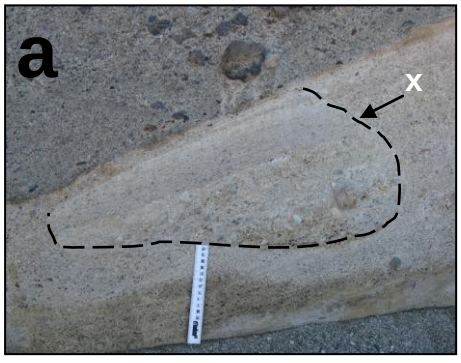
a
x

The indication of an obsidian-rich source vent in the southeast of the present Cañadas depression prior to the Aldea eruption (319 ka) is unexpected; it does not fit on the NE-trend of the Cordillera Dorsal, and is in a different location to the source zones of the Aldea, Fasnia and Poris eruptions, west of the current Diego Hernandez wall. Further study of the tuff ring may therefore be relevant in investigating how the structure of the Cañadas region changed prior to the Aldea eruption.

A1.4 Large scour features

In the northern part of the wall, the Aldea Formation is ~15 m thick and is separated from the lavas overlying the tuff ring by >20 m of sediments, including at least 2 minor Plinian units and a thick unit (>14 m) of cross-stratified boulder-bearing sands and gravels supported in a brown matrix. This succession pinches out in the centre of the wall, where the Aldea thins to ~5 m and directly overlies the lava on top of the main tuff ring outcrop.

A large-scale bedform, >20 m wide and 9 m thick, occurs in Aldea deposits 30 m south of the large dyke in the northern DH wall. (Box 3, Fig A1). A succession of ≥5 ignimbrite lithofacies contains evidence of steep scour and non-uniform deposition. The lowermost unit is a stratified pumice block tuff containing mingled pumice blocks that lies in direct contact with the pre-Aldea substrate sediments. The spBT facies is not laterally continuous, and is in erosive contact with the overlying massive lapilli tuff facies, which in places is rich in pumice blocks (mpLT).

Locally, the mLT/mpLT is in very steeply dipping contact with spBT and the latter is completely removed (Box 3, Fig. A4). Above this, three overlying mLT units are also steeply dipping, the third of which is relatively rich in lithics (mlLT) and fills a channel-shaped bedform. A planar surface at the top of the bedform may be evidence that a final unit is in erosive, planar contact with the mlLT, but could be a weathering feature. Ten metres north of the bedform the 3-4 facies exposed at the top of the Aldea are thinner, and a lack of clear connecting exposure makes stratigraphic correlation along each unit difficult.

Significance

This complicated bedform is evidence that at this location, conditions favoured steep scour of previously deposited material. The entire feature is reminiscent of the valley fill and ignimbrite veneer deposits that occur in the distal Poris succession (described in Brown and Branney, 2004b), but that this 'valley' was created *during* the eruption. Although features of scour and non-deposition are common in the younger proximal Poris formation, they are on a smaller scale than those observed in the proximal Aldea. The Poris Formation was deposited on top of a relatively planar lava flow substrate, whereas the presence of the tuff ring below the Aldea would have created highly irregular topography. The study and comparison of scour features preserved in the Aldea, Fasnia and Poris Formations in the DH wall could therefore be significant in establishing what causes variations in the depth and nature of substrate erosion, and how localised topographic changes may affect deposition from PDCs in the near-vent zone.

Figure A4 (overleaf) Photomap of a large bedform in the 319 ka (Edgar *et al.*, 2007) Aldea Formation. (a) Brown cross stratified sediments of the pre-Aldea substrate. (b) The contact between substrate and spBT. No Plinian deposit is preserved here, and the contact is not erosive, indicating that Plinian deposition and density current deposition occurred simultaneously at the start of the Aldea eruption. (c) mLT in steep erosive contact with spBT. (d) A thin layer of massive tuff occurs between two mLT units; possibly an ignimbrite veneer deposit stratigraphically related to one of the thicker deposits in the bedform. (e) Slightly north of the bedform, a cross cutting view shows at least one of the units pinches out to the north. The stratigraphic correlations across this area are unclear.

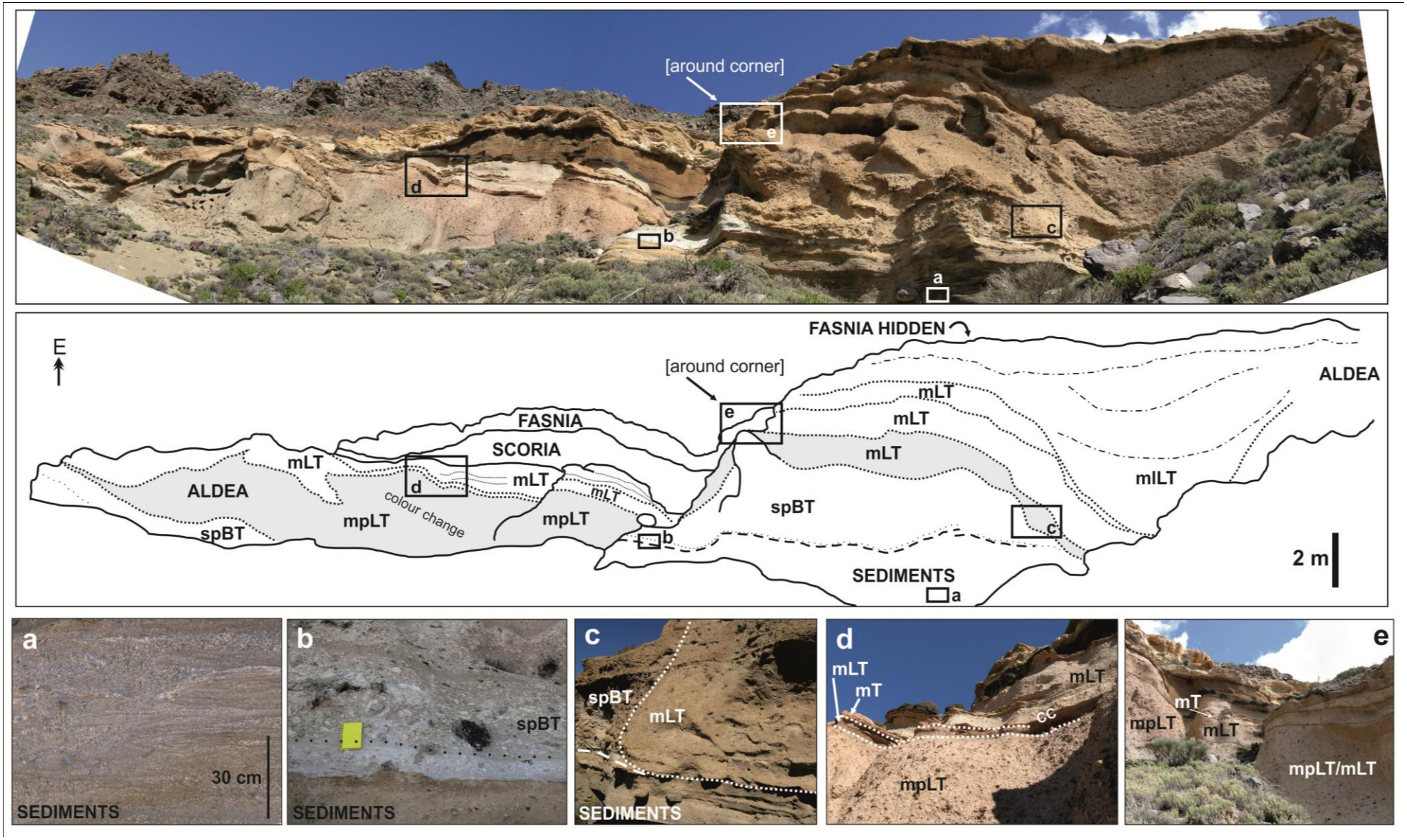
[around corner]
e
d
b
c
a
E
FASNIA HIDDEN
[around corner]
ALDEA
FASNIA
SCORIA
mLT
mLT
mLT
mLT
mLT
mLT
mILT
ALDEA
colour change
mpLT
mpLT
spBT
spBT
SEDIMENTS
2 m
a
30 cm
SEDIMENTS
b
spBT
SEDIMENTS
c
spBT
mLT
SEDIMENTS
d
mLT
mT
mLT
cc
mpLT
e
mT
mpLT
mLT
mpLT/mLT

A2. Methods

A2.1 Grain Mount Preparation

A thin layer of araldite 2020 epoxy resin is smeared over a 50x28 mm glass thin section slide. The sieved and separated/handpicked grains are sprinkled onto this layer and encouraged to sick through and touch the glass. The slide is left to partially go off for 2 hours on a 40°C hot plate, and another thin layer of resin is then applied. This layer ensures that the grains sink, and prevents grains from being 'plucked' during the grinding and polishing process. After being left to go off overnight, the resin on the mounts is ground down using a series of silicon carbide papers; (500, 800 and 1200 were used in this case). Once as many grains as possible have been intersected, the mounts are polished using diamond paste, at 6, 3, 1 and finally 0.25 micron grade.

Transmitted light scanner images are taken of the mounts to aid navigation in the probe, and they are carbon coated before being put into the instrument.

A2.2 Fusion Bead Preparation

Following milling, the powdered samples are placed into an oven overnight at 110°C to dry. They are then weighed before and after they are placed into a Lenton furnace at 950°C for 1.5hrs. The Loss on Ignition (LOI) is thus calculated. The sample is then added to a metaborate flux, which contains 20% lithium tetraborate and 80% lithium metaborate, at a ratio of one part powder to five parts flux. This mixture is placed in platinum crucibles and fused over a Spartan oxygen-enhanced Bunsen burner at 1100°C. Beads are cast from the fused molten material and left to cool.

A2.3 Pellet Preparation

Roughly 7g of the milled powdered sample is weighed out and mixed with ~25 drops of Movoil 88 glue (a mix of deionised water, methanol and crystals). The sticky mix is placed into a mould and put under hydraulic pressure to a force of 10 tons. The pressure is slowly released, and the pellet is pressed out.

See Figure A5 for photos of sample preparation for XRF.

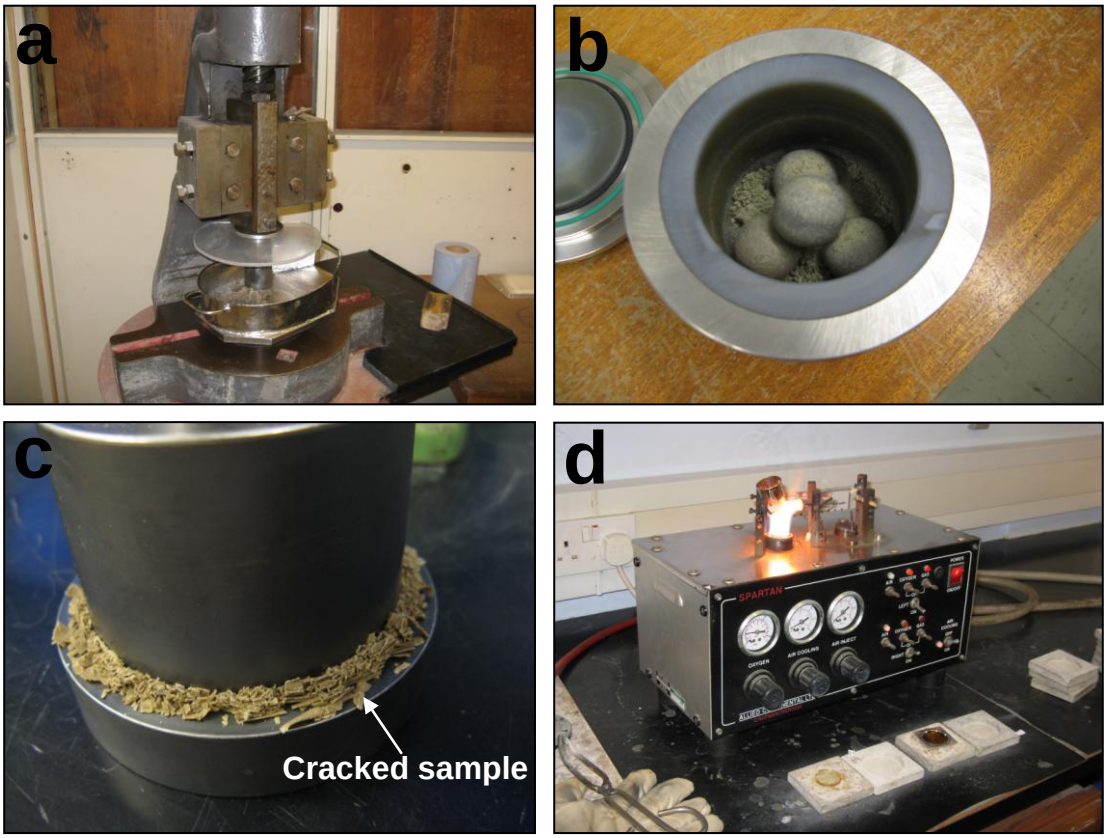

Figure A5 Sample preparation for XRF analysis. (a) Samples are crushed using a splitter engineering fly press. (b) Crushed pumices are milled using an agate planetary mill. (c) During the pellet making process, sample FSS1 cracked, showing signs of clay alteration. (d) Fusion beads made by heating sample in a platinum crucible.

A3. EPMA standards

Na, Al	natural jadeite
Ca, Si	natural wollastonite
K	natural microcline
Ti	natural rutile
Mn	natural rhodonite
Fe	synthetic Fe_3O_4
Mg	synthetic MgO
Cr	pure metal
Ni	pure metal

A4. Full XRF dataset

Table A1 = Proximal and distal major data

Table A2 = Proximal minor data

Table A3 = Distal minor data

† FSS1 was affected by clay-alteration.
ǂ FSS19 is the only sample NOT from the Poris Formation.
* These pumices are black or green in colour.

Sample	SiO_2	TiO_2	Al_2O_3	Fe_2O_3	MnO	MgO	CaO	Na_2O	K_2O	P_2O_5	SO_3	LOI	Total
Proximal													
FSS1†	50.6	0.51	24.0	3.29	0.208	0.300	0.824	5.77	5.02	0.062	0.051	9.66	100.3
FSS2	56.5	0.46	19.8	2.82	0.178	0.220	1.06	8.09	5.71	0.064	0.073	5.28	100.2
FSS3	55.5	0.84	19.6	3.76	0.179	0.619	2.14	8.17	5.30	0.167	0.088	3.81	100.2
FSS4	56.2	0.67	19.7	3.36	0.177	0.425	1.75	7.82	5.54	0.113	0.062	4.48	100.2
FSS5	55.9	0.81	19.9	3.77	0.176	0.583	1.81	7.75	5.17	0.138	0.075	4.30	100.3
FSS6	56.4	0.62	19.9	3.21	0.181	0.303	1.38	8.43	5.52	0.109	0.057	3.76	99.9
FSS6a*	50.5	2.33	18.3	7.55	0.196	2.55	6.37	6.31	3.37	0.770	0.194	1.95	100.4
FSS7*	56.9	0.94	19.8	3.96	0.179	0.648	2.24	8.81	4.96	0.179	0.108	1.84	100.5
FSS8	57.8	0.44	20.3	2.81	0.184	0.088	0.90	8.53	5.51	0.046	0.030	4.15	100.8
FSS9	57.0	0.56	20.1	3.05	0.177	0.240	1.22	8.49	5.37	0.087	0.050	4.07	100.4
FSS10	57.5	0.61	20.3	3.27	0.192	0.305	1.38	9.23	5.19	0.117	0.058	2.60	100.7
FSS11	57.2	0.50	20.1	2.92	0.180	0.163	1.05	8.47	5.41	0.066	0.040	4.56	100.6
FSS12	55.9	0.43	20.5	2.86	0.180	0.074	0.79	7.66	5.42	0.036	0.036	4.99	98.8
FSS13*	53.5	1.86	18.9	6.13	0.172	1.79	4.66	6.33	3.79	0.507	0.136	1.74	99.5
FSS14	57.6	0.47	20.7	2.94	0.184	0.121	0.940	8.22	5.52	0.052	0.039	2.97	99.7
FSS15*	56.6	0.94	20.2	4.02	0.181	0.678	2.18	7.64	4.98	0.204	0.071	1.99	99.6
FSS16*	56.3	1.18	20.0	4.59	0.180	0.966	2.83	7.38	4.72	0.282	0.088	1.01	99.6
FSS17*	52.4	1.87	18.7	6.57	0.186	2.12	4.77	6.55	3.75	0.486	0.077	1.81	99.4
FSS18	57.9	0.73	19.3	2.95	0.147	0.350	1.38	7.12	5.73	0.105	0.059	3.11	98.9
FSS19	57.0	0.55	20.0	2.86	0.152	0.222	1.17	6.48	5.45	0.056	0.021	4.63	98.7
Distal													
DIST1	55.4	0.38	19.4	2.64	0.158	0.464	1.09	7.63	4.77	0.034	0.027	7.01	99.0
DIST2	55.2	0.37	19.3	2.60	0.174	0.226	0.740	8.73	5.24	0.034	0.115	6.19	98.9
DIST3	54.7	0.41	19.1	2.68	0.174	0.550	1.89	8.10	5.74	0.057	0.088	5.93	99.3
DIST4	53.3	0.41	18.7	2.61	0.169	0.526	3.14	8.00	5.62	0.079	0.077	6.80	99.3
DIST5	51.9	0.40	18.7	2.61	0.163	0.424	4.71	7.50	5.01	0.075	0.093	7.23	98.9
DIST6	55.8	0.40	19.6	2.67	0.177	0.175	0.951	8.66	5.46	0.041	0.075	4.98	99.0
DIST7*	49.0	2.63	17.8	8.35	0.193	3.04	7.34	6.02	2.76	0.815	0.278	1.17	99.3
DIST8	54.5	0.62	18.9	3.11	0.169	0.919	3.29	8.10	5.23	0.132	0.088	5.47	100.6
DIST9*	53.3	2.08	19.0	6.65	0.181	2.07	5.63	6.68	3.51	0.593	0.215	0.65	100.5
DIST10*	56.4	1.39	19.3	4.80	0.161	1.19	3.50	7.61	4.67	0.371	0.174	0.90	100.4
DIST11	54.3	0.52	19.0	2.94	0.173	0.554	2.88	7.90	5.69	0.102	0.092	6.14	100.3
DIST12*	48.2	2.92	17.4	9.30	0.197	3.77	7.98	5.23	2.73	0.915	0.179	1.32	100.2
DIST13	53.2	0.54	18.4	2.94	0.167	0.966	3.72	7.51	5.55	0.099	0.233	7.08	100.4

Table A1

Sample	Ba	Ce	Cl	Co	Cr	Cs	Cu	Ga	La	Mo	Nb	Nd	Ni	Pb	Rb	Sc	Sr	Th	U	V	Y	Zn	Zr
Proximal																							
FSS1†	26.7	202.3	24220	3.54	16.5	6.08	11.5	53.7	109.4	3.95	273.8	49.1	2.43	26.6	122.4	2.02	108.1	43.0	6.60	23.6	58.7	128.8	1538.2
FSS2	120.2	175.5	5509	3.12	<0.6	4.49	6.62	33.9	112.0	5.56	240.4	44.0	2.02	19.2	193.9	1.55	79.9	37.2	9.40	30.3	26.5	110.2	1317.7
FSS3	395.7	182.0	5084	5.40	<0.6	7.03	5.70	31.9	112.5	6.05	224.3	52.1	0.75	17.1	176.1	1.09	306.5	30.4	8.39	54.1	28.6	109.1	1129.6
FSS4	347.5	171.9	5798	2.76	14.1	3.99	<0.4	31.4	110.9	5.53	224.7	46.6	0.86	135.8	180.8	1.81	199.1	32.7	8.10	44.6	26.6	107.2	1167.2
FSS5	424.5	173.9	3998	3.03	<0.6	5.87	<0.5	32.1	108.5	6.33	223.9	48.2	1.62	17.3	170.5	1.67	242.5	30.5	8.23	52.7	27.2	108.7	1142.9
FSS6	247.1	175.6	3383	2.90	<0.6	7.62	<0.4	32.8	112.6	5.85	231.5	44.4	<0.5	18.3	191.4	<1.1	155.0	32.9	8.83	39.8	24.9	106.7	1220.9
FSS6a*	1017.7	202.9	1683	14.6	<0.7	2.52	5.01	25.3	103.0	6.28	165.2	83.7	<0.6	10.0	87.6	8.25	1069.4	14.7	4.43	148.4	39.6	109.0	624.5
FSS7*	610.3	190.3	2960	5.46	<0.7	4.74	2.57	32.0	110.4	6.40	222.5	57.6	<0.6	143.0	167.6	2.07	327.3	29.2	6.65	60.0	30.5	108.2	1076.4
FSS8	84.4	168.5	3880	2.83	<0.6	6.97	<0.4	33.6	113.7	6.08	241.8	38.2	<0.5	19.9	209.3	1.38	57.1	36.0	9.33	30.3	22.9	109.7	1328.9
FSS9	307.6	170.9	3499	2.89	<0.6	6.81	<0.4	32.1	113.0	5.97	236.2	42.6	<0.5	21.6	191.2	<1.1	143.9	33.7	8.70	36.9	25.5	109.4	1242.6
FSS10	178.4	174.0	3318	4.83	<0.6	5.07	1.80	33.8	109.8	6.11	238.9	40.6	<0.5	18.1	200.9	1.50	142.5	34.9	9.10	41.4	24.7	111.7	1282.0
FSS11	73.1	167.5	6039	2.45	17.0	6.41	0.69	33.4	109.8	5.93	238.6	38.8	<0.5	19.1	205.8	<1.1	57.7	36.7	9.24	30.7	22.9	109.0	1314.8
FSS12	92.4	174.0	3502	2.15	<0.6	9.19	<0.4	35.5	117.9	5.43	245.6	43.1	<0.5	39.2	201.8	<1.0	43.8	37.6	9.87	25.7	25.5	114.0	1355.7
FSS13*	1488.4	205.0	1220	12.0	<0.7	<1.7	3.89	25.8	149.4	4.50	178.2	100.0	<0.6	9.22	88.7	5.75	813.1	15.0	4.34	106.3	47.0	99.5	610.3
FSS14	945.7	204.2	1284	1.17	24.1	<1.7	<0.4	25.5	109.1	7.01	179.4	74.9	<0.5	8.00	101.7	2.03	170.0	13.5	3.07	47.6	37.1	97.6	680.7
FSS15*	750.2	184.6	985	<1.1	<0.6	4.59	<0.4	22.6	98.4	7.09	146.8	69.0	<0.5	7.05	88.6	1.48	74.9	10.6	2.87	39.1	32.3	84.7	537.3
FSS16*	1886.8	177.7	913	3.34	<0.7	<1.7	<0.4	21.4	94.1	7.14	138.4	68.4	<0.5	6.84	79.7	<1.1	244.5	9.89	2.14	47.3	31.9	85.9	510.1
FSS17*	950.4	191.9	1540	11.7	3.64	4.47	6.89	27.8	103.6	4.71	183.6	70.7	5.70	10.4	106.9	5.32	801.4	18.9	5.54	108.9	38.4	103.5	737.1
FSS18	624.1	179.3	2045	<1.1	<0.6	3.33	<0.4	25.1	102.6	5.40	207.3	55.4	<0.5	12.8	140.2	1.17	143.1	21.5	5.44	38.7	33.5	83.3	827.8
FSS19	272.7	118.7	2340	3.30	<0.6	3.09	<0.4	29.4	79.2	5.25	158.4	27.9	<0.5	13.4	161.7	<1.0	103.1	25.4	5.66	28.6	14.3	82.4	991.9

Table A2

Sample	Ba	Ce	Cl	Co	Cr	Cs	Cu	Ga	La	Mo	Nb	Nd	Ni	Pb	Rb	Sc	Sr	Th	U	V	Y	Zn	Zr
Distal																							
DIST1	17.9	155.2	6367	2.12	<0.6	7.28	4.08	31.9	100.9	5.54	226.6	34.2	<0.5	18.1	185.1	<1.0	42.3	36.4	7.76	22.5	19.7	102.8	1332.6
DIST2	48.6	157.4	17788	1.60	21.3	7.86	3.91	31.3	105.9	5.77	231.2	35.3	1.85	18.5	197.4	<1.0	29.9	35.2	8.43	25.8	21.2	104.6	1291.9
DIST3	38.3	158.8	3743	3.09	<0.6	5.85	8.07	31.8	111.8	5.81	233.7	36.7	1.19	22.1	205.1	1.61	72.1	35.4	8.46	27.3	23.2	117.0	1304.8
DIST4	83.5	156.7	3478	1.35	<0.6	4.98	6.08	31.5	111.7	5.82	227.8	37.9	1.66	19.1	199.6	<1.1	110.0	34.8	8.67	27.6	24.4	114.0	1257.2
DIST5	57.7	154.6	6293	2.33	<0.6	5.26	4.02	31.5	103.7	5.69	220.0	34.7	<0.5	17.8	184.3	3.34	90.4	33.7	13.34	26.6	25.1	104.5	1280.9
DIST6	60.2	165.2	6476	3.29	<0.6	3.68	4.18	33.6	113.4	6.08	240.6	38.6	<0.5	19.3	206.9	1.55	48.7	36.7	9.53	25.3	23.4	108.3	1332.7
DIST7*	1518.8	193.2	3534	17.2	39.7	<1.8	14.8	23.4	95.8	5.31	142.9	89.1	4.36	5.75	59.9	9.94	1285.3	9.6	2.30	163.3	41.4	100.4	468.7
DIST8	271.9	166.5	3176	3.50	<0.6	5.69	5.94	29.6	107.4	5.99	218.5	46.7	0.88	16.4	176.1	<1.1	220.6	30.2	7.38	40.1	25.3	101.3	1139.5
DIST9*	1889.7	204.4	1174	10.50	6.12	<1.8	9.58	23.4	102.8	5.61	163.5	84.7	1.34	6.94	74.8	6.69	1092.4	11.4	3.31	118.2	42.0	95.0	524.6
DIST10*	1290.5	201.2	1502	7.51	5.36	<1.7	8.26	24.7	107.8	6.18	186.8	73.4	<0.6	9.26	103.2	3.90	563.8	15.5	4.45	84.3	38.0	92.1	656.9
DIST11	132.8	168.2	3480	3.35	<0.6	5.64	7.81	30.4	117.9	5.57	213.3	47.9	1.27	18.6	182.0	<1.1	139.3	31.7	8.08	35.5	24.5	104.9	1148.6
DIST12*	1079.0	188.5	1152	19.4	13.1	<1.9	17.6	22.1	93.4	4.82	137.1	79.8	9.25	5.78	61.5	10.80	1175.5	9.22	2.56	186.0	40.7	102.6	462.0
DIST13	180.8	164.0	3593	4.45	10.0	5.74	8.51	30.2	110.9	5.92	216.7	43.9	2.52	19.4	183.6	2.39	193.9	31.6	8.66	35.0	24.5	109.9	1163.1

Table A3

A5. Full EPMA dataset

Tables A4 (2 pages) and A5 (3 pages): Alkali feldspars

Tables A6 and A7: Amphiboles

Table A8: Biotites

Table A9: Nosean-Haüynes

Table A10: Olivines

Tables A11 and A12: Plagioclases

Tables A13 and A14: Pyroxenes

Table A15: Titanite

Tables A16 and A17: Titanomagnetites

Table A18: Ilmenites

(For each mineral type, data are shown for both sieved and handpicked phenocrysts)

Table A4

	Event	SiO2	TiO2	Al2O3	Cr2O3	FeO	MnO	MgO	CaO	Na2O	K2O	NiO	Total	Or	Ab	An	total
		Major Elements (wt%)												**Or-Ab-An (cation %)**			
Sieved 100-300µm																	
ex2.117	7	62.41	0.779	20.80	0.015	2.949	0.126	0.469	1.674	8.311	5.568	0.000	103.11	28.40	64.43	7.171	100.00
ex3.1	7	66.04	0.040	19.45	0.000	0.245	0.000	0.000	0.594	6.884	6.945	0.015	100.21	38.79	58.43	2.786	100.00
ex3.3	7	65.36	0.000	19.22	0.000	0.209	0.000	0.000	0.562	6.781	7.154	0.027	99.31	39.90	57.47	2.632	100.00
ex3.4	7	65.46	0.060	19.21	0.000	0.197	0.023	0.000	0.519	6.753	7.141	0.000	99.37	40.03	57.53	2.443	100.00
ex3.7	7	64.53	0.111	19.00	0.015	0.258	0.003	0.000	0.682	6.736	6.766	0.000	98.10	38.50	58.25	3.259	100.00
ex3.8	7	65.47	0.033	19.21	0.000	0.243	0.029	0.000	0.450	6.762	7.382	0.000	99.58	40.93	56.98	2.095	100.00
ex3.13	7	65.89	0.000	19.17	0.000	0.260	0.000	0.000	0.363	6.502	7.763	0.001	99.95	43.25	55.05	1.698	100.00
ex3.14	7	65.40	0.000	19.62	0.006	0.224	0.009	0.000	0.684	7.067	6.53	0.022	99.56	36.59	60.19	3.219	100.00
ex3.17	7	65.49	0.078	19.16	0.000	0.227	0.020	0.000	0.421	6.488	7.53	0.000	99.42	42.44	55.57	1.993	100.00
fss2.16	1	61.33	0.193	21.54	0.012	0.296	0.000	0.000	2.831	7.177	3.486	0.040	96.90	20.79	65.04	14.177	100.00
fss2.23	1	65.06	0.056	18.68	0.000	0.495	0.036	0.000	0.174	6.968	6.757	0.018	98.24	38.63	60.54	0.835	100.00
fss2.24	1	62.77	0.079	20.56	0.000	0.305	0.000	0.002	1.990	7.372	4.447	0.000	97.53	25.67	64.68	9.648	100.00
fss5.94	4	63.06	0.098	20.71	0.027	0.263	0.036	0.019	1.989	7.303	4.385	0.000	97.89	25.56	64.70	9.738	100.00
fss5.98	4	65.84	0.000	19.27	0.021	0.202	0.007	0.000	0.465	6.989	6.876	0.012	99.68	38.44	59.38	2.183	100.00
fss5.108	4	62.94	0.101	20.91	0.000	0.272	0.000	0.000	2.212	7.764	3.992	0.000	98.20	22.62	66.86	10.526	100.00
fss10.48	5	65.01	0.083	18.99	0.000	0.303	0.000	0.000	0.695	6.278	7.165	0.000	98.53	41.44	55.18	3.376	100.00
fss10.50	5	65.43	0.000	19.50	0.025	0.293	0.000	0.000	0.645	6.934	6.499	0.017	99.34	36.97	59.95	3.082	100.00
fss10.52	5	65.91	0.000	19.19	0.000	0.233	0.024	0.000	0.383	6.304	7.668	0.000	99.71	43.64	54.53	1.831	100.00
fss10.54	5	64.33	0.052	20.73	0.010	0.353	0.007	0.000	1.905	7.816	4.089	0.021	99.32	23.28	67.62	9.107	100.00
fss10.58	5	66.21	0.000	19.59	0.000	0.229	0.000	0.000	0.714	7.492	6.071	0.000	100.30	33.62	63.06	3.321	100.00
fss10.60	5	63.70	0.461	22.12	0.000	2.188	0.137	0.172	0.816	8.633	5.697	0.000	103.93	29.21	67.27	3.514	100.00
fss10.61	5	65.55	0.022	19.39	0.000	0.170	0.001	0.000	0.815	7.582	5.657	0.000	99.18	31.67	64.50	3.831	100.00
fss11.31	5	58.52	1.450	19.66	0.000	4.142	0.166	1.196	3.133	7.108	4.882	0.028	100.28	26.65	58.98	14.366	100.00
fss11.36	5	63.95	0.000	18.97	0.000	0.243	0.000	0.000	0.682	6.918	6.073	0.003	96.84	35.39	61.27	3.338	100.00
fss11.41	5	65.58	0.050	19.08	0.000	0.260	0.016	0.000	0.366	6.554	7.427	0.017	99.35	41.97	56.29	1.737	100.00
fss11.45	5	58.30	0.344	19.17	0.000	2.243	0.189	0.180	0.756	4.957	9.552	0.000	95.68	53.90	42.51	3.583	100.00
fss14.71	7	62.29	0.138	20.39	0.000	0.390	0.031	0.000	2.032	7.661	3.566	0.020	96.52	21.08	68.83	10.089	100.00
fss15.77	7	63.72	0.099	19.44	0.000	0.350	0.000	0.000	1.174	7.523	4.837	0.004	97.15	28.03	66.26	5.714	100.00
fss15.80	7	61.92	0.095	20.44	0.044	0.345	0.000	0.000	2.410	7.938	2.995	0.023	96.22	17.53	70.62	11.848	100.00
fss15.84	7	62.35	0.110	20.74	0.000	0.363	0.000	0.000	2.160	7.725	3.421	0.005	96.87	20.15	69.16	10.686	100.00
fss15.85	7	64.83	0.137	20.37	0.000	0.350	0.000	0.000	1.408	8.152	4.3	0.004	99.55	24.06	69.32	6.617	100.00

fss15.88	7	62.23	0.189	20.98	0.000	0.292	0.000	0.000	2.339	7.628	3.643	0.000	97.30	21.18	67.40	11.421	100.00
dist1.42	1	63.33	0.027	18.47	0.000	0.237	0.000	0.000	0.364	6.387	7.518	0.000	96.33	42.88	55.37	1.744	100.00
dist1.44	1	62.82	0.000	18.84	0.015	0.242	0.000	0.000	0.406	6.563	7.33	0.012	96.22	41.54	56.53	1.932	100.00
dist1.45	1	65.74	0.000	19.22	0.000	0.271	0.000	0.000	0.476	6.766	7.164	0.020	99.65	40.14	57.62	2.240	100.00
dist1.47	1	64.55	0.016	19.06	0.014	0.235	0.000	0.000	0.514	6.984	6.617	0.000	97.99	37.46	60.09	2.444	100.00
dist1.50	1	64.13	0.008	18.85	0.016	0.237	0.018	0.000	0.624	6.938	6.626	0.028	97.47	37.45	59.59	2.962	100.00
dist1.51	1	60.96	0.000	17.54	0.002	0.240	0.000	0.000	0.341	5.732	7.417	0.000	92.23	45.18	53.07	1.745	100.00
dist1.53	1	67.33	0.691	12.72	0.000	6.867	0.295	0.213	0.941	5.659	4.938	0.008	99.66	34.46	60.02	5.515	100.00
dist1.55	1	63.31	0.000	18.99	0.004	0.249	0.000	0.000	0.764	7.044	6.102	0.000	96.46	34.97	61.35	3.677	100.00
dist1.54	1	62.38	0.000	17.80	0.000	0.062	0.000	0.012	0.061	2.916	11.903	0.000	95.13	72.64	27.05	0.313	100.00
dist3.57	1	62.82	0.002	18.37	0.024	0.239	0.000	0.000	0.380	6.109	7.881	0.009	95.83	45.07	53.10	1.825	100.00
dist3.58	1	64.09	0.000	18.60	0.028	0.296	0.000	0.000	0.500	6.471	6.97	0.019	96.98	40.47	57.10	2.438	100.00
dist3.62	1	64.84	0.050	18.62	0.000	0.009	0.000	0.005	0.277	9.973	1.651	0.000	95.43	9.69	88.95	1.365	100.00
dist6.72	5	65.39	0.073	18.93	0.032	0.224	0.000	0.000	0.392	6.621	7.349	0.000	99.01	41.42	56.72	1.856	100.00
dist6.73	5	70.11	0.832	6.60	0.023	8.959	0.419	0.158	0.339	4.565	4.278	0.028	96.31	37.20	60.33	2.476	100.00
dist6.79	5	55.47	0.119	18.98	0.022	1.087	0.004	0.000	0.091	6.916	7.506	0.000	90.19	41.48	58.09	0.422	100.00
dist6.80	5	64.96	0.079	19.54	0.018	0.290	0.000	0.000	0.797	7.372	5.288	0.005	98.35	30.81	65.29	3.900	100.00
dist6.82	5	62.85	0.037	18.43	0.030	0.240	0.003	0.000	0.531	6.47	7.091	0.010	95.69	40.82	56.61	2.567	100.00
dist8.22	7	65.68	0.055	19.19	0.035	0.237	0.016	0.000	0.458	6.206	8.082	0.007	99.97	45.15	52.70	2.149	100.00
dist8.27	7	65.77	0.018	18.92	0.000	0.235	0.000	0.000	0.476	6.535	7.599	0.000	99.55	42.38	55.39	2.230	100.00
dist8.28	7	64.45	0.000	18.60	0.023	0.063	0.000	0.020	0.294	10.157	1.375	0.000	94.98	8.06	90.49	1.447	100.00
dist8.30	7	65.59	0.075	19.05	0.000	0.235	0.000	0.000	0.415	6.676	7.25	0.000	99.29	40.86	57.18	1.964	100.00
dist8.33	7	65.88	0.000	19.44	0.000	0.200	0.046	0.000	0.532	6.904	6.921	0.035	99.96	38.75	58.75	2.502	100.00
dist8.36	7	64.74	0.297	19.52	0.013	0.674	0.067	0.115	0.956	7.566	5.54	0.025	99.52	31.05	64.45	4.500	100.00
dist8.38	7	65.71	0.000	19.28	0.012	0.224	0.000	0.000	0.430	6.844	7.288	0.000	99.79	40.38	57.62	2.001	100.00
dist12.114	8	62.90	0.117	19.34	0.000	0.300	0.000	0.005	1.214	6.956	5.862	0.000	96.69	33.59	60.57	5.842	100.00
dist13.4	4	65.13	0.053	19.16	0.000	0.360	0.000	0.000	0.451	6.34	7.633	0.006	99.12	43.25	54.60	2.146	100.00
dist13.8	4	64.49	0.000	19.28	0.000	0.236	0.000	0.000	0.741	6.695	6.621	0.000	98.06	38.01	58.42	3.573	100.00
dist13.15	4	65.62	0.006	19.15	0.000	0.217	0.000	0.000	0.563	6.849	6.967	0.000	99.37	39.03	58.32	2.649	100.00

Table A5

		Major Elements (wt%)												Or-Ab-An (cation %)			
	Event	SiO2	TiO2	Al2O3	Cr2O3	FeO	MnO	MgO	CaO	Na2O	K2O	NiO	Total	Or	Ab	An	total
Handpicked																	
ex2.17	7	66.18	0.000	18.60	0.000	0.236	0.000	0.000	0.023	5.698	9.04	0.000	99.77	51.02	48.87	0.109	100.00
ex2.23	7	66.10	0.000	18.74	0.000	0.177	0.000	0.000	0.044	6.129	8.237	0.000	99.43	46.83	52.96	0.210	100.00
ex2.24	7	65.90	0.000	18.64	0.000	0.224	0.000	0.000	0.046	5.873	8.562	0.000	99.24	48.85	50.93	0.220	100.00
ex2.25	7	66.25	0.000	18.71	0.000	0.106	0.000	0.000	0.042	6.122	8.356	0.000	99.58	47.22	52.58	0.199	100.00
ex2.26	7	65.04	0.000	18.62	0.004	0.092	0.007	0.000	0.105	6.241	7.654	0.000	97.76	44.43	55.06	0.512	100.00
ex2.27	7	65.78	0.000	18.47	0.000	0.335	0.011	0.000	0.069	5.791	8.686	0.000	99.15	49.51	50.16	0.330	100.00
ex2.28	7	65.62	0.000	19.41	0.000	0.235	0.000	0.000	0.727	7.195	5.899	0.000	99.08	33.82	62.68	3.500	100.00
ex2.29	7	65.54	0.055	19.00	0.014	0.166	0.019	0.000	0.321	6.762	7.251	0.036	99.17	40.74	57.74	1.515	100.00
ex2.30	7	65.44	0.000	19.25	0.000	0.188	0.000	0.000	0.419	6.895	6.752	0.013	98.95	38.40	59.60	2.001	100.00
ex2.31	7	65.37	0.034	18.60	0.015	0.332	0.017	0.000	0.123	6.092	8.164	0.000	98.75	46.58	52.83	0.589	100.00
ex2.33	7	65.13	0.000	19.04	0.010	0.205	0.000	0.000	0.469	6.371	7.009	0.000	98.23	41.02	56.67	2.305	100.00
ex2.36	7	65.12	0.000	18.48	0.000	0.174	0.006	0.000	0.014	5.604	8.9	0.000	98.30	51.07	48.87	0.067	100.00
ex3.2	7	65.07	0.037	19.96	0.000	0.286	0.000	0.015	1.109	7.598	5.458	0.033	99.57	30.43	64.38	5.193	100.00
ex3.3	7	64.95	0.016	18.98	0.000	0.207	0.000	0.000	0.354	6.172	7.911	0.000	98.59	44.98	53.33	1.690	100.00
ex3.4	7	64.62	0.057	19.63	0.000	0.258	0.000	0.000	0.946	7.396	5.854	0.000	98.76	32.72	62.83	4.441	100.00
ex3.5	7	65.42	0.060	19.34	0.006	0.282	0.001	0.000	0.473	6.538	7.273	0.019	99.41	41.31	56.44	2.256	100.00
ex3.7	7	66.31	0.000	19.27	0.000	0.302	0.000	0.000	0.401	6.657	7.454	0.000	100.39	41.62	56.50	1.881	100.00
ex3.8	7	65.00	0.001	19.39	0.019	0.252	0.023	0.000	0.701	6.893	6.575	0.000	98.86	37.27	59.39	3.338	100.00
ex3.9	7	65.03	0.000	19.11	0.004	0.237	0.011	0.000	0.562	6.88	6.984	0.000	98.82	38.99	58.37	2.635	100.00
ex3.10	7	65.08	0.054	19.10	0.000	0.212	0.004	0.000	0.565	6.822	6.786	0.000	98.63	38.49	58.81	2.692	100.00
ex3.12	7	65.28	0.056	19.16	0.000	0.255	0.000	0.000	0.532	6.711	7.239	0.000	99.23	40.47	57.03	2.498	100.00
ex3.13	7	65.82	0.042	18.86	0.002	0.312	0.019	0.000	0.270	6.768	7.254	0.023	99.37	40.83	57.89	1.276	100.00
ex3.15	7	67.24	0.000	20.08	0.000	0.261	0.058	0.000	0.845	7.606	5.667	0.000	101.75	31.60	64.45	3.957	100.00
ex3.16	7	63.84	0.117	18.73	0.012	0.186	0.031	0.000	0.519	6.345	7.18	0.021	96.98	41.60	55.87	2.526	100.00
ex3.17	7	66.22	0.051	19.06	0.050	0.224	0.020	0.000	0.398	6.589	7.506	0.021	100.14	42.04	56.09	1.872	100.00
ex3.18	7	65.39	0.034	19.10	0.000	0.216	0.000	0.000	0.353	6.254	7.982	0.000	99.33	44.88	53.45	1.667	100.00
ex3.20	7	65.95	0.015	19.11	0.012	0.231	0.000	0.000	0.384	6.355	7.758	0.018	99.83	43.73	54.45	1.818	100.00
ex3.21	7	64.59	0.059	19.05	0.000	0.212	0.013	0.000	0.433	6.658	7.234	0.000	98.25	40.83	57.12	2.053	100.00
fss2.38	1	61.67	0.090	21.62	0.066	0.344	0.010	0.000	3.047	7.619	2.986	0.000	97.45	17.44	67.62	14.944	100.00
fss2.47	1	59.74	0.198	21.21	0.000	2.206	0.037	0.508	0.478	4.861	5.432	0.000	94.67	41.09	55.88	3.036	100.00
fss10.77	5	63.43	0.039	20.43	0.000	0.283	0.007	0.000	1.893	7.297	4.42	0.000	97.80	25.85	64.85	9.297	100.00
fss10.78	5	64.08	0.044	18.82	0.062	0.191	0.000	0.000	0.605	6.757	6.55	0.000	97.10	37.80	59.27	2.932	100.00

fss10.79	5	63.51	0.072	19.88	0.000	0.253	0.037	0.000	1.246	6.956	5.587	0.000	97.54	32.47	61.45	6.082	100.00
fss10.82	5	62.46	0.096	19.04	0.019	0.212	0.000	0.000	1.226	6.304	5.796	0.000	95.16	35.33	58.40	6.276	100.00
fss10.83	5	64.22	0.000	18.89	0.017	0.249	0.000	0.000	0.699	6.592	6.719	0.000	97.38	38.78	57.83	3.389	100.00
fss10.84	5	65.40	0.000	18.81	0.000	0.195	0.000	0.000	0.484	6.317	6.679	0.007	97.89	40.03	57.54	2.436	100.00
fss11.88	5	65.70	0.000	19.13	0.000	0.134	0.014	0.000	0.437	6.684	7.28	0.000	99.37	40.89	57.05	2.061	100.00
fss11.89	5	64.60	0.000	19.04	0.012	0.203	0.000	0.000	0.354	6.499	7.538	0.009	98.25	42.56	55.76	1.679	100.00
fss11.93	5	56.94	0.082	22.70	0.000	1.720	0.184	0.010	0.172	9.345	6.393	0.000	97.55	30.82	68.48	0.696	100.00
fss11.98	5	62.85	0.080	18.87	0.000	0.280	0.000	0.000	0.903	7.867	4.343	0.016	95.21	25.46	70.09	4.446	100.00
fss11.99	5	62.38	0.266	22.50	0.000	2.139	0.208	0.135	0.689	9.06	5.749	0.009	103.13	28.61	68.51	2.879	100.00
fss14.103	7	65.60	0.045	18.90	0.008	0.332	0.000	0.000	0.340	7.254	6.533	0.000	99.01	36.61	61.79	1.600	100.00
fss14.104	7	65.12	0.109	20.17	0.000	0.286	0.000	0.000	1.265	7.772	4.728	0.000	99.45	26.86	67.10	6.036	100.00
fss14.110	7	65.57	0.082	18.93	0.006	0.236	0.001	0.000	0.429	7.049	6.622	0.066	98.99	37.42	60.54	2.036	100.00
fss15.23	7	65.63	0.051	19.94	0.017	0.287	0.023	0.000	1.181	7.7	5.141	0.019	99.98	28.82	65.61	5.561	100.00
fss15.24	7	62.79	0.056	19.31	0.000	0.292	0.000	0.000	1.246	7.316	5.037	0.000	96.05	29.28	64.64	6.083	100.00
fss15.25	7	62.79	0.055	19.94	0.039	0.299	0.007	0.000	1.767	7.854	3.978	0.050	96.78	22.86	68.61	8.529	100.00
fss15.26	7	63.90	0.067	19.95	0.008	0.362	0.000	0.000	1.412	7.643	4.602	0.000	97.94	26.44	66.74	6.814	100.00
fss15.27	7	65.26	0.087	19.94	0.006	0.232	0.023	0.000	1.196	7.821	4.916	0.019	99.49	27.61	66.75	5.641	100.00
fss15.28	7	64.84	0.117	19.83	0.054	0.292	0.000	0.000	1.148	7.552	5.109	0.000	98.94	29.11	65.40	5.493	100.00
fss15.29	7	64.15	0.140	19.37	0.008	0.310	0.001	0.000	1.197	7.153	4.632	0.018	96.98	28.06	65.85	6.090	100.00
fss15.34	7	65.24	0.037	19.87	0.000	0.332	0.023	0.000	1.034	7.59	5.211	0.055	99.38	29.58	65.49	4.930	100.00
fss15.35	7	65.63	0.073	19.75	0.000	0.281	0.000	0.000	0.956	7.682	5.391	0.000	99.77	30.17	65.34	4.493	100.00
fss15.36	7	63.45	0.131	19.95	0.000	0.364	0.017	0.000	1.642	7.589	4.272	0.000	97.42	24.86	67.12	8.025	100.00
fss15.37	7	65.48	0.105	19.70	0.012	0.315	0.080	0.000	1.027	7.812	5.383	0.000	99.91	29.71	65.53	4.761	100.00
fss15.39	7	65.04	0.085	19.95	0.000	0.308	0.000	0.000	1.128	7.768	5.106	0.000	99.39	28.59	66.11	5.305	100.00
fss15.40	7	64.51	0.069	19.82	0.000	0.275	0.000	0.000	1.290	7.575	4.647	0.022	98.21	26.95	66.77	6.283	100.00
fss15.41	7	64.79	0.123	19.81	0.000	0.286	0.020	0.000	1.205	7.642	5.038	0.015	98.92	28.52	65.75	5.729	100.00
fss15.42	7	64.98	0.082	20.06	0.000	0.262	0.023	0.000	1.463	7.125	4.046	0.039	98.08	25.13	67.24	7.630	100.00
dist1.43	1	64.26	0.327	22.53	0.000	2.454	0.243	0.202	0.586	8.255	6.282	0.006	105.15	32.52	64.94	2.547	100.00
dist1.46	1	64.81	0.418	22.59	0.008	2.299	0.226	0.123	0.701	8.269	6.008	0.000	105.45	31.35	65.58	3.072	100.00
dist3.58	1	61.97	0.533	20.55	0.000	2.672	0.230	0.470	1.102	5.317	5.715	0.012	98.57	38.82	54.89	6.287	100.00
dist10.1	7	63.00	0.043	20.04	0.021	0.309	0.004	0.000	1.342	6.879	5.451	0.037	97.12	32.00	61.38	6.617	100.00
dist10.2	7	65.66	0.000	19.66	0.014	0.261	0.006	0.000	0.769	7.409	5.93	0.000	99.71	33.25	63.13	3.621	100.00
dist10.3	7	64.07	0.000	19.10	0.000	0.241	0.000	0.000	0.873	6.719	6.012	0.018	97.03	35.45	60.22	4.324	100.00
dist10.4	7	64.75	0.043	20.06	0.006	0.257	0.007	0.000	1.279	7.171	5.54	0.004	99.11	31.63	62.23	6.134	100.00
dist10.5	7	65.72	0.045	19.37	0.000	0.210	0.000	0.000	0.502	6.663	7.178	0.000	99.68	40.49	57.13	2.378	100.00
dist10.6	7	65.58	0.030	19.21	0.010	0.223	0.010	0.000	0.546	6.701	7.118	0.000	99.44	40.08	57.34	2.582	100.00

dist10.7	7	65.42	0.000	19.35	0.000	0.270	0.000	0.000	0.683	7.093	6.24	0.020	99.08	35.47	61.27	3.260	100.00
dist10.8	7	64.58	0.046	18.93	0.008	0.191	0.003	0.000	0.355	6.29	7.519	0.000	97.92	43.27	55.01	1.716	100.00
dist10.9	7	65.62	0.025	18.99	0.000	0.232	0.013	0.000	0.385	6.517	7.446	0.027	99.26	42.13	56.04	1.829	100.00
dist10.11	7	63.36	0.696	20.19	0.006	2.616	0.139	0.449	1.568	7.068	5.728	0.000	101.83	32.20	60.39	7.404	100.00
dist10.12	7	66.24	0.052	19.91	0.025	0.241	0.038	0.000	0.866	6.883	6.352	0.017	100.62	36.21	59.64	4.147	100.00
dist10.13	7	62.49	0.103	21.05	0.008	0.295	0.000	0.000	2.306	7.577	3.597	0.019	97.45	21.10	67.54	11.359	100.00
dist10.15	7	63.53	0.020	20.71	0.000	0.261	0.036	0.000	2.202	7.487	4.073	0.000	98.31	23.54	65.77	10.689	100.00
dist12.80	8	66.13	0.012	19.69	0.029	0.210	0.000	0.000	0.753	6.828	6.591	0.000	100.24	37.45	58.96	3.593	100.00
dist12.82	8	65.87	0.081	19.27	0.006	0.261	0.043	0.000	0.534	6.646	7.442	0.000	100.15	41.36	56.14	2.493	100.00
dist12.86	8	64.96	0.059	19.50	0.008	0.265	0.020	0.000	0.928	6.552	7.138	0.000	99.43	39.93	55.71	4.360	100.00
dist12.87	8	66.42	0.000	19.35	0.000	0.200	0.000	0.000	0.385	6.32	7.996	0.017	100.68	44.61	53.59	1.804	100.00
dist12.89	8	65.37	0.102	19.67	0.000	0.247	0.000	0.000	0.727	6.716	6.966	0.000	99.79	39.17	57.40	3.433	100.00
dist12.91	8	65.24	0.015	19.40	0.000	0.256	0.011	0.000	0.732	7.073	6.603	0.007	99.33	36.75	59.83	3.422	100.00
dist12.92	8	66.19	0.000	19.37	0.000	0.212	0.001	0.000	0.488	6.841	7.107	0.007	100.22	39.67	58.04	2.288	100.00
dist12.93	8	66.70	0.000	19.31	0.000	0.180	0.027	0.000	0.727	6.659	7.241	0.014	100.87	40.29	56.31	3.397	100.00
dist12.94	8	65.41	0.011	19.20	0.002	0.220	0.000	0.000	0.395	6.356	7.778	0.000	99.37	43.77	54.36	1.867	100.00
dist12.96	8	60.62	0.151	21.06	0.008	0.232	0.000	0.014	2.466	6.558	2.991	0.000	94.10	19.90	66.32	13.780	100.00
dist13.96	8	60.62	0.151	21.06	0.008	0.232	0.000	0.014	2.466	6.558	2.991	0.000	94.10	19.90	66.32	13.780	100.00
dist13.108	8	63.69	0.101	20.01	0.035	0.323	0.000	0.000	1.403	6.891	5.098	0.008	97.57	30.44	62.53	7.035	100.00

Table A6

	Major Elements (wt%)											
	SiO_2	TiO_2	Al_2O_3	Cr_2O_3	FeO	MnO	MgO	CaO	Na_2O	K_2O	NiO	Total
Sieved 100-300µm												
ex2.110	39.70	5.992	12.50	0.004	11.20	0.234	12.31	11.77	2.883	0.991	0.000	97.58
ex2.111	38.87	6.737	13.01	0.000	9.36	0.170	12.82	12.21	2.672	0.860	0.000	96.70
ex2.118	39.85	6.250	12.17	0.000	11.29	0.241	12.54	11.77	2.831	1.013	0.014	97.97
ex2.120	39.34	6.096	12.67	0.013	11.61	0.237	12.14	11.79	2.857	0.987	0.016	97.75
ex2.121	39.23	6.530	13.25	0.002	10.60	0.178	13.09	12.04	2.710	0.855	0.000	98.49
ex2.122	39.71	6.495	12.81	0.026	10.24	0.230	12.74	11.94	2.731	0.863	0.000	97.79
fss2.22	38.85	6.384	13.57	0.039	12.22	0.283	11.90	11.66	2.870	0.982	0.000	98.76
fss5.97	39.24	6.063	12.77	0.009	11.47	0.252	11.87	11.77	2.766	0.931	0.005	97.14
fss5.103	38.96	6.616	13.16	0.000	9.71	0.114	12.93	12.14	2.581	0.928	0.000	97.14
fss5.107	39.06	6.186	12.60	0.015	10.70	0.196	12.49	11.82	2.760	1.006	0.047	96.89
fss10.46	39.13	6.493	13.68	0.000	10.10	0.116	13.00	12.17	2.655	0.989	0.000	98.32
fss10.56	38.74	5.519	11.51	0.000	12.33	0.377	11.22	11.46	2.629	1.118	0.000	94.90
fss10.59	37.94	7.038	13.83	0.000	10.36	0.161	12.21	12.04	2.664	0.990	0.000	97.23
fss11.34	40.66	5.253	10.97	0.026	12.42	0.464	12.08	11.37	2.902	1.281	0.001	97.41
fss11.39	36.90	7.072	13.11	0.000	10.45	0.148	12.29	11.81	2.502	1.017	0.005	95.31
fss11.44	37.86	6.837	13.63	0.028	10.05	0.161	12.54	12.38	2.607	0.977	0.002	97.08
fss14.65	38.63	5.979	11.72	0.000	11.46	0.387	11.85	11.45	2.761	0.864	0.000	95.10
fss14.67	40.44	6.082	12.33	0.000	10.94	0.225	12.92	11.83	2.953	0.924	0.000	98.65
fss14.70	39.32	6.096	11.88	0.030	10.53	0.281	12.81	11.63	2.966	0.802	0.000	96.35
fss14.74	42.03	5.482	10.70	0.000	10.80	0.509	13.54	11.03	3.161	1.025	0.015	98.29
dist3.66	37.92	6.910	13.19	0.010	10.06	0.135	12.22	12.42	2.592	0.922	0.000	96.37
dist6.85	39.96	5.411	11.36	0.011	12.81	0.475	11.34	11.21	2.877	1.127	0.000	96.57
dist8.21	39.55	5.392	10.88	0.017	12.79	0.496	11.61	11.54	2.953	1.345	0.025	96.60
dist8.24	38.50	6.611	13.18	0.000	10.07	0.141	13.07	12.41	2.711	0.920	0.000	97.62
dist8.29	38.32	6.652	12.80	0.006	11.57	0.230	11.82	11.99	2.825	0.993	0.000	97.21
dist8.37	38.77	6.652	13.18	0.000	10.40	0.204	12.59	12.30	2.777	0.906	0.000	97.77
dist8.40	38.74	6.317	12.82	0.045	11.19	0.197	12.37	12.17	2.780	0.940	0.006	97.58
dist10.87	38.75	6.736	13.52	0.000	9.99	0.160	12.76	12.47	2.693	0.903	0.000	97.97
dist10.93	37.19	6.220	12.34	0.019	10.47	0.156	11.23	12.08	2.660	0.939	0.001	93.29
dist10.94	40.12	5.581	14.12	0.000	10.78	0.259	13.00	10.20	3.151	0.787	0.004	98.00
dist10.95	37.52	6.848	13.54	0.000	10.11	0.156	12.41	12.47	2.509	0.945	0.023	96.53
dist10.100	37.34	6.514	13.20	0.000	11.64	0.170	11.10	12.25	2.640	1.085	0.002	95.93
dist10.103	40.17	4.617	12.50	0.000	12.14	0.316	12.93	11.48	2.994	1.185	0.022	98.35
dist12.106	37.37	6.710	13.00	0.000	10.33	0.173	12.14	12.25	2.502	0.898	0.006	95.38
dist12.107	38.75	6.327	12.14	0.006	11.67	0.257	11.71	12.03	2.899	0.938	0.001	96.73
dist12.108	39.09	6.188	12.95	0.000	11.24	0.273	12.24	12.15	2.776	1.041	0.000	97.94
dist12.111	39.34	6.065	12.22	0.000	10.79	0.305	12.76	11.97	2.999	0.853	0.000	97.30
dist12.122	38.00	6.709	13.79	0.000	10.02	0.150	12.83	12.45	2.555	0.982	0.006	97.50
dist12.124	37.60	6.721	13.35	0.000	10.03	0.154	12.53	12.34	2.569	0.990	0.000	96.29
dist13.6	38.40	5.831	11.25	0.006	12.31	0.372	11.37	11.58	2.737	1.172	0.000	95.03

Table A7

Major Elements (wt%)

	SiO_2	TiO_2	Al_2O_3	Cr_2O_3	FeO	MnO	MgO	CaO	Na_2O	K_2O	NiO	Total
Handpicked												
ex2.18	39.62	6.424	12.40	0.000	10.47	0.183	12.93	11.74	2.812	0.830	0.000	97.40
fss5.52	38.61	6.825	13.18	0.000	9.41	0.171	12.94	12.15	2.617	0.905	0.000	96.81
fss5.56	38.49	6.501	13.09	0.041	10.15	0.192	12.58	12.13	2.767	0.903	0.012	96.85
fss10.80	37.89	6.556	13.29	0.013	9.91	0.075	12.48	11.97	2.471	0.936	0.000	95.59
fss10.86	37.15	6.898	13.31	0.000	8.57	0.141	12.66	12.40	2.399	0.928	0.026	94.49
fss11.87	39.02	6.813	13.05	0.006	9.31	0.135	13.13	12.22	2.755	0.848	0.000	97.28
fss14.105	39.42	6.498	12.73	0.019	10.30	0.156	13.07	11.86	2.941	0.839	0.001	97.84
fss14.108	39.80	6.744	12.79	0.026	9.40	0.207	13.53	11.96	2.678	0.714	0.000	97.85
fss14.109	37.81	6.923	13.53	0.015	8.93	0.106	13.22	12.42	2.418	0.922	0.001	96.30
fss14.111	37.89	6.450	12.95	0.000	10.06	0.193	12.25	11.99	2.659	0.899	0.019	95.36
fss14.112	37.83	6.545	12.43	0.000	9.61	0.166	12.35	11.99	2.560	0.920	0.000	94.39
fss14.113	40.91	6.096	11.28	0.009	10.83	0.377	13.39	11.18	3.265	0.869	0.017	98.22
dist3.60	38.72	6.216	11.17	0.021	9.72	0.168	11.78	15.08	1.822	0.561	0.001	95.25
dist6.68	39.70	5.660	11.70	0.026	11.97	0.374	11.63	11.58	2.951	1.234	0.013	96.84
dist6.74	42.52	5.242	15.57	0.000	8.59	0.141	9.00	10.30	3.920	1.805	0.000	97.08
dist8.70	39.20	6.446	13.15	0.004	10.27	0.130	12.93	11.90	2.727	0.927	0.043	97.72
dist12.77	38.37	6.206	12.16	0.000	11.16	0.218	12.03	11.89	2.753	0.928	0.040	95.76
dist12.78	39.52	6.275	13.14	0.000	10.65	0.214	12.81	12.20	2.849	0.970	0.000	98.63
dist12.79	38.57	6.788	13.37	0.023	9.90	0.137	13.01	12.18	2.619	0.950	0.021	97.55
dist12.83	38.19	6.479	13.50	0.000	9.00	0.121	12.72	12.28	2.541	0.957	0.028	95.81
dist12.85	38.90	6.732	13.66	0.000	9.76	0.115	13.27	12.21	2.653	0.965	0.000	98.25
dist12.90	39.24	6.627	13.44	0.011	10.04	0.137	13.05	12.08	2.749	0.872	0.023	98.26
dist13.102	37.57	6.467	12.24	0.000	8.46	0.149	12.54	11.98	2.555	0.806	0.000	92.77
dist13.104	38.70	6.753	13.34	0.000	9.08	0.117	13.13	12.42	2.639	0.898	0.024	97.11
dist13.110	38.10	6.049	12.72	0.000	10.95	0.232	12.05	12.24	2.680	1.059	0.000	96.09

Table A8

Major Elements (wt%)

	SiO_2	TiO_2	Al_2O_3	Cr_2O_3	FeO	MnO	MgO	CaO	Na_2O	K_2O	NiO	Total
Sieved 100-300µm												
ex3.10	35.72	5.083	13.22	0.000	16.84	0.828	12.73	0.127	0.762	8.619	0.000	93.94
fss2.27	36.14	5.710	12.69	0.017	14.20	0.731	12.86	1.998	0.911	8.248	0.004	93.51
fss14.62	37.72	7.177	13.03	0.000	11.20	0.328	16.03	0.042	1.169	8.516	0.036	95.24
fss14.69	37.47	7.651	13.13	0.000	11.32	0.358	15.53	0.109	1.095	8.492	0.000	95.16
fss14.73	35.86	6.962	12.35	0.000	13.02	0.583	14.20	0.074	0.815	8.380	0.000	92.24
fss15.76	35.87	7.455	12.63	0.000	11.38	0.349	15.28	0.021	0.994	8.869	0.031	92.89
fss15.87	36.37	7.988	14.17	0.000	11.52	0.388	14.33	0.070	1.058	7.983	0.000	93.88
fss15.90	36.78	7.635	12.78	0.043	11.27	0.364	15.35	0.132	0.944	8.466	0.000	93.77
dist10.88	36.96	6.825	13.90	0.006	13.39	0.402	14.48	0.122	0.849	8.431	0.014	95.37
Handpicked												
fss2.37	36.19	6.853	13.80	0.002	12.96	0.373	14.24	0.016	1.033	8.763	0.000	94.22
fss2.40	36.66	6.806	13.78	0.011	13.14	0.346	14.61	0.000	0.981	8.836	0.000	95.18
fss15.30	38.26	7.139	13.45	0.015	11.34	0.294	16.29	0.065	1.072	8.166	0.015	96.10
fss15.32	36.86	7.450	12.98	0.000	11.41	0.400	15.66	0.011	1.218	8.838	0.061	94.89
fss15.33	36.28	7.344	13.61	0.004	11.50	0.399	14.58	0.152	0.908	7.671	0.000	92.44
fss15.38	36.52	6.583	12.53	0.009	11.62	0.380	15.71	0.059	0.981	8.248	0.020	92.65
dist1.52	43.67	0.109	25.33	0.000	12.84	0.093	7.62	0.283	0.864	5.158	0.032	96.00
dist12.88	36.69	6.068	13.37	0.033	16.22	0.727	13.24	0.114	0.826	8.765	0.017	96.07

Table A9

	Major Elements (wt%)												Na-K-Ca (cation %)				
	SiO_2	TiO_2	Al_2O_3	Cr_2O_3	FeO	MnO	MgO	CaO	Na_2O	K_2O	NiO	Total	Na	K	Ca	total	**Mineral**
Sieved 100-300µm																	
fss11.33	40.40	0.000	31.28	0.000	0.237	0.040	0.006	5.085	16.02	2.089	0.000	95.16	79.29	6.80	13.91	100.00	Nosean
dist3.60	40.79	0.000	32.27	0.022	0.288	0.010	0.000	5.245	18.56	0.953	0.000	98.14	84.04	2.84	13.12	100.00	Nosean
dist3.61	38.56	0.000	30.36	0.000	0.312	0.000	0.000	5.466	15.15	1.092	0.019	90.95	80.20	3.81	15.99	100.00	Nosean
dist3.64	36.78	0.000	29.27	0.000	0.281	0.000	0.000	6.452	14.92	1.049	0.000	88.74	77.80	3.60	18.60	100.00	Nosean
dist3.67	39.71	0.000	31.77	0.004	0.239	0.007	0.000	5.397	16.47	1.056	0.003	94.66	81.75	3.45	14.80	100.00	Nosean
dist8.23	39.33	0.037	31.61	0.015	0.257	0.028	0.000	5.258	19.07	0.493	0.000	96.10	85.51	1.46	13.03	100.00	Nosean
dist13.7	37.98	0.053	30.16	0.000	0.307	0.000	0.000	7.016	16.41	1.216	0.000	93.14	77.82	3.80	18.38	100.00	Nosean
Handpicked																	
ex2.34pc	41.22	0.000	32.53	0.033	0.191	0.037	0.000	3.540	18.60	0.711	0.000	96.86	88.47	2.22	9.31	100.00	Nosean
fss5.49pc	37.61	0.104	28.14	0.000	0.578	0.009	0.260	10.315	13.76	1.053	0.000	91.81	68.27	3.44	28.29	100.00	Haüyne
dist13.105	35.47	0.000	28.84	0.000	0.279	0.034	0.182	11.203	14.12	0.810	0.000	90.93	67.74	2.56	29.70	100.00	Haüyne

Table A10

	Major Elements (wt%)											
	SiO_2	TiO_2	Al_2O_3	Cr_2O_3	FeO	MnO	MgO	CaO	Na_2O	K_2O	NiO	Total
Sieved 100-300µm												
fss2.28 (high)	38.73	0.046	0.036	0.015	17.48	0.226	42.36	0.338	0.034	0.000	0.145	99.41
Handpicked												
ex2.19	38.72	0.025	0.009	0.064	16.88	0.248	42.34	0.281	0.047	0.000	0.156	98.77
ex2.21	39.11	0.000	0.000	0.000	17.69	0.248	42.90	0.265	0.000	0.000	0.132	100.34

Table A11

	Major Elements (wt%)												Or-Ab-An (cation %)			
	SiO_2	TiO_2	Al_2O_3	Cr_2O_3	FeO	MnO	MgO	CaO	Na_2O	K_2O	NiO	Total	Or	Ab	An	total
Sieved 100-300µm																
ex2.109	45.87	0.000	33.55	0.000	0.508	0.046	0.046	17.14	1.57	0.055	0.000	98.79	0.33	14.20	85.47	100.00
fss2.17	55.36	0.104	26.26	0.014	0.540	0.014	0.047	8.84	6.03	0.538	0.002	97.76	3.14	53.52	43.34	100.00
fss2.20	57.71	0.123	25.06	0.052	0.411	0.000	0.024	6.86	6.64	0.866	0.000	97.74	5.18	60.36	34.46	100.00
fss5.91	56.90	0.080	26.13	0.000	0.488	0.006	0.021	8.19	6.36	0.604	0.027	98.81	3.52	56.39	40.09	100.00
fss5.93	52.69	0.109	29.10	0.000	0.504	0.003	0.058	11.57	4.55	0.276	0.009	98.87	1.63	40.91	57.45	100.00
fss5.96	55.37	0.080	27.47	0.000	0.516	0.004	0.023	9.77	5.72	0.398	0.000	99.35	2.30	50.26	47.44	100.00
fss5.102	56.95	0.040	26.20	0.027	0.499	0.014	0.061	8.04	6.41	0.606	0.044	98.89	3.54	56.98	39.47	100.00
fss5.105	52.49	0.148	29.19	0.004	0.609	0.011	0.044	11.85	4.46	0.249	0.000	99.05	1.47	39.91	58.62	100.00
fss10.47	58.34	0.172	24.90	0.000	0.833	0.004	0.096	6.75	6.72	1.226	0.000	99.04	7.17	59.69	33.14	100.00
fss11.40	58.15	0.130	24.32	0.006	0.421	0.013	0.000	6.31	6.93	0.982	0.000	97.25	5.84	62.65	31.51	100.00
fss14.63	54.12	0.150	27.93	0.000	0.522	0.000	0.064	10.43	5.15	0.653	0.000	99.01	3.79	45.42	50.80	100.00
fss14.68	54.75	0.083	27.00	0.000	0.543	0.000	0.038	9.71	5.58	0.335	0.000	98.04	1.98	49.97	48.05	100.00
dist3.68	52.12	0.152	26.89	0.020	0.586	0.004	0.024	10.82	4.72	0.379	0.000	95.71	2.28	43.11	54.62	100.00
dist6.77	55.47	0.073	26.18	0.000	0.464	0.000	0.099	8.67	6.24	0.546	0.000	97.74	3.15	54.79	42.06	100.00
dist8.25	57.01	1.570	21.05	0.000	3.080	0.192	0.097	4.93	7.99	3.828	0.012	99.76	19.03	60.39	20.58	100.00
dist8.39	55.40	0.051	26.88	0.000	0.502	0.011	0.041	9.27	6.10	0.520	0.000	98.77	2.96	52.77	44.28	100.00
dist10.89	51.31	0.121	27.75	0.000	0.604	0.026	0.022	11.43	4.64	0.429	0.017	96.35	2.51	41.29	56.20	100.00
dist10.97	56.40	0.125	25.70	0.000	0.387	0.000	0.013	8.01	6.52	0.644	0.000	97.79	3.73	57.34	38.93	100.00
dist10.101	53.45	0.131	26.95	0.010	0.657	0.009	0.059	10.15	5.39	0.450	0.019	97.27	2.62	47.71	49.67	100.00
dist12.112	52.24	0.083	28.99	0.002	0.463	0.000	0.054	11.96	4.47	0.304	0.000	98.57	1.77	39.64	58.59	100.00
dist12.116	51.89	0.239	27.55	0.026	0.855	0.000	0.034	10.63	4.92	0.335	0.000	96.48	2.00	44.68	53.32	100.00
dist13.10	53.27	0.077	28.71	0.000	0.432	0.032	0.030	11.14	4.93	0.351	0.000	98.98	2.04	43.56	54.40	100.00
dist13.12	55.72	0.090	26.83	0.000	0.483	0.031	0.051	8.87	6.06	0.500	0.000	98.62	2.91	53.67	43.41	100.00

Table A12

	Major Elements (wt%)												Or-Ab-An (cation %)			
	SiO_2	TiO_2	Al_2O_3	Cr_2O_3	FeO	MnO	MgO	CaO	Na_2O	K_2O	NiO	Total	Or	Ab	An	total
Handpicked																
ex2.32	61.17	0.162	20.53	0.004	0.347	0.011	0.000	2.43	7.45	3.725	0.000	95.82	21.80	66.25	11.95	100.00
fss2.43	59.66	0.077	23.72	0.000	0.363	0.000	0.000	5.65	7.24	1.245	0.009	97.96	7.33	64.74	27.93	100.00
fss2.45	55.02	0.044	26.88	0.015	0.489	0.000	0.028	9.23	5.85	0.462	0.000	98.01	2.70	51.95	45.35	100.00
fss2.42	50.39	0.722	21.40	0.000	1.713	0.415	0.038	1.03	12.33	4.380	0.000	92.42	18.26	78.14	3.61	100.00
fss5.53	57.39	0.071	22.84	0.010	0.328	0.020	0.019	5.57	7.05	1.249	0.013	94.57	7.51	64.38	28.11	100.00
fss5.55	52.28	0.047	29.67	0.006	0.474	0.000	0.069	12.22	4.34	0.243	0.013	99.36	1.42	38.54	60.04	100.00
fss5.58	55.34	0.120	26.25	0.000	0.569	0.001	0.055	8.79	6.01	0.559	0.000	97.69	3.27	53.49	43.23	100.00
fss5.59	51.73	0.134	28.68	0.012	0.431	0.014	0.061	11.69	4.49	0.279	0.000	97.53	1.65	40.36	57.99	100.00
fss5.60	59.51	0.089	23.48	0.000	0.354	0.017	0.020	5.18	7.28	1.321	0.000	97.25	7.89	66.09	26.02	100.00
fss10.85	59.52	0.077	26.04	0.000	0.310	0.006	0.000	6.98	7.30	0.812	0.000	101.05	4.57	62.44	32.99	100.00
fss14.107	55.72	0.098	27.09	0.000	0.487	0.000	0.040	9.03	6.01	0.358	0.051	98.89	2.10	53.47	44.43	100.00
dist1.44	53.64	0.168	27.06	0.000	0.435	0.000	0.070	10.08	5.50	0.383	0.000	97.33	2.23	48.55	49.22	100.00
dist1.48	54.68	0.105	29.31	0.000	0.577	0.000	0.016	11.56	5.09	0.322	0.021	101.68	1.81	43.56	54.63	100.00
dist3.63	50.64	0.104	29.05	0.000	0.704	0.021	0.221	10.62	5.00	0.563	0.000	96.92	3.30	44.47	52.23	100.00
dist6.73	53.86	0.077	28.40	0.029	0.439	0.000	0.032	10.76	5.18	0.392	0.007	99.17	2.26	45.52	52.21	100.00
dist8.63	51.39	0.099	27.18	0.000	0.422	0.000	0.031	10.71	4.86	0.349	0.000	95.04	2.08	44.13	53.79	100.00
dist8.64	51.14	0.187	29.44	0.000	0.826	0.001	0.145	12.27	4.46	0.612	0.000	99.08	3.46	38.27	58.27	100.00
dist8.65	51.32	0.013	29.43	0.012	0.561	0.006	0.041	12.38	4.14	0.241	0.000	98.14	1.42	37.15	61.43	100.00
dist8.71	48.07	0.041	30.37	0.002	0.515	0.000	0.054	13.91	3.13	0.130	0.000	96.23	0.78	28.74	70.48	100.00
dist8.73	48.51	0.103	32.01	0.012	0.528	0.000	0.037	15.07	2.67	0.136	0.010	99.09	0.81	24.07	75.12	100.00
dist8.75	53.63	0.102	28.09	0.021	0.548	0.000	0.081	10.71	4.95	0.332	0.006	98.46	1.97	44.65	53.38	100.00
dist13.99	51.66	0.044	26.35	0.023	0.432	0.000	0.022	10.21	4.85	0.337	0.000	93.92	2.07	45.26	52.67	100.00
dist13.111	53.00	0.089	28.81	0.000	0.522	0.000	0.053	11.16	5.02	0.352	0.004	99.01	2.03	43.94	54.04	100.00
dist13.112	51.26	0.126	29.63	0.000	0.557	0.028	0.032	12.24	4.21	0.214	0.000	98.29	1.27	37.90	60.83	100.00

Table A13

	Major Elements (wt%)											
	SiO_2	TiO_2	Al_2O_3	Cr_2O_3	FeO	MnO	MgO	CaO	Na_2O	K_2O	NiO	Total
Sieved 100-300µm												
ex2.112	47.17	2.358	5.501	0.000	7.275	0.228	12.49	22.71	0.739	0.013	0.000	98.49
ex2.113	47.93	2.255	5.024	0.015	7.211	0.229	12.92	22.77	0.783	0.000	0.005	99.15
ex2.114	47.12	2.501	5.559	0.000	6.838	0.195	12.89	22.66	0.716	0.017	0.007	98.50
ex2.116	48.67	2.073	4.590	0.000	7.704	0.327	12.80	22.66	0.770	0.006	0.005	99.60
ex2.119	50.45	1.256	2.878	0.000	7.500	0.357	13.51	22.68	0.775	0.000	0.000	99.40
ex2.123	49.50	1.153	2.549	0.031	7.217	0.398	13.07	22.25	0.973	0.029	0.000	97.17
ex2.124	44.48	3.325	8.180	0.000	6.985	0.075	12.19	22.42	0.542	0.029	0.024	98.25
ex2.125	49.75	0.911	2.070	0.000	7.979	0.603	12.52	21.79	1.158	0.000	0.002	96.79
ex2.126	49.11	1.951	4.553	0.015	7.516	0.348	12.96	22.23	0.882	0.015	0.000	99.57
ex3.5	49.71	0.973	2.245	0.017	10.430	0.903	10.97	21.95	1.658	0.011	0.016	98.88
ex3.6	50.48	1.043	2.400	0.000	10.373	0.952	11.29	21.72	1.646	0.007	0.000	99.90
ex3.11	49.39	0.905	2.274	0.015	9.971	0.767	11.56	21.68	1.570	0.000	0.013	98.14
ex3.16	48.81	1.956	3.659	0.006	10.294	0.772	11.25	21.73	1.455	0.010	0.000	99.94
ex3.20	51.23	0.614	1.486	0.000	8.575	0.827	12.45	22.62	1.274	0.002	0.020	99.11
fss2.30	47.33	1.674	4.961	0.000	8.873	0.495	11.34	22.49	0.820	0.014	0.000	97.99
fss5.100	49.27	1.886	4.266	0.000	7.488	0.241	13.12	22.77	0.662	0.002	0.000	99.70
fss10.49	48.47	2.118	4.852	0.000	7.631	0.209	13.27	21.97	0.633	0.000	0.000	99.16
fss10.53	51.05	0.740	2.499	0.000	11.829	1.073	10.06	20.40	1.932	0.000	0.021	99.60
fss10.57	49.48	1.648	3.663	0.010	7.929	0.450	12.38	22.34	1.018	0.000	0.000	98.91
fss11.37	43.53	3.562	7.941	0.000	7.156	0.111	11.93	22.58	0.493	0.049	0.000	97.35
fss15.79	51.62	0.673	1.033	0.000	8.518	1.017	12.70	21.63	1.498	0.000	0.059	98.75
fss15.82	52.19	0.985	1.624	0.027	8.280	0.815	12.80	21.46	1.561	0.009	0.000	99.75
dist3.63	49.35	0.499	1.375	0.035	10.029	1.122	10.56	22.23	1.551	0.005	0.021	96.77
dist6.81	45.70	2.791	6.482	0.002	6.947	0.151	12.76	22.91	0.577	0.006	0.000	98.33
dist8.34	45.45	3.399	6.652	0.000	8.839	0.284	12.53	22.11	0.614	0.020	0.054	99.95
dist10.96	46.06	2.242	4.529	0.012	6.489	0.188	12.72	23.09	0.471	0.013	0.000	95.82
dist10.105	46.95	1.970	4.535	0.000	8.266	0.461	11.75	22.55	0.801	0.015	0.035	97.34
dist12.109	48.70	1.102	2.383	0.000	7.508	0.469	12.67	22.17	1.404	0.245	0.000	96.65
dist12.121	48.38	2.159	4.794	0.000	7.443	0.315	13.12	22.66	0.775	0.016	0.000	99.67
dist13.1	45.72	3.109	7.198	0.000	6.874	0.143	12.71	22.64	0.737	0.063	0.001	99.20
dist13.3	45.30	2.652	5.689	0.000	7.350	0.250	11.03	22.57	0.729	0.027	0.037	95.63
dist13.9	45.42	3.224	7.903	0.010	6.764	0.156	12.75	22.73	0.536	0.019	0.029	99.54
dist13.11	45.58	2.404	5.698	0.000	8.054	0.285	11.57	22.49	0.737	0.001	0.009	96.83

Table A14

	Major Elements (wt%)											
	SiO_2	TiO_2	Al_2O_3	Cr_2O_3	FeO	MnO	MgO	CaO	Na_2O	K_2O	NiO	Total
Handpicked												
ex3.1	51.75	0.470	1.494	0.004	10.001	1.010	11.50	21.74	1.554	0.013	0.023	99.56
ex3.6	50.60	0.654	2.079	0.021	10.601	0.901	10.79	22.08	1.674	0.023	0.000	99.42
fss5.48	50.59	1.074	2.438	0.013	8.268	0.609	12.53	22.03	1.135	0.000	0.000	98.68
fss5.50	47.84	2.298	5.573	0.002	6.182	0.104	13.75	22.73	0.400	0.000	0.000	98.89
fss5.54	46.45	2.068	4.645	0.000	8.393	0.438	11.56	22.07	0.936	0.021	0.018	96.59
fss5.57	45.07	3.404	7.557	0.000	7.675	0.213	11.74	21.95	0.662	0.032	0.005	98.31
fss5.61	44.50	3.590	8.263	0.000	6.848	0.126	12.26	22.74	0.490	0.000	0.003	98.82
fss5.62	47.52	2.446	5.793	0.015	7.397	0.308	12.69	22.56	0.857	0.006	0.000	99.58
fss11.90	43.02	4.217	9.196	0.011	6.738	0.133	11.63	22.72	0.491	0.000	0.000	98.15
fss11.91	44.12	3.772	8.307	0.000	6.519	0.114	12.34	22.64	0.546	0.002	0.055	98.42
fss11.92	41.66	4.453	8.747	0.000	6.897	0.138	10.48	22.36	0.514	0.000	0.000	95.25
fss11.94	46.61	3.725	9.094	0.040	6.755	0.095	13.47	22.54	0.543	0.010	0.000	102.88
fss11.95	48.03	2.081	4.440	0.000	8.803	0.458	11.88	22.22	0.893	0.000	0.000	98.82
fss11.96	44.70	3.585	8.208	0.013	6.569	0.104	12.48	22.81	0.519	0.005	0.041	99.04
fss11.100	44.38	3.333	7.504	0.021	6.587	0.156	12.15	22.61	0.577	0.000	0.018	97.33
fss14.101	45.40	3.021	6.411	0.015	6.933	0.186	12.32	22.45	0.556	0.000	0.000	97.30
dist1.49	44.80	4.067	7.498	0.103	8.802	0.164	12.16	21.44	0.664	0.100	0.021	99.82
dist3.55	47.54	2.460	5.551	0.032	6.864	0.134	13.88	22.32	0.499	0.031	0.000	99.31
dist3.57	51.52	0.577	1.797	0.008	9.858	0.933	11.29	21.62	1.767	0.022	0.000	99.40
dist3.61	44.92	3.126	7.993	0.000	7.813	0.157	12.04	22.31	0.736	0.022	0.009	99.13
dist3.64	50.01	1.806	4.393	0.000	6.970	0.271	13.37	22.79	0.734	0.000	0.068	100.42
dist3.67	49.91	1.340	3.225	0.038	7.819	0.577	12.65	22.31	1.117	0.020	0.000	99.00
dist6.69	46.60	2.835	7.327	0.042	7.017	0.111	13.06	22.32	0.539	0.037	0.000	99.89
dist6.71	48.25	2.151	5.142	0.050	5.923	0.119	14.16	22.51	0.369	0.027	0.000	98.71
dist8.66	45.80	2.460	5.545	0.032	7.557	0.306	12.08	21.82	1.455	0.028	0.000	97.08
dist8.68	49.86	1.083	2.553	0.023	7.966	0.579	12.64	22.29	0.909	0.000	0.022	97.93
dist8.72	46.01	2.555	5.804	0.025	6.952	0.202	12.29	21.96	0.776	0.052	0.000	96.63
dist13.100	44.88	3.151	7.604	0.000	6.399	0.106	12.38	22.78	0.555	0.034	0.000	97.89
dist13.106	46.93	2.252	4.935	0.000	8.062	0.307	11.66	22.55	0.863	0.013	0.000	97.57

Table A15

	Major Elements (wt%)											
	SiO_2	TiO_2	Al_2O_3	Cr_2O_3	FeO	MnO	MgO	CaO	Na_2O	K_2O	NiO	Total
Sieved 100-300µm												
ex3.2	29.50	36.09	1.040	0.000	1.767	0.111	0.045	26.97	0.111	0.027	0.000	95.66
ex3.9	29.50	36.70	0.927	0.000	1.567	0.152	0.000	27.06	0.099	0.008	0.042	96.05
ex3.15	28.89	35.49	1.013	0.000	1.770	0.056	0.046	26.71	0.061	0.002	0.000	94.03
fss2.18	28.95	35.31	1.052	0.000	1.864	0.106	0.038	25.58	0.078	0.039	0.047	93.06
fss10.55	29.70	35.68	0.921	0.000	1.717	0.113	0.025	26.49	0.103	0.003	0.015	94.77
fss11.32	28.96	35.79	0.907	0.000	1.683	0.107	0.000	26.48	0.120	0.010	0.009	94.06
fss11.35	29.12	35.64	0.932	0.000	1.540	0.120	0.015	25.82	0.140	0.004	0.000	93.33
dist3.70	28.90	36.22	1.028	0.000	1.784	0.121	0.037	27.10	0.038	0.000	0.004	95.23
dist6.76	28.84	35.94	0.989	0.008	1.564	0.101	0.116	26.70	0.104	0.019	0.000	94.38
dist8.26	28.98	34.91	0.985	0.000	1.983	0.125	0.006	26.92	0.151	0.004	0.000	94.06
dist13.13	28.60	36.62	1.265	0.000	1.570	0.093	0.056	27.03	0.000	0.000	0.000	95.23
Handpicked												
dist10.10	29.15	35.26	0.948	0.000	1.921	0.087	0.000	26.28	0.101	0.000	0.026	93.78

Table A16

	Major Elements (wt%)											
	SiO_2	TiO_2	Al_2O_3	Cr_2O_3	FeO	MnO	MgO	CaO	Na_2O	K_2O	NiO	Total
Sieved 100-300µm												
ex2.115	0.003	12.22	1.344	0.035	69.23	1.952	1.921	0.000	0.011	0.006	0.026	86.75
ex3.18	1.212	24.28	0.404	0.040	64.48	0.151	0.023	0.161	0.096	0.071	0.000	90.92
ex3.19	7.020	26.44	3.312	0.035	50.23	0.301	0.666	0.185	0.152	0.802	0.025	89.17
fss2.21	0.000	9.40	0.975	0.030	80.07	2.596	1.231	0.017	0.063	0.008	0.000	94.38
fss2.25	6.772	0.46	1.263	0.000	62.73	6.835	0.162	0.711	1.095	0.433	0.000	80.46
fss2.29	0.000	10.42	11.639	10.391	52.11	0.425	7.912	0.005	0.000	0.020	0.156	93.07
fss5.101	0.000	15.74	3.605	0.033	67.74	0.902	4.484	0.069	0.000	0.024	0.028	92.62
fss5.104	0.000	15.65	3.994	0.000	67.58	1.071	4.936	0.043	0.043	0.000	0.000	93.31
fss10.51	0.000	11.21	1.339	0.000	78.65	2.147	1.757	0.038	0.070	0.000	0.016	95.22
fss11.38	0.000	9.46	1.022	0.010	79.57	2.637	0.890	0.019	0.000	0.017	0.053	93.67
fss11.42	0.000	13.90	1.979	0.034	74.64	1.808	2.585	0.000	0.000	0.007	0.006	94.96
fss14.64	0.000	13.69	1.723	0.000	73.02	1.785	3.094	0.000	0.036	0.000	0.000	93.35
fss14.66	0.008	15.16	2.890	0.020	68.71	1.061	3.947	0.031	0.000	0.002	0.042	91.87
fss14.72	0.000	14.52	2.456	0.000	67.97	1.499	3.754	0.031	0.000	0.009	0.000	90.23
fss15.83	0.000	13.90	1.441	0.000	70.26	2.067	2.177	0.014	0.014	0.031	0.012	89.92
fss15.86	0.000	13.65	1.510	0.000	70.85	2.068	2.802	0.075	0.057	0.004	0.000	91.01
fss15.89	0.000	13.77	1.664	0.011	68.88	1.891	3.278	0.008	0.108	0.018	0.000	89.63
dist1.41	0.000	9.25	0.917	0.001	76.29	2.645	0.709	0.022	0.000	0.000	0.002	89.84
dist1.43	0.000	9.47	0.828	0.063	77.18	2.608	0.887	0.092	0.059	0.012	0.000	91.20
dist1.46	0.000	9.35	0.720	0.000	79.79	2.724	0.923	0.000	0.041	0.000	0.021	93.56
dist1.48	0.138	10.01	3.723	0.020	73.05	0.304	2.594	0.038	0.057	0.039	0.016	89.99
dist1.52	0.004	9.55	0.856	0.023	76.55	2.670	0.946	0.000	0.089	0.000	0.000	90.69
dist3.59	0.000	9.53	0.878	0.021	78.12	2.728	0.796	0.000	0.038	0.000	0.000	92.11
dist3.65	0.083	12.14	1.533	0.014	73.10	2.471	1.495	0.030	0.000	0.000	0.010	90.88
dist6.71	0.000	9.48	1.014	0.000	79.41	2.615	0.975	0.000	0.000	0.000	0.081	93.57
dist6.74	0.010	13.37	2.232	0.036	74.10	3.004	1.576	0.000	0.067	0.000	0.000	94.39
dist6.75	0.000	9.23	0.949	0.006	79.40	2.722	1.011	0.000	0.000	0.000	0.000	93.32
dist6.78	0.052	15.33	4.105	0.000	69.81	0.953	4.791	0.036	0.000	0.017	0.000	95.09
dist6.83	0.132	11.92	1.717	0.044	74.60	1.903	2.594	0.062	0.076	0.016	0.000	93.06
dist6.84	0.000	12.33	1.558	0.084	75.23	1.890	2.062	0.012	0.075	0.013	0.015	93.26
dist8.32	0.000	17.02	5.946	0.029	65.77	0.579	6.260	0.116	0.000	0.001	0.037	95.76
dist8.35	0.009	9.55	0.938	0.021	80.29	2.014	1.487	0.014	0.063	0.009	0.000	94.39
dist10.86	0.055	16.57	4.709	0.023	63.10	0.524	5.511	0.147	0.000	0.002	0.000	90.64
dist10.91	0.000	14.87	3.172	0.000	71.32	1.132	3.673	0.024	0.085	0.000	0.000	94.28
dist10.92	0.022	11.43	0.927	0.000	72.64	1.932	0.921	0.021	0.007	0.000	0.000	87.91
dist10.98	0.355	12.13	1.477	0.053	73.37	1.832	1.861	0.037	0.030	0.032	0.007	91.18
dist10.102	0.000	12.08	1.772	0.000	75.79	1.922	2.353	0.018	0.011	0.028	0.009	93.98
dist10.104	0.000	12.92	1.839	0.000	75.65	1.684	2.579	0.000	0.045	0.031	0.000	94.75
dist12.113	0.016	16.98	7.653	0.000	63.28	0.401	8.020	0.000	0.000	0.006	0.012	96.36
dist12.117	0.000	9.62	1.146	0.014	78.33	2.245	1.075	0.040	0.178	0.034	0.052	92.73
dist12.118	0.047	17.26	5.204	0.000	66.59	0.606	6.417	0.007	0.052	0.016	0.018	96.22
dist12.120	0.297	14.90	2.467	0.013	72.21	1.303	3.213	0.061	0.070	0.013	0.009	94.56
dist12.123	0.000	15.12	3.673	0.025	72.54	0.910	4.534	0.011	0.002	0.000	0.000	96.82
dist12.125	0.007	16.97	5.568	0.000	66.02	0.695	6.494	0.000	0.013	0.000	0.000	95.76
dist13.2	1.195	14.81	4.022	0.013	65.63	0.890	5.040	1.007	0.101	0.000	0.058	92.77
dist13.5	0.024	15.43	3.161	0.016	72.79	1.140	3.963	0.014	0.000	0.000	0.053	96.59
dist13.14	0.015	15.66	3.500	0.000	68.57	1.010	4.191	0.031	0.054	0.006	0.000	93.03

Table A17

	Major Elements (wt%)											
	SiO_2	TiO_2	Al_2O_3	Cr_2O_3	FeO	MnO	MgO	CaO	Na_2O	K_2O	NiO	Total
Handpicked												
ex2.35	0.000	11.14	1.104	0.000	79.11	2.315	0.658	0.046	0.045	0.000	0.000	94.41
ex2.20	0.000	4.16	16.445	26.072	39.19	0.260	10.062	0.047	0.062	0.031	0.185	96.52
ex2.22	0.000	8.00	13.331	15.616	47.62	0.349	8.773	0.068	0.000	0.014	0.135	93.90
ex3.11	0.000	10.13	1.042	0.000	75.63	2.469	0.832	0.030	0.108	0.087	0.051	90.38
ex3.19	0.006	8.87	1.045	0.000	80.14	2.515	0.863	0.000	0.000	0.000	0.000	93.44
fss5.51	0.000	15.71	3.927	0.038	68.47	0.916	4.868	0.073	0.000	0.000	0.044	94.05
fss10.81	0.000	16.13	4.324	0.002	68.55	0.772	5.517	0.044	0.000	0.009	0.000	95.35
fss11.97	0.014	18.15	5.594	0.000	59.26	0.546	6.477	0.011	0.000	0.000	0.020	90.07
fss14.102	0.019	18.01	6.833	0.000	62.05	0.411	8.066	0.039	0.034	0.000	0.052	95.51
fss14.106	0.000	15.83	4.190	0.036	69.04	0.893	4.935	0.007	0.040	0.014	0.008	95.00
dist1.45	0.257	9.31	1.010	0.000	78.09	2.733	0.761	0.000	0.096	0.003	0.010	92.27
dist1.50	11.508	28.68	3.161	0.152	41.31	0.355	1.346	1.005	0.792	0.990	0.010	89.31
dist3.56	0.527	15.15	4.454	0.000	68.06	1.247	2.744	0.904	0.011	0.128	0.036	93.26
dist3.59	0.067	9.52	1.099	0.009	73.13	1.903	1.707	0.092	0.090	0.028	0.065	87.71
dist3.66	0.035	16.00	3.512	0.041	63.83	0.736	4.046	0.054	0.227	0.035	0.014	88.53
dist6.70	0.001	15.84	7.333	0.093	64.99	0.776	5.164	0.014	0.087	0.000	0.086	94.38
dist10.16	0.000	9.25	1.004	0.031	79.66	2.287	0.953	0.007	0.049	0.028	0.000	93.27
dist12.76	0.003	16.08	4.754	0.000	69.17	0.839	5.177	0.029	0.009	0.011	0.000	96.08
dist12.81	0.000	14.64	3.188	0.000	72.27	1.193	4.223	0.039	0.000	0.000	0.000	95.56
dist12.84	0.003	16.88	4.986	0.002	55.66	0.409	5.432	0.000	0.045	0.000	0.052	83.47
dist13.97	0.017	17.07	7.070	0.027	63.98	0.461	7.477	0.034	0.030	0.000	0.040	96.21
dist13.98	0.016	16.81	6.596	0.000	64.18	0.344	6.859	0.011	0.115	0.000	0.026	94.96
dist13.101	0.286	17.18	7.025	0.031	56.73	0.368	7.021	0.093	0.086	0.015	0.058	88.89
dist13.109	0.000	15.64	3.877	0.000	67.79	0.755	5.141	0.053	0.000	0.003	0.000	93.26

Table A18

	Major Elements (wt%)											
	SiO_2	TiO_2	Al_2O_3	Cr_2O_3	FeO	MnO	MgO	CaO	Na_2O	K_2O	NiO	Total
Sieved 100-300µm												
fss2.26	0.000	46.62	0.357	0.023	45.32	2.737	2.921	0.080	0.023	0.003	0.000	98.08
fss5.92	0.000	47.03	0.533	0.000	43.47	0.829	6.345	0.066	0.042	0.000	0.000	98.32
fss5.95	0.000	47.20	0.430	0.000	43.65	0.955	5.600	0.073	0.012	0.011	0.000	97.93
fss5.99	0.000	47.56	0.459	0.030	44.09	1.122	5.485	0.021	0.000	0.000	0.000	98.77
fss14.75	0.000	47.16	0.269	0.000	44.18	1.694	5.516	0.000	0.000	0.000	0.000	98.82
fss15.78	0.000	47.53	0.197	0.017	41.67	2.406	3.813	0.041	0.000	0.000	0.000	95.68
fss15.81	0.001	47.77	0.124	0.017	41.84	2.477	4.521	0.022	0.000	0.000	0.000	96.78
dist10.90	0.000	47.83	0.551	0.057	42.14	0.582	6.806	0.054	0.000	0.000	0.034	98.05
dist12.110	0.027	47.55	0.489	0.014	41.57	0.745	6.235	0.048	0.041	0.027	0.001	96.75
dist12.115	0.019	45.93	0.409	0.004	45.35	1.262	5.048	0.146	0.000	0.000	0.000	98.17
dist12.119	0.000	46.81	0.229	0.000	44.73	1.551	4.259	0.070	0.040	0.000	0.000	97.69
Handpicked												
dist3.62	0.008	46.35	0.512	0.000	43.00	0.957	4.859	0.265	0.264	0.058	0.019	96.29
dist3.65	0.142	30.82	2.005	0.033	58.09	0.766	1.574	0.074	0.147	0.045	0.013	93.71
dist8.69	0.000	48.01	0.592	0.000	41.96	0.750	6.804	0.055	0.000	0.000	0.000	98.17
dist13.103	0.000	47.85	0.489	0.052	42.27	0.785	6.196	0.044	0.000	0.000	0.000	97.68
dist13.107	0.000	47.62	0.434	0.010	41.43	0.709	6.510	0.113	0.019	0.001	0.000	96.85


That's all Folks!

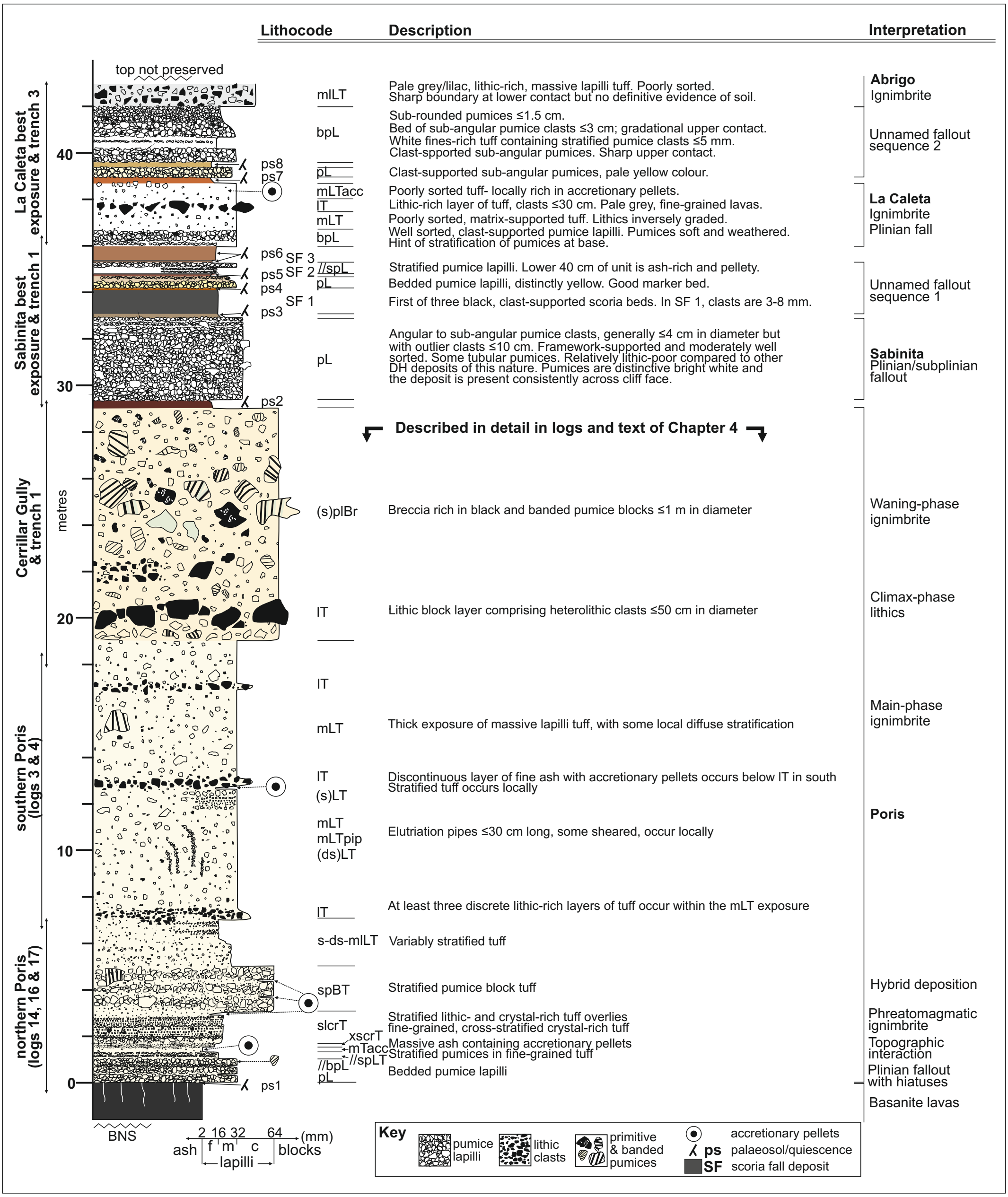

Figure 3.1 (above) General vertical section of the upper Diego Hernandez wall. Text to left of log indicates the outcrop area most representative of that section. Colours used are representative of general outcrop appearance.

Figure 3.2 (i) (overleaf) The upper Diego Hernandez wall. Boxes a, c and d show northern, central and southern exposures of Poris ignimbrite respectively. Trenches were dug to investigate the material above the Poris; trench locations are shown in boxes a and b.
Figure 3.2 (ii) (a) Trench 1. Scoria fallout units SF2 and SF3 are exposed. (b) Trench 2. The upper part of the Poris Formation is separated from the Sabinita by a palaesol (ps2). (c) Trench 3. The second upper fallout sequence occurs beneath thin scree. (d) 'Best exposure' of the Sabinita pumice. (e) 'Best exposure of La Caleta ignimbrite.

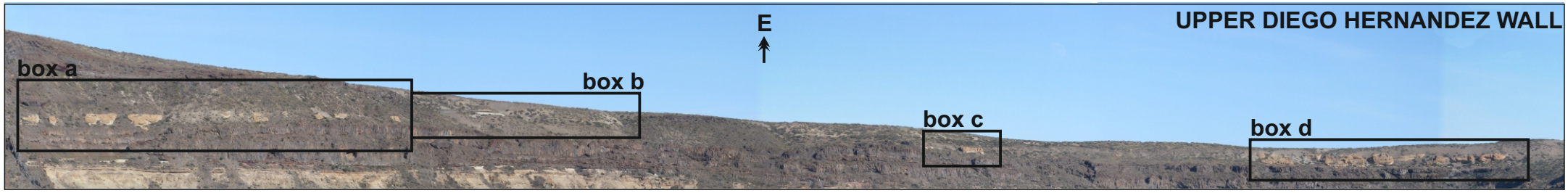
UPPER DIEGO HERNANDEZ WALL
E
box a
box b
box c
box d


box a- northern exposures, trench 1 and La Caleta best exposure
Ca
1
10 m


box b- Sabinita best exposure and trenches 2 & 3
2
Sa
3
10 m

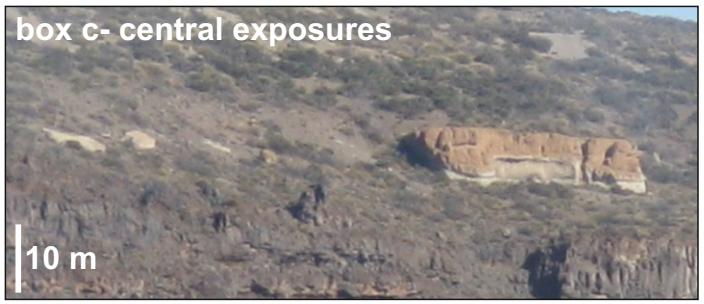
box c- central exposures
10 m


box d- southern exposures
10 m

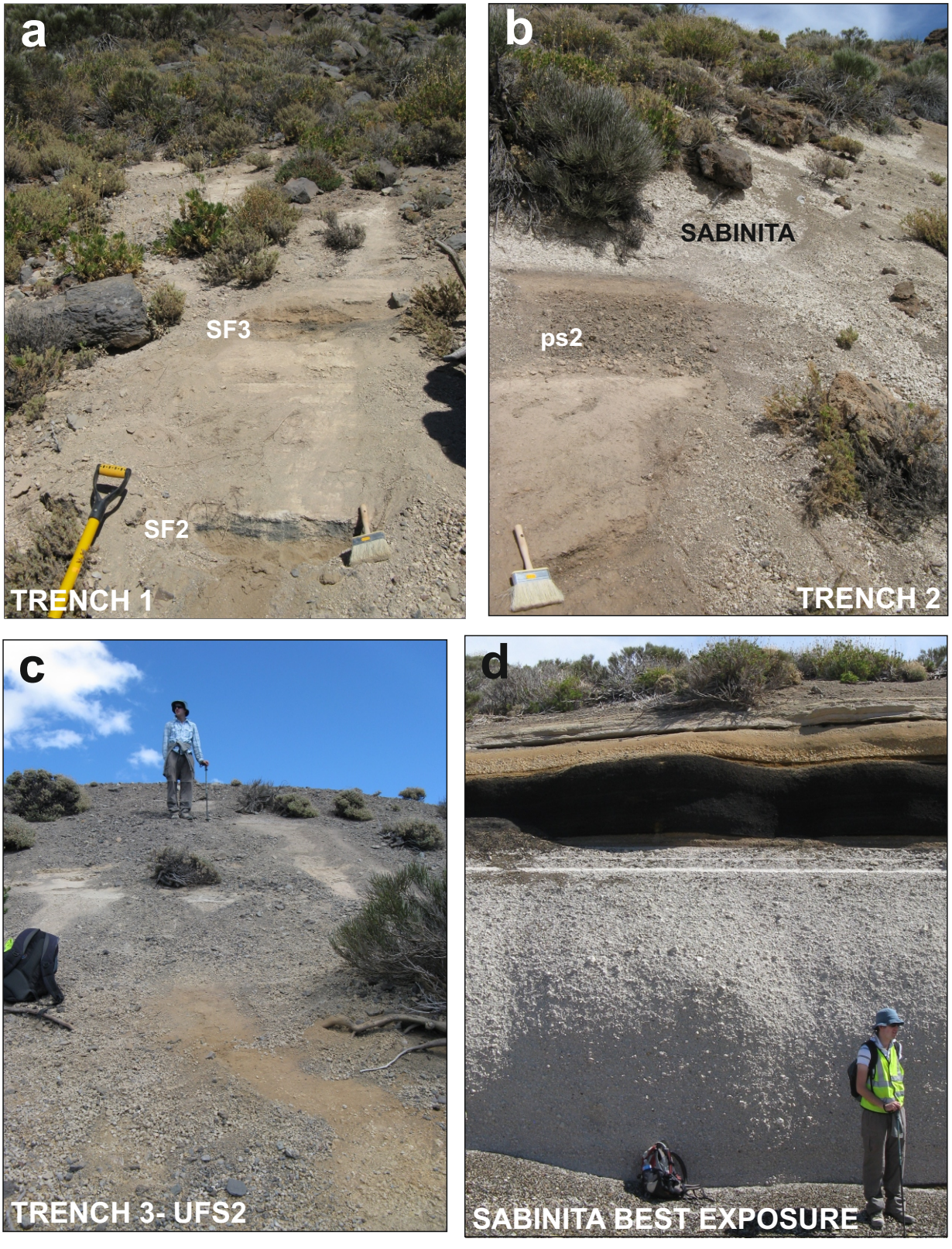
a
SF3
SF2
TRENCH 1
b
SABINITA
ps2
TRENCH 2
c
TRENCH 3- UFS2
d
SABINITA BEST EXPOSURE
e
LA CALETA BEST EXPOSURE

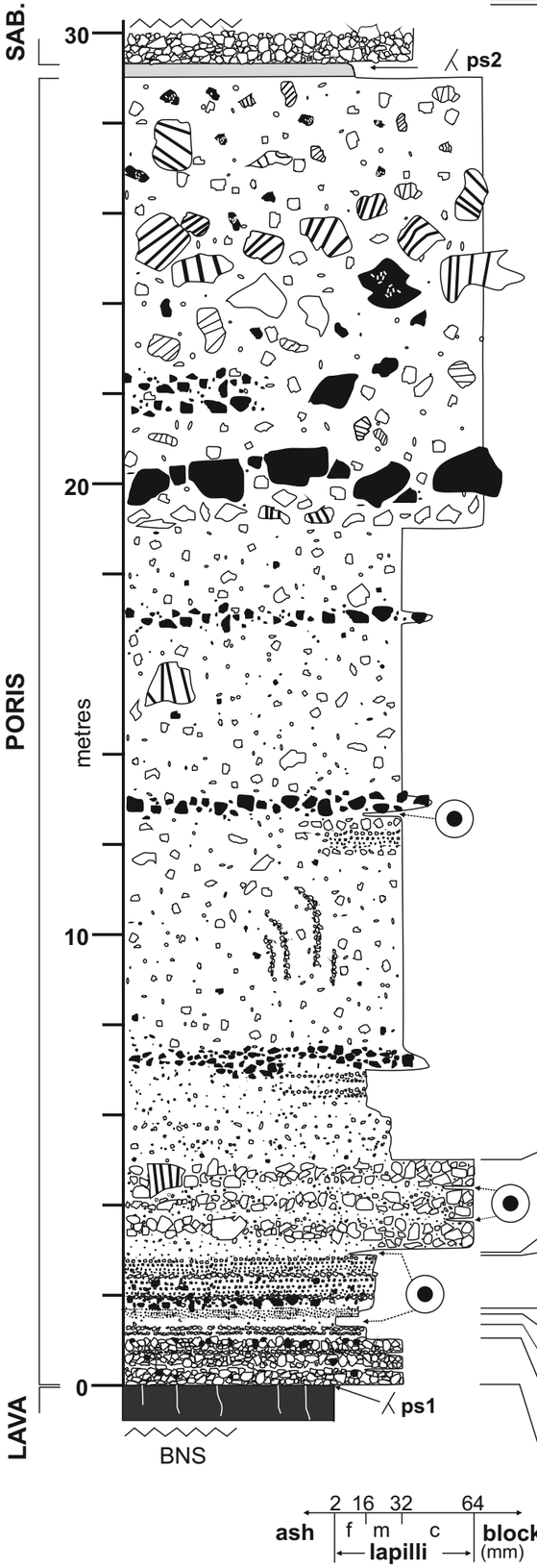

Lithocode	Description	Distribution	Interpretation
pL	Clast supported pumice lapilli. 38 cm thick, brown, weathered soil layer.	Widespread, marked by distinct white pumice clasts in scree.	Plinian/subplinian fallout event. Extended period of quiesence.
(s)plBr	Breccia lithofacies, rich in pumice blocks up to 1 m diameter. Poorly sorted, but with subtle stratification of larger blocks at some locations. Pumices are cream, pale green, and black. Many show evidence of magma mingling, where the three glass types are streaked together. Pumice blocks are contorted shapes with no evidence of rounding. In larger clasts, crystals visible with naked eye include tabular feldspars, amphiboles, pyroxenes, and cubic blue feldspathoids.	Poorly exposed in scree above cliff outcrops. Banded blocks occur in scree above log localities 8--17. Best in-situ exposures are at log locality13 and in the gully east of Montaña el Cerrillar.	Large influx of mafic pumices following eruption climax indicates that magma plumbing has changed as a result of collapse. Large blocks may reflect that mafic pumice is more resistant to abrasion.
IT	Lithic blocks ≤50 cm concentrated in a layer at base of breccia. Range of lithologies. Spallation textures and red and pink altered clasts occur. Sharp boundary where grainsize increases from mLT to plBr.	Occurs in scree directly above flat surface of cliff outcrops. Best exposed at log 10 and northern outcrops.	Lithic-rich currents generated following climactic collapse of Poris edifice. Much of this material may have bypassed to distal region.
IT	Thick exposure of massive lapilli tuff, with some local diffuse stratification. Poorly sorted and matrix-supported, pumice clasts generally ≤4 cm in diameter but some outlier clasts up to 30 cm in diameter occur. Subordinate heterogeneous lithics occur throughout, and the matrix material contains mm-scale lithics, pumices and crystals. mLT is particularly pumice rich in areas where it occurs in unconformable contact with slcrT.	Widespread.	mLT indicates periods of relative PDC steadiness.
mLT			
IT	Discontinuous layer of fine ash with accretionary pellets in south.	Log 1.	Temporary local hiatus.
(s)LT	Stratified tuff occurs locally.	Logs 1-3, and 14.	PDCs non-uniform across DH.
mLT mLTpip (ds)LT	Clast-supported, fines-poor vertical pipes of clasts ≤30 cm long occur locally. Some show evidence of shearing towards a preferred orientation. Diffusely stratified tuff occurs locally.	Only exposed at logs 3 and 4.	Elutriation pipes form as gas and fines escape following deposition, and are sheared by subsequent currents.
IT	At least three discrete lithic rich layers of tuff, ≤10 cm thick, occur within mLT. Lithics are typically ≤8 cm in diameter. Locally clasts ≤15 cm diameter occur. Clasts are heterolithic and angular to sub-angular.	Widespread. Can be correlated across 10 outcrops in south.	Lithic-rich layers are a result of increased input of lithics at source, possibly due to vent widening and/or incremental collapse, and are associated with scour and bypass.
s-ds-mLT	Variably stratified tuff occurs at this stratigraphic height, locally rich in lithics ≤3 cm in diameter at base. Stratification better developed in north than south.	Log 1-3, 5, 10 and 17: removed by scour elsewhere?	Lateral variability results from deposition from non-uniform, unsteady PDCs.
spBT spBTacc	Locally clast-supported pumice-block-rich beds stratified with fine-grained layers. Pumices typically 1-10 cm in diameter, blocks ≤30 cm in diameter occur. Larger clasts are more angular, smaller clasts are subrounded.	Widespread. Thickens into cliff at log 10. Scoured out by IT at log 7.	Hybrid deposition: coarse fallout and ballistics enter PDCs.
mTacc2	Massive ash ≤6 cm thick contains grey accretionary pellets <1 cm in diameter.	Logs 16 and 17.	Co-ig ash deposited during local hiatus.
slcrT	Planar-stratified lithic- and crystal-rich tuff (some low-angle x-strat). Inverse grading of pumices and lithics common. Hydrothermally altered lithics occur. Lower contact widely erosive with associated scour.	Widespread. Stratification varies; inverse grading at many outcrops.	Phreatomagmatic explosivity leads to influx of fine-grained, heterogeneous lithics and crystals into PDCs, and a pulsatory nature to deposition.
xscrT	Crystal-rich, cross stratified, fine-grained tuff with erosive base.	xscrT occurs across DH. Contact with slcrT can be sharp or graded.	
mTacc1	Massive white ash with AP1 and AP2 accretionary pellets ≤2 cm in diameter. Scattered subangular pumice lapilli.		Deposition from hybrid ash cloud.
//spLT	Stratified pumices in fine-grained tuff. Evidence of reworking of pumices.	Consistent exposure of mTacc and //spLT across DH.	Proximal topography affects deposition from PDCs.
//bpL pL	Three framework-supported, sub-angular to angular pumice lapilli beds (1, 3 and 5) separated by one ash rich bed (2) and one bed containing smaller, more rounded pumices (4).	Best exposed in north. 5 beds exposed at log 16. Considerable thickness changes.	Plinian fallout with hiatuses in deposition.
	Soil ≤ 5 cm thick. Fine-grained vesicular lava sequence >30 m thick.		

Key: pumice lapilli; lithic clasts; black & banded pumices; accretionary pellets; palaeosol; flow unit boundary

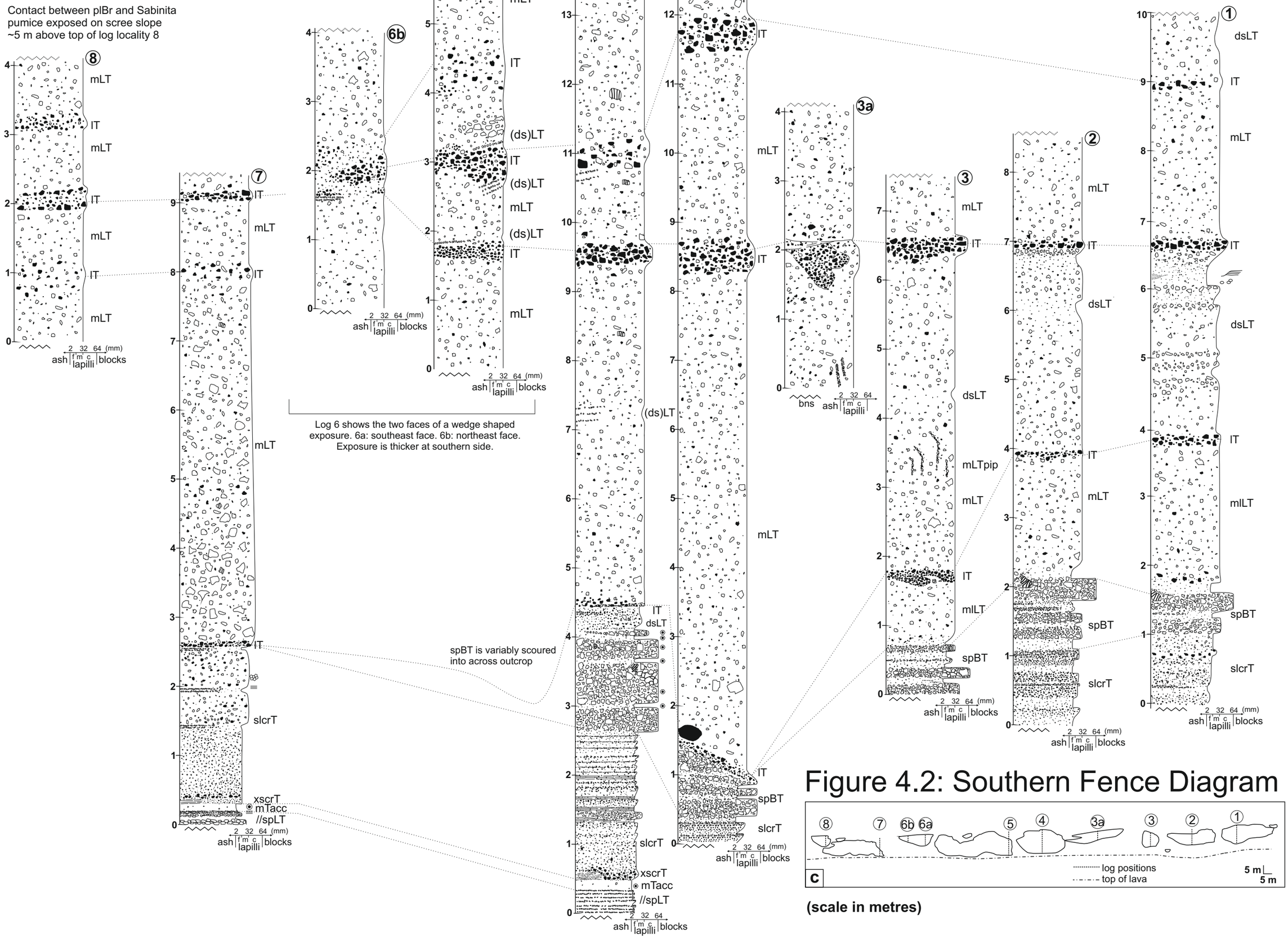

Figure 4.2: Southern Fence Diagram

(scale in metres)

Figure 4.3: Central Fence Diagram

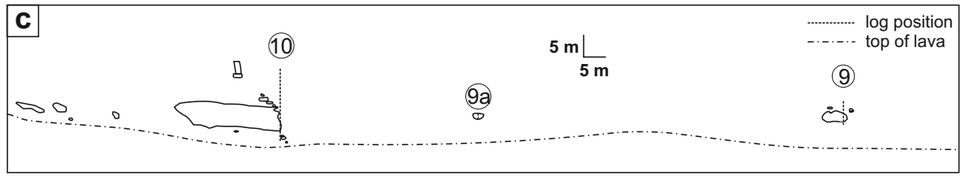

(scale in metres)

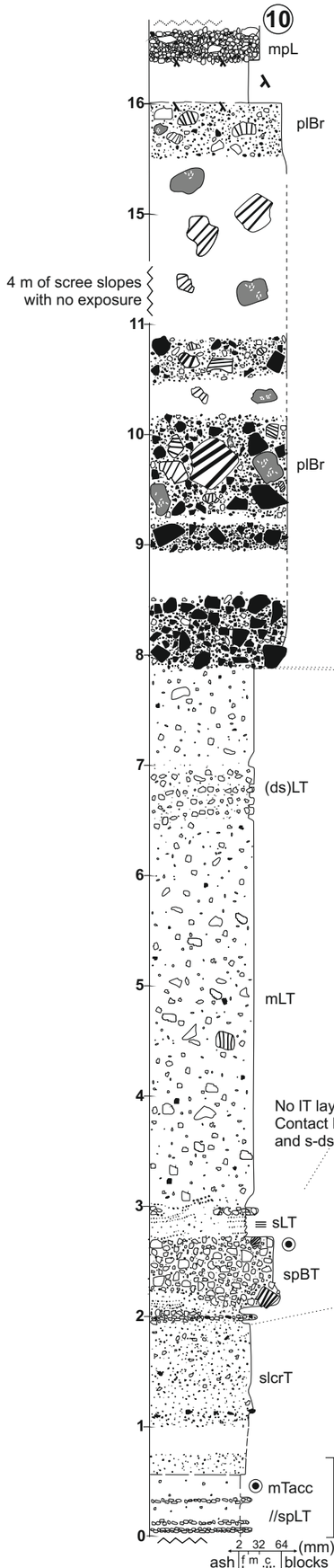

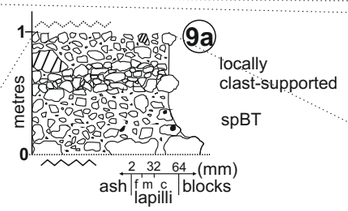

?

Outcrops 9 and 9a are set further back
on the cliff slope than 10 (see box c).
The apparent change in spBT stratigraphic
position between outcrops is thus partly a
3D-cut effect. At locality 10 spBT beds are
seen to develop outwards from sLT with
increasing distance from source.

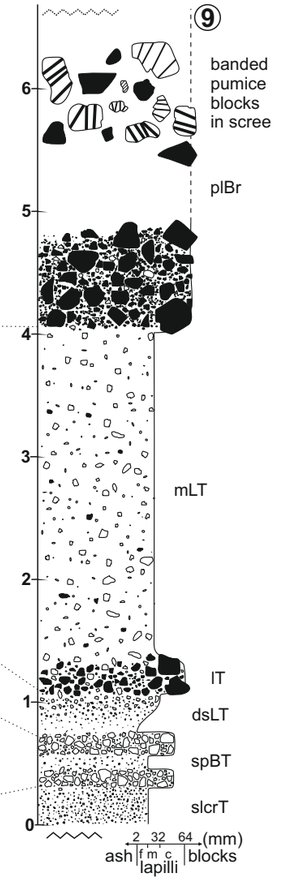

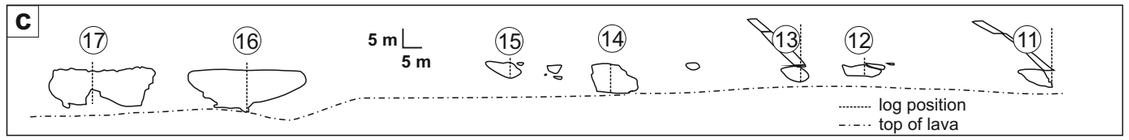

Figure 4.4: Northern Fence Diagram

(scale in metres)

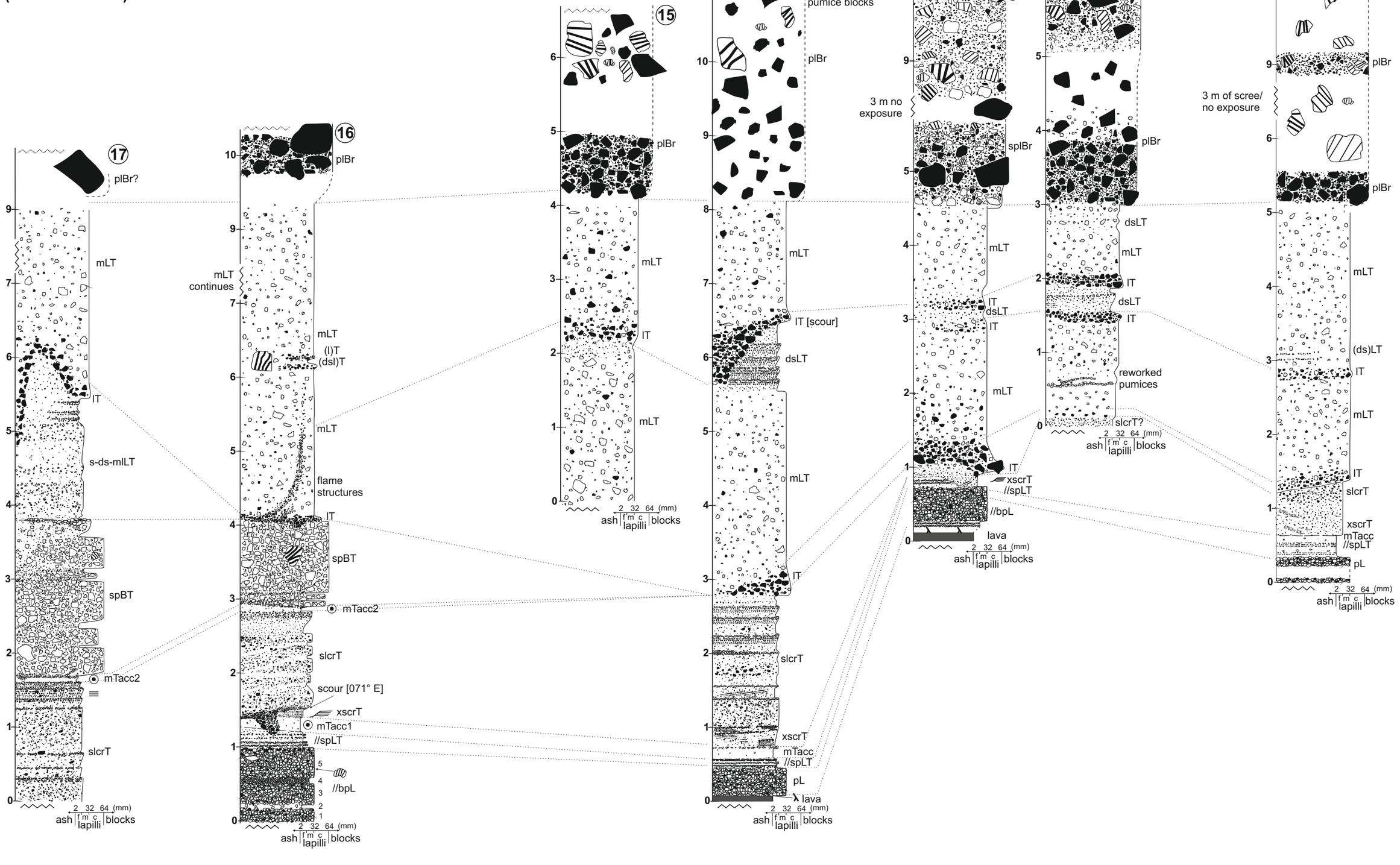

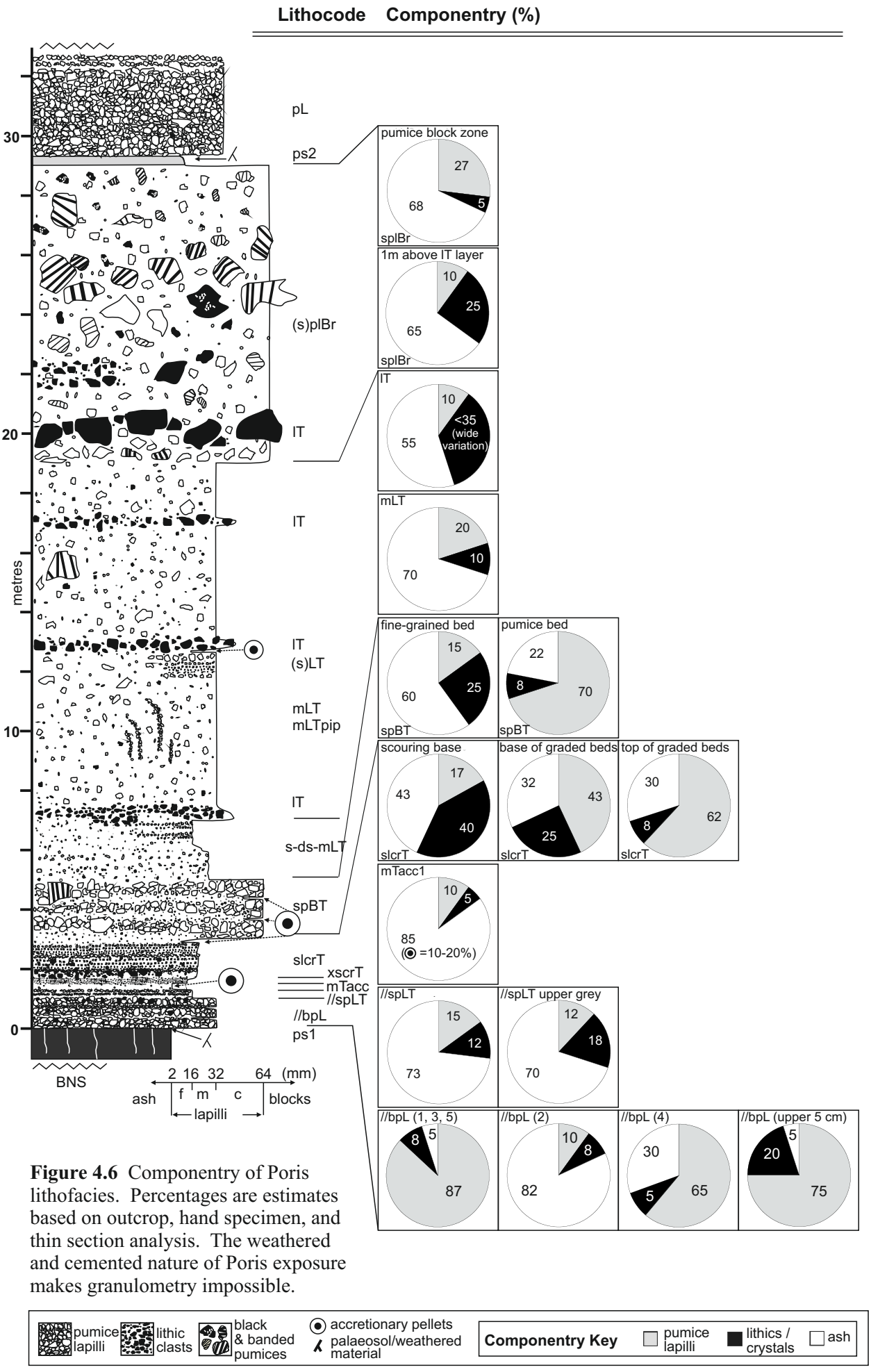

Figure 4.6 Componentry of Poris lithofacies. Percentages are estimates based on outcrop, hand specimen, and thin section analysis. The weathered and cemented nature of Poris exposure makes granulometry impossible.

Key

pumices

lithics

accretionary pellets

full outcrop not shown

coated lapilli (pumice centre)

mm-scale stratification

(scale in centimetres)

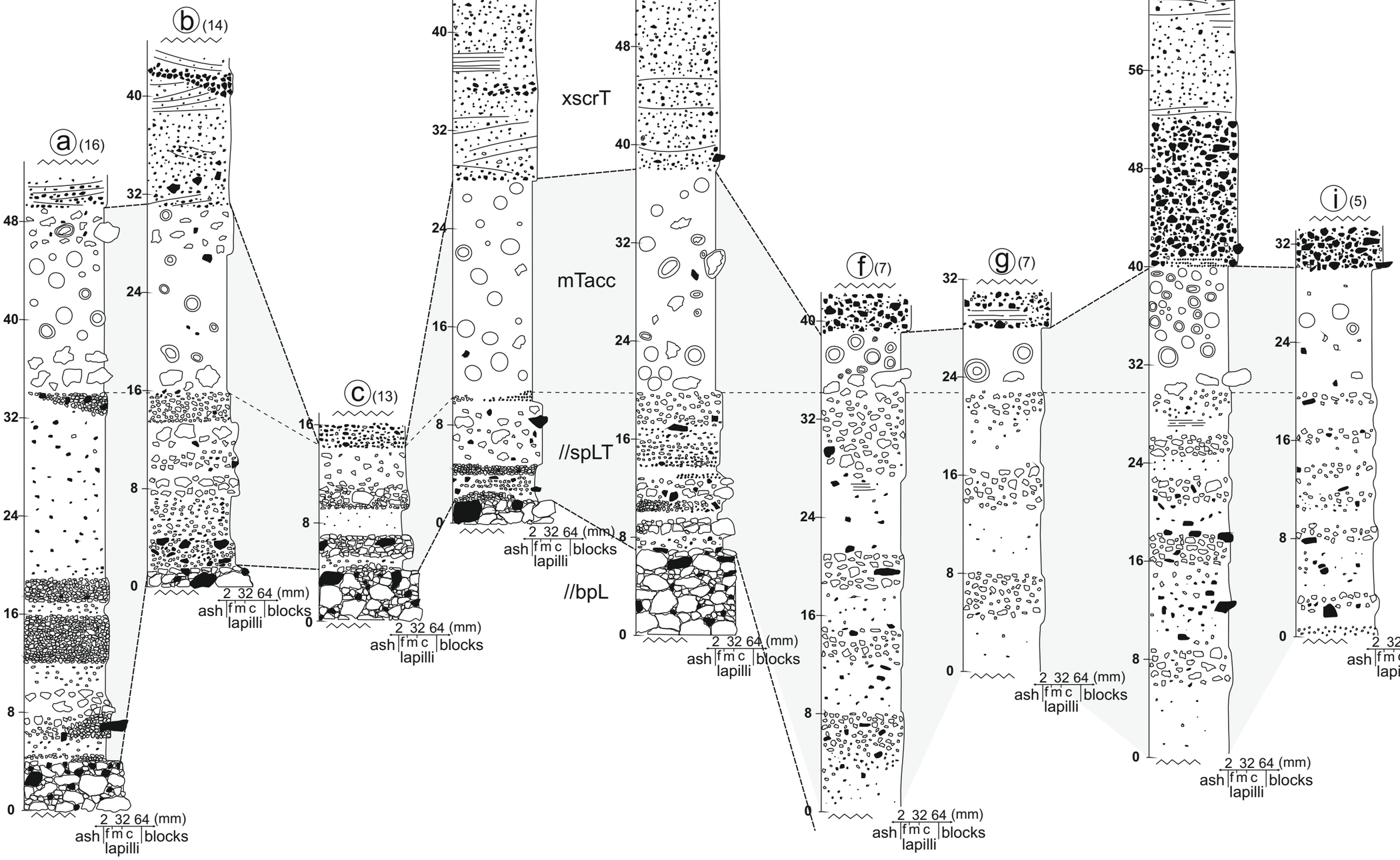

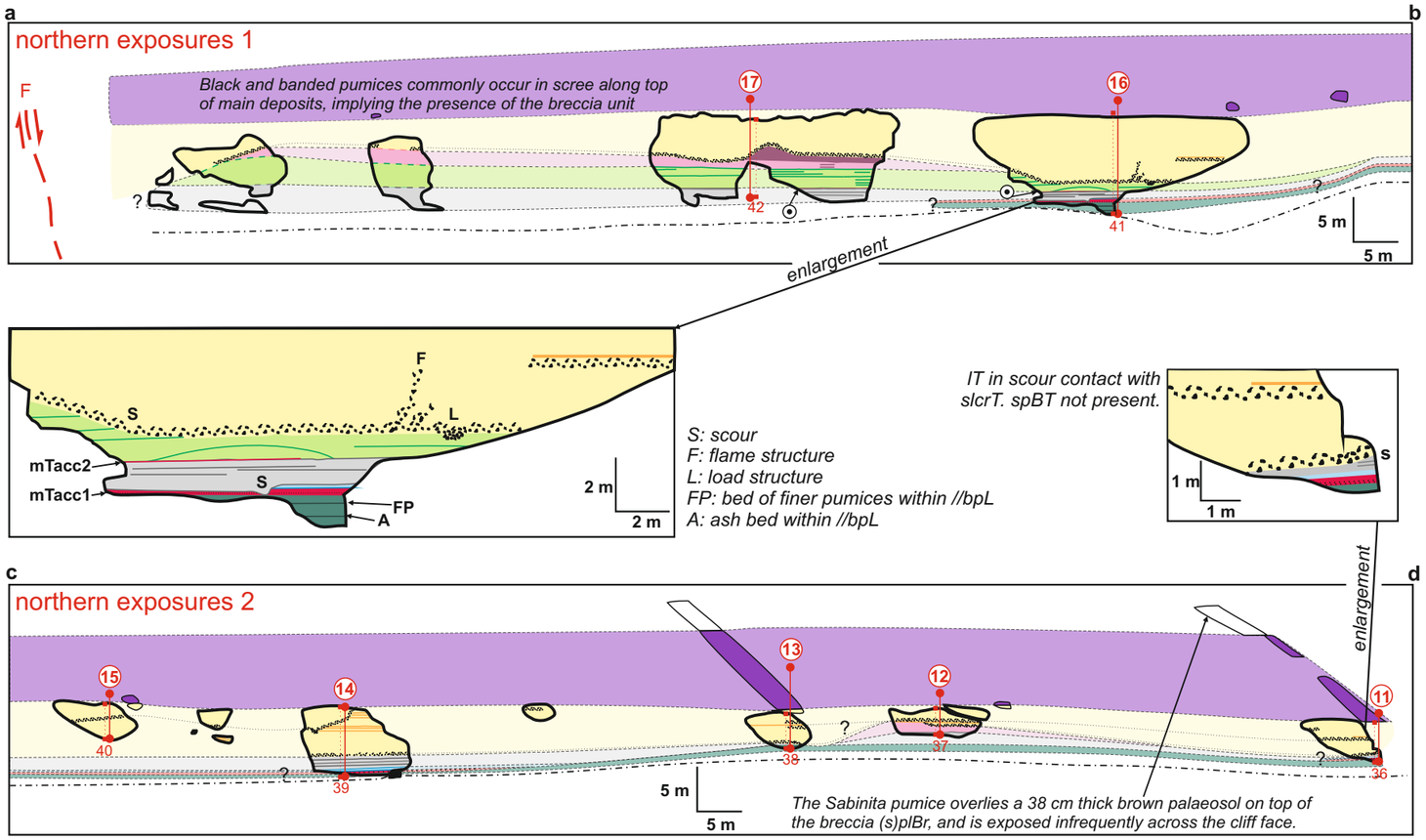

KEY

- **Sabinita[1] pumice:** Plinian/sub-Plinian fallout unit [also known as 'Arafo[2]']
- [soil and weathered material 38 cm thick]
- **(s)plBr:** locally stratified pumice-block breccia with lithic-block layer at base
- **mLTpip:** massive lapilli tuff with elutriation pipes
- **mLT:** massive lapilli tuff
- **dsLT:** diffuse-stratified lapilli tuff
- **lT:** lithic-rich tuff [lithic ornament not to scale]
- **s-ds-mlLT:** stratified to diffuse-stratified to massive lapilli tuff, locally lithic rich [dark pink = finer-grained layer]
- **spBT:** stratified pumice-block tuff [dark green represents fine-grained layers]
- **slcrT(i):** stratified lithic- and crystal-rich tuff [dark grey = finer grained layers]
- **xscrT:** cross-stratified crystal-rich tuff
- **mTacc:** tuff with accretionary pellets
- **//spLT:** parallel stratified pumice lapilli within tuff
- **//bpL:** parallel bedded pumice lapilli [dark turqouise = layers of ash/finer pumices]
- [soil ≤5 cm thick]
- **lava**
- **top of exposed lava flows along section**
- **inferred lithofacies boundary**
- **inferred continuation of scour**
- F — — **fault**
- 1 — ● **digitised log location**
- 6 ····· ▪ **field log location**
- ◉ **accretionary pellets**
- ? **unknown relationship**

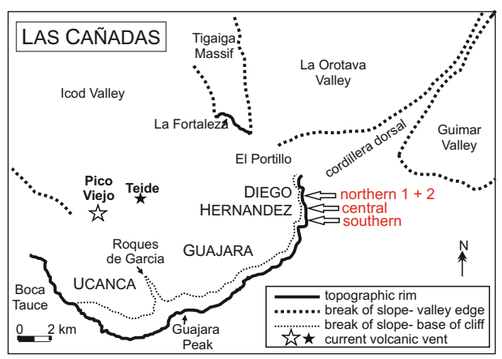

PHASE 1: PLINIAN DEPOSITION

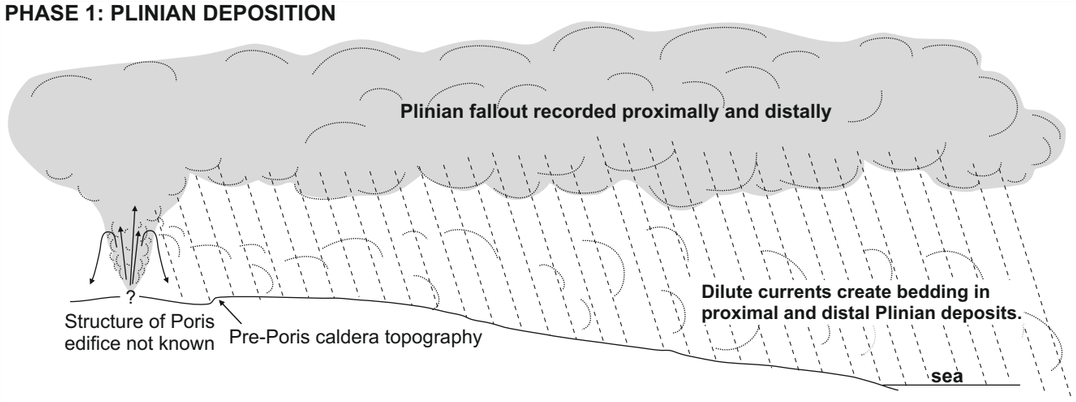

PHASE 2: FIRST PDC GENERATED

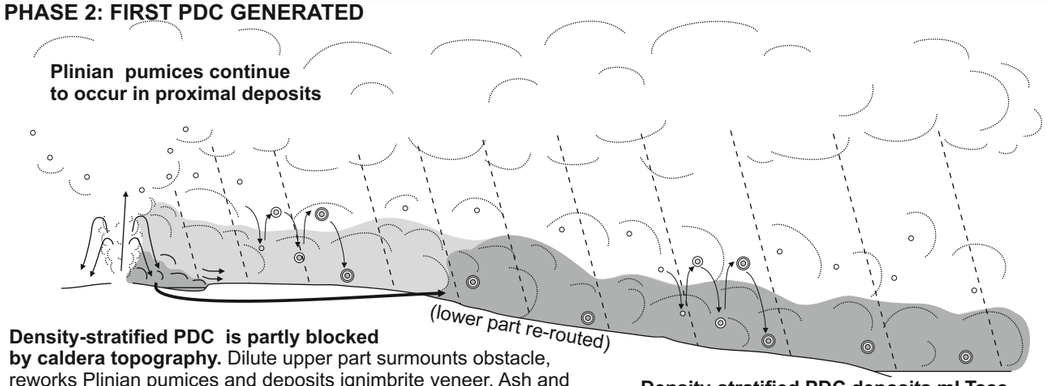

Density-stratified PDC is partly blocked by caldera topography. Dilute upper part surmounts obstacle, reworks Plinian pumices and deposits ignimbrite veneer. Ash and accpells deposited from hybrid zone of plume margin and co-ig cloud.

Density-stratified PDC deposits mLTacc valley-fill and veneer facies distally.

PHASE 3: PHREATOMAGMATISM

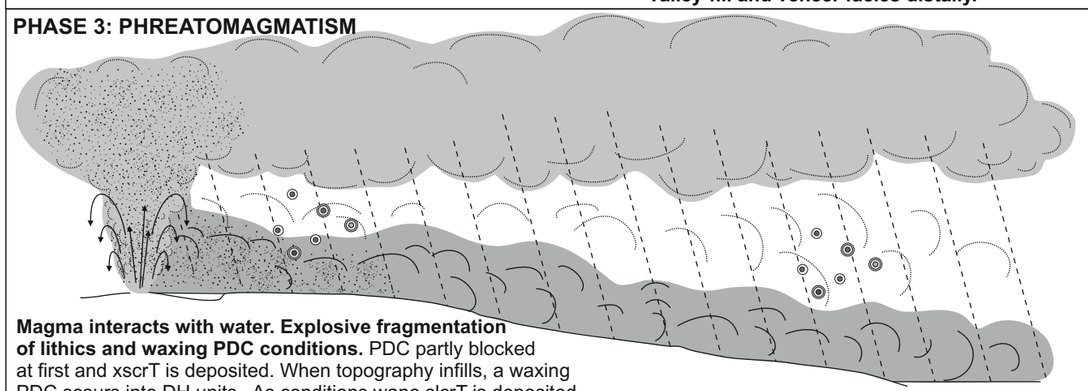

Magma interacts with water. Explosive fragmentation of lithics and waxing PDC conditions. PDC partly blocked at first and xscrT is deposited. When topography infills, a waxing PDC scours into DH units. As conditions wane slcrT is deposited. Pulsatory conditions, either at source or in the current, are recorded as graded beds. Grey accpels deposit during localised hiatus.

mLT valley-fill and veneer facies are deposited distally. Grey accpels deposit during distal hiatus.

PHASE 4: HYBRID FALL AND FLOW

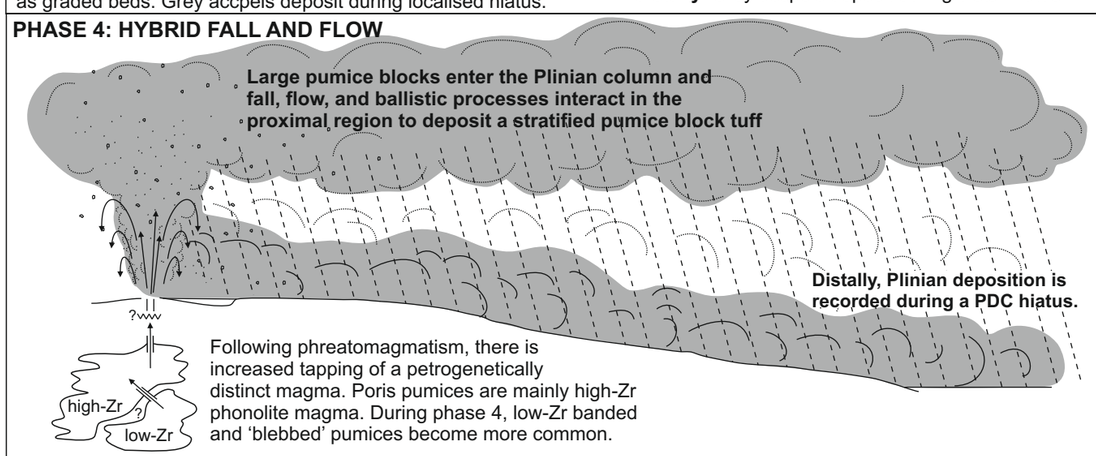

Following phreatomagmatism, there is increased tapping of a petrogenetically distinct magma. Poris pumices are mainly high-Zr phonolite magma. During phase 4, low-Zr banded and 'blebbed' pumices become more common.

PHASE 5: MAIN STAGE PDC SCOUR, BYPASS AND DEPOSITION

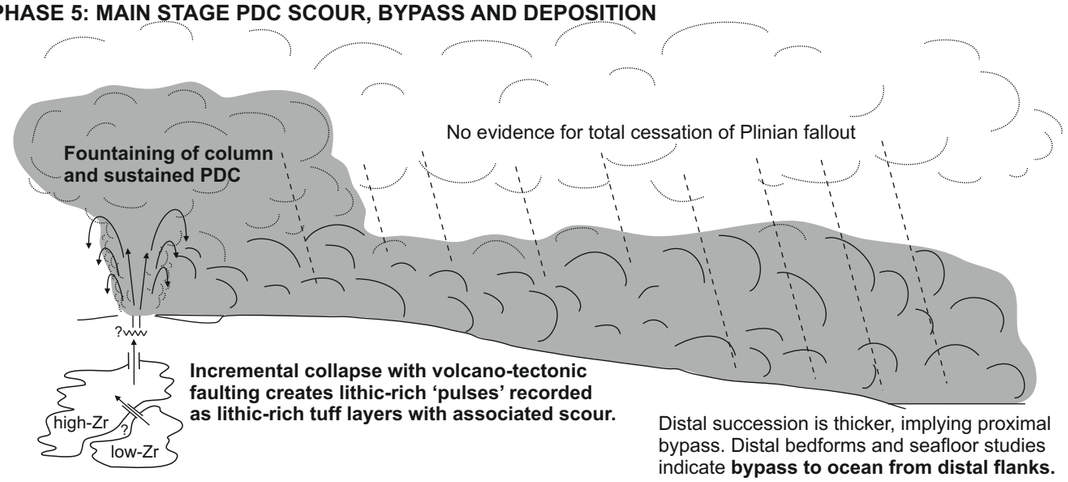

Incremental collapse with volcano-tectonic faulting creates lithic-rich 'pulses' recorded as lithic-rich tuff layers with associated scour.

Distal succession is thicker, implying proximal bypass. Distal bedforms and seafloor studies indicate **bypass to ocean from distal flanks.**

PHASE 6: CLIMACTIC COLLAPSE

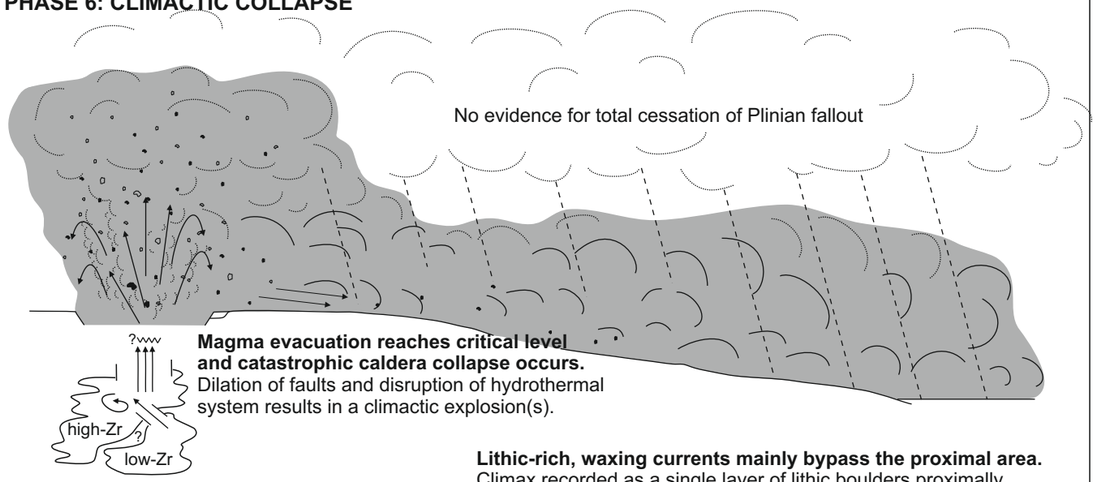

Magma evacuation reaches critical level and catastrophic caldera collapse occurs. Dilation of faults and disruption of hydrothermal system results in a climactic explosion(s).

Lithic-rich, waxing currents mainly bypass the proximal area. Climax recorded as a single layer of lithic boulders proximally. Distally, ignimbrite containing lithic-rich breccia layers are deposited. Bypass of pyroclastic material to the ocean continues.

PHASES 7 & 8: WANING PDC AND FALLOUT

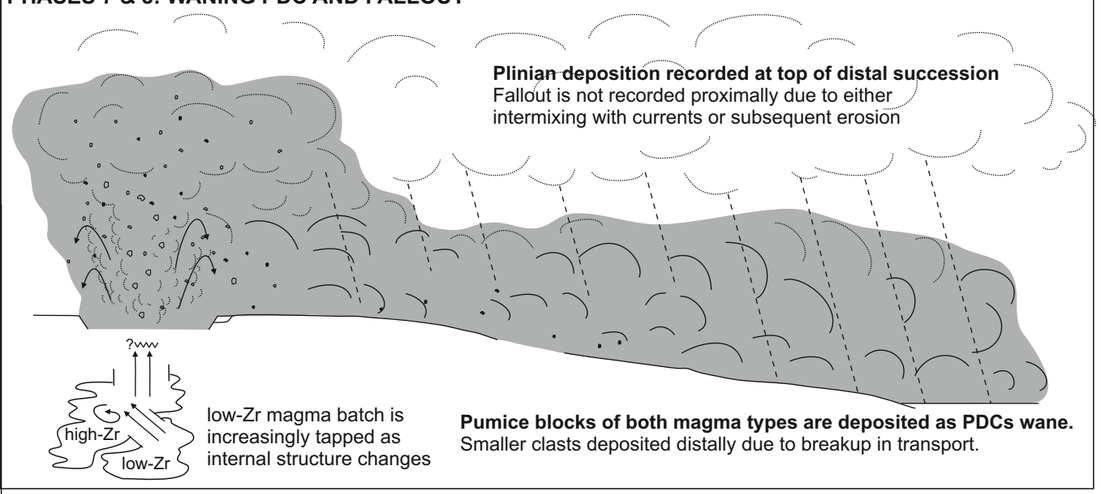

low-Zr magma batch is increasingly tapped as internal structure changes

Pumice blocks of both magma types are deposited as PDCs wane. Smaller clasts deposited distally due to breakup in transport.

PROXIMAL (this study) ←— ~15 km (**DIAGRAMS NOT TO SCALE**) —→ DISTAL (Brown & Branney, 2004, Edgar *et al.*, 2002, and this study)